

AWARD NUMBER: W81XWH-12-1-0138

TITLE: Early Detection of Amyloid Plaque in Alzheimer's Disease via X-ray Phase CT

PRINCIPAL INVESTIGATOR: Xiangyang Tang

CONTRACTING ORGANIZATION: Emory University
Atlanta, GA 30322

REPORT DATE: August 2016

TYPE OF REPORT: Final

PREPARED FOR: U.S. Army Medical Research and Materiel Command
Fort Detrick, Maryland 21702-5012

DISTRIBUTION STATEMENT: Approved for Public Release;
Distribution Unlimited

The views, opinions and/or findings contained in this report are those of the author(s) and should not be construed as an official Department of the Army position, policy or decision unless so designated by other documentation.

REPORT DOCUMENTATION PAGE

*Form Approved
OMB No. 0704-0188*

Public reporting burden for this collection of information is estimated to average 1 hour per response, including the time for reviewing instructions, searching existing data sources, gathering and maintaining the data needed, and completing and reviewing this collection of information. Send comments regarding this burden estimate or any other aspect of this collection of information, including suggestions for reducing this burden to Department of Defense, Washington Headquarters Services, Directorate for Information Operations and Reports (0704-0188), 1215 Jefferson Davis Highway, Suite 1204, Arlington, VA 22202-4302. Respondents should be aware that notwithstanding any other provision of law, no person shall be subject to any penalty for failing to comply with a collection of information if it does not display a currently valid OMB control number. **PLEASE DO NOT RETURN YOUR FORM TO THE ABOVE ADDRESS.**

1. REPORT DATE August 2016			2. REPORT TYPE Final		3. DATES COVERED 15May2012 – 14May2016	
4. TITLE AND SUBTITLE Early Detection of Amyloid Plaque in Alzheimer's Disease via X-ray Phase CT			5a. CONTRACT NUMBER W81XWH-12-1-0138		5b. GRANT NUMBER	
					5c. PROGRAM ELEMENT NUMBER	
6. AUTHOR(S) Xiangyang Tang E-Mail: xiangyang.tang@emory.edu			5d. PROJECT NUMBER		5e. TASK NUMBER	
					5f. WORK UNIT NUMBER	
7. PERFORMING ORGANIZATION NAME(S) AND ADDRESS(ES) Emory University Office of Grant and Cont Acctng 201 Dowman Drive Atlanta, GA 30322-1018			8. PERFORMING ORGANIZATION REPORT NUMBER			
9. SPONSORING / MONITORING AGENCY NAME(S) AND ADDRESS(ES) U.S. Army Medical Research and Materiel Command Fort Detrick, Maryland 21702-5012			10. SPONSOR/MONITOR'S ACRONYM(S)			
			11. SPONSOR/MONITOR'S REPORT NUMBER(S)			
12. DISTRIBUTION / AVAILABILITY STATEMENT Approved for Public Release; Distribution Unlimited						
13. SUPPLEMENTARY NOTES						
14. ABSTRACT <p>In this project, we proposed to develop the x-ray phase contrast CT (PCCT) imaging method for early detection of amyloid plaque in Alzheimer's disease, with three Specific Aims: #1 Develop and optimize an x-ray PCCT to explore the methodology of direct imaging of AP; #2 Evaluate the PCCT's capability of imaging Aβ₁₋₄₀/Aβ₁₋₄₂ peptides/fibrils at the concentrations existing in AD brain; #3 Verify the PCCT's capability of direct imaging of AP in AD using postmortem brain specimens. Even though the fabrication of x-ray gratings were much more complicated and challenging than initially anticipated, the prototype x-ray PCCT has been built successfully and works in full functionality. We imaged the specimens of AD brain, normally aged brain and pathologically aged brain, with three major findings: (i) the contrast between grey matter and white matter in x-ray PCCT image is substantially higher than that in conventional CT image, (ii) given identical x-ray dose, the PCCT image of brain specimen is of substantially higher signal-to-noise ratio (SNR) than that of conventional CT image, and (iii) even with substantially improved SNR, the PCCT still cannot convincingly differentiate the AD brain specimen with amyloid plaques from the normal aged brain specimen without amyloid plaques, probably due to the fact that, limited by the output power of micro-focus x-ray tube, the acquisition of one set of projection by the prototype system takes about 12 hours, which may degrade the prototype system's imaging performance significantly (thus opportunity for future research). Under partial support of this grant, five journal papers have been published in <i>Medical Physics</i>, and more than eight papers in leading international conferences.</p>						
15. SUBJECT TERMS Alzheimer disease, Amyloid plaque, X-ray phase contrast, X-ray phase contrast imaging, X-ray phase contrast CT						
16. SECURITY CLASSIFICATION OF:			17. LIMITATION OF ABSTRACT Unclassified	18. NUMBER OF PAGES 109	19a. NAME OF RESPONSIBLE PERSON USAMRMC	
a. REPORT Unclassified	b. ABSTRACT Unclassified	c. THIS PAGE Unclassified			19b. TELEPHONE NUMBER (include area code)	

Table of Contents

	<u>Page</u>
1. Introduction.....	1
2. Keywords.....	1
3. Accomplishments.....	1
4. Impact.....	10
5. Changes/Problems.....	10
6. Products.....	10
7. Participants & Other Collaborating Organizations.....	12
8. Special Reporting Requirements.....	12
9. Appendices.....	12
10. References.....	13

1. INTRODUCTION: As the elderly population increases, dementia due to Alzheimer's disease (AD) has emerged as a major threat to human's health¹⁻³. Recently, the x-ray CT based on a new imaging mechanism—refraction—is emerging as a new technology to improve CT's capability of differentiating soft tissues⁴⁻¹⁰. We propose to develop the x-ray phase contrast CT imaging method with an x-ray tube and gratings for direct detecting of amyloid plaques in Alzheimer's brain. It is hypothesized that the disparity in their refractive property can generate contrast between amyloid plaques and surrounding neuronal tissues in AD and the contrast is sufficient for imaging. Without the involvement of contrast agent or molecular probes, the so-called BBB (brain blood barrier) can thus be avoided. The project started on 05/15/2012 and ended on 05/14/2016, with a no cost one year extension from 05/15/2015 to 05/14/2016. Here is the final report of the project, covering the key research accomplishments, reportable outcomes and conclusions, based on the preliminary data acquired over the span of four years.

2. KEYWORDS: Alzheimer's disease, amyloid plaque, A-beta, x-ray phase contrast, CT, x-ray phase contrast CT, x-ray differential phase contrast CT, Talbot interferometer, grating-based differential phase contrast CT.

3. ACCOMPLISHMENTS:

What were the major goals of the project?

In order to be objective and complete, the three Specific Aims (SAs) specified in the Statement of Work (SOW) are reiterated here, and the final report is organized in line with these SAs as adequately as possible.

SA#1 Develop and optimize an x-ray phase CT to explore the methodology of direct imaging of AP;
Outcome: An x-ray tube- and grating-based phase CT as the foundation for the pursuit of SA #2 and #3.

SA#2 Evaluate the x-ray phase CT's capability of imaging $A\beta_{1-40}/A\beta_{1-42}$ peptides/fibrils at the concentrations existing in AD brain;

Outcome: A quantitative understanding of x-ray phase CT's capability in imaging the $A\beta_{1-40}$ and $A\beta_{1-42}$ fibrils.

SA#3 Verify the x-ray phase CT's capability of direct imaging of AP in AD using postmortem brain specimens.

Outcome: Quantitatively evaluated and verified performance of x-ray phase CT for imaging APs in AD.

What was accomplished under these goals?

Project Timeline: The original timeline specified in the SOW is presented in Table I. Mainly due to two reasons – (i) the fabrication/optimization of x-ray gratings were much more complicated and challenging than what we initially anticipated and (ii) the acquisition of one set of projection data in the x-ray phase contrast CT takes about 12 hours because of the limitation in output power of the micro-focus x-ray tube, a one year no-cost extension of this project has been request and approved. Presented in Table II is the revised timeline, with the new ending date at 05/14/2016/.

Table I. The original project timeline specified in the project's SOW.

Tasks	Q1	Q2	Q3	Q4	Q5	Q6	Q7	Q8	Q9	Q10	Q11	Q12
D.1.1: System construction			→									
D.1.2: System optimization				→								
D.2: Performance: Phantom study						→						
D.3: Performance: Specimen study									→			

Table II. The revised project timeline specified in the project's SOW with one year extension.

Tasks	Q ₁	Q ₂	Q ₃	Q ₄	Q ₅	Q ₆	Q ₇	Q ₈	Q ₉	Q ₁₀	Q ₁₁	Q ₁₂	Q ₁₃	Q ₁₄	Q ₁₅	Q ₁₆
D.1.1: System construction																
D.1.2: System optimization																
D.2: Phantom study																
D.3: Specimen study																

Accomplishments towards Specific Aim 1 and 2:

An x-ray phase contrast CT, which consists of a micro-focus tube, a C-MOS flat panel x-ray detector with $48\mu\text{m}$ detector cell dimension, a linear motor-driven stepper and two x-ray gratings G_1 and G_2 , has been prototyped in the PI's lab (see Fig. 1) for carrying out the tasks of this project. The two gratings G_1 and G_2 are the key components of the prototype system, which were fabricated in the NanoTechnology Research Center of GaTech (see Fig. 2). The imaging performance of this prototype system has gone through optimization, with an emphasis on coping with phase wrapping¹¹ and the imperfection¹³ in G_1 and G_2 and the possible negative influence on imaging performance. The prototype x-ray phase contrast CT system is now fully functioning, with every aspect of imaging performance, but the x-ray source power and the resultant data acquisition time, approaches what is designed (see Fig. 1). The relatively long data acquisition time can be proportionally shortened using a micro-focus tube with a larger output power. We summarize the development and optimization that have been made by us to substantially improve the prototype x-ray phase contrast CT system's imaging performance for imaging specimen of AD brain as listed below.

A. System integration and optimization–Phase de-wrapping: There inevitably exists imperfection in either grating G_1 or G_2 , or both, which may cause the so-called phase wrapping phenomenon in projection data, as illustrated in Fig. 3 (a). We developed a phase de-wrapping approach based on a theoretical framework derived by us¹¹, which can substantially reduce, if not eliminate, the artifacts caused by the phase-wrapping phenomenon, as demonstrated in Fig. 3 (b), in which a cylindrical water phantom consisting of four (4) cylindrical targets made of glycerol, alcohol, isopropanol and air (namely organic phantom henceforth) is utilized.

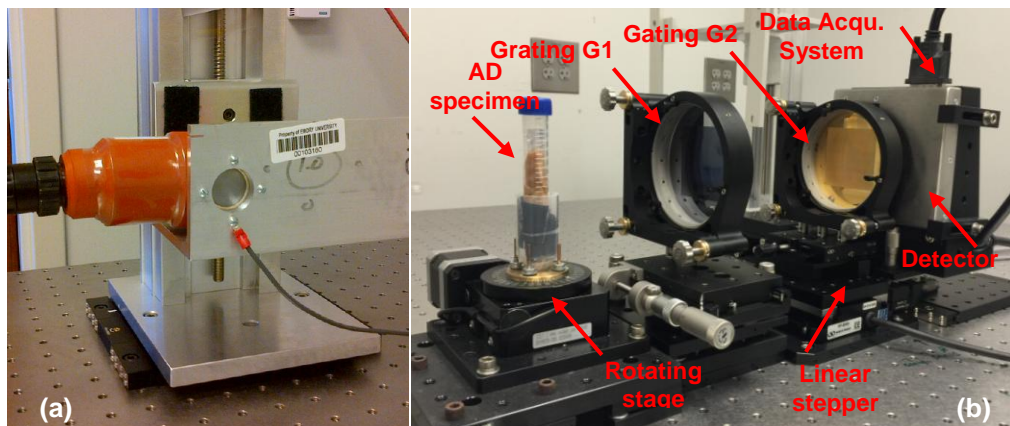


Figure 1. A picture of the prototype x-ray phase CT system that is fully functioning in the PI's lab: (a) the micro focus x-ray tube and (b) the rest of the system, including rotating stage, grating G1, grating G2, linear stepper, flat panel x-ray detector and data acquisition system.

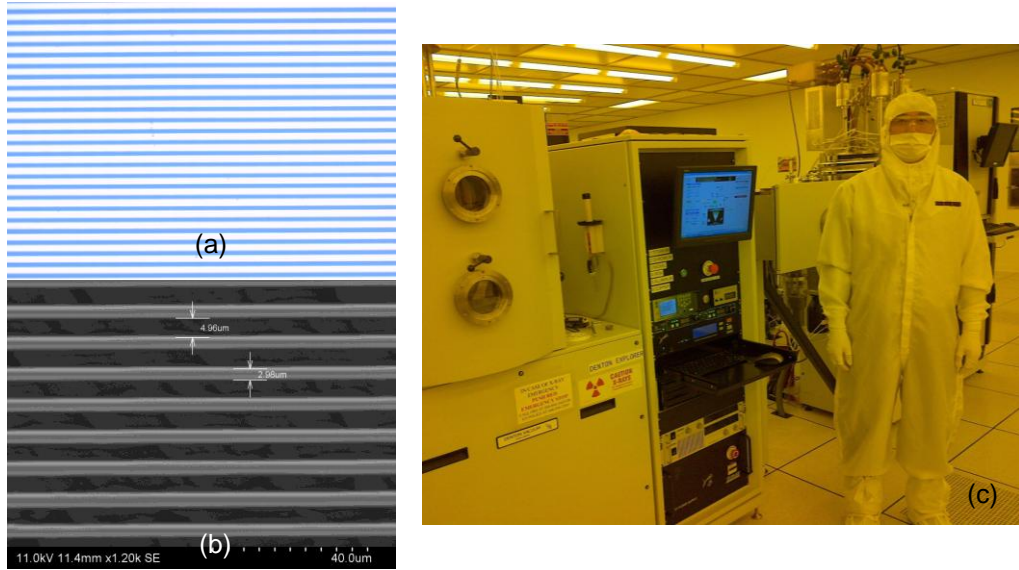


Figure 2. The lithography mask of phase grating G_1 photographed by a microscope at 50 time magnification (a), the grating G_1 photographed by an SEM (scanning electronic microscope) (b), and a picture of the PI who is working at the clean room of GaTech's NanoTechnology Research Center (c).

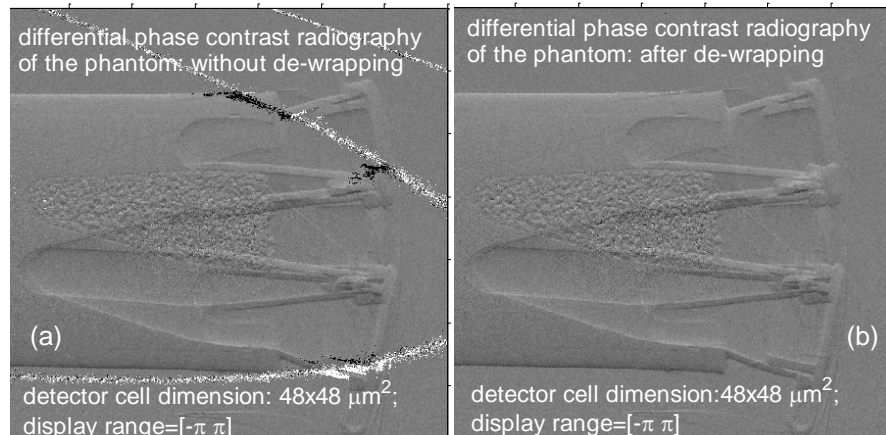


Figure 3. The x-ray phase contrast projection images of an organic material phantom without phase de-wrapping (a) and with phase de-wrapping (b).

B. System integration and optimization–Extension of FOV: As we can see in Fig. 4, with phase de-wrapping, the field of view in the projection image can be effectively extended to be equal to the active area of gratings G_1 and G_2 ($60 \times 60 \text{ mm}^2$). As such, the FOV in tomographic image can be extended accordingly, as demonstrated in Fig. 4.

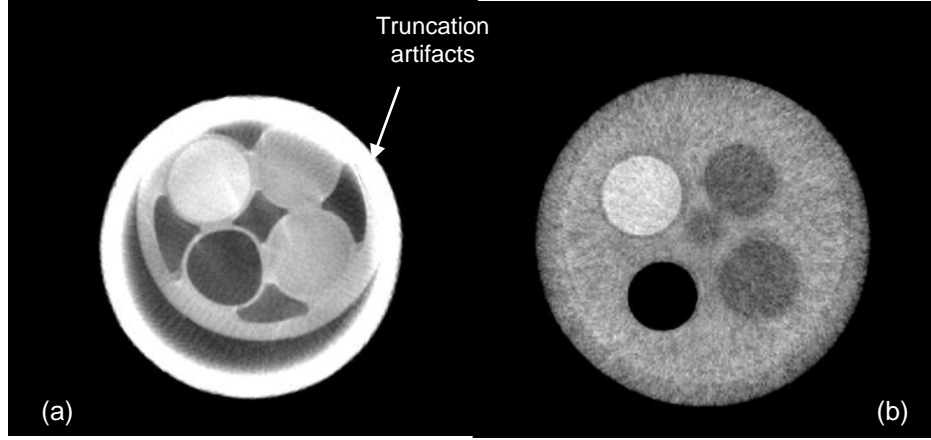


Figure 4. The x-ray phase contrast CT images of the organic material phantom with FOV truncated by artifacts due to phase-wrapping (**a**) and with FOV extended by removing the artifacts caused by phase wrapping in the projection domain (**b**).

C. System integration and optimization—Reduction of artifacts caused by twin-peaks: The imperfection in fabrication of grating G1 and G2 causes not only phase wrapping in data acquisition, but also the so-called feature of “twin-peaks” in the phase-shifting curves (PSCs), as illustrated in Fig. 5(a)^{13,14}. If not handled adequately, the twin-peaks can generate artifacts in reconstructed x-ray phase contrast images, as exemplified in Fig. 5 (b). We derived a theoretical framework to characterize the twin-peaks phenomenon and developed an algorithm to significantly reduce, if not eliminate, the artifacts caused by the phenomenon of twin peaks, as shown in Fig. 5 (c).

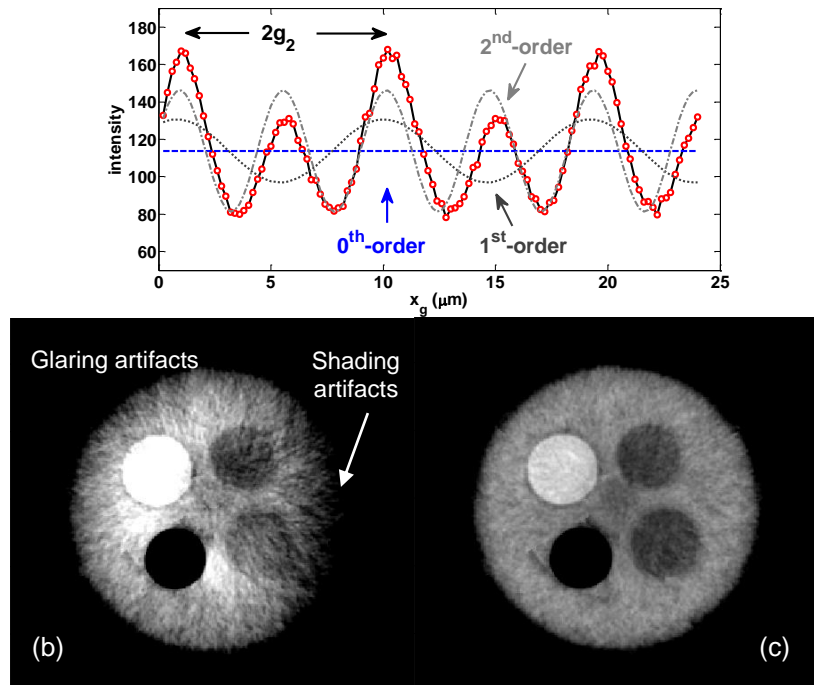


Figure 5. The twin-peaks phenomenon existing in phase stepping curve of the phase contrast CT prototyped in the PI’s lab (**a**) and image of the organic material phantom with artifacts caused by the twin-peaks phenomenon (**b**) and that with the artifacts removed.

D. System integration & optimization–Imaging performance: Transverse x-ray phase contrast CT image of the organic material phantom reconstructed from the projection data acquired at cell dimension $96 \times 96 \mu\text{m}^2$ and $144 \times 144 \mu\text{m}^2$ are presented in Fig. 6 (a') and (b'), respectively. For comparison, their counterparts in the attenuation contrast acquired at roughly identical x-ray dose are displayed in Fig. 6 (a) and (b). The contrast-to-noise ratio (CNR) is measured between the glycerol target and its surroundings. It is observed that, given identical x-ray dose, the CNR in phase contrast CT images at detector cell dimension $96 \times 96 \mu\text{m}^2$ and $144 \times 144 \mu\text{m}^2$ are 140- and 76-folds larger than their counterparts in the attenuation contrast, showing the huge potential capability of x-ray phase contrast CT in soft tissue differentiation.

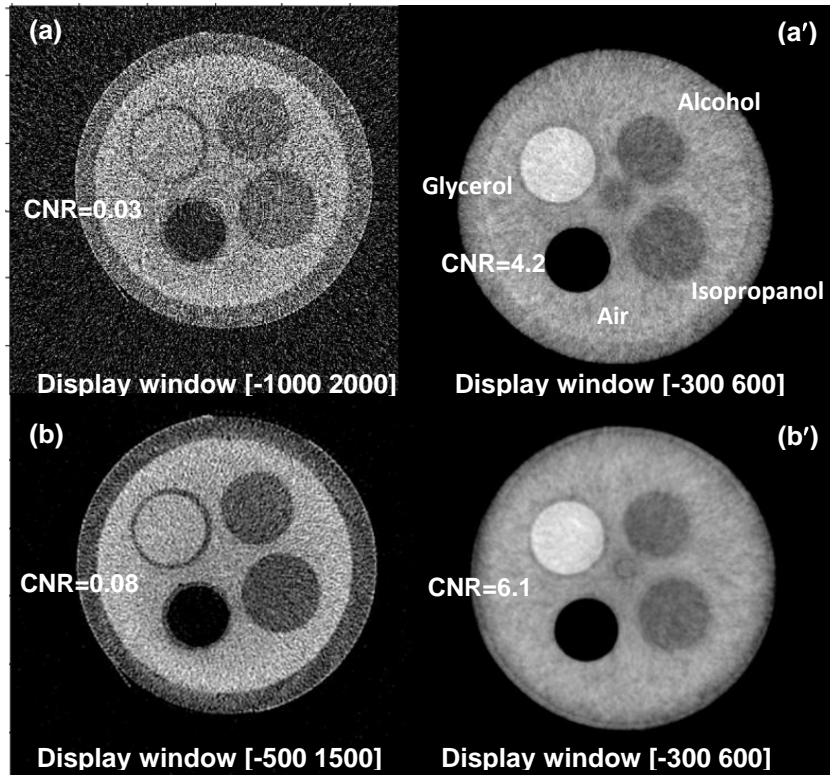


Figure 6. CT images of the organic material phantom corresponding to attenuation contrast (left column) and phase contrast (right column) at detector cell dimension $96 \mu\text{m}$ (top row) and $144 \mu\text{m}$ (bottom row).

E. Subsystem/components–A β -peptide phantoms: As specified in SA#2 of the SOW, using the specially designed A β -phantoms, we'll investigate the CNR of A β_{1-40} and A β_{1-42} fibrils in x-ray phase contrast CT imaging, as a function over the molar concentrations corresponding to normal, pathologic and Alzheimer's brains, in which the amyloid precursor protein (APP) will be included as a reference. Toward this goal, we have made three PMMA (Polymethyl methacrylate) frames for installing the A β -phantoms, and shown in Fig. 7(a) are the major parts (bodies and caps). As initially specified, the tunnels drilled in the PMMA body will be filled with A β_{1-40} /A β_{1-42} peptides/fibrils solutions at selected concentrations (see Table I). The A β -phantoms with the A β_{1-40} and A β_{1-42} fibrils filled and sealed will be installed in the rotation stage of the prototype x-ray phase contrast CT in the way illustrated in Fig. 1(b) to carry out the tasks toward SA#2. However, to avoid biological decay, these targets filled with the A β_{1-40} and A β_{1-42} and their fibrils have to be stored in refrigerator at -20°C . For convenience in storage and

repeated scan, the $\text{A}\beta_{1-40}$ and $\text{A}\beta_{1-42}$ peptides and fibrils are filled in PCR (Polymerase Chain Reaction) tubes as illustrated in Fig. 7(b). These A-beta targets are stored in refrigerator and are mounted on top of the $\text{A}\beta$ -phantom body made of PMMA (Fig. 7(a)) during scan.

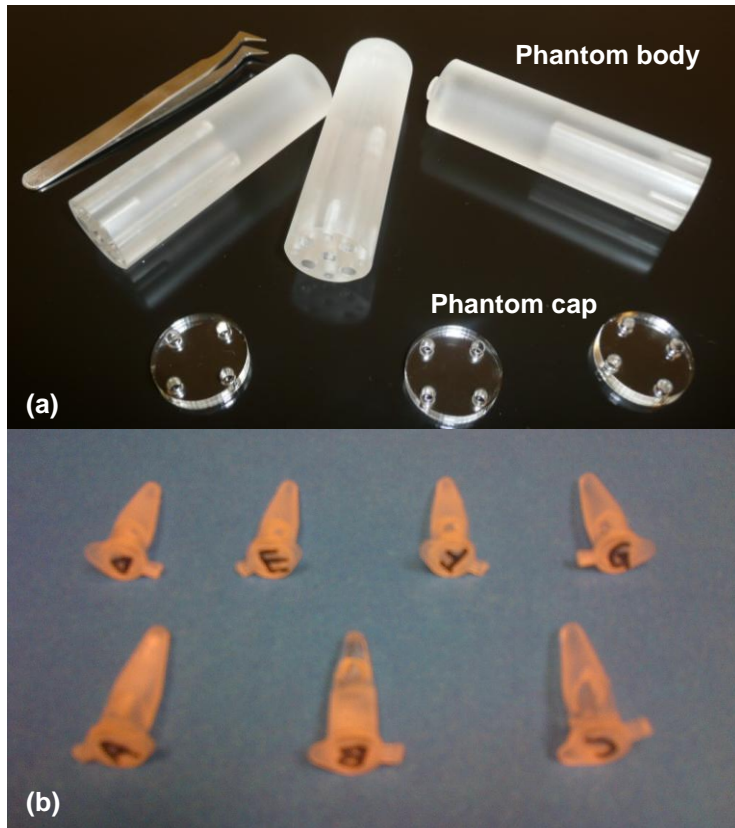


Figure 7. A picture showing: (a) the phantom body made of PMMA for making the image quality phantom and (b) the PCR tubes filled with amyloid precursor protein (A) and $\text{A}\beta$ peptides (B, C, D) and $\text{A}\beta$ peptides/fibrils (E, F, G) to be installed on top of the phantom body (see Table I).

Accomplishments towards Specific Aim 3.

To complete the tasks towards Specific Aim 3, we need to have a collection of specimen of AD brain, normally aged brain and pathologically aged brain. Then, we scan them using the prototyped x-ray phase contrast CT, sort and analyze the acquired images.

A. **Collection of AD brain specimen:** Itemized in Table III are the specimen, including AD brain, normally aged brain and pathologically aged brain, collected by us for the project at the Emory Alzheimer Disease Research Center. Displayed in Fig. 8 are the pictures of an AD brain specimen (Fig. 8(a)) and a normally aged brain. Note that amyloid plaques are visible in the AD brain specimen (Fig. 8(a)).

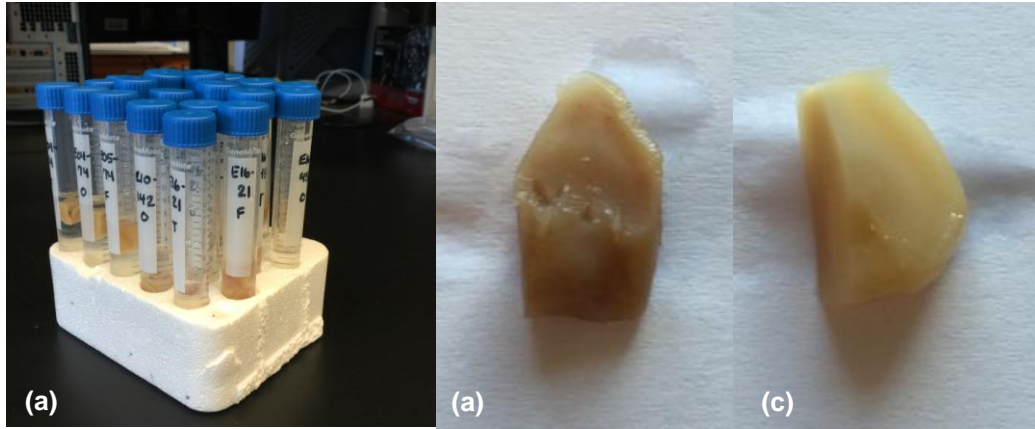


Figure 8. Photographs showing the collection of brain tissue specimen (a), a AD brain specimen with amyloid plaques (b) and normal brain specimen without amyloid plaques (c).

Table III. Collection of postmortem specimen of AD brain and normal pathologically aged brain.

Case Number	Emory Number	Wet Tissues Provided	Primary Neuro Diag.	Secondary Neuro Diag.	Tertiary Neuro Diagnosis
E07-38	A07-38	F,T,O	AD		
E16-21	A16-21	F,T,O	AD		
E11-97	A11-97	F	AD		
E11-139	A11-139	F	AD		
E05-74	A05-74	F,T,O	Control		
E10-142	A10-142	F,T,O	Control	Microinfarct-Hp	NFT-Braak stage II
E16-45	A16-45	F,T,O	Control	Braak I	
E04-74	A04-74	F,T,O	Control/MCI	AD - possible	
E15-97	A15-97	F,T,O	Control	Possible AD	Braak IV
= normal aging					
= asymptomatic AD or pathological aging					

B. Evaluation and comparison of imaging AD specimen in phase contrast and attenuation contrast: Typical transverse CT images corresponding to the attenuation contrast and phase contrast acquired by the prototype x-ray phase contrast CT system are presented in Fig. 9 (a) and (b), respectively. Given identical dose, it is observed that, in the tomographic image corresponding to phase contrast, the gray material and white material are in different CT number, though there is no clear boundary between them. However, no such difference in their CT number is observed in the image corresponding to attenuation contrast. In addition, there seem some microstructures in the AD brain specimen visible in the image corresponding to phase contrast, though they need further verification.

Key Research Accomplishments: We have accomplished the tasks specified in the Statement of Work and below is a summary of our major findings, including positive and negative, and related discussions.

Development of x-ray phase contrast CT, system integration and Performance Optimization: The prototype x-ray phase contrast CT has been built and working at its full functionality as a “three-in-one”

imaging system that generates images corresponding to the attenuation contrast, differential phase contrast and dark field contrast, respectively. The imaging performance of the prototype system has been optimized by significantly improving quality of the key components – gratings G1 and G2, as well as the mechanical accuracy and precision in optical component installation and alignment.

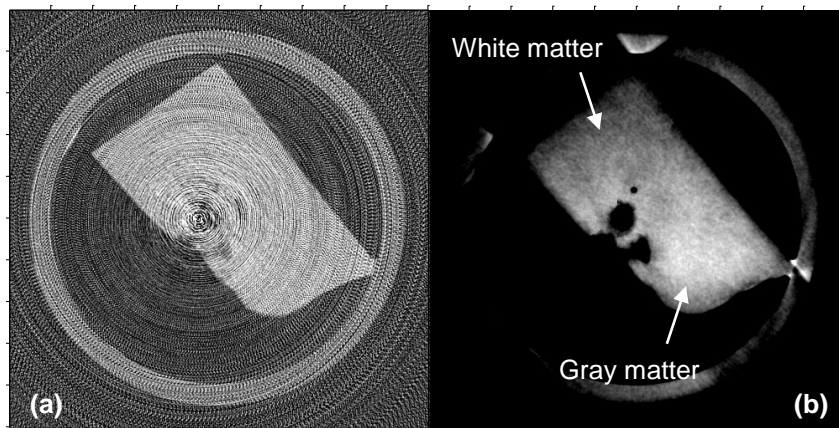


Figure 9. CT images of the AD brain specimen corresponding to attenuation contrast (a) and phase contrast (b) (image in-plane resolution: $48 \times 48 \mu\text{m}$; image slice thickness: 0.96 mm).

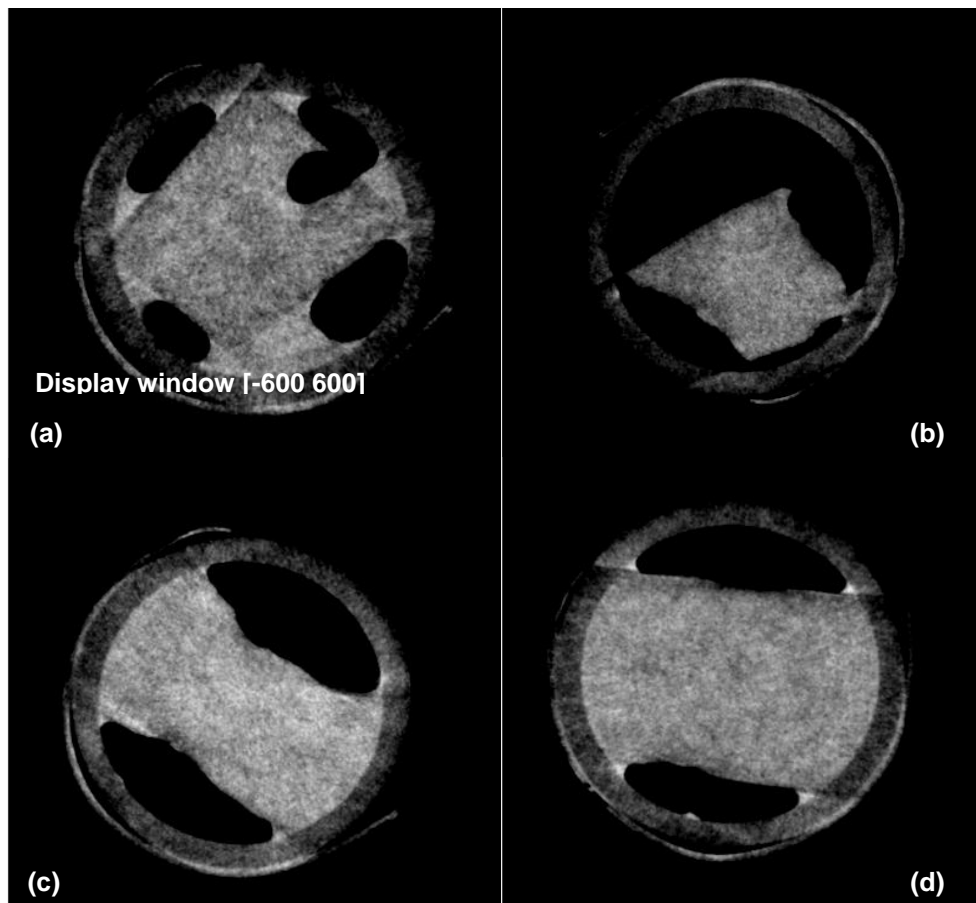


Figure 10. Transverse phase contrast CT images of postmortem AD brain specimen from the front lobe (a), temporal lobe (b), occipital lobe (c) and that of normally aged brain specimen (d) (resolution $48 \mu\text{m}^3$; display window: [-600 600]).

Imaging specimen of AD brain, normally aged brain, and pathologically aged brain, with x-ray phase contrast CT:

- To the best of our knowledge, it is the first time that the specimen of AD brain is imaged and compared to normally aged brain specimen and pathologically aged brain specimen using the grating-based x-ray differential phase contrast CT (Fig. 10).
- It has been shown that the contrast between grey matter and white matter in the grating based differential x-ray phase contrast CT image is substantially higher than that in conventional attenuation contrast CT image (Fig. 9).
- It has been demonstrated that, given identical x-ray dose, the phase contrast CT image of brain specimen is of substantially better signal-to-noise ratio (SNR) than that of conventional attenuation contrast CT image (Fig. 9).
- However, even with substantially improved SNR, the x-ray phase contrast CT still cannot convincingly differentiate the AD brain specimen with amyloid plaques from the normal aged brain specimen without amyloid plaques (Fig. 10).
- Two major factors may contribute to the insufficient SNR for differentiation of the AD brain specimen with amyloid plaques from the normal aged brain specimen without amyloid plaques: (i) the micro-focus x-ray tube is of limited power and cannot reach the tube current that may generate the desired SNR; (ii) the time to acquire the projection data for tomographic image generation is approximately 12 hours, during which the working conditions of both micro-focus x-ray tube and C-MOS x-ray detector drift significantly, which may significantly degrade the performance in SNR.
- These two factors can be effectively addressed simultaneously using a micro-focus tube with significantly larger power and this is believed to be a major opportunity for continuation of the investigation initiated and carried out in this project in the near future.

Scientific leadership establishment: With the valued support by this grant, the research group led by the PI at Emory University has established an international scientific leadership in x-ray phase contrast CT imaging, demonstrated by its publication in the prestigious scientific journals and conferences, and the invitation by journal's editorial board to review manuscripts, and by federal and non-profit funding agencies for the study sections to review research proposals related to x-ray phase contrast CT imaging. Especially, the PI was the co-chair of a session entitled "Phase-contrast CT and Few View CT" in the 3rd International Conference on CT Image Formation in X-ray Computed Tomography (Salt Lake City, Utah, June 22-25, 2014), as well as the chair of another session entitled "Optical, Ultrasound, and Emerging Imaging Techniques" in the AAPM's (American Association of Physicists in Medicine) 52nd Annual Meeting in Austin, TX (August 20-24, 2014).

What opportunities for training and professional development has the project provided?

The project provided a training opportunity for Yi Yang, PhD, a post-doc fellow at the Department of Radiology and Imaging Sciences, Emory University School of Medicine, to transit from the career path of an atomic/plasma physicist and successfully grow into an imaging scientist, with a formal position of senior research associate initially at the Department of Radiology and Imaging Sciences, Emory University School of Medicine and then switched to a formal job position in CT industry after he has gained knowledge, expertise and extensive experience in CT sciences and technologies, via his training supported under this grant.

How were the results disseminated to communities of interest?

Nothing to report.

What do you plan to do during the next reporting period to accomplish the goals?

The project completes at the end of this reporting period.

4. IMPACT

What was the impact on the development of the principal discipline(s) of the project?

- We found that, in addition to the 1st-order derivative (existing art), the 2nd-order derivative also play a significant role in the grating based x-ray phase contrast imaging. We derived the theoretical foundation for system modeling and analysis and provide a practical approach for imaging applications, which has been published in Medical Physics – the scientific journal of American Society of Physicist in Medicine (AAPM)¹¹.
- We found that the dark field signal in the grating based x-ray phase contrast imaging is actually a complex signal, rather than only a real signal as what has been assumed in the literature (existing knowledge). We derived the theoretical foundation for system modeling and analysis and provide a practical approach for signal retrieval and imaging, which has been published in Medical Physics – the scientific journal of AAPM¹².
- We found that there inevitably exists imperfection in gratings – the key components of x-ray phase contrast CT. We derived the theoretical foundation for system modeling and analysis and provide an effective approach to successfully cope with it, which has been published in Medical Physics – the scientific journal of AAPM¹³.
- We found that, in the situation with twin-peaks, the radiation dose required by grating based x-ray phase contrast CT can still be significantly reduced by algebraic method. We derived the theoretical foundation for system modeling and analysis and provide an effective approach to successfully reduce radiation dose. The method and preliminary data have been submitted to Medical Physics as a paper that is in revision¹⁴.

What was the impact on other disciplines?

Nothing to report.

What was the impact on technology transfer?

Nothing to report.

What was the impact on society beyond science and technology?

Nothing to report.

5. CHANGES/PROBLEMS

Nothing to report.

6. PRODUCTS:

Publications, conference papers, and presentations

In Peer-reviewed Journals (manuscript attached in appendix): Five papers that are partially supported by the grant or related to the subject of the project were published in Medical Physics, one of the leading scientific journals in Medical Imaging. In addition, one manuscript has been submitted to Medical Physics and in the revision process.

1. Tang X, Yang Y and Tang S, "Characterization of imaging performance in differential phase contrast CT compared with the conventional CT – Spectrum of noise equivalent quanta NEQ(k)" *Med. Phys.*, v.39(7): 4467-82, 2012.
2. Yang Y and Tang X, "The second-order differential phase contrast and its retrieval for imaging with x-ray Talbot interferometry," *Med. Phys.*, v.39, pp.7237-53, 2012.
3. Tang S and Tang X, "Radial differential interior tomography and its image reconstruction with differentiated backprojection and projection onto convex sets," *Med. Phys.*, v.40, 101914 (14pp.), 2013.
4. Yang Y and Tang X, "Complex dark-field contrast and its retrieval in x-ray phase contrast imaging implemented with Talbot interferometry," *Med. Phys.*, v.41, 101914 (19pp.), 2014.
5. Yang Y, Xie H, Cai W, Mao H and Tang X, "Grating-based x-ray differential phase contrast imaging with twin peaks in phase-stepping curves—phase retrieval and dewrapping," *Med. Phys.*, v.42, pp.2855-69, 2016.
6. Xie H, Cai W, Yang L, Mao H and Tang X, "Reducing radiation dose in grating based x-ray phase contrast CT with twin-peaks in its phase stepping curves," submitted to *Med. Phys.*, *in revision*, 2016

In peer-reviewed Conferences (manuscript not attached in appendix): Seven papers were published in SPIE Medical Imaging Conference, RSNA's Scientific Assembly and Exhibition, and AAPM Annual Meetings etc..

1. X Tang, Y Yang and S Tang, "The potential imaging performance of differential phase contrast CT – NPS(k), MTF(k) and NEQ(k)," *Proc. 2nd International Conf. Image Formation in X-ray CT*, pp.271-74, 2012.
2. X. Tang, Y. Yang and S. Tang, "NEQ(k): The signal and noise transfer properties in differential phase contrast CT," 54th AAPM (American Association of Physicists in Medicine) annual Meeting, Charlotte, NC, July 29 – Aug. 2, 2012.
3. X. Tang, Y. Yang and S. Tang, "The property of signal-to-noise and its variation over spatial frequency in differential phase contrast CT," IEEE Medical Imaging Conference, Anaheim, Oct. 27 – Nov. 3, 2012.
4. X. Tang, Y. Yang and S. Tang, "Spectrum of noise equivalent quanta NEQ(k) – Differential phase contrast CT vs. conventional CT," RSNA 98th Scientific Assembly and Annual Meeting Program, Chicago, Nov. 25 – 30, 2012.
5. X Tang, Y Yang and S Tang, "Detectability index of differential phase contrast CT compared with conventional CT: a preliminary channelized Hotelling observer study," *Proc. SPIE*, v.8668, 2013.
6. X. Tang and Y. Yang, "Internal noise in channelized Hotelling observer (CHO) study of detectability index – differential phase contrast CT vs. conventional CT," *SPIE Proc.* vol. 9033, Medical Imaging 2014: Physics of Medical Imaging, 903326 (March 19, 2014): doi:10.1117/12.2043251.
7. Y. Yang and X. Tang, "Complex dark-field contrast in grating-based x-ray phase contrast imaging," *SPIE Proc.* vol. 9421, Medical Imaging 2014: Physics of Medical Imaging, 941257 (March 18, 2015): doi:10.1117/12.2082294.

Website(s) or other Internet site(s): No

Technologies or techniques: Nothing to report.

Inventions, patent applications, and/or licenses: Nothing to report.

Other Products: Collection of specimens of AD brain, normally aged brain and pathologically aged brain.

7. PARTICIPANTS & OTHER COLLABORATING ORGANIZATIONS

What individuals have worked on the project? The senior personnel who have participated in the project are listed in Table IV.

Table IV. Senior personnel of the project.

Name	Role	Effort (m/yr)	Contribution
X. Tang, PhD	PI	1.2	Project design and leadership, x-ray phase contrast CT development, optimization, data acquisition and image analysis
C Meltzer, MD	Co-inv	0.12	Project design, AD radiologic guidance
H Mao, PhD	Co-inv	0.24	Biochemistry guidance and support
M Gearing, PhD	Co-inv	1.2	AD pathology guidance and support, collection of specimen

Has there been a change in the active other support of the PD/PI(s) or senior/key personnel since the last reporting period?

Nothing to report.

What other organizations were involved as partners?

Nothing to report.

8. SPECIAL REPORTING REQUIREMENTS

COLLABORATIVE AWARDS: Nothing to report.

QUAD CHARTS: Nothing to report.

9. APPENDICES: See attachments.

References:

1. http://www.alz.org/alzheimers_disease_facts_figures.asp, accessed on Dec. 31st, 2010.
2. Roberson ED and Mucke L, "100 years and counting: Prospects for defeating Alzheimer's disease," *Science*, 314:781-84, 2006.
3. Goedert M and Spillantini MG, "A century of Alzheimer's disease," *Science*, v.314, pp 777-81, 2006. Tang X, Ning R, Yu R. and Conover D, "Cone beam volume CT image artifacts caused by defective cells in x-ray flat panel imagers and the artifact removal using a wavelet-analysis-based algorithm" *Med. Phys.*, 28(3): 812-25, 2001.
4. X Wu and H Liu, "Clinical implementation of x-ray phase-contrast imaging: Theoretical foundations and design considerations," *Med. Phys.*, v.30, pp.2169-79, 2003.
5. DM Connor, H Benveniste, FA Dilmanian, MF Kritzer, LM Miller and Z Zhong, "Computed tomography of amyloid plaques in a mouse model of Alzheimer's disease using diffraction enhanced imaging," *NeuroImage*, v.46, pp 908-14, 2009.
6. F Pfeiffer, T Weitkamp, O Bunk, C David, "Phase retrieval and differential phase-contrast imaging with low-brilliance x-ray sources," *Nature Phys.*, v.2, pp.258-61, 2006.
7. M Bech, TH Jensen, R Feidenhan'l, O Bunk, C David and F Pfeiffer, "Soft-tissue phase-contrast tomography with x-ray tube source," *Phys. Med. Biol.*, v.54, pp.2747-53, 2009.
8. Tang X, Yang Y and Tang S, "Characterization of imaging performance in differential phase contrast CT compared with the conventional CT – Noise power spectrum NPS(k)," *Med. Phys.*, vol. 38, pp. 4386-95, 2011.
9. Tang X, Yang Y and Tang S, "Characterization of imaging performance in differential phase contrast CT compared with the conventional CT – Spectrum of noise equivalent quanta NEQ(k)" *Med. Phys.*, 39(7): 4467-82, 2012.
10. C David, J Bruder, T Rohbeck, C Grunzweig, C Kottler, A Diaz, O Bunk and F Pfeiffer, "Fabrication of diffraction gratings for hard x-ray phase contrast imaging," *Microelect. Eng.*, v.84(5-8), pp1172-77, 2007.
11. Yang Y and Tang X, "The second-order differential phase contrast and its retrieval for imaging with x-ray Talbot interferometry," *Med. Phys.*, v.39, pp.7237-53, 2012.
12. Yang Y and Tang X, "Complex dark-field contrast and its retrieval in x-ray phase contrast imaging implemented with Talbot interferometry," *Med. Phys.*, v.41, 101914 (19pp.), 2014.
13. Yang Y, Xie H, Cai W, Mao H and Tang X, "Grating-based x-ray differential phase contrast imaging with twin peaks in phase-stepping curves–phase retrieval and dewrapping," *Med. Phys.*, v.42, pp.2855-69, 2016.
14. Xie H, Cai W, Yang L, Mao H and Tang X, "Reducing radiation dose in grating based x-ray phase contrast CT with twin-peaks in its phase stepping curves," submitted to *Med. Phys.*, *in revision*, 2016

Characterization of imaging performance in differential phase contrast CT compared with the conventional CT: Spectrum of noise equivalent quanta NEQ(k)

Xiangyang Tang,^{a)} Yi Yang, and Shaojie Tang

Imaging and Medical Physics, Department of Radiology and Imaging Sciences, Emory University School of Medicine, 1701 Uppergate Drive, C-5018, Atlanta, Georgia 30322

(Received 8 December 2011; revised 4 June 2012; accepted for publication 6 June 2012; published 29 June 2012)

Purpose: Differential phase contrast CT (DPC-CT) is emerging as a new technology to improve the contrast sensitivity of conventional attenuation-based CT. The noise equivalent quanta as a function over spatial frequency, i.e., the spectrum of noise equivalent quanta NEQ(k), is a decisive indicator of the signal and noise transfer properties of an imaging system. In this work, we derive the functional form of NEQ(k) in DPC-CT. Via system modeling, analysis, and computer simulation, we evaluate and verify the derived NEQ(k) and compare it with that of the conventional attenuation-based CT.

Methods: The DPC-CT is implemented with x-ray tube and gratings. The x-ray propagation and data acquisition are modeled and simulated through Fresnel and Fourier analysis. A monochromatic x-ray source (30 keV) is assumed to exclude any system imperfection and interference caused by scatter and beam hardening, while a 360° full scan is carried out in data acquisition to avoid any weighting scheme that may disrupt noise randomness. Adequate upsampling is implemented to simulate the x-ray beam's propagation through the gratings G_1 and G_2 with periods 8 and 4 μm , respectively, while the intergrating distance is 193.6 mm (1/16 of the Talbot distance). The dimensions of the detector cell for data acquisition are 32 × 32, 64 × 64, 96 × 96, and 128 × 128 μm^2 , respectively, corresponding to a 40.96 × 40.96 mm² field of view in data acquisition. An air phantom is employed to obtain the noise power spectrum NPS(k), spectrum of noise equivalent quanta NEQ(k), and detective quantum efficiency DQE(k). A cylindrical water phantom at 5.1 mm diameter and complex refraction coefficient $n = 1 - \delta + i\beta = 1 - 2.5604 \times 10^{-7} + i1.2353 \times 10^{-10}$ is placed in air to measure the edge transfer function, line spread function and then modulation transfer function MTF(k), of both DPC-CT and the conventional attenuation-based CT. The x-ray flux is set at 5×10^6 photon/cm² per projection and observes the Poisson distribution, which is consistent with that of a micro-CT for preclinical applications. Approximately 360 regions, each at 128 × 128 matrix, are used to calculate the NPS(k) via 2D Fourier transform, in which adequate zero padding is carried out to avoid aliasing in noise.

Results: The preliminary data show that the DPC-CT possesses a signal transfer property [MTF(k)] comparable to that of the conventional attenuation-based CT. Meanwhile, though there exists a radical difference in their noise power spectrum NPS(k) (trait 1/ $|k|$ in DPC-CT but $|k|$ in the conventional attenuation-based CT) the NEQ(k) and DQE(k) of DPC-CT and the conventional attenuation-based CT are in principle identical.

Conclusions: Under the framework of ideal observer study, the joint signal and noise transfer property NEQ(k) and detective quantum efficiency DQE(k) of DPC-CT are essentially the same as those of the conventional attenuation-based CT. The findings reported in this paper may provide insightful guidelines on the research, development, and performance optimization of DPC-CT for extensive preclinical and clinical applications in the future. © 2012 American Association of Physicists in Medicine. [<http://dx.doi.org/10.1118/1.4730287>]

Key words: CT, x-ray CT, x-ray phase CT, x-ray differential phase contrast CT, x-ray tube and grating-based phase CT, imaging performance, modulation transfer function, MTF, noise, noise power spectrum, NPS, noise equivalent quanta, NEQ, detective quantum efficiency, DQE.

I. INTRODUCTION

Motivated to reach higher subject contrast over soft tissues in x-ray CT imaging, the scientific community has devoted increasing effort to the investigation of x-ray tube and grating-based differential phase contrast CT (DPC-CT) for early detection of cancer and other diseases.^{1–5} The initial exploration was relatively qualitative and demonstrated

significant improvement in the contrast of soft tissues in human specimens or very small animals.^{1,2,4,5} Recently, the investigation has become quantitative, and preliminary results on the noise property of DPC-CT,^{6–13} such as pixel-based gross variance,^{6–9} contrast-to-noise ratio,^{8,10} and spatial autocovariance function,⁷ have been reported. It is a fundamental understanding that the subject contrast of soft

tissues in an imaging system is intrinsically determined by their interaction with the x-ray beam,^{14–16} while the system's performance is determined by its signal and noise transfer properties.^{11,17–35} In principle, the signal transfer property of an imaging system is dependent on its modulation transfer function MTF(k),^{17–30} while the noise transfer property can only be thoroughly characterized by its noise power spectrum NPS(k), i.e., the variation of noise intensity as a function over spatial frequency k .^{17–35} It has been reported that there exists a radical difference in the noise power spectrum NPS(k) between DPC-CT and the conventional attenuation-based CT (referred to as conventional CT hereafter): the NPS(k) of the former manifests itself with the trait $1/|k|$, and the latter with $|k|$.^{11,12}

In general, an imaging system can be cascaded into two stages—image formation (or record or detection as termed in the literature) and image presentation or display.^{20,27,28} Such a separation is straightforward in digital imaging modalities, e.g., the DPC-CT and conventional CT to be investigated in this work, but quite intricate in the early days when only analog imaging modalities, e.g., x-ray screen-film radiography, were available. Quite a few factors may degrade the performance of an imaging system, which include but are not limited to (i) the ubiquitous random fluctuation—noise—in data acquisition, (ii) the anatomic and physiologic variation in patient population, and (iii) the intra- and interobserver variability when a diagnosis is made based on the images presented.^{27,28} These factors work in concert with one another and thus make the performance assessment of an imaging system extremely challenging. With recourse to Bayesian statistical decision and information theories, a framework for the performance assessment of an imaging system has been established through the tremendous and successful effort of leading scientists in this field,^{17–28} in which the detection of pathological lesions with a medical imaging system is mathematically treated as a decision making process. An observer makes the decision between two hypotheses—H₁: lesion present (abnormal or positive); H₂: lesion absent (normal or negative)—according to whether the value of a decision function exceeds a threshold or not. If the decision function is the Bayesian likelihood, the decision maker becomes an ideal observer, who minimizes the risks while making the decision, i.e., maximizing the area under the receiver operating characteristics (ROC) curve.^{20,27,28}

Suppose the imaging system under study is linear and shift-invariant, and the noise corrupting the system is Gaussian and stationary. Given a signal specified in the spatial frequency domain as $\Delta S(k)$, i.e., the signal and background known exactly (SKE/BKE),^{27,28,30} the squared signal-to-noise ratio or the detectability index defined by

$$\text{SNR}_{\text{ideal}}^2 = \int |\Delta S(k)|^2 \text{NEQ}(k) dk \quad (1)$$

is an ideal observer figure of merit (FOM) to assess an imaging system's performance,^{27,30} wherein the spectrum of noise equivalent quanta $\text{NEQ}(k)$ may be in different func-

tional forms over imaging modalities.^{20,21,26,28} An ideal observer is assumed to have prior knowledge of the task and the statistical properties of the noise. Equation (1) is an integration of factorization and implies that, given a specific task $|\Delta S(k)|^2$, the ideal observer performance of an imaging system can be optimized by maximizing its $\text{NEQ}(k)$.^{27,30} Usually, the task is to differentiate a lesion from the surrounding tissues or organs or simply an object from its background. Therefore, the signal $\Delta S(k)$ in Eq. (1) should be perceived as a difference or contrast between the object to be imaged and background.^{20,21,27,30} In practice, Eq. (1) can be extended to deal with more complicated situations, wherein the noise observes the Poisson distribution and is not stationary, the imaging system is nonlinear and shift-variant, or the signal is superimposed on a random background.^{20,27,28,30}

Recognizing the important role played by $\text{NEQ}(k)$ as a FOM to assess the ideal observer performance of an imaging system,^{20,27,28,30,32–35} we investigate the $\text{NEQ}(k)$ and resultant spectrum of detective quantum efficiency $\text{DQE}(k)$ of DPC-CT in this work. In a way analogous to the investigation of conventional CT's $\text{NEQ}(k)$ and $\text{DQE}(k)$, we treat the DPC-CT as a linear and shift-invariant system. Owing to the fact that Gaussian noise approaches Poisson noise if the detected number of photons is large, we assume the noise in the DPC-CT is Gaussian.²⁹ To avoid any interference caused by scatter and beam hardening, a monochromatic x-ray source is assumed in both the DPC-CT and conventional CT in this investigation, though they are actually configured with a polychromatic one in practice. Under the framework of an ideal observer, we derive, analyze, evaluate, and verify the $\text{NEQ}(k)$ and $\text{DQE}(k)$ of DPC-CT through computer simulation studies and compare the result with that of conventional CT. For clarity in expression henceforth, $\Delta S(k)$, $\text{SNR}_{\text{ideal}}^2$, $\text{NPS}(k)$, $\text{MTF}(k)$, $\text{NEQ}(k)$, and $\text{DQE}(k)$ denote the quantities corresponding to an imaging system in general, which can be either DPC-CT or conventional CT. Specifically, the quantities corresponding to the DPC-CT are denoted with subscript “ p ,” while those corresponding to the conventional CT are denoted with subscript “ a .”

II. MATERIALS AND METHODS

To characterize the spectrum of noise equivalent quanta $\text{NEQ}_p(k)$ and spectrum of detective quantum efficiency $\text{DQE}_p(k)$ of DPC-CT, we start out by deriving its functional form and comparing it with that of the conventional CT. Subsequently, we introduce the methods and procedures to evaluate and verify the derived $\text{NEQ}_p(k)$ and $\text{DQE}_p(k)$ and compare them with their counterparts in conventional CT. We constrain ourselves in this work to conducting computer simulation study only; thereby the systematic and random errors, such as the fabrication accuracy and alignment of gratings, and the effects due to beam hardening and scattering that may exist in a physical DPC-CT and compromise or bias the accuracy and precision of evaluation and verification can be excluded.

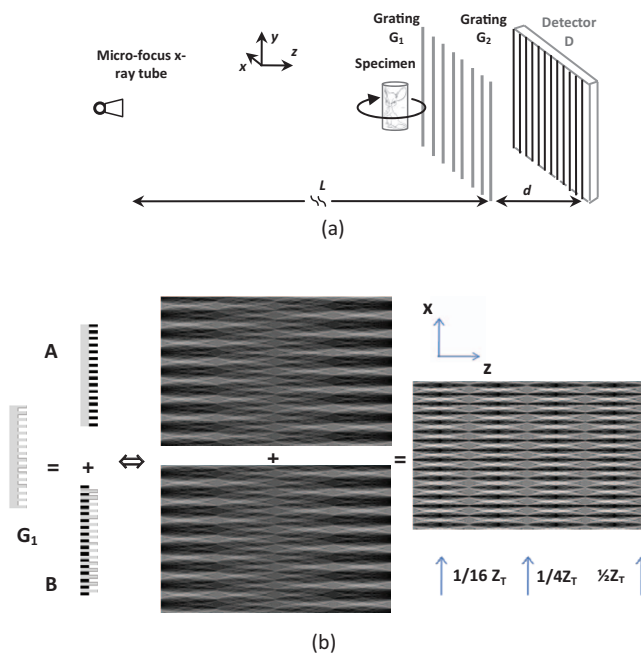


FIG. 1. The diagrams showing (a) the schematic of an x-ray tube and grating-based DPC-CT and (b) the schematic of virtual grating decomposition, in which the upper and lower Talbot patterns are associated with gratings A and B, respectively.

II.A. Imaging mechanism of DPC-CT implemented with x-ray tube and gratings

The architecture of DPC-CT implemented with a micro-focus x-ray tube and gratings² is shown in Fig. 1(a). G_1 is a phase grating and G_2 an absorption grating, which can be fabricated with photolithography, deep chemical etching, and electroplating.³⁶ G_1 and G_2 work together as a shearing interferometer^{37–39} to detect the wavefront alteration caused by the object in x-ray beam. The x-ray tube irradiates the specimen, while the specimen stage rotates by a range satisfying the data sufficiency condition, and the CCD x-ray detector is employed for data acquisition. The key component of the imaging chain is grating G_1 , a diffraction interferometer based on the Talbot effect.^{37–39} Figure 1(b) shows how G_1 works by virtually decomposing it into gratings A and B. The extra optical path corresponding to grating B relative to that through grating A is half wavelength, which is equivalent to a 180° phase shift. The beams corresponding to gratings A and B recombine after they pass through the gratings, and interference fringe appears if the object to be imaged is in the x-ray beam.

The imaging mechanism of x-ray tube and grating-based DPC-CT is elaborated in Refs. 11–13 and 37–39 and only a concise review is given below. According to Fresnel analysis,^{40,41} the irradiance $I(x, z)$ at the CCD detector is

$$\begin{aligned} I_{A+B}(x, z) &\sim \phi\left(x + \Delta \frac{x}{2}, y\right) - \phi\left(x - \Delta \frac{x}{2}, y\right) \\ &\cong \frac{\partial \phi(x, y)}{\partial x} \Delta x, \end{aligned} \quad (2)$$

where Δx is a displacement in the x -direction, and $\phi(x, y)$ is the phase variation over Δx , which is the projection of refractive coefficient $\hat{\delta}(x, y, z)$ along the x-ray path

$$\phi(x, y) = \frac{2\pi}{\lambda} \int_z \hat{\delta}(x, y, z) dz. \quad (3)$$

Note that the refractive coefficient has been denoted by $\delta(x, y, z)$ in the literature. However, to avoid its confusion with the Dirac function and Kronecker delta that are used to derive the functional form of $NEQ_p(k)$ later in this paper, $\hat{\delta}(x, y, z)$ is adopted to represent the refractive coefficient.

Equation (2) shows that the irradiance depends on the derivative of the phase variation along the x axis. After the x-ray passes grating G_2 , the irradiance at detector D is⁴¹

$$I_{u,v}(x) = a_0(u, v) + \sum_{m=1}^{\infty} a_m(u, v) \cos\left(\frac{2\pi mx}{g_2} + \varphi_m(u, v)\right), \quad (4)$$

where (u, v) is the coordinate of a detector cell and g_2 the period of grating G_2 . By linearly shifting grating G_2 along the x axis and carrying out a Fourier analysis, one can determine $a_0(u, v)$, $a_1(u, v)$, and $\varphi_1(u, v)$ from Eq. (4).⁴¹ In fact, one has

$$\frac{\partial \phi(x, y)}{\partial x} = \varphi_1(u, v) \frac{g_2}{\lambda z_T}, \quad (5)$$

where z_T is the fractional Talbot distance.^{2,37–41} Substituting the $\phi(x, y)$ defined in Eq. (3) into Eq. (5), one gets

$$\begin{aligned} \varphi_1(u, v) &= \frac{\lambda z_T}{g_2} \frac{\partial \phi(x, y)}{\partial x} = \frac{2\pi z_T}{g_2} \frac{\partial}{\partial x} \int_z \hat{\delta}(x, y, z) dz \\ &= \frac{2\pi z_T}{g_2} \int_z \frac{\partial}{\partial x} \hat{\delta}(x, y, z) dz. \end{aligned} \quad (6)$$

This means that the phase retrieved through a Fourier analysis of Eq. (4) is the projection of the refractive coefficient's derivative, and this is the underlying reason that the phase CT implemented with x-ray tube and gratings is called differential phase contrast CT. Once data $\varphi_1(u, v)$ are acquired, tomographic images of refraction are reconstructed using the filtered backprojection (FBP) algorithms.^{42–45} Since the reconstruction is carried out directly from $\partial \hat{\delta}(x, y, z)/\partial x$, the ramp kernel is replaced with the Hilbert kernel. It should be pointed out that the modeling of data acquisition in the x-ray tube and grating-based DPC-CT through the schematic of Fig. 1(b) and Eqs. (2)–(6) has been evaluated and verified in Ref. 11, which is in principle the same as the five steps detailed in Ref. 13. The well-known contrast-detail (C-D) phantom²⁹ (see Sec. III) is used to evaluate and verify the correctness and accuracy of the data acquisition modeling and image reconstruction, and the result is presented in Fig. 2.

II.B. Spectrum of noise equivalent quanta in DPC-CT and conventional CT

In the early days of conventional CT, an observation of the morphologic difference in the noise of CT images against

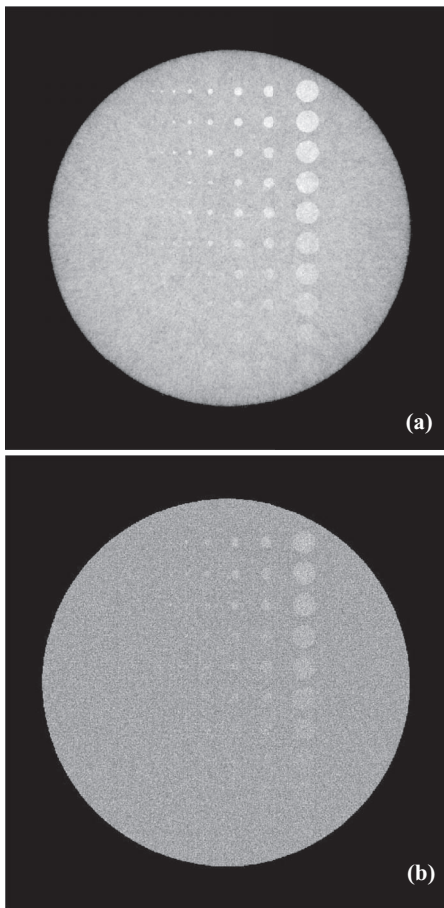


FIG. 2. Transverse images of the C-D phantom generated by the x-ray tube and grating-based DPC-CT CT (a) and the conventional CT (b) (x-ray exposure 10^7 photon/cm 2 per projection, detector cell $48 \times 48 \mu\text{m}^2$).

the white noise suggested that there existed an interpixel correlation. By analyzing the distribution of noise power over spatial frequency k , i.e., the noise power spectrum $\text{NPS}_a(k)$, the interpixel correlation is confirmed, even though there is no intercell correlation in the noise of the detector used for data acquisition. Since then, the groundwork of using noise power spectrum $\text{NPS}_a(k)$ and spectrum of noise equivalent quanta $\text{NEQ}_a(k)$ to analyze the signal and noise behavior of a conventional CT system or CT imaging method has been laid out.^{17–25} In this section, we follow the mathematic treatment to derive the functional form of $\text{NPS}_p(k)$ and $\text{NEQ}_p(k)$ in the DPC-CT implemented with x-ray tube and gratings and compare it with that of the conventional CT.

II.B.1. Spectrum of noise equivalent quanta $\text{NEQ}_a(k)$ of the conventional CT

A number of strategies, e.g., the method proposed by Barret,¹⁸ the central slice theorem,¹⁹ information theory,²⁰ and statistical detection theory,²¹ have been exercised to obtain the noise power spectrum $\text{NPS}_a(k)$ of the conventional

CT, and all lead to the same functional form

$$\begin{aligned}\text{NPS}_a(k) &= \frac{a\pi}{N_\theta \bar{N}} |k| |\text{MTF}_a(k)|^2 \\ &= \frac{\pi}{b N_\theta I_0} |k| |\text{MTF}_a(k)|^2,\end{aligned}\quad (7)$$

where a is the detector pitch, b is the detector height, and k is the radial frequency defined as

$$k = \sqrt{k_x^2 + k_y^2}. \quad (8)$$

N_θ is the number of angular locations at which the projection data are acquired, I_0 is the measured photon flux, and \bar{N} is the mean number of x-ray photons detected at each detector cell. Since no object should be placed in the x-ray beam in the investigation of noise property, \bar{N} is assumed equal across all the detector cells. $\text{MTF}_a(k)$ is the overall algorithmic contribution, including the windowing and/or boosting in the frequency domain for an optimization between noise and spatial resolution, to the modulation transfer function.

The multiplication of N_θ and I_0 has been defined as the noise equivalent quanta.^{20,21,23} Accordingly, Eq. (7) can be expressed as

$$\text{NPS}_a(k) = \frac{\pi}{b \text{NEQ}_a} |k| |\text{MTF}_a(k)|^2. \quad (9)$$

Consequently, the spectrum of noise equivalent quanta $\text{NEQ}_a(k)$ and detective quantum efficiency $\text{DQE}_a(k)$ of the conventional CT are^{18–21}

$$\text{NEQ}_a(k) = \frac{\pi}{b \text{NPS}_a(k)} |k| |\text{MTF}_a(k)|^2, \quad (10)$$

$$\text{DQE}_a(k) = \frac{\text{NEQ}_a(k)}{N_\theta I_0}. \quad (11)$$

II.B.2. Spectrum of noise equivalent quanta $\text{NEQ}_p(k)$ of the DPC-CT

As indicated above, the phase information $\varphi_l(u, v)$ can be retrieved by stepping grating G_2 linearly along the x axis (see Fig. 1). At each step

$$x_g = \frac{k}{M} g_2, \quad k = 1, 2, \dots, M, \quad (12)$$

the measured x-ray irradiance at (u, v) in a detector represented in Eq. (4) can be rewritten as

$$N^{(k)}(u, v) = \sum_{l=-\frac{M}{2}}^{\frac{M}{2}-1} N_l \frac{1+\delta_{l0}}{2} \exp \left[i \varphi_l(u, v) + 2\pi i \frac{lk}{M} \right], \quad (13)$$

where N_l is non-negative and real and δ_{l0} is the Kronecker's delta δ_{lm} by setting the 2nd subscript m equal to zero, i.e.,

$$\delta_{l0} = \begin{cases} 1 & l = 0 \\ 0 & l \neq 0 \end{cases}. \quad (14)$$

Note that $\varphi_l(u, v)$ ($l = 1$) is the phase we want to retrieve for reconstruction of the 3D distribution of refractive coefficient [see Eq. (6)].

The discrete Fourier transform of both sides of Eq. (13) gives

$$\frac{1}{2}MN_1 \exp[i\varphi_1(u, v)] = \sum_{k=1}^M N^{(k)}(u, v) \exp\left(-2\pi i \frac{k}{M}\right). \quad (15)$$

Since N_1 is non-negative and real, Eq. (15) further gives

$$\exp[i\varphi_1(u, v)] = \frac{\sum_{k=1}^M N^{(k)}(u, v) \exp(-2\pi i \frac{k}{M})}{\left|\sum_{k=1}^M N^{(k)}(u, v) \exp(-2\pi i \frac{k}{M})\right|}, \quad (16)$$

or equivalently

$$\exp[i\varphi_1(u, v)] = \frac{\sum_{k=1}^M N^{(k)}(u, v) \exp(-2\pi i \frac{k}{M})}{\left\{\left[\sum_{k=1}^M N^{(k)}(u, v) \exp(2\pi i \frac{k}{M})\right] \left[\sum_{k=1}^M N^{(k)}(u, v) \exp(-2\pi i \frac{k}{M})\right]\right\}^{1/2}}. \quad (17)$$

Differentiating both sides of Eq. (17), one gets

$$\begin{aligned} & i \exp[i\varphi_1(u, v)] \Delta\varphi_1(u, v) \\ &= \frac{\sum_{k=1}^M \Delta N^{(k)}(u, v) \exp\left(-2\pi i \frac{k}{M}\right)}{\left\{\left[\sum_{k=1}^M N^{(k)}(u, v) \exp\left(2\pi i \frac{k}{M}\right)\right] \left[\sum_{k=1}^M N^{(k)}(u, v) \exp\left(-2\pi i \frac{k}{M}\right)\right]\right\}^{1/2}} \\ &\quad - \frac{1}{2} \frac{\left[\sum_{k=1}^M N^{(k)}(u, v) \exp\left(-2\pi i \frac{k}{M}\right)\right]^2 \left[\sum_{k=1}^M \Delta N^{(k)}(u, v) \exp\left(2\pi i \frac{k}{M}\right)\right]}{\left\{\left[\sum_{k=1}^M N^{(k)}(u, v) \exp\left(2\pi i \frac{k}{M}\right)\right] \left[\sum_{k=1}^M N^{(k)}(u, v) \exp\left(-2\pi i \frac{k}{M}\right)\right]\right\}^{3/2}} \\ &\quad - \frac{1}{2} \frac{\left[\sum_{k=1}^M N^{(k)}(u, v) \exp\left(-2\pi i \frac{k}{M}\right)\right] \left[\sum_{k=1}^M N^{(k)}(u, v) \exp\left(2\pi i \frac{k}{M}\right)\right] \left[\sum_{k=1}^M \Delta N^{(k)}(u, v) \exp\left(-2\pi i \frac{k}{M}\right)\right]}{\left\{\left[\sum_{k=1}^M N^{(k)}(u, v) \exp\left(2\pi i \frac{k}{M}\right)\right] \left[\sum_{k=1}^M N^{(k)}(u, v) \exp\left(-2\pi i \frac{k}{M}\right)\right]\right\}^{3/2}}. \end{aligned} \quad (18)$$

Substituting Eq. (15) into Eq. (18) yields

$$\begin{aligned} & i \exp[i\varphi_1(u, v)] \Delta\varphi_1(u, v) \\ &= \frac{\sum_{k=1}^M \Delta N^{(k)}(u, v) \exp\left(-2\pi i \frac{k}{M}\right)}{\frac{1}{2} MN_1} - \frac{1}{2} \frac{\exp[2i\varphi_1(u, v)] 2^{-2} M^2 N_1^2 \left[\sum_{k=1}^M \Delta N^{(k)}(u, v) \exp\left(2\pi i \frac{k}{M}\right)\right]}{2^{-3} M^3 N_1^3} \\ &\quad - \frac{1}{2} \frac{2^{-2} M^2 N_1^2 \left[\sum_{k=1}^M \Delta N^{(k)}(u, v) \exp\left(-2\pi i \frac{k}{M}\right)\right]}{2^{-3} M^3 N_1^3}, \end{aligned} \quad (19)$$

which can be concisely rewritten as

$$\Delta\varphi_1(u, v) = -i \sum_{k=1}^M \left\{ \frac{\exp\left(-2\pi i \frac{k}{M}\right)}{MN_1 \exp[i\varphi_1(u, v)]} - \frac{\exp\left(2\pi i \frac{k}{M}\right)}{MN_1 \exp[-i\varphi_1(u, v)]} \right\} \Delta N^{(k)}(u, v). \quad (20)$$

Consequently, one has

$$\langle \Delta\varphi_1(u, v) \Delta\varphi_1(u_1, v_1) \rangle = - \sum_{k,k_1=1}^M \left\{ \frac{\exp\left(-2\pi i \frac{k}{M}\right)}{MN_1 \exp[i\varphi_1(u, v)]} - \frac{\exp\left(2\pi i \frac{k}{M}\right)}{MN_1 \exp[-i\varphi_1(u, v)]} \right\} \\ \times \left\{ \frac{\exp\left(-2\pi i \frac{k_1}{M}\right)}{MN_1 \exp[i\varphi_1(u_1, v_1)]} - \frac{\exp\left(2\pi i \frac{k_1}{M}\right)}{MN_1 \exp[-i\varphi_1(u_1, v_1)]} \right\} \langle \Delta N^{(k)}(u, v) \Delta N^{(k_1)}(u_1, v_1) \rangle, \quad (21)$$

where (u_1, v_1) represents a location that is different from (u, v) in the detector. Since the measured x-ray flux observes the Poisson distribution and is spatially uncorrelated, one has

$$\langle \Delta N^{(k)}(u, v) \Delta N^{(k_1)}(u_1, v_1) \rangle = N^{(k)}(u, v) \delta_{kk_1} \delta\left(\frac{u-u_1}{a}\right) \delta\left(\frac{v-v_1}{b}\right), \quad (22)$$

where subscripts k and k_1 correspond to different shifting steps of grating G_2 . Inserting Eq. (22) into Eq. (21) and substituting $N^{(k)}(u, v)$ with Eq. (13), one obtains

$$\begin{aligned} & \langle \Delta\varphi_1(u, v) \Delta\varphi_1(u_1, v_1) \rangle \\ &= - \sum_{k=1}^M \left\{ \frac{\exp\left(-2\pi i \frac{k}{M}\right)}{MN_1 \exp[i\varphi_1(u, v)]} - \frac{\exp\left(2\pi i \frac{k}{M}\right)}{MN_1 \exp[-i\varphi_1(u, v)]} \right\}^2 N^{(k)}(u, v) \delta\left(\frac{u-u_1}{a}\right) \delta\left(\frac{v-v_1}{b}\right) \\ &= \frac{2}{M^2 N_1^2} \left\{ \sum_{k=1}^M N^{(k)}(u, v) - \frac{1}{2} \sum_{k=1}^M \left\{ \frac{\exp\left(-4\pi i \frac{k}{M}\right)}{\exp[2i\varphi_1(u, v)]} + \frac{\exp\left(4\pi i \frac{k}{M}\right)}{\exp[-2i\varphi_1(u, v)]} \right\} N^{(k)}(u, v) \right\} \delta\left(\frac{u-u_1}{a}\right) \delta\left(\frac{v-v_1}{b}\right) \\ &= \frac{2}{M^2 N_1^2} \left\{ MN_0 - \frac{M}{4} \left\{ \frac{N_2 \exp[i\varphi_2(u, v)]}{\exp[2i\varphi_1(u, v)]} + \frac{N_{-2} \exp[-i\varphi_2(u, v)]}{\exp[-2i\varphi_1(u, v)]} \right\} \right\} \delta\left(\frac{u-u_1}{a}\right) \delta\left(\frac{v-v_1}{b}\right). \end{aligned} \quad (23)$$

It is interesting to note that only N_{-2} , N_{-1} , N_0 , N_1 , and N_2 survive the last step in getting Eq. (23).

Subsequently, defining

$$\varepsilon_1 = \frac{\bar{N}_1}{\bar{N}_0}, \quad (24)$$

$$\varepsilon_2 = \frac{\bar{N}_2}{4\bar{N}_0} \left[\frac{\exp(i\bar{\varphi}_2)}{\exp(2i\bar{\varphi}_1)} + \frac{\exp(-i\bar{\varphi}_2)}{\exp(-2i\bar{\varphi}_1)} \right], \quad (25)$$

Eq. (23) can be concisely rewritten as

$$\begin{aligned} & \langle \Delta\varphi_1(u, v) \Delta\varphi_1(u_1, v_1) \rangle \\ &= \frac{2(1-\varepsilon_2)}{M\bar{N}_0\varepsilon_1^2} \delta\left(\frac{u-u_1}{a}\right) \delta\left(\frac{v-v_1}{b}\right). \end{aligned} \quad (26)$$

Note that the random variables N_0 , N_1 , and N_2 have been replaced with their corresponding mean values \bar{N}_0 , \bar{N}_1 and \bar{N}_2 , respectively, in a way analogous to that in Ref. 10. Consequently, one gets

$$\sigma_\varphi^2 = \frac{2(1-\varepsilon_2)}{M\bar{N}_0\varepsilon_1^2}. \quad (27)$$

Meanwhile, according to Eq. (6), it is not hard for one to get

$$\frac{N_\theta}{\sigma_D^2} = \left(\frac{\lambda z_T}{g_2}\right)^2 \frac{N_\theta}{\sigma_\varphi^2} = \left(\frac{\lambda z_T}{g_2}\right)^2 \frac{\varepsilon_1^2}{2(1-\varepsilon_2)} N_\theta M \bar{N}_0$$

$$= \left(\frac{\lambda z_T}{g_2}\right)^2 \frac{\varepsilon_1^2}{2(1-\varepsilon_2)} N_\theta M I_0 ab q_0, \quad (28)$$

where N_θ is the total number of projections in data acquisition, σ_D^2 is the noise at each detector cell, and $q_0 = N_0/abI_0$. In a way analogous to that of the conventional CT,^{20,21,23} we define the noise equivalent quanta as

$$\text{NEQ}_p = N_\theta M I_0, \quad (29)$$

and then Eq. (28) can be rewritten as

$$\frac{N_\theta}{\sigma_D^2} = \left(\frac{\lambda z_T}{g_2}\right)^2 \frac{abq_0\varepsilon_1^2}{2(1-\varepsilon_2)} \text{NEQ}_p. \quad (30)$$

On the other hand, according to Eq. (A25) in the Appendix, one has

$$\frac{N_\theta}{\sigma_D^2} = \frac{a}{4\pi |k| \text{NPS}_p(k)} \text{MTF}_p^2(k). \quad (31)$$

By equating the right sides of Eqs. (30) and (31), one attains

$$\text{NEQ}_p(k) = \left(\frac{g_2}{\lambda z_T} \right)^2 \frac{1 - \varepsilon_2}{2\pi b q_0 \varepsilon_1^2 |k| \text{NPS}_p(k)} \text{MTF}_p^2(k), \quad (32)$$

$$\text{DQE}_p(k) = \frac{\text{NEQ}_p(k)}{N_\theta M I_0}. \quad (33)$$

Furthermore, as derived in the Appendix, the noise power spectrum $\text{NPS}_p(k)$ is

$$\begin{aligned} \text{NPS}_p(k) &= \left(\frac{g_2}{\lambda z_T} \right)^2 \frac{a(1 - \varepsilon_2)}{2\pi \varepsilon_1^2 |k| N_\theta M \bar{N}_0} \text{MTF}_p^2(k) \\ &= \left(\frac{g_2}{\lambda z_T} \right)^2 \frac{1 - \varepsilon_2}{2\pi b q_0 \varepsilon_1^2 |k| \text{NEQ}_p} \text{MTF}_p^2(k). \end{aligned} \quad (34)$$

It should be pointed out that, if N_2 and N_{-2} are assumed to be zero, one gets $\varepsilon_2 = 0$ and Eq. (27) becomes exactly the same as that derived in Ref. 10, in which only N_0 , N_1 , and N_{-1} are considered. In general, however, N_2 and N_{-2} are small but not equal to zero. Hence, the derivation given here is a more general treatment in physics and mathematics. In addition, the factor $|k|$ in the numerator of Eqs. (9) and (10) moves to the denominators of Eqs. (32) and (34). Readers are referred to the Appendix of this paper for the details related to the derivation of Eq. (34).

II.C. Measurement of the modulation transfer function $\text{MTF}_p(k)$ of DPC-CT

It has been an established practice in conventional CT to measure the $\text{MTF}_a(k)$ with a thin wire phantom.^{29,46,47} The wire is usually made of metal, such as tungsten, and placed in either air or water, as long as the attenuation of the thin wire does not exceed the dynamic range of the CT detector. Moreover, it has been well evaluated and verified that, as long as its diameter is substantially smaller than the detector cell dimension, the influence of the wire's thickness on the $\text{MTF}_a(k)$ measurement can be ignored.⁴⁷ Unfortunately, however, this approach cannot be directly adopted for measurement of $\text{MTF}_p(k)$ in the x-ray tube and grating-based DPC-CT, because the detection of the signal generated by such a thin wire may be substantially compromised.¹³ The major reasons underlying this difficulty are: (i) the signal generated in the DPC-CT is the projection of the refractive coefficient's derivative, which is an odd function in the case of a cylindrical object; (ii) the detection of such a projection can be severely compromised because the integration of an odd function over the finite dimension of a detector cell may be null. As indicated in Ref. 13, a better approach is to utilize a cylindrical object with a diameter substantially larger than the detector cell dimension. The cylinder is placed parallel to the y axis of the DPC-CT and thus it becomes a circle in a reconstructed transverse image. The distribution along a line starting at the center of the circle (namely, a semiradial line) is actually an edge spread function (ESF). In order to reduce

random interference, a total of 360 semiradial lines at 1° intervals are engaged, and the intensity profiles reconstructed along these semiradial lines are averaged to get the ESF. The line spread function (LSF) is attained from the ESF via a numerical method, in which an adequate upsampling is carried out to assure that the distance between adjacent pixels along each semiradial line be $4.0 \mu\text{m}$ for numerical accuracy. Subsequently, the DPC-CT's $\text{MTF}_p(k)$ is attained through a 1D discrete Fourier transform of the LSF. To assure a fair evaluation and comparison between the DPC-CT and conventional CT, this $\text{ESF} \rightarrow \text{LSF} \rightarrow \text{MTF}(k)$ approach, rather than the conventional method using a thin wire, is also employed to obtain the $\text{MTF}_a(k)$ of the conventional CT.

It should be noted that, in theory, the so-called phase wrapping phenomenon, i.e., the detected phase exceeds the unambiguous 2π phase range, can occur in the measurement of DPC-CT's $\text{MTF}_p(k)$ with the method specified above. As indicated in the literature [Eq. (19) in Ref. 13], given a cylindrical object, phase wrapping occurs at

$$x_w = \mp \frac{R}{\sqrt{1 + (mg_2\alpha/\pi)^2}}, \quad (35)$$

where m is the index of fractional Talbot distance, R is the radius of the cylindrical object, and α is the phase shift induced by the object per unit length along the x axis. Since g_2 is very small in comparison to α , [e.g., $\alpha \approx 46 \text{ rad/mm}$ in soft tissues at 25 keV (Ref. 13)], x_w is almost equal to R , i.e., phase wrapping occurs at the locations immediately adjacent to the cylinder's edge. It is argued in Ref. 13 that, because of the finite size of a detector cell, the phase wrapping in the case of a cylindrical object made of soft tissue may be reduced to an extent that is not detectable in the DPC-CT. This may be perceived as a form of the partial volume effect as we experienced in the conventional CT, and interested readers are referred to Ref. 13 for more details.

II.D. Quantitative evaluation of the spectrum of noise equivalent quanta $\text{NEQ}(k)$ and detective quantum efficiency $\text{DQE}(k)$

According to Eqs. (9) and (34), the noise power spectrum $\text{NPS}(k)$ and modulation transfer function $\text{MTF}(k)$ are the two prerequisites to obtain the spectrum of noise equivalent quanta $\text{NEQ}(k)$. The noise power spectrum can be calculated by taking the Fourier transform of the autocorrelation function that is obtained using a large number of noise images. An alternative approach that is more efficient in computation is to take the average of the squared Fourier transform of a large number of noise images or regions within the images containing noise only.²¹ The obtained 2D $\text{NPS}(k)$ is circularly symmetric about its origin, as predicted in Eqs. (9) and (34). The modulation transfer function $\text{MTF}(k)$ is acquired using the method depicted in Subsection II.C and is also in circular symmetry. Thereby, the spectra of noise equivalent quanta $\text{NEQ}(k)$ of the conventional CT and DPC-CT can be obtained using Eqs. (10) and (32), which are also in circular

symmetry, followed by the spectra of detective quantum efficiency DQE(k) using Eqs. (11) and (33), respectively.

III. EVALUATION VIA SIMULATION STUDIES

The spectrum of noise equivalent quanta $\text{NEQ}_a(k)$ of conventional CT specified in Eq. (10) has been evaluated and verified through studies based on computer simulation and physical CT systems.^{20,21,23,33–35} It is essential for us to evaluate and verify the DPC-CT's spectrum of noise equivalent quanta $\text{NEQ}_p(k)$ derived in this paper. We carry out a computer simulation study as the initial effort. For the following reasons, we constrain ourselves to conducting the computer simulation study in the parallel beam geometry: (i) the x-ray beam in differential phase contrast CT satisfies the paraxial condition and thus the beam is almost parallel, (ii) the image reconstruction algorithms in the parallel beam geometry outperform those in the fan beam geometry from the perspective of noise uniformity and thus almost all the clinical CT scanners based on the third generation geometry (fan beam or cone beam) adopt the parallel beam reconstruction algorithms via fan-to-parallel rebidding,^{45,46} and (iii) most of the simulation studies to investigate the noise power spectrum of CT imaging thus far have been carried out in the parallel beam geometry to exclude the influence of rebidding and weighting schemes. The x-ray source is assumed monochromatic at 30 keV, which irradiates an object by 360° at 1° steps so that no weighting effect can be induced to degrade the noise uniformity. At 30 keV, a 20-fold upsampling is assumed to simulate the x-ray beam's propagation through the gratings G_1 and G_2 with periods 8 and 4 μm , respectively, while the distance between these two gratings is 193.6 mm, i.e., 1/16 of the Talbot distance. The field of view (FOV) in data acquisition and image reconstruction is $40.96 \times 40.96 \text{ mm}^2$. The size of each detector cell is set at $32 \times 32 \mu\text{m}^2$, $64 \times 64 \mu\text{m}^2$, $96 \times 96 \mu\text{m}^2$, and $128 \times 128 \mu\text{m}^2$, resulting in the detector consisting of 1280, 640, 426 and 320 cells, respectively. Grating G_2 shifts ten times at step 0.4 μm along the x axis to retrieve the phase information corresponding to the refractive property of the object to be imaged.

Since the purpose of this work is to investigate the potential imaging performance of the DPC-CT and compare it with that of the conventional CT, no windowing or boosting techniques⁴² are adopted in image reconstruction for both the DPC-CT and conventional CT. The data $\varphi_1(u, v)$ specified in Eq. (6) is used to reconstruct the DPC-CT images, in which the classical FBP (Ref. 42) with the Hilbert transform^{43,44} is used. The projection data corresponding to the conventional CT are acquired without the G_1 and G_2 gratings in place, and the ramp filter is used to reconstruct the images with the classical FBP algorithm.⁴² It has been claimed in the literature that the data corresponding to the $a_0(u, v)$ in Eq. (4), which are acquired with the gratings G_1 and G_2 in place, are equal to the attenuation projection data acquired in the conventional CT. However, we agree with the discussion presented in Ref. 13 that such a claim only holds approximately, i.e., the $a_0(u, v)$ in Eq. (4) is not exactly the same as the attenuation projection acquired in the conventional CT. Hence, we do not

include the results corresponding to the $a_0(u, v)$ in Eq. (4) in this paper.

Prior to analyzing the spectrum of noise equivalent quanta $\text{NEQ}(k)$, the C-D phantom²⁴ with outer dimension $37.68 \times 28.26 \text{ mm}^2$ is employed to evaluate and verify the modeling and simulation accuracy of x-ray propagation, data acquisition and image reconstruction of the DPC-CT. The bulk of the C-D phantom is made of water with its complex refractive coefficient equal to $n = 1 - \delta + i\beta = 1 - 2.5604 \times 10^{-7} + i1.2353 \times 10^{-10}$, which is consistent with that specified in Ref. 2. Other parameters used to simulate the C-D phantom are: rod size (left to right): 16, 32, 64, 96, 128, 192, 256, 384, 512, and 1024 μm ; contrast of the rods against phantom body (bottom to top): 5%–50% at step 5%.

To have an accurate and precise measurement of the modulation transfer functions $\text{MTF}_p(k)$ and $\text{MTF}_a(k)$, a cylindrical water phantom at diameter 5.1 mm is placed in air and thus the edge is sharp and at high contrast. To avoid any interference caused by noise nonuniformity, other than a water phantom, an air phantom, i.e., nothing placed in the x-ray beam, is employed to study the noise power spectra $\text{NPS}_p(k)$ and $\text{NPS}_a(k)$, and the spectra of noise equivalent quanta $\text{NEQ}_p(k)$ and $\text{NEQ}_a(k)$. The x-ray flux observing the Poisson distribution is set at $5 \times 10^6 \text{ photon/cm}^2$ per projection in the simulation study, which is consistent with that of an x-ray micro-CT in preclinical applications. At the detector cell size corresponding to $32 \times 32 \mu\text{m}^2$, $64 \times 64 \mu\text{m}^2$, $96 \times 96 \mu\text{m}^2$, and $128 \times 128 \mu\text{m}^2$, ~ 360 regions of interest (ROI) at 128×128 matrix dimension are used to obtain the noise power spectrum via 2D Fourier transform,¹⁶ in which the technique of zero padding is implemented to convert the data matrix from the dimension 128×128 to 256×256 so that the noise aliasing effect can be avoided.

By definition, the noise equivalent quanta is the total effective number of x-ray quanta detected per unit of detector area in the data acquisition.^{20–23,27,28,30,32} Hence, the specification of the total number of x-ray quanta, i.e., x-ray exposure, is crucial in the investigation of noise equivalent quanta, particularly in the scenario wherein two imaging methods are to be compared. As indicated in Sec. II.A, at each angular position in the data acquisition of DPC-CT implemented with x-ray tube and gratings, grating G_2 needs to linearly shift M steps ($M = 10$ in this work). To take this fact into account, we set the x-ray exposure corresponding to the conventional CT as M times as that of the DPC-CT at each angular position. Thus, the x-ray exposure in the data acquisition of DPC-CT and the conventional CT are kept identical.

IV. RESULTS

IV.A. $\text{MTF}_p(k)$ of DPC-CT compared with $\text{MTF}_a(k)$ of the conventional CT

The modulation transfer functions of the DPC-CT and conventional CT have been thoroughly evaluated in our quantitative investigation. Plotted in Figs. 3–6(a) are the $\text{MTF}_p(k)$ and $\text{MTF}_a(k)$ at detector cell size $32 \times 32 \mu\text{m}^2$, $64 \times 64 \mu\text{m}^2$, $96 \times 96 \mu\text{m}^2$, and $128 \times 128 \mu\text{m}^2$, respectively. A close

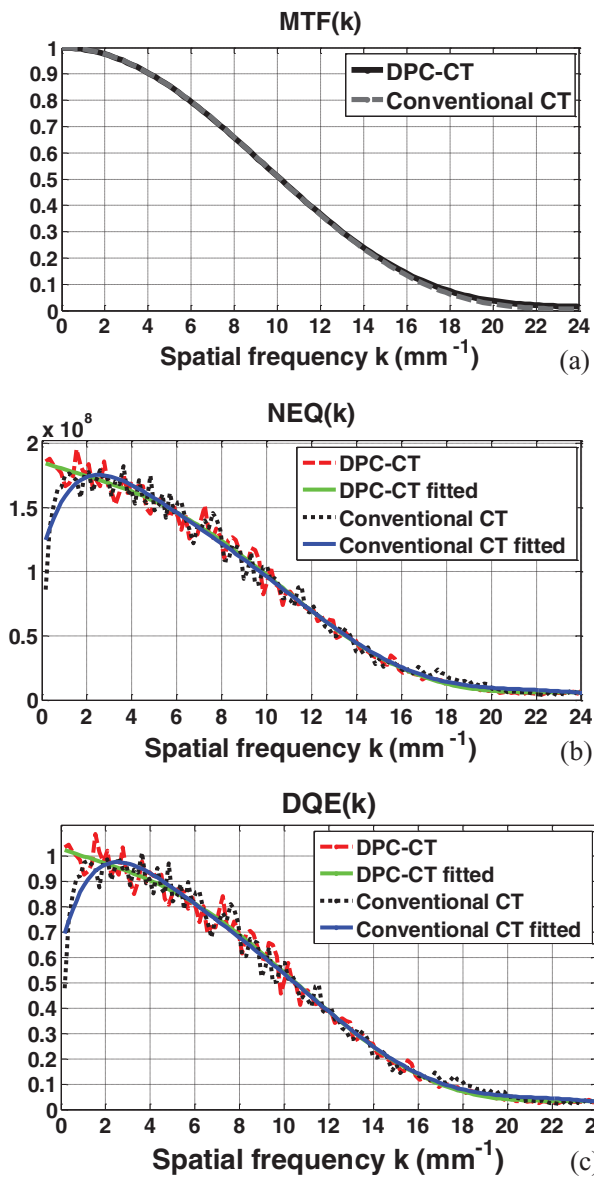


FIG. 3. The imaging performance of DPC-CT compared with that of the conventional CT: (a) $\text{MTF}_p(k)$ and $\text{MTF}_a(k)$, (b) $\text{NEQ}_p(k)$ and $\text{NEQ}_a(k)$, and (c) $\text{DQE}_p(k)$ and $\text{DQE}_a(k)$ (detector cell dimension: $32 \times 32 \mu\text{m}^2$; x-ray exposure $5 \times 10^6 \text{ photon}/\text{cm}^2$ per projection).

inspection of these plots shows that their spatial resolution measured by the modulation transfer functions $\text{MTF}_p(k)$ and $\text{MTF}_a(k)$ is almost identical. We have experienced in the conventional CT that a difference in the noise texture/granularity in general means a difference in the spatial resolution. Fortunately, however, this is not the case with regards to the $\text{MTF}_p(k)$ and $\text{MTF}_a(k)$ between DPC-CT and conventional CT. It is important to note that the equality between $\text{MTF}_p(k)$ and $\text{MTF}_a(k)$ is of theoretical and practical relevance, and a detailed discussion on this respect is deferred to Sec. V.

IV.B. $\text{NEQ}_p(k)$ of DPC-CT compared with $\text{NEQ}_a(k)$ of the conventional CT

The profiles along the radial line that crosses the 2D spectra of noise equivalent quanta $\text{NEQ}(k)$ of both DPC-

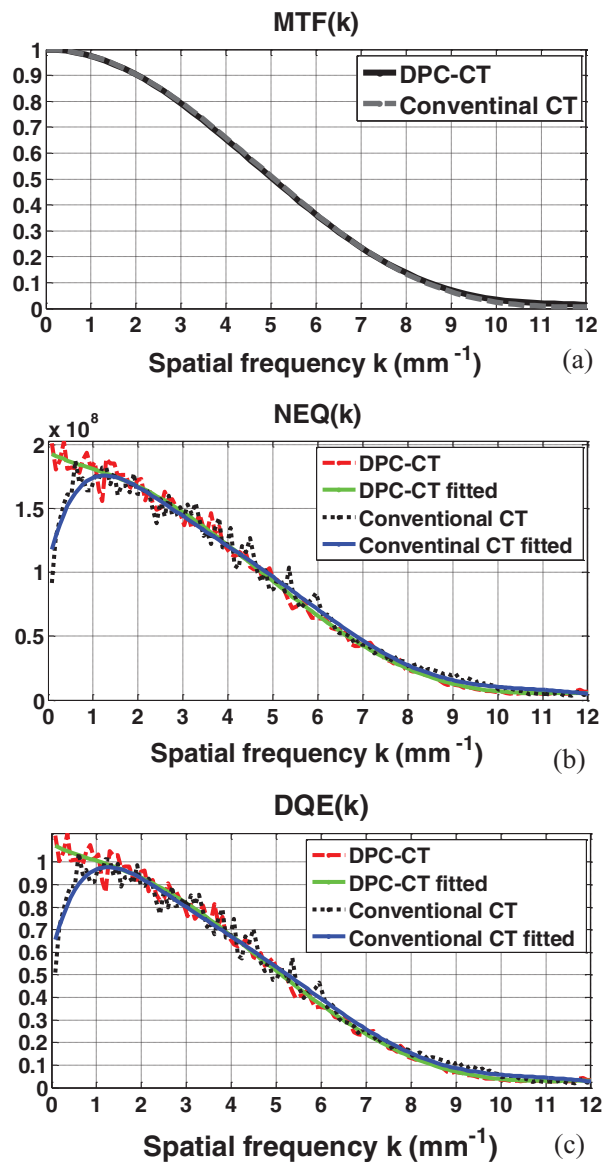


FIG. 4. The imaging performance of DPC-CT compared with that of the conventional CT: (a) $\text{MTF}_p(k)$ and $\text{MTF}_a(k)$, (b) $\text{NEQ}_p(k)$ and $\text{NEQ}_a(k)$, and (c) $\text{DQE}_p(k)$ and $\text{DQE}_a(k)$ (detector cell dimension: $64 \times 64 \mu\text{m}^2$; x-ray exposure $5 \times 10^6 \text{ photon}/\text{cm}^2$ per projection).

CT and conventional CT at 45° are plotted in Figs. 3–6(b), corresponding to detector cell dimension $32 \times 32 \mu\text{m}^2$, $64 \times 64 \mu\text{m}^2$, $96 \times 96 \mu\text{m}^2$, and $128 \times 128 \mu\text{m}^2$, respectively. As such, the variation of $\text{NEQ}_p(k)$ of the DPC-CT as a function over the detector cell dimension can be evaluated. Note that the fluctuation in the profiles of the spectra of noise equivalent quanta $\text{NEQ}_p(k)$ and $\text{NEQ}_a(k)$ are quite severe, because only 360 ROIs at matrix dimension 128×128 in the air phantom are engaged in the measurement. With an increasing number, e.g., more than 1000 (see Ref. 21), of ensemble samples (images or ROIs within the images of the air phantom), smoother profiles corresponding to the noise power spectra can be obtained. Note that the order of the polynomial fitting is determined empirically via trial-and-error to assure that the fitted profile adequately follows the trend in $\text{NEQ}_p(k)$ and $\text{NEQ}_a(k)$.

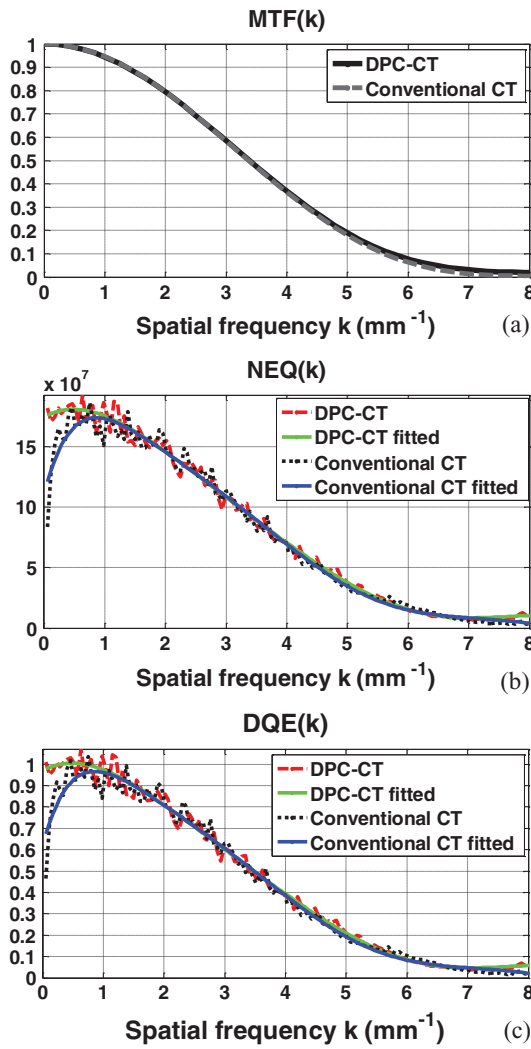


FIG. 5. The imaging performance of DPC-CT compared with that of the conventional CT: (a) $\text{MTF}_p(k)$ and $\text{MTF}_a(k)$, (b) $\text{NEQ}_p(k)$ and $\text{NEQ}_a(k)$, and (c) $\text{DQE}_p(k)$ and $\text{DQE}_a(k)$ (detector cell dimension: $96 \times 96 \mu\text{m}^2$; x-ray exposure $5 \times 10^6 \text{ photon/cm}^2$ per projection).

IV.C. $\text{DQE}_p(k)$ of DPC-CT compared with $\text{DQE}_a(k)$ of the conventional CT

The profiles along the radial line that crosses the 2D spectra of detective quantum efficiency $\text{DQE}(k)$ of both DPC-CT and conventional CT at 45° are plotted in Figs. 3–6(c), corresponding to detector cell dimension $32 \times 32 \mu\text{m}^2$, $64 \times 64 \mu\text{m}^2$, $96 \times 96 \mu\text{m}^2$, and $128 \times 128 \mu\text{m}^2$, respectively. It should be noted that the only difference between Figs. 3–6(b) and 6(c) is the scaling by the x-ray exposure in the DPC-CT and conventional CT, respectively.

V. DISCUSSIONS

This work is a continuation of our previous investigation focused on the noise power spectrum $\text{NPS}_p(k)$ of DPC-CT.¹¹ The primary contribution of this work is derivation of the functional forms of noise power spectrum $\text{NPS}_p(k)$, spectrum of noise equivalent quanta $\text{NEQ}_p(k)$, and $\text{DQE}_p(k)$ of the DPC-CT. By conducting a computer simulation study, we

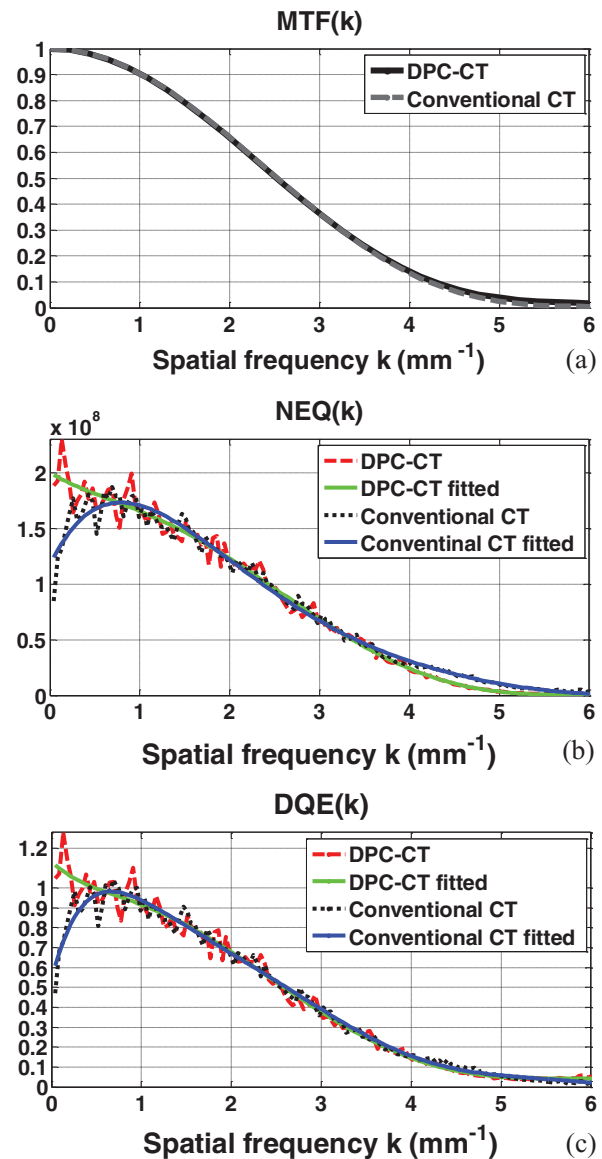


FIG. 6. The imaging performance of DPC-CT compared with that of the conventional CT: (a) $\text{MTF}_p(k)$ and $\text{MTF}_a(k)$, (b) $\text{NEQ}_p(k)$ and $\text{NEQ}_a(k)$, and (c) $\text{DQE}_p(k)$ and $\text{DQE}_a(k)$ (detector cell dimension: $128 \times 128 \mu\text{m}^2$; x-ray exposure $5 \times 10^6 \text{ photon/cm}^2$ per projection).

evaluate and verify the derived functional forms and compare them with their counterparts in the conventional CT. To summarize the results, a number of observations and clarifications are given below.

In general, the spectrum of noise equivalent quanta of an imaging system is in the functional form^{20,21,26–30}

$$\text{NEQ}(k) = G^2 \frac{\text{MTF}^2(k)}{\text{NPS}(k)}. \quad (36)$$

By definition, G , $\text{MTF}(k)$ and $\text{NPS}(k)$ denote the imaging system's transfer characteristics of large area gain, signal, and noise, respectively. In various imaging modalities, Eq. (36) can be in different expressions. For instance, the spectrum of noise equivalent quanta of x-ray radiography and fluoroscopy is expressed in exactly the same way as Eq. (36), whereas that

of the conventional CT is expressed in Eq. (10). The spectrum of noise equivalent quanta $\text{NEQ}_p(k)$ of the DPC-CT implemented with x-ray tube and grating is specified in Eq. (32). It is interesting and important to note that the term $|k|$ is in the denominator of $\text{NEQ}_p(k)$, whereas it is in the numerator of $\text{NEQ}_a(k)$.

The computer simulation study shows that, given detector cell dimension, the modulation transfer function $\text{MTF}_p(k)$ of the DPC-CT is virtually the same as the $\text{MTF}_a(k)$ of the conventional CT [see Figs. 3–6(a)]. It should be indicated that no widow or boosting technique is utilized to obtain the modulation transfer functions investigated in this work. This means that, despite the difference in the imaging mechanisms between DPC-CT and conventional CT, their modulation transfer functions are essentially determined by dimension of the detector cells used for data acquisition, warranting that the signal transfer characteristics and spatial resolution are in principle identical in these two imaging methods. This result is consistent with what has been published in the literature.^{12,13} Note that such a fact is of not only theoretical but also practical importance, especially in the scenarios wherein the complementary information drawn from the DPC-CT and the conventional CT are jointly of relevance for applications.

The primary finding of this work is that, except at the spatial frequency close to zero, the spectrum of noise equivalent quanta $\text{NEQ}_p(k)$ and detective quantum efficiency $\text{DQE}_p(k)$ of DPC-CT are in principle identical to their counterparts $\text{NEQ}_a(k)$ and $\text{DQE}_a(k)$ in the conventional CT, though there exists a radical difference in their noise power spectrum $\text{NPS}_p(k)$ and $\text{NPS}_a(k)$. This means that the DPC-CT makes use of x-ray flux as efficiently as the conventional CT if the object to be imaged is of finite size. This fact initially seems surprising since there is a significant difference between $\text{NPS}_p(k)$ and $\text{NPS}_a(k)$. However, it should become readily understandable if we inspect Eqs. (10) and (32) carefully. The term $|k|$ is at the numerator and denominator of $\text{NEQ}_a(k)$ and $\text{NEQ}_p(k)$, respectively, offsetting the substantial difference in their corresponding $\text{NPS}_a(k)$ and $\text{NPS}_p(k)$. Hence, $\text{NEQ}_p(k)$, $\text{DQE}_p(k)$, $\text{NEQ}_a(k)$, and $\text{DQE}_a(k)$ are essentially determined by $\text{MTF}_a(k)$ and $\text{MTF}_p(k)$, as analytically specified by Eqs. (10), (11), (32) and (33) and experimentally verified by the simulation study as demonstrated in Figs. 3–6(b) and 6(c).

By referring to Eq. (1), one may reason that the advantage of DPC-CT in squared signal-to-noise ratio or detectability index over the conventional CT is solely dependent on the extent to which the $\Delta S_p(f)$ in DPC-CT is larger than its counterpart $\Delta S_a(f)$ in the conventional CT, since the $\text{NEQ}_p(k)$ and $\text{NEQ}_a(k)$ are essentially identical. Again, this seems inconsistent with our anticipation based on the observation that there exists a radical difference in their noise power spectrum $\text{NPS}_p(k)$ and $\text{NPS}_a(k)$. However, it should be understood that the $\text{SNR}^2_{\text{ideal}}$ specified in Eq. (1) is defined under the framework of ideal observer, wherein an ideal observer is assumed to be capable of undoing or removing any correlation in noise, i.e., “pre-whitening” colored noise.^{26,28} It is interesting and important to note that, the “pre-whitening” is accomplished

by the term $|k|$ at the numerator and denominator of $\text{NEQ}_a(k)$ and $\text{NEQ}_p(k)$, respectively, which offsets the substantial difference in their corresponding $\text{NPS}_a(k)$ and $\text{NPS}_p(k)$.

We would like to point out and emphasize that a human observer is not an ideal observer, i.e., a human observer is not able to “pre-whiten” colored noise while making a decision. The colored noise plays a significant role in disturbing a human observer’s realistic decision-making capacity.^{26,28} As we have observed, the noise in DPC-CT is abundant at low frequencies (see Fig. 2), while that in the conventional CT occurs at high frequencies. Hence, it is reasonable to anticipate that, if the object to be imaged is of relatively higher frequency, i.e., smaller in size, a human observer may make a better decision based on DPC-CT images than that made based on conventional CT images. This means that, even if $\Delta S_p(f) = \Delta S_a(f)$, the $\text{SNR}^2_{\text{nonideal}}$ of DPC-CT can still be higher than $\text{SNR}^2_{\text{nonideal}}$ of the conventional CT, while the object to be imaged is small in size. In practice, a tomographic imaging method that is less susceptible to high frequency noise has been desired for a long time. The DPC-CT implemented with x-ray tube and grating is just such an imaging modality, which can be of profound significance in clinical and preclinical applications, e.g., the early detection of tumor or atherosclerosis, because a pathophysiological lesion usually starts at a small size.

We have indicated that the root cause for the radical difference between $\text{NPS}_p(k)$ and $\text{NPS}_a(k)$ is the adoption of the Hilbert filter kernel, rather than the ramp filter kernel, for image reconstruction in the DPC-CT using a filtered backprojection algorithm.¹¹ However, it is interesting to note that such a radical difference between the $\text{NPS}_p(k)$ and $\text{NPS}_a(k)$ has also been reported in Ref. 12, wherein an integration is carried out on the projection data, followed by the well-known ramp filtering, i.e., no Hilbert filtering is carried out explicitly. In fact, however, a cascading of integration and ramp filtering is equivalent to a Hilbert filtering. Thus, we still believe that the root cause underlying the significant difference between $\text{NPS}_p(k)$ and $\text{NPS}_a(k)$ and the resultant difference in $\text{NEQ}_p(k)$ and $\text{NEQ}_a(k)$ is that the data acquired in DPC-CT is the projection of the derivative of the refractive coefficient and in principle only a Hilbert filtering is needed for image reconstruction. In addition, we would like to indicate that, though the image reconstruction scheme used in Ref. 12 may be beneficial in terms of inheriting the filtering strategies established in the conventional CT, the degradation in accuracy and spatial resolution due to the cumulative sum cannot be ignored in practice, especially in the cases wherein the detector cell dimension is not small.

The imaging chain of both DPC-CT and conventional CT is assumed ideal, which should not be confused with the concept of an ideal observer mentioned above, in its system modeling, analysis, and evaluation. For example, the x-ray source is assumed monochromatic in this work and thus the conventional CT investigated in this work is actually a “monochromatic” one. However, the conventional CT in reality usually utilizes a polychromatic x-ray source. Hence, the readers are advised to understand that the imaging performance, including the spectrum of noise equivalent quanta and detective

quantum efficiency, of both DPC-CT and the conventional CT may be degraded by the imperfection in its imaging chain in practical situations.

The implementation of a DPC-CT is more challenging, because of the stringent requirements on the optoelectronic accuracy of grating fabrication, mechanical alignment, and stability. The time for data acquisition in the grating-based DPC-CT can be longer if grating G_1 or G_2 needs to shift multiple times. Owing to the phase wrapping phenomenon, the unambiguous phase detection range of DPC-CT is 2π , which may impose limitations on the dynamic range over preclinical and clinical applications. In addition, the noise morphology in DPC-CT images is similar to the texture of some soft tissues. On the other hand, it has been tabulated in Ref. 15 that the refractive coefficients of low atomic number materials are substantially larger than their attenuation counterpart. The preliminary data reported in the literature^{1,4,5} have demonstrated that the $\Delta S_p(f)$ in soft tissues is significantly larger than its counterpart $\Delta S_a(f)$. Moreover, as indicated above, there may exist an extra gain in the DPC-CT's SNR²_{nonideal} over that of the conventional CT. Hence, it is hoped that the potential of significantly increased contrast sensitivity over soft tissues may outweigh the DPC-CT's implemental shortcomings and enable it to outperform the conventional CT as an imaging modality for extensive preclinical and clinical applications.

VI. CONCLUSIONS

The spectrum of noise equivalent quanta $NEQ_p(k)$ and detective quantum efficiency $DQE_p(k)$ of the DPC-CT is analytically derived in this paper, followed by an evaluation and verification via computer simulation study, as well as its comparison with that of the conventional CT. The signal transfer property of the DPC-CT characterized by the modulation transfer function $MTF_p(k)$ is virtually identical to the $MTF_a(k)$ of conventional CT. Moreover, though there exists a radical difference in their noise property characterized by the noise power spectrum $NPS_p(k)$ and $NPS_a(k)$, the spectrum of noise equivalent quanta $NEQ_p(k)$ and detective quantum efficiency $DQE_p(k)$ of DPC-CT are essentially identical to their counterparts $NEQ_a(k)$ and $DQE_a(k)$ in the conventional CT. It is believed that the $NEQ_p(k)$ and $DQE_p(k)$ characteristics of the DPC-CT unveiled in this study can be of theoretical and practical relevance in the design and optimization of DPC-CT for extensive preclinical and ultimately clinical applications.

ACKNOWLEDGMENTS

This work is partially supported by the U.S. National Institute of Health through Grant No. 5P50CA128301, as well as by the Telemedicine and Advanced Technology Research Center (TATRC) at the U.S. Army Medical Research and Material Command (USAMRMC) Fort Detrick, MD via the award under Contract No. W81XWH-12-1-0138. In addition, the authors would like to express their appreciation to Ms. Jessica Paulishen for her proof reading of this paper.

APPENDIX: DERIVATION OF THE NOISE POWER SPECTRUM $NPS_p(k)$ IN DPC-CT

Letting the projection of an object function $f(x, y)$ be

$$P_\theta(t) = \int_{-\infty}^{\infty} dx \int_{-\infty}^{\infty} dy f(x, y) \delta(x \cos\theta + y \sin\theta - t), \quad (\text{A1})$$

the object function $f(x, y)$ can be reconstructed from its projection by

$$\hat{f}(x, y) = \int_0^\pi d\theta \int_{-\infty}^{\infty} |k| S_\theta(k) \times \exp[2\pi i k(x \cos\theta + y \sin\theta)] dk, \quad (\text{A2})$$

where the character \wedge is used to differentiate the reconstructed object function from the original object function. The Fourier transform of projection $P_\theta(t)$ is defined as

$$S_\theta(k) = \int_{-\infty}^{\infty} P_\theta(t) \exp(-2\pi i kt) dt, \quad (\text{A3})$$

and its inverse Fourier transform can be written as

$$P_\theta(t) = \int_{-\infty}^{\infty} S_\theta(k) \exp(2\pi i kt) dk. \quad (\text{A4})$$

According to the property of Fourier transform, if $D_\theta(t)$ denotes the derivative of $P_\theta(t)$, one has the Fourier transform pair

$$D_\theta(t) = \frac{\partial P_\theta(t)}{\partial t} = \int_{-\infty}^{\infty} 2\pi i k S_\theta(k) \exp(2\pi i kt) dk, \quad (\text{A5a})$$

$$D_\theta(k) = \int_{-\infty}^{\infty} D_\theta(t) \exp(-2\pi i kt) dt = 2\pi i k S_\theta(k). \quad (\text{A5b})$$

Substituting Eq. (A5b) into Eq. (A2), one obtains

$$\begin{aligned} \hat{f}(x, y) &= \frac{1}{2\pi} \int_0^\pi d\theta \int_{-\infty}^{\infty} D_\theta(k) \frac{|k|}{ik} \exp[2\pi i k(x \cos\theta + y \sin\theta)] dk \\ &= \frac{1}{2\pi} \int_0^\pi d\theta \int_{-\infty}^{\infty} D_\theta(k) (-i \operatorname{sgn}(k)) \exp[2\pi i k(x \cos\theta + y \sin\theta)] dk \\ &= \frac{1}{2\pi} \int_0^\pi d\theta \int_{-\infty}^{\infty} D_\theta(k) H(k) \exp[2\pi i k(x \cos\theta + y \sin\theta)] dk, \end{aligned} \quad (\text{A6})$$

where $H(k)$ represents the Fourier transform of Hilbert filter kernel $h(t)$, i.e.,

$$H(k) = \int_{-\infty}^{\infty} h(t) \exp(-2\pi i k t) dt, \quad (\text{A7a})$$

$$h(t) = \int_{-\infty}^{\infty} (-i \operatorname{sgn}(k)) \exp(2\pi i k t) dk. \quad (\text{A7b})$$

In the way similar to Ref. 20, without losing generality, we assume the object function $f(x, y)$ is circularly symmetric, i.e., $f(x, y) = f(r, \theta) = f(r, 0) = f(r)$. In the polar coordinate system, one has

$$\hat{f}(r) = \frac{1}{2\pi} \int_0^\pi d\theta \int_{-\infty}^{\infty} D_\theta(k) H(k) \exp(2\pi i kr \cos\theta) dk. \quad (\text{A8})$$

Note that the subscript θ is kept in $D_\theta(t)$ for consistence in expression, though $D_\theta(t)$ is actually not a function of θ due to the circular symmetry in $f(x, y)$. It should be easy to show that the Fourier transform $F(k)$ of a circularly symmetric function $f(r)$ is an even function and thus

$$\begin{aligned} \hat{f}(r) &= \int_0^{2\pi} d\theta \int_0^{\infty} dk \hat{F}(k) k \exp(2\pi i rk \cos\theta) \\ &= \int_0^\pi d\theta \int_0^{\infty} dk \hat{F}(k) k \exp(2\pi i rk \cos\theta) + \int_\pi^{2\pi} d\theta \int_0^{\infty} dk \hat{F}(k) k \exp(2\pi i rk \cos\theta) \\ &= \int_0^\pi d\theta \int_0^{\infty} dk \hat{F}(k) k \exp(2\pi i rk \cos\theta) + \int_0^\pi d\theta \int_0^{\infty} dk \hat{F}(k) k \exp(-2\pi i rk \cos\theta) \\ &= \int_0^\pi d\theta \int_0^{\infty} dk \hat{F}(k) k \exp(2\pi i rk \cos\theta) - \int_0^\pi d\theta \int_0^{-\infty} dk \hat{F}(-k) |k| \exp(2\pi i rk \cos\theta) \\ &= \int_0^\pi d\theta \int_0^{\infty} dk \hat{F}(k) |k| \exp(2\pi i rk \cos\theta) + \int_0^\pi d\theta \int_{-\infty}^0 dk \hat{F}(k) |k| \exp(2\pi i rk \cos\theta) \\ &= \int_0^\pi d\theta \int_{-\infty}^{\infty} dk \hat{F}(k) |k| \exp(2\pi i rk \cos\theta). \end{aligned} \quad (\text{A9})$$

Comparing Eqs. (A8) and (A9), one gets

$$\hat{F}(k) = \frac{D_\theta(k) H(k)}{2\pi |k|}. \quad (\text{A10})$$

Letting the object function $f(x, y)$ be a delta function, i.e., $f(x, y) = \delta(x)\delta(y)$, the magnitude of the Fourier Transform of the reconstructed object function is the modulation transfer function, i.e.,

$$\text{MTF}_p(k) = |\hat{F}(k)| \text{ while } f(x, y) = \delta(x)\delta(y). \quad (\text{A11})$$

Noting that

$$\begin{aligned} D_\theta(k) &= \int_{-\infty}^{\infty} dt \exp(-2\pi i kt) \frac{\partial P_\theta(t)}{\partial t} = 2\pi i k \int_{-\infty}^{\infty} dt P_\theta(t) \exp(-2\pi i kt) \\ &= 2\pi i k \int_{-\infty}^{\infty} dt \exp(-2\pi i kt) \int_{-\infty}^{\infty} dx \int_{-\infty}^{\infty} dy \delta(x)\delta(y) \delta(x \cos\theta + y \sin\theta - t) \\ &= 2\pi i k \int_{-\infty}^{\infty} dt \exp(-2\pi i kt) \delta(-t) = 2\pi i k, \end{aligned} \quad (\text{A12})$$

and substituting Eqs. (A11) and (A12) into Eq. (A10), one obtains

$$\text{MTF}_p(k) = \left| \frac{i k H(k)}{|k|} \right| = |i \operatorname{sgn}(k) H(k)| = |H(k)|. \quad (\text{A13})$$

On the other hand, the autocovariance function of the reconstructed object function is

$$C(x, y) = \langle \Delta \hat{f}(x, y) \Delta \hat{f}(0, 0) \rangle, \quad (\text{A14})$$

where $\Delta \hat{f}(x, y)$ represents the deviation of $\hat{f}(x, y)$ from its mean value.²⁰ Substituting Eqs. (A5b) and (A7a) into Eq. (A6), one gets

$$\begin{aligned}\hat{f}(x, y) &= \int_0^\pi \frac{d\theta}{2\pi} \int_{-\infty}^\infty dk \exp[2\pi ik(x \cos\theta + y \sin\theta)] \int_{-\infty}^\infty dt D_\theta(t) \exp(-2\pi ikt) \\ &\quad \times \int_{-\infty}^\infty dt_1 h(t_1) \exp(-2\pi ikt_1) \\ &= \int_0^\pi \frac{d\theta}{2\pi} \int_{-\infty}^\infty dt D_\theta(t) \int_{-\infty}^\infty dt_1 h(t_1) \int_{-\infty}^\infty dk \exp[2\pi ik(x \cos\theta + y \sin\theta - t - t_1)] \\ &= \int_0^\pi \frac{d\theta}{2\pi} \int_{-\infty}^\infty dt D_\theta(t) \int_{-\infty}^\infty dt_1 h(t_1) \delta(x \cos\theta + y \sin\theta - t - t_1) \\ &= \int_0^\pi \frac{d\theta}{2\pi} \int_{-\infty}^\infty dt D_\theta(t) h(x \cos\theta + y \sin\theta - t),\end{aligned}\tag{A15}$$

$$\Delta \hat{f}(x, y) = \int_0^\pi \frac{d\theta}{2\pi} \int_{-\infty}^\infty dt \Delta D_\theta(t) h(x \cos\theta + y \sin\theta - t).\tag{A16}$$

Subsequently, the autocovariance function becomes

$$\begin{aligned}C(x, y) &= \left\langle \int_0^\pi \frac{d\theta}{2\pi} \int_{-\infty}^\infty dt \Delta D_\theta(t) h(x \cos\theta + y \sin\theta - t) \int_0^\pi \frac{d\theta_1}{2\pi} \int_{-\infty}^\infty dt_1 \Delta D_{\theta_1}(t_1) h(-t_1) \right\rangle \\ &= \int_0^\pi \frac{d\theta}{2\pi} \int_{-\infty}^\infty dt h(x \cos\theta + y \sin\theta - t) \int_0^\pi \frac{d\theta_1}{2\pi} \int_{-\infty}^\infty dt_1 h(-t_1) \langle \Delta D_\theta(t) \Delta D_{\theta_1}(t_1) \rangle.\end{aligned}\tag{A17}$$

Assuming the recorded data $D_\theta(t)$ are uncorrelated, i.e.,

$$\int_0^\pi d\theta_1 \int_{-\infty}^\infty dt_1 h(x \cos\theta + y \sin\theta - t) h(-t_1) \langle \Delta D_\theta(t) \Delta D_{\theta_1}(t_1) \rangle\tag{A18}$$

$$= \frac{a\pi}{N_\theta} \sigma_D^2 h(x \cos\theta + y \sin\theta - t) h(-t)\tag{A19}$$

where σ_D^2 is the noise at each detector cell, a is the detector pitch, and N_θ is the total number of projection $D_\theta(t)$. Then, Eq. (A17) becomes

$$C(x, y) = \frac{a\sigma_D^2}{4\pi N_\theta} \int_0^\pi d\theta \int_{-\infty}^\infty dt h(x \cos\theta + y \sin\theta - t) h(-t).\tag{A20}$$

Again, without losing generality, we assume a circular symmetry in $C(x, y)$, i.e.,

$$C(x, y) = C(r, 0) = C(r) = \frac{a\sigma_D^2}{4\pi N_\theta} \int_0^\pi d\theta \int_{-\infty}^\infty dt h(r \cos\theta - t) h(-t).\tag{A21}$$

Substituting Eq. (A7b) into Eq. (A21), one gets

$$\begin{aligned}C(r) &= -\frac{a\sigma_D^2}{4\pi N_\theta} \int_0^\pi d\theta \int_{-\infty}^\infty dt \int_{-\infty}^\infty dk H(k) \exp[2\pi ik(r \cos\theta - t)] \int_{-\infty}^\infty dk_1 H(k_1) \exp(-2\pi ik_1 t) \\ &= \frac{a\sigma_D^2}{4\pi N_\theta} \int_0^\pi d\theta \int_{-\infty}^\infty dk H(k) \exp(2\pi ikr \cos\theta) \int_{-\infty}^\infty dk_1 H(k_1) \int_{-\infty}^\infty dt \exp(-2\pi ik_1 t - 2\pi ikt) \\ &= \frac{a\sigma_D^2}{4\pi N_\theta} \int_0^\pi d\theta \int_{-\infty}^\infty dk H(k) \exp(2\pi ikr \cos\theta) \int_{-\infty}^\infty dk_1 H(k_1) \delta(k_1 + k) \\ &= \frac{a\sigma_D^2}{4\pi N_\theta} \int_0^\pi d\theta \int_{-\infty}^\infty dk |H(k)|^2 \exp(2\pi ikr \cos\theta).\end{aligned}\tag{A22}$$

The noise power spectrum $NPS_p(k)$, defined as the Fourier transform of autocovariance function, is an even function. Thus, the autocovariance function becomes^{20,21}

$$\begin{aligned}
C(r) &= \int_0^{2\pi} d\theta \int_0^\infty dk \text{NPS}_p(k) k \exp(2\pi ikr \cos\theta) \\
&= \int_0^\pi d\theta \int_0^\infty dk \text{NPS}_p(k) k \exp(2\pi ikr \cos\theta) + \int_\pi^{2\pi} d\theta \int_0^\infty dk \text{NPS}_p(k) k \exp(2\pi ikr \cos\theta) \\
&= \int_0^\pi d\theta \int_0^\infty dk \text{NPS}_p(k) k \exp(2\pi ikr \cos\theta) + \int_0^\pi d\theta \int_0^\infty dk \text{NPS}_p(k) k \exp(-2\pi ikr \cos\theta) \\
&= \int_0^\pi d\theta \int_0^\infty dk \text{NPS}_p(k) |k| \exp(2\pi ikr \cos\theta) - \int_0^\pi d\theta \int_0^{-\infty} dk \text{NPS}_p(-k) |k| \exp(2\pi ikr \cos\theta) \\
&= \int_0^\pi d\theta \int_{-\infty}^\infty dk \text{NPS}_p(k) |k| \exp(2\pi ikr \cos\theta).
\end{aligned} \tag{A23}$$

Comparing Eqs. (A22) and (A23), one obtains

$$\text{NPS}_p(k) = \frac{a\sigma_D^2 |H(k)|^2}{4\pi N_\theta |k|}. \tag{A24}$$

Substituting Eq. (A13) into Eq. (A24) and reformatting, one finally arrives at

$$\frac{N_\theta}{\sigma_D^2} = \frac{a}{4\pi |k| \text{NPS}_p(k)} \text{MTF}_p^2(k). \tag{A25}$$

^aAuthor to whom correspondence should be addressed. Electronic mail: xiangyang.tang@emory.edu; Telephone: (404) 778-1732; Fax: (404) 712-5813.

¹A. Momose and J. Fukuda, "Phase-contrast radiographs of nonstained rat cerebellar specimen," *Med. Phys.* **22**, 375–379 (1995).

²F. Pfeiffer, T. Weitkamp, O. Bunk, and C. David, "Phase retrieval and differential phase-contrast imaging with low-brilliance x-ray sources," *Nat. Phys.* **2**, 258–261 (2006).

³X. Wu and H. Liu, "Clinical implementation of x-ray phase-contrast imaging: Theoretical foundations and design considerations," *Med. Phys.* **30**, 2169–2179 (2003).

⁴T. Donath, F. Pfeiffer, O. Bunk, C. Grünzweig, E. Hempel, S. Popescu, P. Vock, and C. David, "Toward clinical x-ray phase-contrast CT demonstration of enhanced soft-tissue contrast in human specimen," *Invest. Radiol.* **45**, 445–452 (2010).

⁵M. Bech, T. H. Jensen, R. Feidenhan'l, O. Bunk, C. David, and F. Pfeiffer, "Soft-tissue phase-contrast tomography with x-ray tube source," *Phys. Med. Biol.* **54**, 2747–2753 (2009).

⁶W. Cai and R. Ning, "Dose efficiency consideration for volume-of-interest breast imaging using x-ray differential phase-contrast CT," *Proc. SPIE* **7258**, 72584D-7–72584D-9 (2009).

⁷C. Chou and M. A. Anastasio, "Noise texture and signal detectability in propagation-based x-ray phase-contrast tomography," *Med. Phys.* **37**, 270–281 (2010).

⁸J. Zambelli, N. Bevins, Z. Qi, and G.-H. Chen, "Radiation dose efficiency comparison between differential phase contrast CT and conventional absorption CT," *Med. Phys.* **37**, 2473–2479 (2010).

⁹X. Tang, Y. Yang, and S. Tang, "Noise characteristics of x-ray tube and grating based phase CT over spatial resolution," *1068th American Mathematics Society Meeting*, Statesboro, GA, 12–13 March, 2011.

¹⁰G.-H. Chen, J. Zambelli, K. Li, N. Bevins, and Z. Qi, "Scaling law for noise variance and spatial resolution in differential phase contrast computed tomography," *Med. Phys.* **38**, 584–588 (2011).

¹¹X. Tang, Y. Yang, and S. Tang, "Characterization of imaging performance in differential phase contrast CT compared with the conventional CT: Noise power spectrum NPS(k)," *Med. Phys.* **38**, 4386–4395 (2011).

¹²R. Raupach and Thomas G. Flohr, "Analytic evaluation of the signal and noise propagation in x-ray differential phase-contrast computed tomography," *Phys. Med. Biol.* **56**, 2219–2244 (2011).

¹³T. Köhler and E. Roessl, "Noise properties of grating-based x-ray phase contrast computed tomography," *Med. Phys.* **38**, S106–S116 (2011).

¹⁴M. Born and E. Wolf, *Principles of Optics: Electromagnetic Theory of Propagation, Interference and Diffraction of Light*, 7th ed. (Cambridge University Press, Cambridge, England, 1999).

¹⁵B. L. Henke, E. M. Gullikson, and J. C. Davis, "X-ray interaction: Photoabsorption, scattering, transmission, and deflection," *At. Data Nucl. Data Tables* **54**, 181–342 (1993).

¹⁶R. Fitzgerald, "Phase-sensitive x-ray imaging," *Phys. Today* **53**(7), 23–26 (2000).

¹⁷C. Dainty and R. Shaw, *Image Science* (Academic, London, 1974).

¹⁸H. H. Barrett, S. K. Gordon, and R. S. Hershel, "Statistical limitations in transaxial tomography," *Comput. Biol. Med.* **6**, 307–323 (1976).

¹⁹S. J. Riederer, N. J. Norbert, and D. A. Chesler, "The noise power spectrum in computed x-ray tomography," *Phys. Med. Biol.* **23**, 446–454 (1978).

²⁰R. F. Wagner, D. G. Brown, and M. S. Pastel, "Application of information theory to the assessment of computed tomography," *Med. Phys.* **6**, 83–84 (1979).

²¹K. M. Hanson, "Detectability in computed tomography images," *Med. Phys.* **6**, 441–451 (1979).

²²H. H. Barrett and W. Swindell, *Radiological Imaging: The Theory of Image Formation, Detection, and Process* (Academic, San Diego, CA, 1981).

²³K. M. Hanson, "Noise and contrast discrimination in computed tomography," in *Radiology of the Skull and Brain, Vol. V: Technical Aspects of Computed Tomography*, edited by T. H. Newton and D. G. Potts (Mosby, St. Louis, MO, 1981), pp. 3941–3955.

²⁴J. M. Sandrik and R. F. Wagner, "Absolute measures of physical image quality: Measurement and application to radiographic magnification," *Med. Phys.* **9**, 540–549 (1982).

²⁵K. Faulkner and B. M. Moores, "Analysis of x-ray computed tomography images using the noise power spectrum and autocorrelation function," *Phys. Med. Biol.* **29**, 1343–1352 (1984).

²⁶R. F. Wagner and D. G. Brown, "Unified SNR analysis of medical imaging systems," *Phys. Med. Biol.* **30**, 489–518 (1985).

²⁷C. E. Metz, R. F. Wagner, K. Doi, D. A. Brown, R. M. Nishikawa, and K. J. Myers, "Toward consensus on quantitative assessment of medical imaging systems," *Med. Phys.* **22**, 1057–1061 (1995).

²⁸ICRP (International Commission on Radiation Units and Measurements), "Medical Imaging: The assessment of image quality," ICRP Report No. 54 (ICRP, Bethesda, MD, 1996), pp. 11–67.

²⁹J. T. Bushberg, J. A. Seibert, E. M. Leidholdt, Jr., and J. M. Boone, *The Essential Physics of Medical Imaging*, 2nd ed. (Lippincott, Philadelphia, PA, 2002).

³⁰H. H. Barrett, "NEQ: Its progenitors and progeny," *Proc. SPIE* **7263**, 72630F-7-72630F-7 (2009).

³¹J. H. Siewersen, I. A. Cunningham, and D. A. Jeffray, "A framework for noise-power spectrum analysis of multidimensional images," *Med. Phys.* **29**, 2655–2671 (2002).

³²J. H. Siewersen and D. A. Jeffray, "Three-dimensional NEQ transfer characteristics of volume CT using direct and indirect-detection flat-panel imagers," *Proc. SPIE* **5030**, 92–102 (2003).

³³K. L. Boedeker, V. N. Cooper, and M. F. McNitt-Gray, "Application of the noise power spectrum in modern diagnostic MDCT: Part I. Measurement of noise power spectra and noise equivalent quanta," *Phys. Med. Biol.* **52**, 4027–4046 (2007).

³⁴D. J. Tward and J. H. Siewersen, "Cascaded systems analysis of the 3D noise transfer characteristics of flat-panel cone-beam CT," *Med. Phys.* **35**, 5510–5529 (2008).

³⁵J. Baek and N. J. Pelc, "Local and global 3D noise power spectrum in cone beam CT system with FDK reconstruction," *Med. Phys.* **38**, 2122–2131 (2011).

³⁶C. David, J. Bruder, T. Rohbeck, C. Grunzweig, C. Kottler, A. Diaz, O. Bunk, and F. Pfeiffer, "Fabrication of diffraction gratings for hard x-ray phase contrast imaging," *Microelectron. Eng.* **84**(5–8), 1172–1177 (2007).

³⁷E. Keren and O. Kafri, "Diffraction effects in moiré deflectometry," *J. Opt. Soc. Am. A* **2**, 111–120 (1985).

³⁸C. Siegel, F. Loewenthal, and J. E. Balmer, "A wavefront sensor based on the fractional Talbot effect," *Opt. Commun.* **194**, 265–275 (2001).

³⁹A. W. Lohmann, H. Knuppertz, and J. Jahns, "Fractional montgomery effect: A self-imaging phenomenon," *J. Opt. Soc. Am. A* **22**, 1500–1508 (2005).

⁴⁰R. Grella, "Fresnel propagation and diffraction and paraxial wave equation," *J. Opt. (Paris)* **13**, 367–374 (1982).

⁴¹M. Bech, "X-ray imaging with a grating interferometer," Ph.D. thesis, University of Copenhagen, Denmark, 2009.

⁴²A. C. Kak and M. Slaney, *Principles of Computerized Tomographic Imaging* (IEEE, New York, 1988).

⁴³Z. Qi, J. Zambelli, N. Bevins, and G.-H. Chen, "A novel quantitative imaging technique for material differentiation based on differential phase contrast CT," *Proc. SPIE* **7622**, 76220O-7-76220O-6 (2010).

⁴⁴F. Noo, R. Clackdoyle, and J. D. Pack, "A two-step Hilbert transform method for 2D image reconstruction," *Phys. Med. Biol.* **49**, 3903–3923 (2004).

⁴⁵X. Tang, J. Hsieh, R. A. Nilsen, S. Dutta, D. Samsonov, A. Hagiwara, C. Shaughnessy, and E. Drapkin, "A three-dimensional weighted cone beam filtered backprojection (CB-FBP) algorithm for image reconstruction in volumetric CT: Helical scanning," *Phys. Med. Biol.* **51**, 855–874 (2006).

⁴⁶X. Tang, S. Narayanan, J. Hsieh, J. D. Pack, S. M. McColash, P. Sainath, R. A. Nilsen, and B. Taha, "Enhancement of in-plane spatial resolution in volumetric computed tomography with focal spot wobbling: Overcoming the constraint on number of projection views per gantry rotation," *J. X-ray Sci. Technol.* **18**, 251–265 (2010).

⁴⁷E. L. Nickoloff, "Measurement of the PSF for a CT scanner: Appropriate wire diameter and pixel size," *Phys. Med. Biol.* **33**, 149–155 (1988).

The second-order differential phase contrast and its retrieval for imaging with x-ray Talbot interferometry

Yi Yang and Xiangyang Tang^{a)}

Imaging and Medical Physics, Department of Radiology and Imaging Sciences, Emory University School of Medicine, 1701 Uppergate Dr., C-5018, Atlanta, Georgia 30322

(Received 8 August 2012; revised 30 September 2012; accepted for publication 15 October 2012; published 26 November 2012)

Purpose: The x-ray differential phase contrast imaging implemented with the Talbot interferometry has recently been reported to be capable of providing tomographic images corresponding to attenuation-contrast, phase-contrast, and dark-field contrast, simultaneously, from a single set of projection data. The authors believe that, along with small-angle x-ray scattering, the second-order phase derivative $\Phi''_s(x)$ plays a role in the generation of dark-field contrast. In this paper, the authors derive the analytic formulae to characterize the contribution made by the second-order phase derivative to the dark-field contrast (namely, second-order differential phase contrast) and validate them via computer simulation study. By proposing a practical retrieval method, the authors investigate the potential of second-order differential phase contrast imaging for extensive applications.

Methods: The theoretical derivation starts at assuming that the refractive index decrement of an object can be decomposed into $\delta = \delta_s + \delta_f$, where δ_f corresponds to the object's fine structures and manifests itself in the dark-field contrast via small-angle scattering. Based on the paraxial Fresnel-Kirchhoff theory, the analytic formulae to characterize the contribution made by δ_s , which corresponds to the object's smooth structures, to the dark-field contrast are derived. Through computer simulation with specially designed numerical phantoms, an x-ray differential phase contrast imaging system implemented with the Talbot interferometry is utilized to evaluate and validate the derived formulae. The same imaging system is also utilized to evaluate and verify the capability of the proposed method to retrieve the second-order differential phase contrast for imaging, as well as its robustness over the dimension of detector cell and the number of steps in grating shifting.

Results: Both analytic formulae and computer simulations show that, in addition to small-angle scattering, the contrast generated by the second-order derivative is magnified substantially by the ratio of detector cell dimension over grating period, which plays a significant role in dark-field imaging implemented with the Talbot interferometry.

Conclusions: The analytic formulae derived in this work to characterize the second-order differential phase contrast in the dark-field imaging implemented with the Talbot interferometry are of significance, which may initiate more activities in the research and development of x-ray differential phase contrast imaging for extensive preclinical and eventually clinical applications. © 2012 American Association of Physicists in Medicine. [<http://dx.doi.org/10.1118/1.4764901>]

Key words: x-ray phase contrast imaging, x-ray differential phase contrast imaging, x-ray Talbot interferometry, x-ray phase contrast CT, x-ray differential phase contrast CT, second-order derivative, second-order differential phase contrast

I. INTRODUCTION

In the energy range of x ray, the refractive index of a material is expressed as $n = 1 - \delta + i\beta$.^{1–3} The variation in x ray's amplitude (attenuation) depends on the distribution of attenuation index β and can be utilized for imaging in x-ray radiography/fluoroscopy and computed tomography (CT), while that in the phase (refraction) is determined by the distribution of refractive index decrement δ and can also be utilized for imaging, as has been implemented in the recently proposed x-ray differential phase contrast imaging and CT.^{4–6}

In the literature,^{7–9} the structure of an object is assumed falling into two categories: smooth and fine. Smooth structure is the feature at a scale that is comparable to or larger than the dimension of detector cell used for signal detection and thus is resolvable by the detector, whereas the fine structure

is that at a scale that is significantly smaller than the detector dimension and thus not resolvable by the detector. According to Refs. 7–9, one in principle has

$$\beta = \beta_s + \beta_f \approx \beta_s, \quad (1)$$

i.e., the attenuation index β of an object can be decomposed into β_s and β_f , corresponding to the object's smooth (resolvable) and fine (unresolvable) structures, respectively. Equation (1) also means that the effect induced by the fine component of attenuation index in x ray's propagation is negligible⁸. In analogue, the refractive index decrement δ of an object can be decomposed into^{7–9}

$$\delta = \delta_s + \delta_f, \quad (2)$$

where δ_s and δ_f correspond to the object's smooth (resolvable) and fine (unresolvable) structures, respectively. In

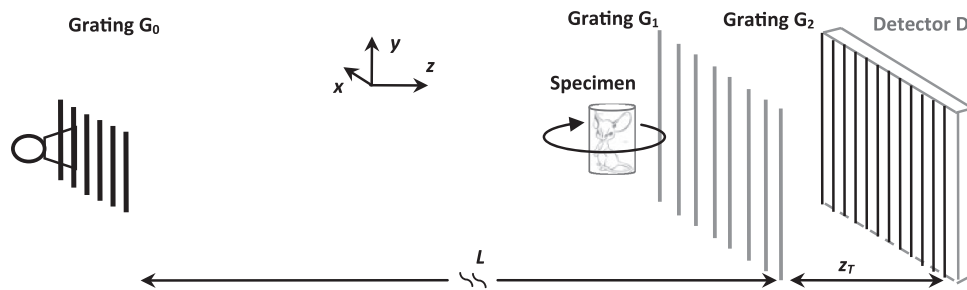


FIG. 1. The schematic of a grating based x-ray differential phase contrast CT system.

the investigation^{7–9} into the x-ray differential phase contrast imaging, it has been shown that the following relationships hold:

$$\Phi_s(x, y) = \frac{2\pi}{\lambda} \int_Z \delta_s(x, y, z) dz, \quad (3)$$

$$\Phi_f(x, y) = \frac{2\pi}{\lambda} \int_Z \delta_f(x, y, z) dz, \quad (4)$$

where $\Phi_s(x, y)$ and $\Phi_f(x, y)$ are the phase shifts induced by the smooth (resolvable) and fine (unresolvable) features of an object, respectively. Usually, $\Phi_s(x, y)$ is assumed to be a function that varies slowly in space, while $\Phi_f(x, y)$ is modeled as a Gaussian random process and is determined by the object's small-angle scattering.^{8,9}

The x-ray differential phase contrast CT (DPC-CT) implemented with the Talbot interferometry has recently been reported to be capable of providing tomographic images corresponding to the attenuation-contrast (β), phase-contrast (δ_s), and dark-field contrast (δ_f), simultaneously, from a single set of projection data.^{10–12} Figure 1 shows the schematic of a DPC-CT implemented with an x-ray tube and three gratings.^{5,13} The source grating G_0 is employed to enable the system using a conventional x-ray source with finite focal spot such that the spatial coherence condition can be satisfied.^{4,5,13} Based on the Talbot interferometry,¹³ phase grating G_1 and absorption grating G_2 work together as a shearing interferometer^{5,12} to detect the wavefront alteration caused by the object in the x-ray beam. Keeping grating G_1 fixed and shifting grating G_2 along the transverse direction x_g , the x-ray irradiance recorded at each pixel (m, n) of detector D oscillates as a periodic function and thus can be expanded into a Fourier series,^{10,11}

$$I_{m,n}(x_g) = a_0(m, n) + \sum_{l=1}^{\infty} a_l(m, n) \times \cos \left(2\pi l \frac{x_g}{g_2} + \phi_l(m, n) \right), \quad (5)$$

where g_2 is the period of grating G_2 . The attenuation-contrast (β), phase-contrast (δ_s), and dark-field contrast (δ_f) images can be reconstructed from the zeroth- and first-order Fourier components a_0 , ϕ_1 , and a_1 , respectively. Specifically, the reduction in the interference fringe visibility is defined as¹¹

$$V(m, n) = \frac{a_1^s(m, n)/a_0^s(m, n)}{a_1^r(m, n)/a_0^r(m, n)} = \frac{a_1^s(m, n)a_0^r(m, n)}{a_0^s(m, n)a_1^r(m, n)}, \quad (6)$$

where the superscripts “ s ” and “ r ” refer to the projection data obtained with and without the object in x-ray beam, respectively. A relationship between the scaled logarithm of $V(m, n)$ and the projection of the so-called linear diffusion coefficient $\varepsilon_{m,n}(z)$ along x-ray propagation direction z has been denoted as^{10–12}

$$\int \varepsilon_{m,n}(z) dz = -\frac{g_2^2}{2\pi^2 z_T^2} \ln V(m, n), \quad (7)$$

where z_T is the distance between gratings G_1 and G_2 . A tomographic image corresponding to $\varepsilon_{m,n}(z)$ can be reconstructed from $V(m, n)$ using Eq. (7).^{11,12}

It has been claimed^{10,11} that $a_0(m, n)$ in Eq. (5) is equivalent to the attenuation that is solely determined by β . Moreover, in the derivation of Eq. (7),^{11,14} it is implicitly assumed that the reduction in the interference fringe visibility is attributed to δ_f , the fine component of refractive index decrement δ that is solely dependent on the small-angle scattering caused by the microstructures of an object. The small-angle scattering is characterized by a Gaussian angle distribution^{11,14,15} and the linear diffusion coefficient is determined by the width of the Gaussian angle distribution.^{11,14} Hence, Eq. (7) implies that, under the existing theoretical framework of x-ray dark-field imaging implemented with the Talbot interferometry, δ_s —the smooth component of the refractive index decrement δ —does not play a role. Moreover, in the investigation of x-ray phase contrast imaging with the Talbot interferometry that has so far been reported in the literature, the second and higher order derivatives of the resolvable phase shift $\Phi_s(x)$ are assumed negligible. For example, under the assumption that the derivative of $\Phi_s(x)$ higher than the first-order can be ignored, Yashiro *et al.*⁸ derived a formula for the interference fringe visibility based on the first-principle wave calculation, in which $\Phi_s(x)$ and its first-order derivative are absent.

However, based on our understanding and analysis of the existing results, we speculate that, even though $\Phi_s(x)$ and its first-order derivative $\Phi'_s(x)$ have no influence on the interference fringe visibility of the Talbot interferometry, the second-order derivative $\Phi''_s(x)$ may play a role and thus contribute to the signal $V(m, n)$ [Eq. (6)] and generate dark-field contrast in the x-ray phase contrast imaging implemented with the Talbot interferometry. Therefore, in this work, we investigate the effect of $\Phi''_s(x)$ on the reduction of interference fringe visibility in the x-ray phase contrast imaging implemented with the Talbot interferometry. In particular, we focus on the

grating-based differential phase contrast imaging system with its detector cell dimension l_d large enough to satisfy

$$2n_d = \frac{l_d}{g_2} \gg 1, \quad (8)$$

where n_d is assumed to be an integer. It should be noted that Eq. (8) can be readily fulfilled in x-ray phase contrast imaging implemented with the Talbot interferometry.^{10,11} By taking the second-order differential phase shift into account, we derive the analytic formulae based on the paraxial Fresnel-Kirchhoff theory to characterize the effect of the second-order differential contrast and its potential for imaging. Through computer simulation studies, we evaluate and verify the accuracy of the derived analytic formulae with specially designed numerical phantoms. We show and analyze the contribution of second-order differential contrast to dark-field imaging, and investigate the approaches to retrieve the second-order differential contrast for imaging. Finally, we provide an in-depth discussion on the underlying reasons why the second-order derivative $\Phi_s''(x)$ manifests itself as contrast in phase contrast imaging implemented with the Talbot interferometry, as well as its potential for preclinical and eventually clinical applications.

II. MATERIALS AND METHODS

Since the paraxial condition is met in the Talbot interferometry,¹² the analytic formulae to characterize the second-order derivative $\Phi_s''(x)$ in x-ray phase contrast imaging implemented with the Talbot interferometry are derived in the parallel beam geometry. The x-ray beam propagates along the z -axis, and the object to be imaged and the detector are placed immediately in front of the phase grating G_1 and behind the analyzer grating G_2 , respectively.⁸ As illustrated in Fig. 1, since the orientation of gratings is along the y -axis, we assume henceforth

$$\beta(x, y, z) = \beta(x, z), \text{ and } \delta(x, y, z) = \delta(x, z). \quad (9)$$

II.A. The second-order derivative in x-ray phase imaging implemented with the Talbot interferometry

We constrain our focus on the smooth (resolvable) features of an object by letting $\delta_f = 0$. Supposing grating G_2 be linearly shifted along the transverse direction x_g , the mean intensity of the interference fringe intensity recorded at a cell indexed by (m, n) in a detector can be expressed as^{8,9}

$$I_{m,n}(x_g) = \frac{1}{l_d^2} \int_{-\frac{l_d}{2}}^{\frac{l_d}{2}} dy \int_{-\frac{l_d}{2}}^{\frac{l_d}{2}} dx |E_{x_g}(x_m + x, y_n + y, z_{2b})|^2, \quad (10)$$

where

$$x_m = \left(m - \frac{1}{2}\right) l_d, \quad m = 0, \pm 1, \pm 2, \dots, \quad (11)$$

$$y_n = \left(n - \frac{1}{2}\right) l_d, \quad n = 0, \pm 1, \pm 2, \dots, \quad (12)$$

$E_{x_g}(x, y, z_{2b})$ is the electric field at location (x, y, z_{2b}) , and z_{2b} is the distance between the detector and the x-ray source along the direction of x-ray propagation. The incident x-ray beam is assumed as a monochromatic plane wave with wavelength λ and amplitude E_0 . G_1 is a phase grating and G_2 is an absorption grating with 50% duty cycle. Furthermore, suppose that the distance from G_1 to G_2 be selected as the m_T th fractional Talbot distance

$$z_T = m_T \frac{g_1^2}{8\lambda}, \quad m_T = 1, 3, 5, \dots, \quad (13)$$

where g_1 is the pitch of the phase grating G_1 . If one sets

$$g_1 = 2g_2, \quad (14)$$

a maxima in the interference fringe visibility can occur in the detector plane. According to the derivation detailed in the Appendix, the intensity $I_{m,n}(x_g)$ is a periodic function of x_g with period g_2 and thus can be expanded into a Fourier series

$$I_{m,n}(x_g) = \sum_{l=-\infty}^{\infty} C_l(m, n) \exp\left(2\pi i l \frac{x_g}{g_2}\right), \quad (15)$$

and the zeroth- and first-order Fourier coefficients are given by

$$C_0(m, n) = a_0(m, n) = \frac{\alpha_n l_d m_T g_2^2}{8} \frac{\exp(-S(x_m))}{1 - \frac{\lambda z_T}{2\pi} \Phi_s''(x_m)}, \quad (16)$$

$$\begin{aligned} C_1(m, n) &= \frac{a_1(m, n)}{2} \exp(i\phi_1(m, n)) \\ &= -\frac{\alpha_n l_d m_T g_2^2}{2\pi^2} \frac{i \exp\left(-S(x_m) + i \frac{\frac{\lambda z_T}{g_2} \Phi_s'(x_m)}{1 - \frac{\lambda z_T}{2\pi} \Phi_s''(x_m)}\right)}{1 - \frac{\lambda z_T}{2\pi} \Phi_s''(x_m)} \\ &\times \text{sinc}\left(2n_d \frac{\frac{\lambda z_T}{2\pi} \Phi_s''(x_m)}{1 - \frac{\lambda z_T}{2\pi} \Phi_s''(x_m)}\right), \end{aligned} \quad (17)$$

in which Eq. (5) is utilized. In addition,

$$S(x_m) = \frac{4\pi}{\lambda} \int_Z \beta(x_m, z) dz, \quad (18)$$

$$\alpha_n = \frac{|E_0|^2}{\lambda^2 l_d^2 z_T^2} \int_{-\frac{l_d}{2}}^{\frac{l_d}{2}} \left| \int_{-\frac{L_y}{2}}^{\frac{L_y}{2}} \exp\left(i\pi \frac{(y + y_n - y_1)^2}{\lambda z_T}\right) dy_1 \right|^2 dy, \quad (19)$$

and L_y is the dimension of gratings along the y direction. Combining Eqs. (16) and (17), one may analytically express the reduction in the maxima of interference fringe visibility induced by the second-order derivative $\Phi_s''(x)$ as

$$\begin{aligned} V_s(m, n) &= \left| \text{sinc}\left(2n_d \frac{\frac{\lambda z_T}{2\pi} \Phi_s''(x_m)}{1 - \frac{\lambda z_T}{2\pi} \Phi_s''(x_m)}\right) \right| \\ &\approx \left| \text{sinc}\left(2n_d \frac{\lambda z_T}{2\pi} |\Phi_s''(x_m)|\right) \right| \\ &= \left| \text{sinc}\left(\frac{l_d}{g_2} |\Lambda_s(x_m)|\right) \right| = |\text{sinc}(|\Theta(x_m)|)|, \end{aligned} \quad (20)$$

where

$$\Lambda_s(x_m) = \frac{\lambda z_T}{2\pi} \Phi_s''(x_m), \quad (21)$$

$$\Theta(x_m) \equiv \frac{l_d}{g_2} \Lambda_s(x_m) = 2n_d \frac{\lambda z_T}{2\pi} \Phi_s''(x_m), \quad (22)$$

in which, similar to the smooth-phase condition in the in-line x-ray phase contrast imaging,^{16–18} we have assumed that the resolvable phase shift varies slowly, i.e.,

$$|\Lambda_s(x_m)| \ll 1. \quad (23)$$

II.B. The effect of second-order derivative on the attenuation-equivalent imaging

It has been claimed that the attenuation-equivalent image, as termed in the literature,^{10,11} in the x-ray phase contrast imaging implemented with the Talbot interferometry, can be formed by $C_0(m, n)$ [or $a_0(m, n)$]. In the conventional attenuation-contrast x-ray radiography, the contrast is assumed to be solely determined by attenuation index β . However, as shown in Eq. (16), in addition to depending on the attenuation index β [$\exp(-S(x_m))$ in the numerator], the attenuation-equivalent image formed in the x-ray phase contrast imaging implemented with the Talbot interferometry is also dependent on $\Phi_s''(x_m)$ in a way that is the same as that in the propagation-based in-line x-ray phase contrast imaging.^{16,17,19–22} Based on the paraxial Fresnel-Kirchhoff diffraction theory, the x-ray intensity at the detector plane in the propagation-based in-line phase contrast imaging can be estimated as^{16,17,21}

$$I(x, y, z) = I(x, y, 0) \left(1 + \frac{\lambda z}{2\pi} \left(\frac{\partial^2}{\partial x^2} + \frac{\partial^2}{\partial y^2} \right) \Phi_s(x, y) \right) \approx \frac{I(x, y, 0)}{1 - \frac{\lambda z}{2\pi} \left(\frac{\partial^2}{\partial x^2} + \frac{\partial^2}{\partial y^2} \right) \Phi_s(x, y)}, \quad (24)$$

in which the slowly varying phase (SVP) approximation²³ was used and the absorption is assumed to vary slowly in comparison to phase modulation. $I(x, y, 0)$ and $I(x, y, z)$ denote the intensity immediately and at distance z , respectively, behind the object to be imaged. It should be noted that Eq. (24) is similar to Eq. (16). According to Eq. (24), the image contrast in the propagation-based in-line x-ray phase contrast imaging can be written as^{16,17,23}

$$\Lambda(x, y, z) = \frac{I(x, y, z)}{I(x, y, 0)} - 1 = \frac{\lambda z}{2\pi} \left(\frac{\partial^2}{\partial x^2} + \frac{\partial^2}{\partial y^2} \right) \Phi_s(x, y). \quad (25)$$

Equation (25) means that an edge between different tissues or organs, e.g., between a tumor and surrounding structures, can be substantially enhanced.^{22,24}

II.C. The effect of second-order derivative on dark-field imaging contrast

According to Eq. (57) in Ref. 9, and the convolution relationship shown in Refs. 11 and 14, if both the smooth (resolv-

able) and fine (unresolvable) features of an object are considered, the measured interference fringe visibility is the product of two factors

$$V_{\text{measured}}(m, n) = V_s(m, n) V_f(m, n), \quad (26)$$

where

$$V_f(m, n) = \exp \left(-\frac{2\pi^2 z_T^2}{g_2^2} \int \varepsilon_{m,n}(z) dz \right) \quad (27)$$

is actually a reformat of Eq. (7).^{11,12} Thus far, it has been implicitly assumed that $V_s(m, n) \approx 1$ in the literature.^{11,14,15} As such, $V_f(m, n)$, the contribution from small-angle scattering, is the only source of the contrast in the dark-field imaging implemented with the Talbot interferometry. However, as shown in Eq. (20), the assumption $V_s(m, n) \approx 1$ is quite heuristic. In fact, as illustrated below, the second-order derivative $|\Phi_s''(x_m)|$ may make significant contribution to the contrast in dark-field imaging, in addition to the small-angle scattering.

In a way analogous to Eq. (25),^{16,17,23} given Eq. (20), the contrast induced by the second-order derivative $|\Phi_s''(x_m)|$ in $V_s(m, n)$ can be denoted as

$$\begin{aligned} \Gamma_s(m, n) &= 1 - \left| \text{sinc} \left(\frac{l_d}{g_2} \frac{\lambda z_T}{2\pi} |\Phi_s''(x_m)| \right) \right| \\ &= 1 - \left| \text{sinc} \left(\frac{l_d}{g_2} |\Lambda_s(x_m)| \right) \right|. \end{aligned} \quad (28)$$

As shown in Eq. (23), $|\Lambda_s(x_m)|$ is usually significantly smaller than unity, but the factor l_d/g_2 is very large in x-ray phase contrast imaging implemented with the Talbot interferometry, which magnifies the effect induced by $|\Lambda_s(x_m)|$ substantially. Hence, the contrast induced by the second-order derivative $|\Phi_s''(x_m)|$, i.e., the edge enhancement, can be significant. For example, in a typical x-ray phase contrast imaging system implemented with Talbot interferometry at $g_2 = 2 \mu\text{m}$, Fig. 2 illustrates how the contrast $\Gamma_s(m, n)$ varies over $|\Lambda_s(x_m)|$, which is proportional to $|\Phi_s''(x_m)|$, and l_d , the detector cell size. It is observed that, $\Gamma_s(m, n)$ increases rapidly with $|\Lambda_s(x_m)|$, while $|\Lambda_s(x_m)|$ is relatively small, and reaches its maximum $\Gamma_s(m, n) = 1$ at $|\Lambda_s(x_m)| = g_2/l_d$.

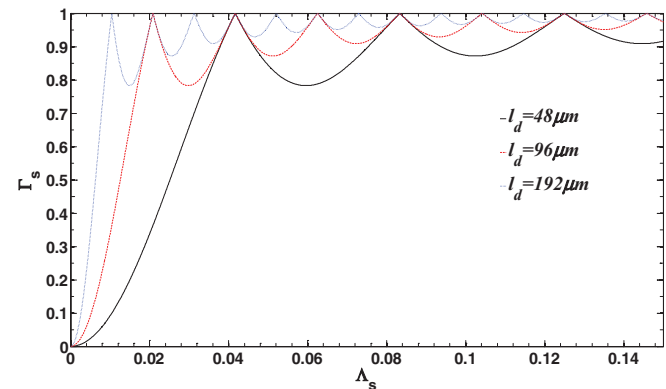


FIG. 2. The variation of visibility contrast Γ_s as a function of the second-order derivative $\Lambda_s(x_m) = (\lambda z_T/2\pi) \cdot \Phi_s''(x_m)$ over detector cell dimension l_d .

II.D. The retrieval of second-order differential phase contrast

As shown in Eqs. (20) and (26), the second-order derivative $|\Phi_s''(x_m)|$ modulates the contrast in the dark-field imaging. This means that the effect induced by $|\Phi_s''(x_m)|$ entangles with that induced by small-angle scattering. However, in certain scenarios, it is desirable to have the image generated by the small-angle scattering only¹¹, wherein the effect induced by the second-order derivative $|\Phi_s''(x_m)|$ needs to be removed. In other cases, the tissue or organ features revealed separately from the second-order derivative $|\Phi_s''(x_m)|$ and small-angle scattering may provide valuable pathophysiological information for preclinical and clinical applications.^{11,22} To explore such applications, the retrieval of $|\Phi_s''(x_m)|$ from the measured interference fringe visibility becomes imperative.

II.D.1. A theoretically exact approach

Similar to the way practiced in the propagation-based in-line x-ray phase contrast imaging,^{24,25} we assume $V_{M,T_1}(m, n)$ and $V_{M,T_2}(m, n)$ to represent the measured interference fringe visibility at the G_1 to G_2 distances corresponding to the T_1 th and T_2 th fractional Talbot distances, respectively. Substituting Eqs. (20) and (27) into Eq. (26) and letting z_T be equal to the T_1 th and T_2 th fractional Talbot distances, respectively, one obtains

$$V_{M,T_1}(m, n) = \left| \text{sinc} \left(l_d \frac{T_1 g_2}{4\pi} |\Phi_s''(x_m)| \right) \right| \\ \times \exp \left(-\frac{\pi^2 T_1^2 g_2^2}{2\lambda^2} \int \varepsilon_{m,n}(z) dz \right), \quad (29)$$

$$V_{M,T_2}(m, n) = \left| \text{sinc} \left(l_d \frac{T_2 g_2}{4\pi} |\Phi_s''(x_m)| \right) \right| \\ \times \exp \left(-\frac{\pi^2 T_2^2 g_2^2}{2\lambda^2} \int \varepsilon_{m,n}(z) dz \right), \quad (30)$$

in which Eqs. (13) and (14) are used. Cancellation of $\varepsilon_{m,n}(z)$ from Eqs. (29) and (30) yields the equation to retrieve the module $|\Phi_s''(x_m)|$

$$\frac{\left| \text{sinc} \left(l_d \frac{T_1 g_2}{4\pi} |\Phi_s''(x_m)| \right) \right|^{T_2^2}}{\left| \text{sinc} \left(l_d \frac{T_2 g_2}{4\pi} |\Phi_s''(x_m)| \right) \right|^{T_1^2}} = \frac{(V_{M,T_1}(m, n))^{T_2^2}}{(V_{M,T_2}(m, n))^{T_1^2}}, \quad (31)$$

which can be solved through numerical methods.

II.D.2. A practical approach

Obviously, to repeat the measurements at two distances between G_1 and G_2 may double the x-ray dose and time for data acquisition.^{23,24} It is desirable to develop a method that only measures once to retrieve $|\Phi_s''(x_m)|$. Toward this goal, one may have already noted the significant difference in the variation over detector cell size l_d between $V_s(m, n)$ and $V_f(m, n)$. As shown in Eqs. (20) and (27), $V_s(m, n)$ varies over l_d , whereas $V_f(m, n)$ does not have an explicit dependence on

l_d . Let $V_{M,l_d}(m + 1/2, n)$ denote the measured visibility contrast at a virtual detector cell centered at $(x_m + l_d/2, y_n)$ with dimension $l_d \times l_d$, and $V_{M,2l_d}(m + 1/2, n)$ denote the measured visibility contrast at another virtual detector cell also centered at $(x_m + l_d/2, y_n)$ but with dimension $2l_d$ (in x direction) $\times l_d$ (in y direction), where x_m and y_n are given by Eqs. (11) and (12). Substitution of Eq. (20) into Eq. (26) yields

$$V_{M,l_d} \left(m + \frac{1}{2}, n \right) \\ = \left| \text{sinc} \left(\frac{l_d}{g_2} \frac{\lambda z_T}{2\pi} \left| \Phi_s'' \left(x_m + \frac{l_d}{2} \right) \right| \right) \right| V_{f,l_d} \left(m + \frac{1}{2}, n \right), \quad (32)$$

$$V_{M,2l_d} \left(m + \frac{1}{2}, n \right) \\ = \left| \text{sinc} \left(\frac{2l_d}{g_2} \frac{\lambda z_T}{2\pi} \left| \Phi_s'' \left(x_m + \frac{l_d}{2} \right) \right| \right) \right| V_{f,2l_d} \left(m + \frac{1}{2}, n \right), \quad (33)$$

where $V_{f,l_d}(m + 1/2, n)$ and $V_{f,2l_d}(m + 1/2, n)$ denote the contribution to the interference fringe visibility from the small-angle x-ray scattering. Dividing Eq. (33) by Eq. (32) yields

$$\left| \cos \left(\frac{l_d}{g_2} \frac{\lambda z_T}{2\pi} \left| \Phi_s'' \left(x_m + \frac{l_d}{2} \right) \right| \right) \right| \\ = \frac{V_{M,2l_d}(m + \frac{1}{2}, n)}{V_{M,l_d}(m + \frac{1}{2}, n)} \frac{V_{f,l_d}(m + \frac{1}{2}, n)}{V_{f,2l_d}(m + \frac{1}{2}, n)}. \quad (34)$$

As shown in Refs. 7–9, the $V_f(m, n)$ in Eq. (27), the reduction in the interference fringe visibility caused by the object's fine features is a result of averaging the random phase shift induced by the object's fine features over the detector cell at (m, n) . Thus, $V_f(m, n)$ actually represents the statistical properties of the random phase at detector cell (m, n) ,⁷ and varies at the scales that are not smaller than the detector cell size, despite the fact that the characteristic scales of the object's fine features are significantly smaller than the detector cell size. Keeping this in mind and noting the fact that $V_f(m, n)$, as given in Eq. (27), is not explicitly dependent on l_d , it should be rational for one to assume

$$V_{f,l_d} \left(m + \frac{1}{2}, n \right) \approx V_{f,2l_d} \left(m + \frac{1}{2}, n \right), \quad (35)$$

which immediately results in

$$\cos \left(l_d \frac{m_T g_2}{2\pi} \left| \Phi_s'' \left(x_m + \frac{1}{2} \right) \right| \right) = 2 \left(\frac{V_{M,2l_d}(m + \frac{1}{2}, n)}{V_{M,l_d}(m + \frac{1}{2}, n)} \right)^2 - 1, \quad (36)$$

in which Eqs. (13) and (14) are utilized. Given the intensity variation $I_{m,n}(x_g)$ recorded at each detector cell (m, n) as a function of transverse grating shift x_g , it is straightforward to show that $V_{M,2l_d}(m + 1/2, n)$ can be estimated by replacing $I_{m,n}(x_g)$ in Eq. (5) with $I_{m,n}(x_g) + I_{m+1,n}(x_g)$ to calculate the

Fourier components $a_0(m, n)$ and $a_1(m, n)$, and then substituting the obtained Fourier coefficients into Eq. (6). In addition, one can approximate,

$$V_{M,l_d}(m + 1/2, n) \approx \frac{1}{2} (V_{M,l_d}(m, n) + V_{M,l_d}(m + 1, n)). \quad (37)$$

Thus, one measurement of the interference fringe visibility at a specified distance between the gratings G_1 and G_2 is enough for retrieving $|\Phi_s''(x_m)|$. Apparently, measuring the interference fringe visibility once at a distance between gratings G_1 and G_2 is feasible, in addition to saving radiation dose and speeding up data acquisition. Hence, solving Eq. (36) to retrieve $|\Phi_s''(x_m)|$ is preferable to solving Eq. (31), even though only an approximate solution can be provided.

III. NUMERICAL EVALUATION

We evaluate and validate the analytic formulae derived in Sec. II.A–II.C to describe the second-order derivative and the resultant second-order differential phase contrast. In addition, we evaluate and verify the practical method proposed in Sec. II.D.2 to retrieve the second-order differential phase contrast for imaging. Below is a brief description of the tasks to be conducted.

III.A. Modeling of x-ray differential phase contrast imaging with Talbot interferometry

The modeling of x-ray differential phase contrast imaging implemented with the Talbot interferometry has been evaluated and verified previously.^{26–28} In the simulation study, the x-ray source is assumed monochromatic at 28 keV. The period of gratings G_1 and G_2 are 4 and 2 μm , respectively, and the distance between them is 22.584 cm, corresponding to the fifth fractional Talbot distance. It should be pointed out that these system parameters are comparable with those used in the investigation of dark-field imaging implemented with the Talbot interferometry.^{10,11,29} The x-ray flux is set at 1.28×10^7 photon/cm² per image and observes the Poisson distribution. To assure the simulation study at high fidelity, the dimension of finite x ray along x -direction is 31.3 nm, corresponding to 128 samplings within one period of grating G_1 , while the number of steps in shifting grating G_2 is 16. As a reference, the conventional attenuation-contrast images of Phantom-II (defined in Sec. III.C) at detector cell dimensions 192, 128, and 64 μm are presented in Figs. 3(a)–3(c), respectively.

III.B. Validation of the formulae to characterize second-order differential phase contrast

A numerical phantom (called Phantom-I), consisting of 69 cylinders, is designed to evaluate and verify the accuracy of Eq. (20), and its trans-axial view is presented in Fig. 4(a). The cylinders are deliberately grouped into 6 columns and placed parallel to the y -axis of the differential phase contrast imaging system (see Fig. 1). The cylinders in each column

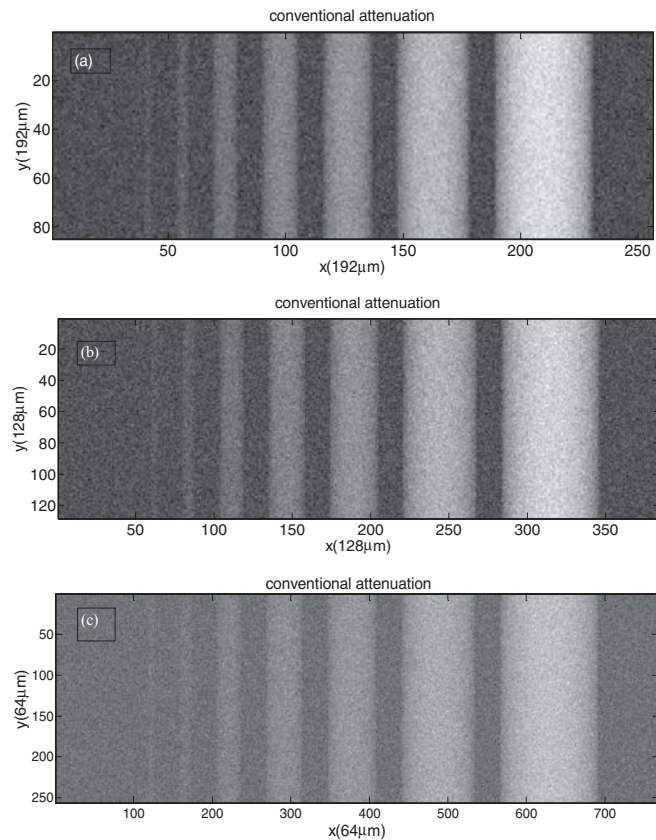


FIG. 3. The conventional attenuation-contrast images of Phantom-II at detector cell dimension 192 (a), 128 (b), and 64 μm (c), respectively. (Exposure: 1.28×10^7 photon/cm² per image.)

are of identical radius R , attenuation index β , and refractive index decrement δ . In such a way, the phantom can assess the accuracy of Eq. (20) over the variation in R , β , and δ . The parameters of each cylinder are detailed in Table I, whereby the refractive index of water is assumed as $n = 1 - \delta_{\text{water}} + i\beta_{\text{water}} = 1 - 2.939 \times 10^{-7} + i1 \cdot 471 \times 10^{-10}$, and M_s is the number of cylinders in a column.

Using the parameters specified above, it is quite straightforward to calculate the resolvable phase shift $\Phi_s(x_m)$ using Eq. (3). Subsequently, the second differential phase shift at each detector cell (m, n) is given by

$$\Phi_s''(x_m) = \frac{\Phi_s(x_{m+1}) + \Phi_s(x_{m-1}) - 2\Phi_s(x_m)}{l_d^2}, \quad (38)$$

where the detector cell dimension l_d is set at 128 μm in the investigation using Phantom-I. The visibility degradation due to the resolvable phase shift can be attained by substituting Eq. (38) into Eq. (20). To evaluate the accuracy of using Eq. (20) to predict the interference fringe visibility degradation, we carry out noise-free computer simulation and take the simulation result as a reference. To assure the simulation study at high fidelity, the dimension of finite x ray along x -direction is 15.6 nm, corresponding to 256 samplings within one period of grating G_1 , while the number of steps in shifting grating G_2 is 64.

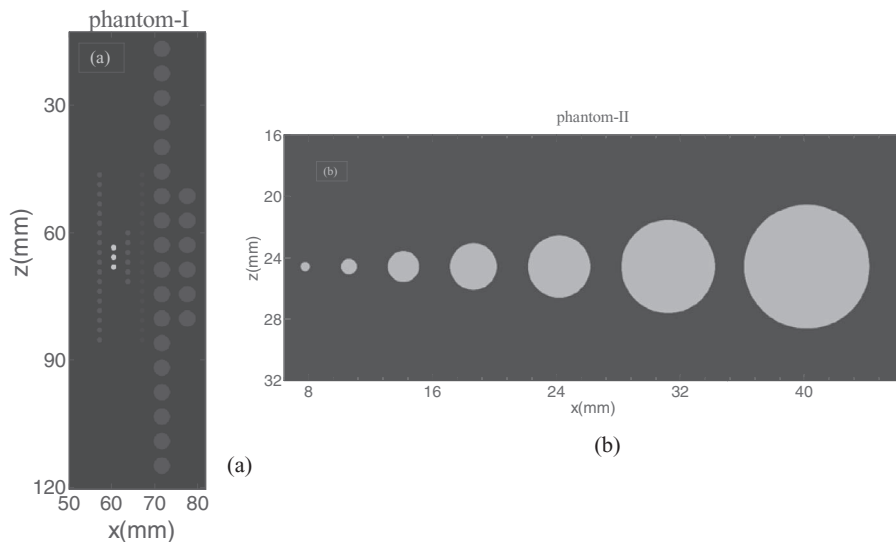


FIG. 4. The trans-axial views showing the dimension and layout of Phantom-I (a) and Phantom-II (b) placed in the scan field of view.

III.C. Exploring the potential of second-order differential phase contrast imaging

To explore the potential of the second-order differential phase contrast for imaging, another numerical phantom (called Phantom-II) is employed and its trans-axial view is presented in Fig. 4(b). Phantom-II consists of 7 cylinders that are placed parallel to the y-axis of the x-ray differential phase contrast imaging system. Each cylinder is of identical refractive index $n = 1 - 2\delta_{\text{water}} + i\beta_{\text{water}} = 1 - 5.878 \times 10^{-7} + i1.471 \times 10^{-10}$, but different radius (0.3, 0.5, 1.0, 1.5, 2.0, 3.0, and 4.0 mm), centering at $x_c = 7.801, 10.601, 14.101, 18.601, 24.101, 31.101$, and 40.126 mm, respectively. In the simulation study with Phantom-II, grating G_2 is shifted 16 steps in data acquisition to assure the accuracy of phase retrieving.

III.D. Second-order differential contrast and its variation over system parameters

As illustrated in Eq. (20), the detector cell dimension l_d plays an important role in generating the second-order differential contrast $|\Phi_s''(x_m)|$. Hence, it is essential for us to investigate the variation of the second-order differential contrast over detector cell dimension. Considering the adequacy for x-ray differential phase contrast imaging, the detector cell dimension of 64, 128, and 192 μm are included in the investigation. In addition, as we already know, the number of grat-

ing shifting steps may play a role in the data acquisition of x-ray differential phase contrast imaging with the Talbot interferometry. Hence, we investigate the variation of the second-order differential phase contrast over grating shifting at 64, 32, 16, and 8 steps, respectively.

IV. RESULTS

The analytic formula given in Sec. II and the potential of the second-order differential phase contrast imaging is evaluated and verified using the methods and parameters specified in Sec. III. Below is a presentation of the preliminary results.

IV.A. Validation of the second-order differential phase contrast

The profile of $|\Lambda_s(x_m)|$ over x_m corresponding to Phantom-I is analytically calculated using Eqs. (21) and (38) and plotted in Fig. 5(a), while that of $V_s(x_m)$ obtained from the $\Lambda_s(x_m)$ with Eq. (20) is plotted in Fig. 5(b) (dotted line). Meanwhile, the profile of $V_s(x_m)$ obtained from the noiseless modeling and simulation of the differential phase contrast imaging is also plotted in Fig. 5(b) as a reference (solid line). It is observed that the second-order differential phase contrast $\Lambda_s(x_m)$ generated by the second-order derivative $\Phi_s''(x_m)$ is magnified by the factor l_d/g_2 , as predicted in Eq. (22). Except at the object's boundaries ("edge-detection" regime),^{17,30} the interference fringe visibility obtained with Eq. (20) in general agrees well with the simulation result (the reference).

IV.B. The second-order differential contrast in dark-field imaging

Figures 6(a)–6(c) show the dark-field images of Phantom-II at detector dimension 192, 128, and 64 μm , respectively, in

TABLE I. The parameters of Phantom-I (l_d : detector cell dimension).

	Column 1	Column 2	Column 3	Column 4	Column 5	Column 6
$R/(5l_d)$	1	1	1	1	3	3
$\delta/\delta_{\text{water}}$	1	6	1	0.333	1	1
$\beta/\beta_{\text{water}}$	1	6	1	0.333	1	1
M_s	18	3	6	18	18	6

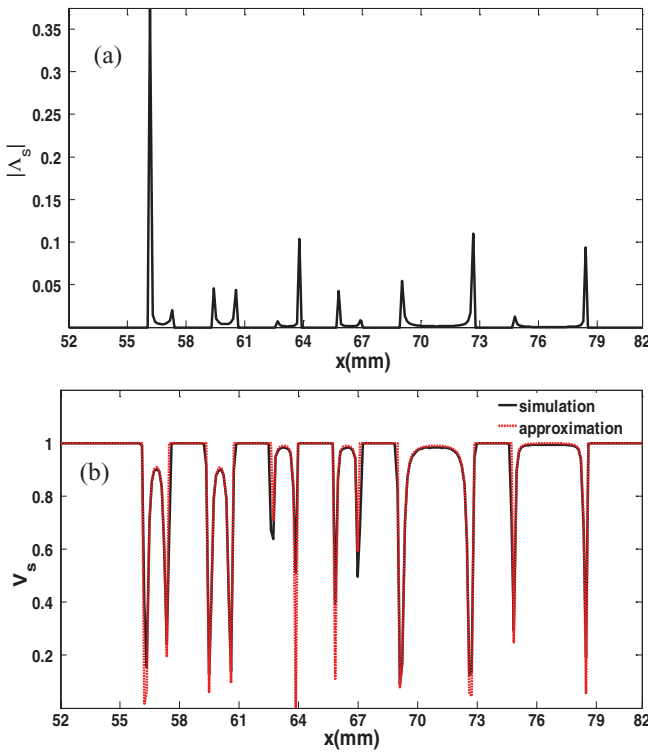


FIG. 5. The profiles of: (a) $|\Lambda_s(x_m)|$ obtained using Eqs. (21) and (38), and (b) $V_s(x_m)$ obtained using Eq. (20) compared with the corresponding simulation result (baseline reference) of Phantom-I at detector cell dimension 128 μm (No. of G_2 shifting steps: 64; noise free.)

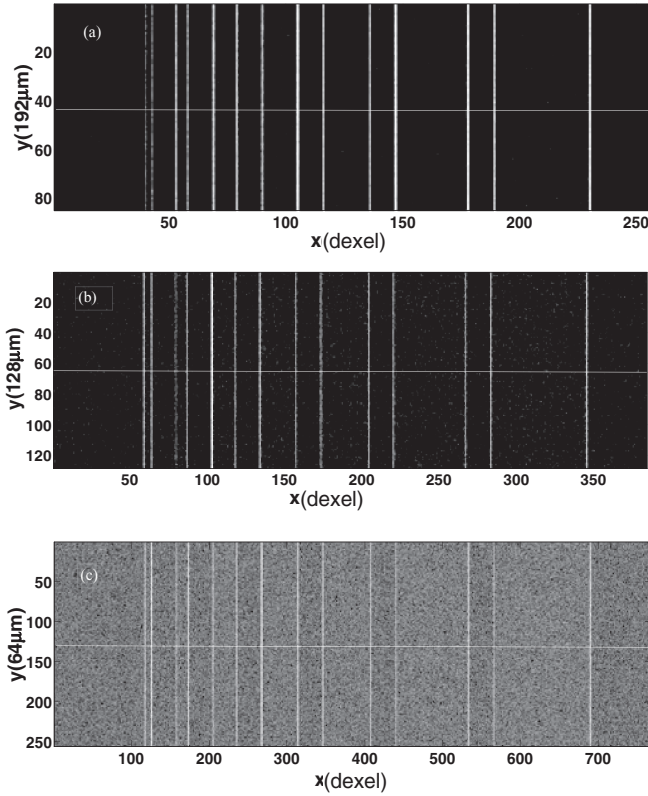


FIG. 6. The dark-field images of Phantom-II acquired at detector cell dimension 192 (a), 128 (b), and 64 μm (c), respectively. (No. of G_2 shifting steps: 16; exposure: 1.28×10^7 photon/cm 2 per image.)

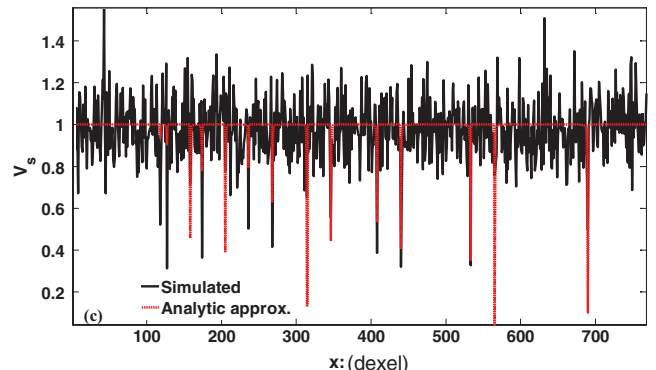
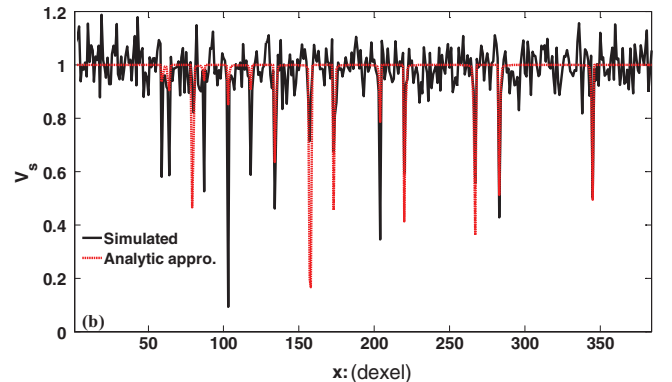
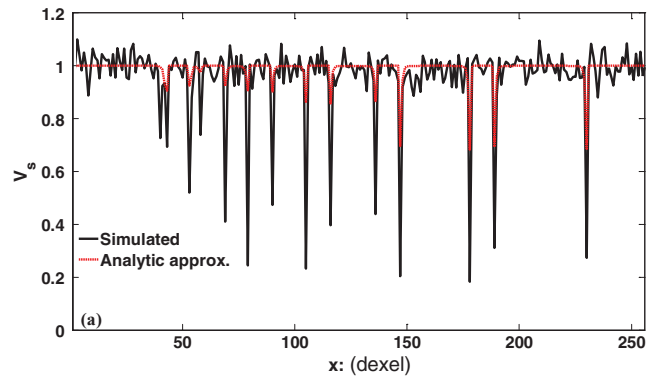


FIG. 7. The profiles of the dark-field images of Phantom-II corresponding to the central lines labeled in Fig. 6 (a), (b), and (c) and compared with that is analytically calculated using Eq. (20).

which the edge of each cylinder can be seen clearly. It should be noted that no small angle scattering is considered in the simulation, and thus the edge enhancement demonstrated in Fig. 6 is solely the contribution made by the modulus of the second-order derivative $|\Phi_s''(x_m)|$. In addition, the profiles corresponding to the central lines in Fig. 6 are correspondingly plotted in Fig. 7, whereby the profile that is analytically calculated using Eqs. (20) and (38) is also presented. A close inspection of Fig. 7 shows that the analytic approximation agrees well with the reference (simulation result), though the agreement degrades with increasing noise.

IV.C. The second-order differential contrast and its variation over detector cell dimension

The second-order differential phase contrast images $|\Lambda_s(x_m)|$ of Phantom-II retrieved using the method proposed

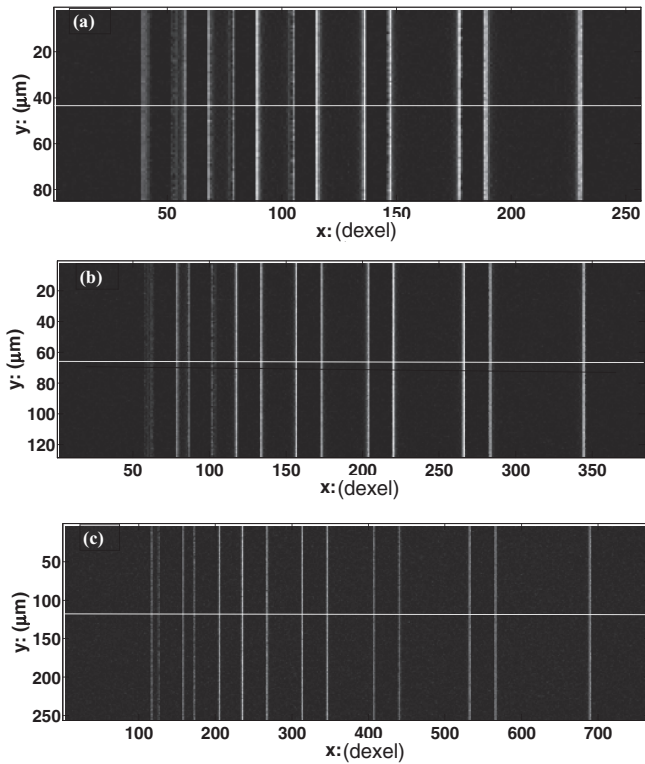


FIG. 8. The second-order differential phase contrast images of Phantom-II retrieved by the proposed method at detector cell dimension 192 (a), 128 (b), and 64 μm (c), respectively. (No. of G_2 shifting steps: 16; exposure: 1.28×10^7 photon/cm 2 per image.)

in Sec. II.D [Eqs. (21) and (36)] at detector cell dimension 192, 128, and 64 μm are presented in Fig. 8. In addition, the profiles across the central lines in Fig. 8 are correspondingly presented in Fig. 9, whereby the profile that is analytically calculated using Eqs. (21) and (38) is presented as a reference. It is observed that the second-order differential phase contrast retrieved using the method proposed in this work agrees well with the analytic result and is robust over detector cell dimension.

IV.D. The second-order differential contrast and its variation over steps of grating shifting

The second-order differential phase contrast images of Phantom-II retrieved using the method proposed in Sec. II.D [Eqs. (21) and (36)] at detector cell dimension 128 μm and 64, 32, 16, and 8 steps of grating shifting are presented in Fig. 10. Meanwhile, the profiles corresponding to the central lines in Fig. 10 are correspondingly displayed in Fig. 11, in which the profile that is analytically calculated using Eqs. (21) and (38) is presented as a reference. Again, it is observed that the second-order differential phase contrast retrieved using the method proposed in this work agrees well with the analytic result and is robust over the number of steps in grating shifting.

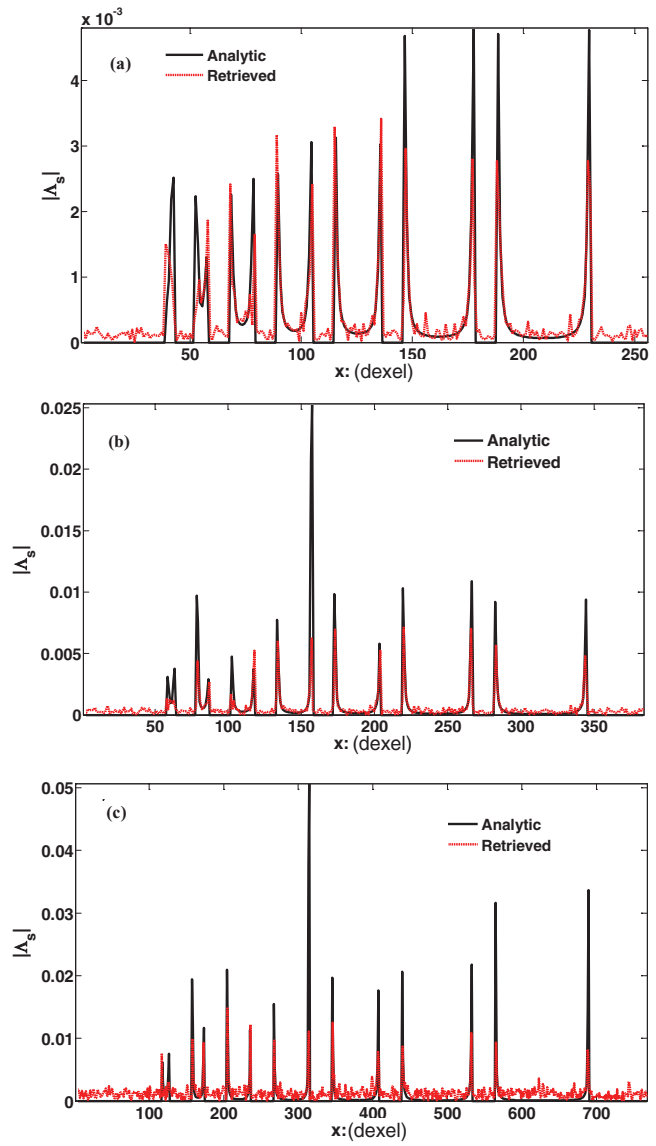


FIG. 9. The profiles of the second-order differential phase contrast images of Phantom-II corresponding to the central lines labeled in Figs. 8(a)–8(c) and compared with that is analytically calculated using Eq. (21).

V. DISCUSSIONS

We conduct a systematic investigation into the contrast generated by the second-order derivative $\Phi''_s(x_m)$ in x-ray dark-field imaging implemented with the Talbot interferometry. Based on the Fresnel-Kirchhoff diffraction theory under the paraxial condition, we derive the analytic formulae to characterize the imaging contrast generated by the second-order derivative $\Phi''_s(x_m)$. Recognizing its potential for imaging applications, we propose a method to retrieve the second-order differential phase contrast. A computer simulation study with specially designed numerical phantoms is carried out to validate the derived analytic formulae and evaluate the robustness of the proposed second-order differential phase contrast retrieval method over conditions. What follows is a summary of the major points we want to make based on our findings of this work.

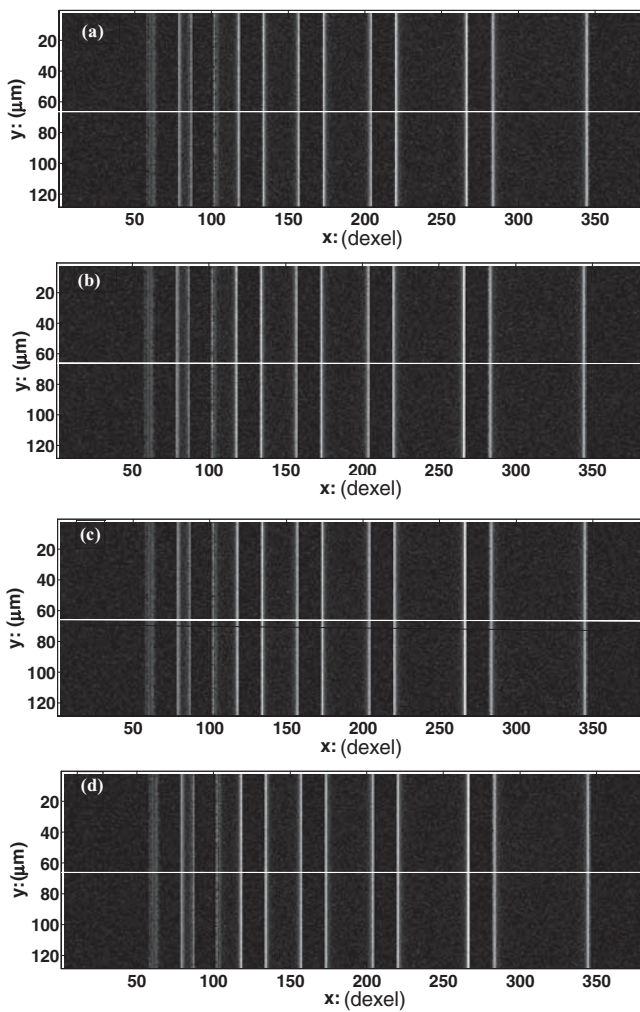


FIG. 10. The second-order differential phase contrast images of Phantom-II retrieved by the proposed method with 64 (a), 32 (b), 16 (c), and 8 (d) steps of G_2 shifting (detector cell dimension: $128 \mu\text{m}$; exposure: 1.28×10^7 photon/cm 2 per image).

The x-ray exposure set in the simulation is relatively low and results in strong Poisson noise. As illustrated in Fig. 3, the detection of the cylinder's boundary is difficult, especially if radius of the cylinder is small. However, a comparison between Figs. 3 and 6 clearly demonstrates that a strong edge enhancement indeed exists in the x-ray dark-field imaging implemented with the Talbot interferometry. Actually, the existence of edge enhancement in the x-ray phase contrast imaging implemented with the Talbot interferometry has been mentioned in the literature.^{12,26,29} Prior to our systematic investigation, Bech *et al.* reported their observation of strong contrast at the edge of a plastic container, powdered sugar,^{12,29} and crystalline sugar suspended in water¹¹ in their experimental investigation. In addition, Köhler *et al.* qualitatively discussed the influence of edge enhancement on the modulation transfer function (MTF) in the so-called coherent absorption contrast imaging (CACI).²⁶ However, our investigation is the first time that a set of analytic formulae, particularly Eqs. (20) and (22), is derived to characterize the second-order differential contrast $\Phi''_s(x_m)$ in

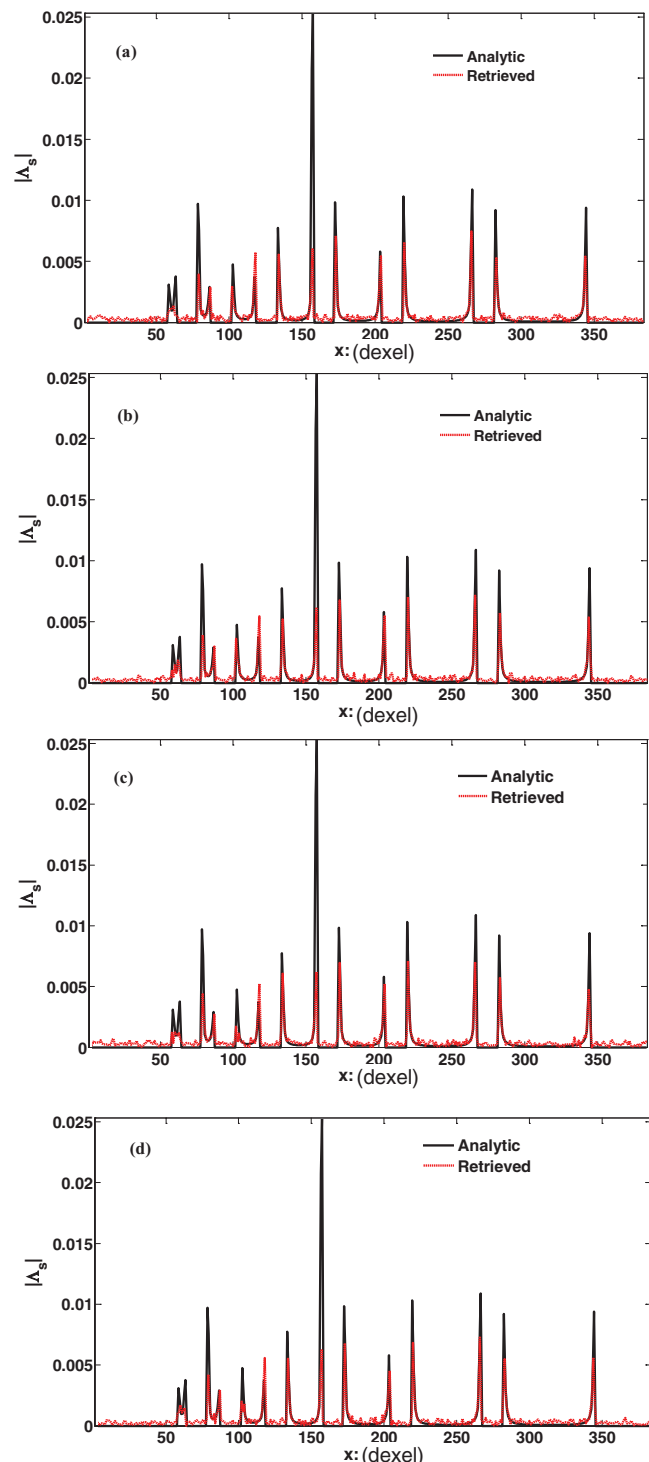


FIG. 11. The profiles of second-order differential phase contrast images of Phantom-II corresponding to the central lines labeled in Fig. 10 and compared with that is analytically calculated using Eq. (21).

the grating-based phase contrast imaging, which reveals that the key point behind the manifestation of second-order differential contrast $\Phi''_s(x_m)$ is the factor l_d/g_2 . In a grating-based x-ray phase contrast imaging system, g_2 , the period of grating G_2 , is usually on the order of $10^0 \mu\text{m}$, while the detector cell dimension l_d is on the order of $10^1\text{--}10^2 \mu\text{m}$. Hence, the edge enhancement effect caused by the second-order

derivative can be readily magnified by 10–100 times in x-ray differential phase contrast imaging implemented with the Talbot interferometry.

Our investigation shows that the small-angle scattering is not the sole contributor to the contrast in the dark-field imaging implemented with the x-ray Talbot interferometry. The second-order differential phase contrast generated by $\Phi''_s(x_m)$ can make a significant contribution to the dark-field contrast, especially in the scenarios whereby the detector cell dimension is relatively large, e.g., on the order of $10^1\text{--}10^2 \mu\text{m}$. This means that, even in the cases wherein the small-angle scattering is weak, the contrast generated by the second-order derivative of an object's smooth structure may still be employed for dark-field imaging implemented with the Talbot interferometry. It should be noted that this finding is of relevance for preclinical and clinical applications, since the small-angle scattering is weak in reality, especially at the situations in which x-ray photons are energetic.

It has been well-known that the contrast in the propagation-based in-line x-ray phase contrast imaging is induced by the second-order derivative of the smooth structure of an object.^{16,17,21,23} This means that the second-order derivative $\Phi''_s(x_m)$ is the root cause of imaging contrast in both the x-ray phase contrast imaging implemented with the Talbot interferometry and the propagation-based in-line phase contrast imaging. However, there is a significant disparity between them in the manifestation of second-order differential contrast. As illustrated in Eqs. (24) and (25), the second-order differential phase contrast in the propagation-based in-line x-ray phase contrast imaging is magnified by a relatively long distance between the object to be imaged and the x-ray detector, whereas that in the dark-field imaging implemented with the Talbot interferometry is magnified by the factor l_d/g_2 , wherein the distance between the object and x-ray detector can be just equal to the distance between grating G_1 and G_2 , i.e., the fractional Talbot distance that is usually substantially shorter than that is required in the propagation-based in-line system. Moreover, the period g_2 and the detector cell dimension l_d are usually on the order of 10^0 and $10^1\text{--}10^2 \mu\text{m}$ in an x-ray Talbot interferometry. The magnification factor may result in a substantially larger second-order differential contrast for retrieval of the phase variation that may not be feasible in the in-line x-ray phase contrast imaging system.

The images presented in Figs. 8 and 10 demonstrate that the second-order differential phase contrast can be directly utilized for imaging, and its performance is robust over detector cell dimension and grating shifting steps. Alternatively, it may be integrated into attenuation-contrast imaging for edge enhancement, similar to what has been achieved in the propagation-based in-line x-ray phase contrast imaging. Nevertheless, it should be pointed out that, in the propagation-based in-line x-ray phase contrast imaging, the second-order differential phase contrast is intrinsically bound with the attenuation-contrast,¹⁷ whereas that in the x-ray phase contrast imaging implemented with the Talbot interferometry is retrieved separately from the attenuation-contrast. Hence, the utilization of the second-order differential phase contrast in the x-ray phase contrast imaging implemented with the Tal-

bot interferometry becomes flexible and may provide more opportunity for applications. Moreover, in addition to being used for edge enhancement, the second-order differential contrast can be utilized for holographic imaging,^{17,30} i.e., to recover the distribution of refraction index decrement through second-order integration, although the performance of this optional imaging method may degrade with decreasing detector cell dimension. Inclusively, all the imaging mechanisms existing in the x-ray phase contrast imaging system implemented with the x-ray Talbot interferometry may make it an imaging modality to provide multicontrast for extensive applications.

A close inspection of Fig. 5(b) shows that the dimension of the object to be imaged plays an important role in generating the second-order differential contrast. For example, the second-order differential contrast only exists at the boundaries of the relatively large cylinders in column 5 and 6, but cross the entire section of the relatively small cylinders in column 1 and 2. This means that the second-order differential contrast manifests itself as edge enhancement if the object to be imaged is large relative to the detector cell, but as elevated contrast against the surroundings when the object is relatively small. It should be pointed out that this may be of relevance for extensive preclinical applications wherein small animals are to be imaged and clinical applications whereby small pathophysiological lesions are to be detected at their early stages.

To the best of our knowledge, no systematic investigation has thus far been conducted to quantify the effect of high order derivatives of $\Phi_s(x_m)$ on the interference fringe visibility in the x-ray differential phase contrast imaging and/or CT implemented with the Talbot interferometry. Due to space limitation, our effort in this work has focused on the investigation of the second-order differential phase contrast for radiographic imaging only. In fact, the second-order differential phase contrast retrieved in the x-ray phase contrast imaging system implemented with the Talbot interferometry can readily be employed for CT imaging. In addition, it should be noted that Eq. (24) is an approximation of the x-ray intensity at detector plane in the propagation-based in-line x-ray phase contrast imaging. It holds only if the resolvable phase shift varies slowly and the attenuation is or almost is x - and y -independent. Similarly, in the derivation of Fourier coefficients $C_0(m, n)$ and $C_1(m, n)$, we have assumed that the contribution from the derivative of attenuation and that from the third or higher order derivatives of the resolvable phase shift $\Phi_s(x)$ is negligible. If these high order terms are taken into account, the mathematical treatment presented in this paper can be expanded to characterize the edge enhancement effect more accurately in the scenarios wherein high spatial resolution at micro-order is desired. Finally, rigorously speaking, the assumption made in Eq. (9) is a little bit heuristic, because, even though the orientation of the gratings is along the y -axis only, the second-order derivative may exist along not only the x -axis but also the y -axis. Hence, an investigation into the possible existence of $\partial_{yy}^2 \Phi_s$ and $\partial_{xy}^2 \Phi_s$ and their influence on dark-field imaging in the x-ray differential phase contrast imaging is deemed.

We will report our further investigational results in our future publication.

VI. CONCLUSIONS

Both theoretical analysis and computer simulation study show that, in addition to the small-angle scattering corresponding to an object's fine structure, the second-order differential phase contrast caused by the second-order derivative of an object's smooth structures makes contribution to the contrast in the x-ray imaging implemented with the Talbot interferometry. With the proposed retrieval method, the second-order differential phase contrast can be directly utilized for imaging, incorporated with other contrast image for edge enhancement, or even holographic imaging. Therefore, it is believed that the theoretical derivation and experimental findings presented here may provide a foundation for the exploration of extensive preclinical and eventually clinical applications by making use of this new imaging mechanism.

ACKNOWLEDGMENTS

This work is partially supported by the Telemedicine and Advanced Technology Research Center (TATRC) at the U.S. Army Medical Research and Material Command (USAMRMC) Fort Detrick, MD via the award under Contract No. W81XWH-12-1-0138. In addition, the authors would like to extend their appreciation to Ms. Jessica Paulishen for her proofreading of this paper.

APPENDIX: DERIVATION OF THE SECOND-ORDER DIFFERENTIAL PHASE CONTRAST

Supposing grating G_2 be linearly shifted along the transverse direction x_g , the mean intensity of the interference fringe intensity recorded at a cell indexed by (m, n) in a detector can be expressed as^{8,9}

$$I_{m,n}(x_g) = \frac{1}{l_d^2} \int_{-\frac{l_d}{2}}^{\frac{l_d}{2}} dy \int_{-\frac{l_d}{2}}^{\frac{l_d}{2}} dx |E_{x_g}(x_m + x, y_n + y, z_{2b})|^2, \quad (\text{A1})$$

where

$$x_m = \left(m - \frac{1}{2}\right) l_d, \quad m = 0, \pm 1, \pm 2, \dots, \quad (\text{A2})$$

$$y_n = \left(n - \frac{1}{2}\right) l_d, \quad n = 0, \pm 1, \pm 2, \dots \quad (\text{A3})$$

l_d is the detector cell dimension, $E_{x_g}(x, y, z_{2b})$ is the electric field at location (x, y, z_{2b}) , and z_{2b} is the distance between the detector and x-ray source. The incident x-ray beam is assumed as a monochromatic plane wave with wavelength λ and amplitude E_0 . G_1 is a phase grating and G_2 is an absorption grating with 50% duty cycle. The distance from G_1 to G_2 is

selected as the m_T th fractional Talbot distance

$$z_T = m_T \frac{g_1^2}{8\lambda}, \quad m_T = 1, 3, 5, \dots, \quad (\text{A4})$$

where g_1 is the pitch of the phase grating G_1 . Usually, one sets

$$g_1 = 2g_2, \quad (\text{A5})$$

where g_2 is the pitch of the absorption grating G_2 . We focus on the grating-based differential phase contrast imaging system with its detector cell dimension l_d large enough to satisfy

$$2n_d = \frac{l_d}{g_2} \gg 1, \quad (\text{A6})$$

where n_d is assumed to be an integer, and gratings G_1 and G_2 be analytically represented by the transmission functions

$$P_1(x) = (-1)^n, \quad \text{for } n \frac{g_1}{2} \leq x < (n+1) \frac{g_1}{2}, \\ n = 0, \pm 1, \pm 2, \dots, \quad (\text{A7})$$

$$P_2(x, x_g) = \frac{1 + (-1)^n}{2}, \quad \text{if } n \frac{g_2}{2} \leq x - x_g < (n+1) \frac{g_2}{2}, \\ n = 0, \pm 1, \pm 2, \dots \quad (\text{A8})$$

Since the projection approximation^{8,9,26} can be used to estimate the electrical field immediately behind the object and the paraxial approximation holds valid in the x-ray beam's propagating from G_1 to G_2 ,^{8,9,12,26} the electric field at (x, y, z_{2b}) in the detector plane can be written as

$$E_{x_g}(x, y, z_{2b}) = \frac{E_0}{i\lambda z_T} \exp\left(2\pi i \frac{z_{2b}}{\lambda}\right) P_2(x, x_g) \\ \times \int_{-\frac{L_y}{2}}^{\frac{L_y}{2}} dy_1 \int_{-\frac{L_x}{2}}^{\frac{L_x}{2}} dx_1 P_1(x_1) \\ \times \exp\left(-\frac{1}{2}S(x_1) - i\Phi_s(x_1)\right) \\ \times \exp\left(i\pi \frac{(x - x_1)^2 + (y - y_1)^2}{\lambda z_T}\right), \quad (\text{A9})$$

where

$$S(x) = \frac{4\pi}{\lambda} \int_Z \beta(x, z) dz, \quad (\text{A10})$$

$$\Phi_s(x) = \frac{2\pi}{\lambda} \int_Z \delta_s(x, z) dz \quad (\text{A11})$$

are the projection of linear attenuation index β and refractive index decrement δ_s , respectively, along the x-ray propagation path z . L_x and L_y are the dimensions of gratings along the x and y directions.

Substituting Eq. (A9) into Eq. (A1), and noting the fact that

$$P_2(x, x_g) P_2^*(x, x_g) = P_2(x, x_g), \quad (\text{A12})$$

one gets

$$\begin{aligned} I_{m,n}(x_g) &= \alpha_n \int_{-\frac{l_d}{2}}^{\frac{l_d}{2}} dx P_2(x_m + x, x_g) \int_{-\frac{L_x}{2}}^{\frac{L_x}{2}} dx_1 P_1(x_1) \\ &\times \exp\left(-\frac{1}{2}S(x_1) - i\Phi_s(x_1)\right) \exp\left(i\pi \frac{(x_m + x - x_1)^2}{\lambda z_T}\right) \\ &\times \int_{-\frac{L_x}{2}}^{\frac{L_x}{2}} dx_2 P_1^*(x_2) \exp\left(-\frac{1}{2}S(x_2) + i\Phi_s(x_2)\right) \\ &\times \exp\left(-i\pi \frac{(x_m + x - x_2)^2}{\lambda z_T}\right), \end{aligned} \quad (\text{A13})$$

where

$$\alpha_n = \frac{|E_0|^2}{\lambda^2 l_d^2 z_T^2} \int_{-\frac{l_d}{2}}^{\frac{l_d}{2}} \left| \int_{-\frac{L_y}{2}}^{\frac{L_y}{2}} \exp\left(i\pi \frac{(y + y_n - y_1)^2}{\lambda z_T}\right) dy_1 \right|^2 dy. \quad (\text{A14})$$

Since $P_1(x)$ and $P_2(x, x_g)$ are periodic functions with periods g_1 and g_2 , respectively, they can be expressed in Fourier series

$$P_1(x) = - \sum_{j=-\infty}^{\infty} \frac{2i}{\pi(2j+1)} \exp\left(i \frac{2\pi(2j+1)}{g_1} x\right), \quad (\text{A15})$$

$$\begin{aligned} P_2(x, x_g) &= \frac{1}{2} \sum_{l=-\infty}^{\infty} \exp\left(-i \frac{\pi}{2} l\right) \\ &\times \text{sinc}\left(\frac{l}{2}\right) \exp\left[i \frac{2\pi l}{g_2} (x - x_g)\right], \end{aligned} \quad (\text{A16})$$

where $\text{sinc}(x) = \sin(\pi x)/(\pi x)$. Substituting Eqs. (A15) and (A16) into Eq. (A13) leads to

$$\begin{aligned} I_{m,n}(x_g) &= \frac{2\alpha_n l_d}{\pi^2} \sum_{l=-\infty}^{\infty} \exp\left(-2\pi i l \left(\frac{x_g}{g_2} + \frac{1}{4}\right)\right) \text{sinc}\left(\frac{l}{2}\right) \sum_{j_1=-\infty}^{\infty} \sum_{j_2=-\infty}^{\infty} \frac{\exp\left(\pi i l \frac{j_1+j_2+1}{2} m_T\right)}{(2j_1+1)(2j_2+1)} \\ &\times \int_{-\frac{L_x}{2}}^{\frac{L_x}{2}} dx_1 \int_{-\frac{L_x}{2}}^{\frac{L_x}{2}} dx_2 \exp\left(2\pi i (j_1 - j_2 + l) \frac{x_1 + x_2}{2g_2}\right) \\ &\times \exp\left(-\frac{S(x_1) + S(x_2)}{2} - i\Phi_s(x_1) + i\Phi_s(x_2)\right) \text{sinc}\left(2n_d \left(l + \frac{4n_d}{m_T} \frac{x_2 - x_1}{l_d}\right)\right) \\ &\times \exp\left(2\pi i \left(\frac{x_m}{g_2} - \frac{j_1 + j_2 + 1}{4} m_T - \frac{x_1 + x_2}{2g_2}\right) \left(l + \frac{4n_d}{m_T} \frac{x_2 - x_1}{l_d}\right)\right), \end{aligned} \quad (\text{A17})$$

in which Eqs. (A4)–(A6) are used. Equation (A17) means that the intensity $I_{m,n}(x_g)$ is a periodic function of x_g with period g_2 and thus can be expanded into a Fourier series

$$I_{m,n}(x_g) = \sum_{l=-\infty}^{\infty} C_l(m, n) \exp\left(2\pi i l \frac{x_g}{g_2}\right) \quad (\text{A18})$$

with the Fourier coefficient given by

$$\begin{aligned} C_l(m, n) &= \frac{2\alpha_n l_d}{\pi^2} \exp\left(\frac{\pi i l}{2}\right) \text{sinc}\left(\frac{l}{2}\right) \sum_{j_1=-\infty}^{\infty} \sum_{j_2=-\infty}^{\infty} \frac{\exp\left(-\pi i l \frac{j_1+j_2+1}{2} m_T\right)}{(2j_1+1)(2j_2+1)} \\ &\times \int_{-\frac{L_x}{2}}^{\frac{L_x}{2}} dx_1 \int_{-\frac{L_x}{2}}^{\frac{L_x}{2}} dx_2 \exp\left(-2\pi i (j_2 - j_1 + l) \frac{x_1 + x_2}{2g_2}\right) \\ &\times \exp\left(-\frac{S(x_1) + S(x_2)}{2} - i\Phi_s(x_1) + i\Phi_s(x_2)\right) \text{sinc}\left(2n_d \left(l - \frac{4n_d}{m_T} \frac{x_2 - x_1}{l_d}\right)\right) \\ &\times \exp\left(-2\pi i \left(\frac{x_m}{g_2} - \frac{j_1 + j_2 + 1}{4} m_T - \frac{x_1 + x_2}{2g_2}\right) \left(l - \frac{4n_d}{m_T} \frac{x_2 - x_1}{l_d}\right)\right). \end{aligned} \quad (\text{A19})$$

On the other hand, one may rewrite Eq. (A18) in a well-known form,^{10,11}

$$I_{m,n}(x_g) = a_0(m, n) + \sum_{l=1}^{\infty} a_l(m, n) \cos\left(2\pi l \frac{x_g}{g_2} + \phi_l(m, n)\right). \quad (\text{A20})$$

Comparing Eq. (A20) with Eq. (A18), one obtains

$$a_0(m, n) = C_0(m, n), \quad (\text{A21})$$

$$\frac{a_1(m, n)}{2} \exp(i\phi_1(m, n)) = C_1(m, n). \quad (\text{A22})$$

Equations (A21) and (A22) mean that all the information needed for the formation of attenuation-contrast, phase-contrast, and dark-field contrast imaging are available in the Fourier coefficients $C_0(m, n)$ and $C_1(m, n)$. In addition, according to Eq. (A6), it is reasonable to assume that

$$m_T \ll 4n_d, \quad (\text{A23})$$

and consequently,

$$\left| \frac{4n_d}{m_T} \frac{x_2 - x_1}{l_d} \right| \gg 1 \quad \text{if } |x_2 - x_1| \gtrsim l_d.$$

Given $l = 0$ or 1 , it is not difficult to show that

$$\left| l - \frac{4n_d}{m_T} \frac{x_2 - x_1}{l_d} \right| \gg 1.$$

According to Eq. (A6), $2n_d \gg 1$, one has

$$\left| 2n_d \left(l - \frac{4n_d}{m_T} \frac{x_2 - x_1}{l_d} \right) \right| \gg 1 \quad \text{provided } |x_2 - x_1| \gtrsim l_d$$

$$\text{and } l = 0 \text{ or } 1, \quad (\text{A24})$$

where the condition $|x_2 - x_1| \gtrsim l_d$ means that the absolute value of $(x_2 - x_1)$ is comparable to or larger than the detector cell dimension. As such, the second sinc function on the right side of Eq. (A19) becomes very small, i.e., the dominant contribution to the Fourier coefficients $C_l(m, n)$ ($l = 0, 1$) comes from the electric field at locations (x_1, x_2) that satisfies

$$|x_2 - x_1| \ll l_d. \quad (\text{A25})$$

Noting that $S(x)$ and $\Phi_s(x)$ vary with the characteristic sizes that are not smaller than l_d , and

$$x_1 = \frac{x_1 + x_2}{2} - \frac{x_2 - x_1}{2}, \quad x_2 = \frac{x_1 + x_2}{2} + \frac{x_2 - x_1}{2}, \quad (\text{A26})$$

it should be straightforward for us to understand that, given x_1 and x_2 that satisfy the condition specified by Eq. (A25),

$S(x_1)$, $S(x_2)$, $\Phi_s(x_1)$, and $\Phi_s(x_2)$ can be expanded into Taylor series around $(x_1 + x_2)/2$. Since β is usually much smaller than δ ,^{24,31} we can approximate the projection $S(x)$ with a zeroth-order Taylor series expansion, and the projection $\Phi_s(x)$ as a Taylor series expansion up to the second-order derivatives, i.e.,

$$S(x_1) \approx S\left(\frac{x_2 + x_1}{2}\right), \quad (\text{A27})$$

$$S(x_2) \approx S\left(\frac{x_2 + x_1}{2}\right), \quad (\text{A28})$$

$$\begin{aligned} \Phi_s(x_1) &\approx \Phi_s\left(\frac{x_2 + x_1}{2}\right) - \Phi'_s\left(\frac{x_2 + x_1}{2}\right) \frac{x_2 - x_1}{2} \\ &\quad + \Phi''_s\left(\frac{x_2 + x_1}{2}\right) \frac{(x_2 - x_1)^2}{8}, \end{aligned} \quad (\text{A29})$$

$$\begin{aligned} \Phi_s(x_2) &\approx \Phi_s\left(\frac{x_2 + x_1}{2}\right) + \Phi'_s\left(\frac{x_2 + x_1}{2}\right) \frac{x_2 - x_1}{2} \\ &\quad + \Phi''_s\left(\frac{x_2 + x_1}{2}\right) \frac{(x_2 - x_1)^2}{8}. \end{aligned} \quad (\text{A30})$$

Since $L_x \gg l_d$ is always satisfied in x-ray phase contrast imaging implemented with the Talbot interferometry, changing the domain of integration in Eq. (A19) from $[-L_x/2, L_x/2]$ to $(-\infty, \infty)$ can only lead to a negligible error. Hence, inserting Eqs. (A27)–(A30) into Eq. (A19), changing the variables of integration with

$$u = \frac{x_1 + x_2}{2}, \quad v = \frac{x_2 - x_1}{2}, \quad (\text{A31})$$

and replacing L_x with ∞ ,⁸ one may approximate the Fourier coefficients as

$$\begin{aligned} C_l(m, n) &= \frac{\alpha_n m_T g_2^2}{2\pi^2} \exp\left(\frac{\pi i l}{2}\right) \operatorname{sinc}\left(\frac{l}{2}\right) \sum_{j_1=-\infty}^{\infty} \sum_{j_2=-\infty}^{\infty} \frac{\exp\left(-\pi i l \frac{j_1+j_2+1}{2} m_T\right)}{(2j_1+1)(2j_2+1)} \\ &\times \int_{-\infty}^{\infty} du \exp\left(-2\pi i (j_2 - j_1 + l) \frac{u}{g_2} - S(u) + il \frac{m_T g_2}{2} \Phi'_s(u)\right) \\ &\times \left(\operatorname{sgn}\left(x_m + \frac{l_d}{2} - \frac{j_1 + j_2 + 1}{8n_d} m_T l_d + \frac{m_T g_2 l_d}{8n_d \pi} \Phi'_s(u) - u\right) \right. \\ &\left. - \operatorname{sgn}\left(x_m - \frac{l_d}{2} - \frac{j_1 + j_2 + 1}{8n_d} m_T l_d + \frac{m_T g_2 l_d}{8n_d \pi} \Phi'_s(u) - u\right) \right). \end{aligned} \quad (\text{A32})$$

Because of the factor $1/(2j_1 + 1)(2j_2 + 1)$ on the right side of Eq. (A32), the dominant contribution to the Fourier coefficients comes from the terms corresponding to the (j_1, j_2) that satisfy

$$|j_1| \sim 10^0 \text{ and } |j_2| \sim 10^0. \quad (\text{A33})$$

Thus, one has

$$\left| \frac{j_1 + j_2 + 1}{8n_d} m_T l_d \right| \ll l_d, \quad (\text{A34})$$

in which Eq. (A23) is used. On the other hand, according to Eq. (A6), it is reasonable for one to assume

$$\left| \frac{\lambda z_T}{g_2} \Phi'_s(u) \right| \ll 4n_d\pi. \quad (\text{A35})$$

It is interesting to note that, in comparison with the condition imposed on x-ray Talbot interferometry to avoid the phenomenon of phase wrapping,³²

$$\left| \frac{\lambda z_T}{g_2} \Phi'_s(u) \right| \leq \pi. \quad (\text{A36})$$

Equation (A35) represents a significantly relaxed constraint.

From Eq. (A35), one immediately gets

$$\left| \frac{m_T g_2 l_d}{8n_d\pi} \Phi'_s(u) \right| = \frac{l_d}{4n_d\pi} \left| \frac{\lambda z_T}{g_2} \Phi'_s(u) \right| \ll l_d, \quad (\text{A37})$$

in which Eqs. (A4) and (A5) are used. Inserting Eqs. (A34) and (A37) into Eq. (A32), it should not be hard to understand that, only if variable u is in the vicinity of x_m and with a size comparable to l_d , the subtraction

between the two sign functions, as given on the right side of Eq. (A32), can be nonzero. This means that the dominant contribution to the Fourier coefficients $C_0(m, n)$ and $C_1(m, n)$ only comes from the variable u that is in the vicinity of x_m . As a result, each of the projection $S(u)$ and $\Phi'_s(u)$ in Eq. (A32) can be expanded as a Taylor series around x_m . Again, since the linear attenuation coefficient β is much smaller than the refractive index decrement δ , we can approximate $S(u)$ with a zeroth-order Taylor expansion, and $\Phi'_s(u)$ a first-order Taylor expansion, respectively,

$$S(u) \approx S(x_m), \quad (\text{A38})$$

$$\Phi'_s(u) \approx \Phi'_s(x_m) + \Phi''_s(x_m)(u - x_m). \quad (\text{A39})$$

Now the integration in Eq. (A32) can be carried out using Eqs. (A38) and (A39),

$$\begin{aligned} C_l(m, n) &= \frac{\alpha_n l_d m_T g_2^2}{2\pi^2} \operatorname{sinc}\left(\frac{l}{2}\right) \exp\left(\frac{\pi}{2}il\right) \sum_{j_1=-\infty}^{\infty} \sum_{j_2=-\infty}^{\infty} \exp\left(\frac{\pi}{2}i(j_2 - j_1)(j_1 + j_2 + 1)m_T\right) \\ &\times \frac{\exp\left(-i(j_2 - j_1)\frac{\frac{\lambda z_T}{g_2} \Phi'_s(x_m)}{1 - \frac{\lambda z_T}{2\pi} \Phi''_s(x_m)}\right)}{1 - \frac{\lambda z_T}{2\pi} \Phi''_s(x_m)} \operatorname{sinc}\left(2n_d\left(\frac{j_2 - j_1}{1 - \frac{\lambda z_T}{2\pi} \Phi''_s(x_m)} + l\right)\right) \\ &\times \frac{\exp\left(-i\frac{(j_1 - \frac{1}{2})^2 m_T \frac{\lambda z_T}{4} \Phi''_s(x_m)}{1 - \frac{\lambda z_T}{2\pi} \Phi''_s(x_m)}\right)}{2j_1 + 1} \frac{\exp\left(i\frac{(j_2 - \frac{1}{2})^2 m_T \frac{\lambda z_T}{4} \Phi''_s(x_m)}{1 - \frac{\lambda z_T}{2\pi} \Phi''_s(x_m)}\right)}{2j_2 + 1}. \end{aligned} \quad (\text{A40})$$

Because of the factors $1/(2j_1 + 1)$ and $1/(2j_2 + 1)$ on the right side of Eq. (A40), only the terms corresponding to the integers j_1 and j_2 that satisfy Eq. (A33) contribute to the Fourier coefficients significantly. Furthermore, similar to the smooth-phase condition in the in-line x-ray phase contrast imaging,^{16–18} we assume that the resolvable phase shift varies slowly such that

$$|\Lambda_s(x_m)| = \left| \frac{\lambda z_T}{2\pi} \Phi''_s(x_m) \right| \ll 1. \quad (\text{A41})$$

Combining Eqs. (A33), (A41), and (A23) one obtains

$$\frac{\exp\left(-i\frac{(j_1 - \frac{1}{2})^2 m_T \frac{\lambda z_T}{4} \Phi''_s(x_m)}{1 - \frac{\lambda z_T}{2\pi} \Phi''_s(x_m)}\right)}{2j_1 + 1} \frac{\exp\left(i\frac{(j_2 - \frac{1}{2})^2 m_T \frac{\lambda z_T}{4} \Phi''_s(x_m)}{1 - \frac{\lambda z_T}{2\pi} \Phi''_s(x_m)}\right)}{2j_2 + 1} \approx \frac{1}{(2j_1 + 1)(2j_2 + 1)}. \quad (\text{A42})$$

Substituting Eq. (A42) into Eq. (A40) and using the relationship

$$\begin{aligned} &\frac{\exp\left(\frac{\pi}{2}i(j_2 - j_1)(j_1 + j_2 + 1)m_T\right)}{(2j_1 + 1)(2j_2 + 1)} \\ &= \frac{\delta_{j_1 j_2}}{(2j_1 + 1)^2} + \frac{1 - \delta_{j_1 j_2}}{2(j_2 - j_1)} \exp\left(\frac{\pi}{2}i(j_2 - j_1)^2 m_T\right) \frac{\exp\left(\frac{\pi}{2}i(j_2 - j_1)(2j_1 + 1)m_T\right)}{2j_1 + 1} \\ &- \frac{1 - \delta_{j_1 j_2}}{2(j_2 - j_1)} \exp\left(-\frac{\pi}{2}i(j_2 - j_1)^2 m_T\right) \frac{\exp\left(\frac{\pi}{2}i(j_2 - j_1)(2j_2 + 1)m_T\right)}{2j_2 + 1}, \end{aligned} \quad (\text{A43})$$

where δ_{ij} is the Kronecker delta, one may rewrite Eq. (A40) as

$$\begin{aligned} C_l(m, n) &= \frac{\alpha_n l_d m_T g_2^2}{8} \frac{\exp(-S(x_m))}{1 - \frac{\lambda z_T}{2\pi} \Phi''_s(x_m)} \delta_{l0} - \frac{\alpha_n l_d m_T g_2^2}{4\pi} \frac{\exp(-S(x_m))}{1 - \frac{\lambda z_T}{2\pi} \Phi''_s(x_m)} \operatorname{sinc}\left(\frac{l}{2}\right) \exp\left(\frac{\pi}{2}il\right) \\ &\times \sum_{j_0=-\infty}^{\infty} \frac{(-1)^{j_0}}{2j_0 + 1} \exp(-i(2j_0 + 1)\psi_1(x_m)) \operatorname{sinc}\left(2n_d\left(\frac{2j_0 + 1}{1 - \frac{\lambda z_T}{2\pi} \Phi''_s(x_m)} + l\right)\right), \end{aligned} \quad (\text{A44})$$

where

$$\psi_1(x_m) = \frac{\frac{\lambda z_T}{g_2} \Phi'_s(x_m)}{1 - \frac{\lambda z_T}{2\pi} \Phi''_s(x_m)}, \quad (\text{A45})$$

in which the following formulae³³

$$\sum_{j=0}^{\infty} \frac{1}{(2j+1)^2} = \frac{\pi^2}{8}, \quad (\text{A46})$$

$$\sum_{j=0}^{\infty} \frac{(-1)^j}{2j+1} = \frac{\pi}{4}, \quad (\text{A47})$$

are used to sum the corresponding series. It should be noted that, using Eqs. (A6) and (A41), one may further estimate the Fourier coefficients as

$$\begin{aligned} C_0(m, n) &= \frac{\alpha_n l_d m_T g_2^2}{8} \frac{\exp(-S(x_m))}{1 - \frac{\lambda z_T}{2\pi} \Phi''_s(x_m)} - \frac{\alpha_n l_d m_T g_2^2}{8\pi^2 n_d} \exp(-S(x_m)) \\ &\times \sum_{j_0=-\infty}^{\infty} \frac{(-1)^{j_0}}{(2j_0+1)^2} \exp(-i(2j_0+1)\psi_1(x_m)) \sin\left(2\pi n_d(2j_0+1) \frac{\frac{\lambda z_T}{2\pi} \Phi''_s(x_m)}{1 - \frac{\lambda z_T}{2\pi} \Phi''_s(x_m)}\right) \\ &\approx \frac{\alpha_n l_d m_T g_2^2}{8} \frac{\exp(-S(x_m))}{1 - \frac{\lambda z_T}{2\pi} \Phi''_s(x_m)}, \end{aligned} \quad (\text{A48})$$

$$\begin{aligned} C_1(m, n) &= \frac{\alpha_n l_d m_T g_2^2}{2\pi^2} \frac{i \exp(-S(x_m))}{1 - \frac{\lambda z_T}{2\pi} \Phi''_s(x_m)} \sum_{j_0=-\infty}^{\infty} \frac{(-1)^{j_0+1}}{2j_0+1} \exp(-i(2j_0+1)\psi_1(x_m)) \\ &\times \text{sinc}\left(2n_d\left(\frac{2j_0+1}{1 - \frac{\lambda z_T}{2\pi} \Phi''_s(x_m)} + 1\right)\right) \\ &= -\frac{\alpha_n l_d m_T g_2^2}{2\pi^2} \frac{i \exp(-S(x_m))}{1 - \frac{\lambda z_T}{2\pi} \Phi''_s(x_m)} \exp(i\psi_1(x_m)) \text{sinc}\left(2n_d\left(\frac{-1}{1 - \frac{\lambda z_T}{2\pi} \Phi''_s(x_m)} + 1\right)\right) \\ &+ \frac{\alpha_n l_d m_T g_2^2}{2\pi^2} \frac{i \exp(-S(x_m))}{2\pi n_d} \sum_{j_0=-\infty, j_0 \neq -1}^{\infty} \frac{(-1)^{j_0+1}}{2j_0+1} \exp(-i(2j_0+1)\psi_1(x_m)) \\ &\times \text{sinc}\left(\frac{2\pi n_d(2j_0+1)}{1 - \frac{\lambda z_T}{2\pi} \Phi''_s(x_m)}\right) \frac{1}{2(j_0+1) - \frac{\lambda z_T}{2\pi} \Phi''_s(x_m)} \\ &\approx -\frac{\alpha_n l_d m_T g_2^2}{2\pi^2} \frac{i \exp(-S(x_m))}{1 - \frac{\lambda z_T}{2\pi} \Phi''_s(x_m)} \exp(i\psi_1(x_m)) \text{sinc}\left(2n_d\left(\frac{-1}{1 - \frac{\lambda z_T}{2\pi} \Phi''_s(x_m)} + 1\right)\right) \\ &= -\frac{\alpha_n l_d m_T g_2^2}{2\pi^2} \frac{i \exp\left(-S(x_m) + i \frac{\frac{\lambda z_T}{g_2} \Phi'_s(x_m)}{1 - \frac{\lambda z_T}{2\pi} \Phi''_s(x_m)}\right)}{1 - \frac{\lambda z_T}{2\pi} \Phi''_s(x_m)} \text{sinc}\left(2n_d \frac{\frac{\lambda z_T}{2\pi} \Phi''_s(x_m)}{1 - \frac{\lambda z_T}{2\pi} \Phi''_s(x_m)}\right). \end{aligned} \quad (\text{A49})$$

Combining Eqs. (A21), (A22), (A48), and (A49) one may represent the reduction in the maxima of interference fringe visibility induced by the resolvable phase shift as

$$\begin{aligned} V_s(m, n) &= \left| \text{sinc}\left(2n_d \frac{\frac{\lambda z_T}{2\pi} \Phi''_s(x_m)}{1 - \frac{\lambda z_T}{2\pi} \Phi''_s(x_m)}\right) \right| \\ &\approx \left| \text{sinc}\left(2n_d \frac{\lambda z_T}{2\pi} |\Phi''_s(x_m)|\right) \right| = \left| \text{sinc}\left(\frac{l_d}{g_2} |\Lambda_s(x_m)|\right) \right| \\ &= |\text{sinc}(|\Theta(x_m)|)|, \end{aligned} \quad (\text{A50})$$

in which Eq. (A41) is used.

^{a)}Author to whom correspondence should be addressed. Electronic mail: xiangyang.tang@emory.edu; Tel.: (404) 778-1732; Fax: (404) 712-5813.

¹R. Fitzgerald, "Phase-sensitive x-ray imaging," *Phys. Today* **53**, 23–26 (2000).

²M. Born and E. Wolf, *Principles of Optics: Electromagnetic Theory of Propagation, Interference and Diffraction of Light*, 7th ed. (Cambridge University Press, Cambridge, England, 1999).

³R. A. Lewis, "Medical phase contrast x-ray imaging: current status and future prospects," *Phys. Med. Biol.* **49**, 3573–3583 (2004).

⁴T. Weitkamp, A. Diaz, C. David, F. Pfeiffer, M. Stampanoni, P. Cloetens, and E. Ziegler, "X-ray phase imaging with a grating interferometer," *Opt. Express* **13**, 6296–6304 (2005).

⁵F. Pfeiffer, T. Weitkamp, O. Bunk, and C. David, "Phase retrieval and differential phase-contrast imaging with low-brilliance x-ray sources," *Nat. Phys.* **2**, 258–261 (2006).

⁶A. Momose and J. Fukuda, "Phase-contrast radiographs of nonstained rat cerebellar specimen," *Med. Phys.* **22**, 375–379 (1997).

⁷Y. I. Nesterets, "On the origins of decoherence and extinction contrast in phase-contrast imaging," *Opt. Commun.* **281**, 533–542 (2008).

⁸W. Yashiro, Y. Terui, K. Kawabata, and A. Momose, "On the origin of visibility contrast in x-ray Talbot interferometry," *Opt. Express* **18**, 16890–16901 (2010).

⁹S. K. Lynch, V. Pai, J. Auxier, A. F. Stein, E. E. Bennett, C. K. Kemble, X. Xiao, W.-K. Lee, N. Y. Morgan, and H. H. Wen, "Interpretation of dark-field contrast and particle-size selectivity in grating interferometers," *Appl. Opt.* **50**, 4310–4319 (2011).

¹⁰F. Pfeiffer, M. Bech, O. Bunk, P. Kraft, E. F. Eikenberry, C. Bronnimann, C. Grunzweig, and C. David, "Hard-x-ray dark-field imaging using a grating interferometer," *Nat. Mater.* **7**, 134–137 (2008).

¹¹M. Bech, O. Bunk, T. Donath, R. Feidenhans'l, C. David, and F. Pfeiffer, "Quantitative x-ray dark-field computed tomography," *Phys. Med. Biol.* **55**, 5529–5539 (2010).

¹²M. Bech, "X-ray imaging with a grating interferometer," Ph.D. dissertation, University of Copenhagen, Denmark, 2009.

¹³A. Momose, S. Kawamoto, I. Koyama, Y. Hamaishi, K. Takai, and Y. Suzuki, "Demonstration of x-ray Talbot interferometry," *Jpn. J. Appl. Phys.* **42**, L866–L868 (2003).

¹⁴Z. T. Wang, K. J. Kang, Z. F. Huang, and Z. Q. Chen, "Quantitative grating-based x-ray dark-field computed tomography," *Appl. Phys. Lett.* **95**, 094105–094108 (2009).

¹⁵G. H. Chen, N. Bevins, J. Zambelli, and Z. Qi, "Small-angle scattering computed tomography (SAS-CT) using a Talbot-Lau interferometer and a rotating anode x-ray tube: theory and experiments," *Opt. Express* **18**, 12960–12970 (2010).

¹⁶A. V. Bronnikov, "Theory of quantitative phase-contrast computed tomography," *J. Opt. Soc. Am. A* **19**, 472–480 (2002).

¹⁷P. Cloetens, M. Pateyron-Salomé, J.-Y. Buffière, G. Peix, J. Baruchel, F. Peyrin, and M. Schlenker, "Observation of microstructure and damage in materials by phase sensitive radiography and tomography," *J. Appl. Phys.* **81**, 5878–5886 (1997).

¹⁸D. Shi and M. A. Anastasio, "Relationships between smooth- and small-phase conditions in x-ray phase-contrast imaging," *IEEE Trans. Med. Imaging* **28**, 1969–1973 (2009).

¹⁹A. Snigirev, I. Snigireva, V. Kohn, S. Kuznetsov, and I. Schelokov, "On the possibilities of x-ray phase contrast microimaging by coherent high-energy synchrotron radiation," *Rev. Sci. Instrum.* **66**, 5486–5492 (1995).

²⁰S. W. Wilkins, T. E. Gureyev, D. Gao, A. Pogany, and A. W. Stevenson, "Phase-contrast imaging using polychromatic hard x-rays," *Nature (London)* **384**, 335–338 (1996).

²¹X. Wu and H. Liu, "Clinical implementation of x-ray phase-contrast imaging: Theoretical foundations and design considerations," *Med. Phys.* **30**, 2169–2179 (2003).

²²X. Wu, and H. Liu, "Clarification of aspects in in-line phase-sensitive x-ray imaging," *Med. Phys.* **34** 737–743 (2007).

²³A. Burvall, U. Lundström, P. A. C. Takman, D. H. Larsson, and H. M. Hertz, "Phase retrieval in x-ray phase-contrast imaging suitable for tomography," *Opt. Express* **19**, 10359–10376 (2011).

²⁴S.-A. Zhou, A. Brahme, and A. Brahme, "Development of phase-contrast x-ray imaging techniques and potential medical applications," *Phys. Med.* **24**, 129–148 (2008).

²⁵P. Cloetens *et al.*, "Holotomography: Quantitative phase tomography with micrometer resolution using hard synchrotron radiation x rays," *Appl. Phys. Lett.* **75**, 2912–2914 (1999).

²⁶T. Köhler and E. Roessl, "Noise properties of grating-based x-ray phase contrast computed tomography," *Med. Phys.* **38**, S106–S116 (2011).

²⁷X. Tang, Y. Yang, and S. Tang, "Characterization of imaging performance in differential phase contrast CT compared with the conventional CT – Noise power spectrum NPS(k)," *Med. Phys.* **38**, 4386–4395 (2011).

²⁸X. Tang, Y. Yang, and S. Tang, "Characterization of imaging performance in differential phase contrast CT compared with the conventional CT: Spectrum of noise equivalent quanta NEQ(k)," *Med. Phys.* **39**, 4467–4482 (2012).

²⁹M. Bech, T. H. Jensen, O. Bunk, T. Donath, C. David, T. Weitkamp, G. L. Duc, A. Bravin, P. Cloetens, and F. Pfeiffer, "Advanced contrast modalities for x-ray radiology: Phase-contrast and dark-field imaging using a grating interferometer," *Med. Phys.* **20**, 7–16 (2010).

³⁰K. A. Nugent, "Coherent methods in the x-ray sciences," *Adv. Phys.* **59**, 1–99 (2010).

³¹A. Momose, "Recent advances in x-ray phase imaging," *Jpn. J. Appl. Phys.* **44**, 6355–6367 (2005).

³²R. Raupach and T. G. Flohr, "Analytic evaluation of the signal and noise propagation in x-ray differential phase-contrast computed tomography," *Phys. Med. Biol.* **56**, 2219–2244 (2011).

³³V. Mangulis, *Handbook of Series for Scientists and Engineers* (Academic, New York, 1965).

Radial differential interior tomography and its image reconstruction with differentiated backprojection and projection onto convex sets

Shaojie Tang

Imaging and Medical Physics, Department of Radiology and Imaging Sciences, Emory University School of Medicine, 1701 Uppergate Drive, C-5018, Atlanta, Georgia 30322 and School of Automation, Xi'an University of Posts and Telecommunications, Xi'an, Shaanxi 710121, China

Xiangyang Tang^{a)}

Imaging and Medical Physics, Department of Radiology and Imaging Sciences, Emory University School of Medicine, 1701 Uppergate Drive, C-5018, Atlanta, Georgia 30322

(Received 29 March 2013; revised 24 May 2013; accepted for publication 11 June 2013;
published 21 August 2013)

Purpose: Interior tomography has been recognized as one of the most effective approaches in computed tomography (CT) to reduce radiation dose rendered to patients. In this work, the authors propose and evaluate an imaging method of radial differential interior tomography.

Methods: In interior tomography, an x-ray beam is collimated to only irradiate the region of interest (ROI) with suspected lesions while the surrounding area/volume of normal tissues/organs is spared. In the proposed imaging method of radial differential interior tomography, the outcome is a ROI image that has gone through a radial differential filtering. The image reconstruction algorithm for the radial differential interior tomography is kept in the fashion of differentiated backprojection and projection onto convex sets, but the required *a priori* knowledge in a small round area becomes zero and may be more readily available in practice.

Results: Using the projection data simulated by computer and acquired by CT scanner, the authors evaluate and verify the performance of the proposed radial differential interior tomography method and its associated image reconstruction algorithm. The preliminary results show that the proposed imaging method can generate an image that is the radial differentiation of a conventional tomographic image and is robust over noise that inevitably exist in practice.

Conclusions: It is believed that the proposed imaging method may find its utility in advanced clinical applications wherein a ROI-based image processing and analysis is required for lesion visualization, characterization, and diagnosis. © 2013 American Association of Physicists in Medicine. [http://dx.doi.org/10.1118/1.4812676]

Key words: CT, tomography, interior tomography, reconstruction, derivative backprojection, projection onto convex sets

1. INTRODUCTION

X-ray computed tomography (CT) is one of the most widely used imaging modalities for diagnostic tasks in the clinic. However, the x-ray radiation rendered to a patient might potentially induce clinical consequences, such as cancer.^{1–7} Though the medical benefits provided by diagnostic CT substantially outweigh the potential risks, it is still mandatory to reduce the radiation dose to a patient as much as possible while maintaining the image quality for diagnosis.

In the conventional CT imaging, a tomographic image is reconstructed from the projection data without lateral truncation. Among the methods to reduce CT radiation dose that have been proposed in the literature,^{8–24} the so-called method of interior tomography^{16–23} is of relevance, wherein only the region of interest (ROI) with suspected lesions is irradiated via dynamic x-ray beam collimation. As a result, the normal tissues/organs surrounding the ROI are spared of x-ray radiation dose, which is definitely of clinical relevance, especially in advanced clinical applications, such as cardiovascular imaging. This means that in the interior

tomography an image is reconstructed from the projection data with lateral truncation. Thus far, under the framework of total-variation (TV) minimization based compressed sensing,^{16,17} or the scheme of differentiated backprojection (DBP) and projection onto convex sets (POCS),^{18–23} the development of image reconstruction algorithms for interior tomography has become a subject of active research.

In the clinical applications of conventional tomography, certain filtering for edge detection or enhancement, which is mathematically local,^{24–27} may facilitate the tasks in image analysis and characterization to improve the accuracy and precision in computer aided diagnosis (CAD) and treatment planning in image-guided radiation therapy.^{28,29} For example, the Laplacian for edge detection/enhancement has played an important role in contour outlining for area/volume measurement, feature extraction for image registration/fusion, and segmentation for image understanding.^{26–29} It is straightforward for us to understand that such edge detection/enhancement filtering may also be desirable in the clinical applications of interior tomography. Moreover, it is our opinion that a radial differential filtering, which is a local

and linear operator for edge detection/enhancement, may provide the morphological information that is relevant for image analysis and characterization in clinical applications. Hence, we propose the imaging method of radial differential interior tomography in this paper and derive its associated image reconstruction algorithm.

In conventional tomography, a transform or filtering may be carried out after a tomographic image has been reconstructed by a filtered backprojection (FBP) algorithm, i.e., via a two-step process. Similarly, in radial differential interior tomography, the radial differential filtering may also be carried out once the tomographic image has been reconstructed with the DBP-POCS algorithm.¹⁸⁻²³ However, it is not hard to understand that the computation efficiency of such a two-step approach can be significantly improved if the radial differential filtering is integrated into image reconstruction and thus the postreconstruction operation can be avoided. It also should be noted that any artifact existing in the reconstructed interior tomographic image may be picked up or even amplified by the postreconstruction radial differential filtering. In addition, by avoiding the postreconstruction filtering, certain properties of the reconstructed images, e.g., the spatial resolution, may not be degraded. All these points clearly show that, in the radial differential interior tomography, the DBP-POCS based one-step image reconstruction algorithm (namely, radial differential DBP-POCS algorithm henceforth) is more desirable than the DBP-POCS based two-step approach.

With the projection data of a phantom simulated by computer and a large animal (sheep) acquired by diagnostic CT scanner, we evaluate the performance of the proposed radial differential interior tomography and the derived DBP-POCS based one-step image reconstruction algorithm. Moreover, we compare the performance of the DBP-POCS based one-step algorithm with that of the DBP-POCS based two-step algorithm. In such a way, the proposed imaging method of radial differential interior tomography and its reconstruction algorithm can be thoroughly investigated and characterized.

2. MATERIALS AND METHODS

2.A. Reconstruction of derivative object function with DBP

In the Cartesian coordinate system, an object function can be denoted as a real function,

$$f(\mathbf{x}) = f(x_1, x_2), \quad \mathbf{x} = (x_1, x_2) \in \mathbb{R}^2, \quad (1)$$

while its parallel-beam projection, i.e., Radon transform, is defined as³⁰

$$\begin{aligned} p(\phi, r) &= \int_{\mathfrak{N}} f(r\phi + t\phi^\perp) dt, \quad \phi = (\cos \phi, \sin \phi), \\ \phi^\perp &= (-\sin \phi, \cos \phi), \quad r \in \mathfrak{N}, \quad \phi \in [0, \pi). \end{aligned} \quad (2)$$

The Hilbert transform of a one-dimensional (1D) function $g(r)$ is defined as

$$Hg(r) = \int_{\mathfrak{N}} \frac{g(r')}{\pi(r - r')} dr' = \int_{\mathfrak{N}} -i \operatorname{sgn}(\rho) G(\rho) e^{i2\pi r\rho} d\rho, \quad (3)$$

where $\operatorname{sgn}(\rho)$ is the sign function of variable ρ , and $G(\rho)$ is the Fourier transform of $g(r)$, i.e.,

$$G(\rho) = \int_{\mathfrak{N}} g(r) e^{-i2\pi r\rho} dr.$$

In the local polar coordinate system with respect to reference point \mathbf{x}_0 , (therein the origin of local polar coordinate system and the reference point are coincident), the object function and its derivative along the radial direction can be expressed as

$$\begin{aligned} \tilde{f}_{\mathbf{x}_0}(s, \theta) &= f(s\theta + \mathbf{x}_0), \quad \theta = (\cos \theta, \sin \theta), \\ s \in \mathfrak{N}, \quad \theta \in [0, \pi), \end{aligned} \quad (4)$$

$$\begin{aligned} \partial_1 \tilde{f}_{\mathbf{x}_0}(s, \theta) &= \frac{\partial}{\partial s} \tilde{f}_{\mathbf{x}_0}(s, \theta) = \frac{\partial}{\partial s} f(s\theta + \mathbf{x}_0) \\ &= \frac{\partial}{\partial \mathbf{x}} f(s\theta + \mathbf{x}_0) \cdot \theta, \quad s \in \mathfrak{N}, \quad \theta \in [0, \pi), \end{aligned} \quad (5)$$

and the radial Hilbert filtering of the derivative object function is defined as

$$\begin{aligned} H_\theta^1 \tilde{f}_{\mathbf{x}_0}(s) &= \int_{\mathfrak{N}} \frac{1}{\pi(s - s')} \partial_1 \tilde{f}_{\mathbf{x}_0}(s', \theta) ds' \\ &= \int_{\mathfrak{N}} \frac{1}{\pi(s - s')} \frac{\partial}{\partial \mathbf{x}} f(s'\theta + \mathbf{x}_0) \cdot \theta ds'. \end{aligned} \quad (6)$$

Starting from the Fourier series of object function $f(\mathbf{x})$

$$f(\mathbf{x}) = \int_{\mathbb{R}^2} F(\mathbf{v}) e^{i2\pi \mathbf{v} \cdot \mathbf{x}} d\mathbf{v}, \quad (7)$$

where $F(\mathbf{v}) = F(v_1, v_2) = \int_{\mathbb{R}^2} f(\mathbf{x}) e^{-i2\pi \mathbf{v} \cdot \mathbf{x}} dx$, we have

$$\frac{\partial}{\partial \mathbf{x}} f(\mathbf{x}) = i2\pi \int_{\mathbb{R}^2} F(\mathbf{v}) e^{i2\pi \mathbf{v} \cdot \mathbf{x}} \mathbf{v} d\mathbf{v}, \quad (8)$$

and

$$\begin{aligned} H_\theta^1 \tilde{f}_{\mathbf{x}_0}(s) &= i2\pi \int_{\mathbb{R}^2} F(\mathbf{v}) e^{i2\pi \mathbf{v} \cdot \mathbf{x}_0} (\mathbf{v} \cdot \theta) \\ &\quad \times \int_{\mathfrak{N}} \frac{1}{\pi(s - s')} e^{i2\pi s' \mathbf{v} \cdot \theta} ds' d\mathbf{v}. \end{aligned} \quad (9)$$

Changing the integral variable as

$$\int_{\mathfrak{N}} \frac{1}{\pi(s - s')} e^{i2\pi s' \mathbf{v} \cdot \theta} ds' = \int_{\mathfrak{N}} \frac{1}{\pi s'} e^{i2\pi(s - s') \mathbf{v} \cdot \theta} ds', \quad (10)$$

we can get

$$\begin{aligned}
 H_\theta^1 \tilde{f}_{x_0}(s) &= i2\pi \int_{\Re^2} F(v) e^{i2\pi v \cdot x_0} (v \cdot \theta) \int_{\Re} \frac{1}{\pi s'} e^{i2\pi(s-s')v \cdot \theta} ds' d\mathbf{v} \\
 &= i2\pi \int_0^\pi \int_{\Re} F(\rho \phi) e^{i2\pi \rho x_0 \cdot \phi} \rho (\phi \cdot \theta) \\
 &\quad \times \int_{\Re} \frac{1}{\pi s'} e^{i2\pi(s-s')\rho \phi \cdot \theta} ds' |\rho| d\rho d\phi \\
 &= i2\pi \int_0^\pi \int_{\Re} F(\rho \phi) e^{i2\pi \rho x_0 \cdot \phi} \rho (\phi \cdot \theta) \\
 &\quad \times \int_{\Re} \frac{1}{\pi s'} e^{i2\pi(s-s')\rho \cos(\phi-\theta)} ds' |\rho| d\rho d\phi \\
 &= i2\pi \int_0^\pi \int_{\Re} \operatorname{sgn}(\rho) \rho^2 (\phi \cdot \theta) P(\phi, \rho) e^{i2\pi \rho x_0 \cdot \phi} \\
 &\quad \times \int_{\Re} \frac{1}{\pi s'} e^{i2\pi(s-s')\rho \cos(\phi-\theta)} ds' d\rho d\phi. \tag{11}
 \end{aligned}$$

Defining

$$K_p(\theta, s, \phi, \rho) = \int_{\Re} \frac{1}{\pi s'} e^{i2\pi(s-s')\rho \cos(\phi-\theta)} ds', \tag{12}$$

we can have

$$\begin{aligned}
 H_\theta^1 \tilde{f}_{x_0}(s) &= i2\pi \int_0^\pi \int_{\Re} \operatorname{sgn}(\rho) \rho^2 (\phi \cdot \theta) P(\phi, \rho) \\
 &\quad \times K_p(\theta, s, \phi, \rho) e^{i2\pi \rho x_0 \cdot \phi} d\rho d\phi. \tag{13}
 \end{aligned}$$

On the other hand, we have

$$\begin{aligned}
 K_p(\theta, s, \phi, \rho) &= e^{i2\pi s \rho \cos(\phi-\theta)} \int_{\Re} \frac{1}{\pi s'} e^{-i2\pi s' \rho \cos(\phi-\theta)} ds' \\
 &= -i2e^{i2\pi s \rho \cos(\phi-\theta)} \int_{\Re^+} \frac{\sin(2\pi s' \rho \cos(\phi-\theta))}{\pi s'} ds' \\
 &= -i \frac{2}{\pi} e^{i2\pi s \rho \cos(\phi-\theta)} \operatorname{sgn}(\rho \cos(\phi-\theta)) \int_{\Re^+} \frac{1}{\lambda} \sin \lambda d\lambda \\
 &= -ie^{i2\pi s \rho \cos(\phi-\theta)} \operatorname{sgn}(\rho \cos(\phi-\theta)). \tag{14}
 \end{aligned}$$

So, we arrive at

$$\begin{aligned}
 H_\theta^1 \tilde{f}_{x_0}(s) &= -2\pi \int_0^\pi \int_{\Re} \operatorname{sgn}(\rho) (i\rho)^2 (\phi \cdot \theta) P(\phi, \rho) \\
 &\quad \times e^{i2\pi \rho(s \cos(\phi-\theta) + x_0 \cdot \phi)} \operatorname{sgn}(\rho \cos(\phi-\theta)) d\rho d\phi
 \end{aligned}$$

$$\begin{aligned}
 &= -2\pi \int_0^\pi \int_{\Re} \operatorname{sgn}(\rho) (i\rho)^2 P(\phi, \rho) \\
 &\quad \times e^{i2\pi \rho(s \cos(\phi-\theta) + x_0 \cdot \phi)} \operatorname{sgn}(\rho) d\rho |\cos(\phi-\theta)| d\phi \\
 &= -2\pi \int_0^\pi \int_{\Re} (i\rho)^2 P(\phi, \rho) \\
 &\quad \times e^{i2\pi \rho(s \cos(\phi-\theta) + x_0 \cdot \phi)} d\rho |\cos(\phi-\theta)| d\phi, \tag{15}
 \end{aligned}$$

where

$$\begin{aligned}
 &\int_{\Re} (i\rho)^2 P(\phi, \rho) e^{i2\pi \rho(s \cos(\phi-\theta) + x_0 \cdot \phi)} d\rho \\
 &= \frac{1}{4\pi^2} p''(\phi, s \cos(\phi-\theta) + x_0 \cdot \phi). \tag{16}
 \end{aligned}$$

Then, the DBP formula of the derivative object function along the radial direction in the parallel-beam geometry becomes

$$\begin{aligned}
 H_\theta^1 \tilde{f}_{x_0}(s) &= -\frac{1}{2\pi} \int_0^\pi p''(\phi, (s \cos(\phi-\theta) \\
 &\quad + x_0 \cdot \phi)) |\cos(\phi-\theta)| d\phi. \tag{17}
 \end{aligned}$$

In practice, the DBP algorithm to reconstruct the derivative object function along the radial direction in the fan-beam geometry is needed. Since $p''(\phi + \pi, r) = p''(\phi, -r)$ holds in general, we can rewrite Eq. (17) in the case of a full (2π) scan as

$$\begin{aligned}
 H_\theta^1 \tilde{f}_{x_0}(s) &= -\frac{1}{4\pi} \int_0^{2\pi} p''(\phi, (s \cos(\phi-\theta) \\
 &\quad + x_0 \cdot \phi)) |\cos(\phi-\theta)| d\phi, \tag{18}
 \end{aligned}$$

and then

$$\begin{aligned}
 H_\theta^1 \tilde{f}_{x_0}(s) &= -\frac{1}{4\pi} \int_0^{2\pi} \int_{\Re} p(\phi, r') \delta''(s \cos(\phi-\theta) \\
 &\quad + x_0 \cdot \phi - r') |\cos(\phi-\theta)| dr' d\phi. \tag{19}
 \end{aligned}$$

Letting $\bar{p}(\xi, u)$ denote projection in the equidistant fan-beam geometry (ξ, u) , there exist the relationships

$$\phi = \xi + \arctan(u/D), \quad r = R_0 u / \sqrt{D^2 + u^2}, \tag{20}$$

$$\xi = \phi - \arctan\left(r / \sqrt{R_0^2 - r^2}\right), \quad u = D r / \sqrt{R_0^2 - r^2}, \tag{21}$$

$$p(\phi, r) = \bar{p}(\xi, u), \tag{22}$$

and the Jacobean

$$\begin{aligned} drd\phi &= \begin{vmatrix} \partial r/\partial u & \partial r/\partial \xi \\ \partial \phi/\partial u & \partial \phi/\partial \xi \end{vmatrix} dud\xi = \begin{vmatrix} \partial r/\partial u & 0 \\ \partial \phi/\partial u & 1 \end{vmatrix} dud\xi \\ &= |\partial r/\partial u| dud\xi = \frac{R_0 D^2}{(\sqrt{D^2 + u^2})^3} dud\xi. \end{aligned} \quad (23)$$

Here D and R_0 are the distances from x-ray source to the detector and the rotation axis, respectively. By denoting $s\theta + \mathbf{x}_0$

with \mathbf{x} , the integral kernel in Eq. (19) becomes $\delta''(s\cos(\phi - \theta) + \mathbf{x}_0 \cdot \boldsymbol{\phi} - r') = \delta''(\mathbf{x} \cdot \boldsymbol{\phi} - r')$. Furthermore, according to the Appendix, we have

$$\delta''(\mathbf{x} \cdot \boldsymbol{\phi} - r') = \delta''(u^* - u)(\sqrt{D^2 + u^2})^3 / T^3, \quad (24)$$

where $T = R_0 - \mathbf{x} \cdot \boldsymbol{\xi}^\perp$, $u^* = D\mathbf{x} \cdot \boldsymbol{\xi}/T$.

In a way similar to that in Ref. 31 the DBP algorithm to reconstruct the derivative object function along the radial direction in the equidistant fan-beam geometry can be obtained

$$\begin{aligned} H_\theta^1 \tilde{f}_{x_0}(s) &= -\frac{1}{4\pi} \int_0^{2\pi} \frac{R_0 D^2}{T^3} \int_{\Re} \bar{p}(\xi, u) \cos(\phi - \theta) \delta''(u^* - u) \operatorname{sgn}(\cos(\phi - \theta)) dud\xi \\ &= -\frac{1}{4\pi} \int_0^{2\pi} \frac{R_0 D^2}{T^3} \frac{\partial^2}{\partial u^2} (\bar{p}(\xi, u) \cos(\phi - \theta) \operatorname{sgn}(\cos(\phi - \theta))) \Big|_{u=u^*} d\xi \\ &= -\frac{1}{4\pi} \int_0^{2\pi} \frac{R_0 D^2}{T^3} \frac{\partial^2}{\partial u^2} (\bar{p}(\xi, u) \cos(\phi - \theta) \operatorname{sgn}(\cos(\phi - \theta))) \Big|_{u=u^*} d\xi \\ &\quad - \frac{1}{2\pi} \int_0^{2\pi} \frac{R_0 D^2}{T^3} \frac{\partial}{\partial u} (\bar{p}(\xi, u) \cos(\phi - \theta)) \frac{\partial}{\partial u} (\operatorname{sgn}(\cos(\phi - \theta))) \Big|_{u=u^*} d\xi \\ &\quad - \frac{1}{4\pi} \int_0^{2\pi} \frac{R_0 D^2}{T^3} \bar{p}(\xi, u) \cos(\phi - \theta) \frac{\partial^2}{\partial u^2} (\operatorname{sgn}(\cos(\phi - \theta))) \Big|_{u=u^*} d\xi \\ &= -\frac{1}{4\pi} \int_0^{2\pi} \frac{R_0 D^2}{T^3} \frac{\partial^2}{\partial u^2} (\bar{p}(\xi, u) \cos(\phi - \theta) \operatorname{sgn}(\cos(\phi - \theta))) \Big|_{u=u^*} d\xi + r_1 + r_2. \end{aligned} \quad (25)$$

In fact, we have

$$\begin{aligned} r_1 &= -\frac{1}{2\pi} \int_0^{2\pi} \frac{R_0 D^2}{T^3} \frac{\partial}{\partial u} (\bar{p}(\xi, u) \cos(\phi - \theta)) \frac{\partial}{\partial u} (\operatorname{sgn}(\cos(\phi - \theta))) \Big|_{u=u^*} d\xi \\ &= \frac{1}{2\pi} \int_0^{2\pi} \frac{R_0 D^2}{T^3} \frac{\partial}{\partial u} (\bar{p}(\xi, u) \cos(\phi - \theta)) \times 2\delta(\cos(\phi - \theta)) \sin(\phi - \theta) \frac{D}{D^2 + u^2} \Big|_{u=u^*} d\xi \\ &= \frac{1}{\pi} \int_0^{2\pi} \frac{R_0 D^2}{T^3} \frac{\partial}{\partial u} \bar{p}(\xi, u) \Big|_{u=u^*} \cos(\phi^* - \theta) \delta(\cos(\phi^* - \theta)) \sin(\phi^* - \theta) \frac{D}{D^2 + u^{*2}} d\xi \\ &\quad - \frac{1}{\pi} \int_0^{2\pi} \frac{R_0 D^2}{T^3} \bar{p}(\xi, u^*) \delta(\cos(\phi^* - \theta)) \sin^2(\phi^* - \theta) \frac{D^2}{(D^2 + u^{*2})^2} d\xi \\ &= -\frac{1}{\pi} \int_0^{2\pi} \frac{R_0 D^4}{T^3 (D^2 + u^{*2})^2} \bar{p}(\xi, u^*) \delta(\cos(\phi^* - \theta)) \sin^2(\phi^* - \theta) d\xi, \end{aligned} \quad (26)$$

where $\phi^* = \xi + \arctan \frac{u^*}{D}$. By referring to Eq. (A5), we can further have

$$r_1 = -\frac{1}{\pi} \sum_{i=1}^2 \frac{D^2}{T_i^2(D^2 + u_i^{*2})} \bar{p}(\xi_i, u_i^*) = -\frac{1}{\pi} \sum_{i=1}^2 \frac{\bar{p}(\xi_i, u_i^*)}{\|x - v_i\|^2}, \quad (27)$$

where $v_i = R_0 \xi_i^\perp$, $i = 1, 2$. Meanwhile, we have

$$\begin{aligned} r_2 &= -\frac{1}{4\pi} \int_0^{2\pi} \frac{R_0 D^2}{T^3} \bar{p}(\xi, u) \cos(\phi - \theta) \frac{\partial^2}{\partial u^2} (\text{sgn}(\cos(\phi - \theta))) \Big|_{u=u^*} d\xi \\ &= -\frac{1}{4\pi} \int_0^{2\pi} \frac{R_0 D^2}{T^3} \bar{p}(\xi, u) \cos(\phi - \theta) \frac{\partial}{\partial u} \left(-2\delta(\cos(\phi - \theta)) \sin(\phi - \theta) \frac{D}{D^2 + u^2} \right) \Big|_{u=u^*} d\xi \\ &= -\frac{1}{2\pi} \int_0^{2\pi} \frac{R_0 D^2}{T^3} \bar{p}(\xi, u^*) \cos(\phi^* - \theta) \left(\delta'(\cos(\phi^* - \theta)) \sin^2(\phi^* - \theta) \frac{D^2}{(D^2 + u^{*2})^2} \right. \\ &\quad \left. - \delta(\cos(\phi^* - \theta)) \cos(\phi^* - \theta) \frac{D^2}{(D^2 + u^{*2})^2} + \delta(\cos(\phi^* - \theta)) \sin(\phi^* - \theta) \frac{2Du^*}{(D^2 + u^{*2})^2} \right) d\xi \\ &= -\frac{1}{2\pi} \int_0^{2\pi} \frac{R_0 D^4}{T^3(D^2 + u^{*2})^2} \bar{p}(\xi, u^*) \cos(\phi^* - \theta) \delta'(\cos(\phi^* - \theta)) \sin^2(\phi^* - \theta) d\xi. \end{aligned} \quad (28)$$

By referring to Eq. (A6), we obtain

$$r_2 = -\frac{1}{2\pi} \sum_{i=1}^2 \frac{1}{R_0 T_i} \bar{p}(\xi_i, u_i^*) \left(1 + \frac{D}{D^2 + u^{*2}} \frac{du^*}{d\xi} \right) \Big|_{\xi=\xi_i}, \quad (29)$$

where

$$\frac{du^*}{d\xi} = \frac{DR_0}{T} - \frac{D^2 + u^{*2}}{D}. \quad (30)$$

Subsequently, we have

$$\begin{aligned} r_2 &= -\frac{1}{2\pi} \sum_{i=1}^2 \frac{1}{R_0 T_i} \bar{p}(\xi_i, u_i^*) \left(1 + \frac{D}{D^2 + u^{*2}} \left(\frac{DR_0}{T} - \frac{D^2 + u^{*2}}{D} \right) \right) \Big|_{\xi=\xi_i} \\ &= -\frac{1}{2\pi} \sum_{i=1}^2 \frac{D^2}{T_i^2(D^2 + u_i^{*2})} \bar{p}(\xi_i, u_i^*) = -\frac{1}{2\pi} \sum_{i=1}^2 \frac{\bar{p}(\xi_i, u_i^*)}{\|x - v_i\|^2}. \end{aligned} \quad (31)$$

By integrating Eqs. (27) and (31) into Eq. (25), we obtain the following DBP formula of the derivative object function along the radial direction in the equidistant fan-beam geometry,

$$\begin{aligned} H_\theta^1 \tilde{f}_{x_0}(s) &= -\frac{1}{4\pi} \int_0^{2\pi} \frac{R_0 D^2}{T^3} \text{sgn}(\cos(\phi - \theta)) \frac{\partial^2}{\partial u^2} (\bar{p}(\xi, u) \cos(\phi - \theta)) \Big|_{u=u^*} d\xi \\ &\quad - \frac{3}{2\pi} \sum_{i=1}^2 \frac{\bar{p}(\xi_i, u_i^*)}{\|x - v_i\|^2}. \end{aligned} \quad (32)$$

Letting $\hat{p}(\xi, \gamma)$ denote projection in the equiangular fan-beam geometry (ξ, γ) , there exist the relationships

$$\phi = \xi + \gamma, \quad r = R_0 \sin \gamma, \quad (33)$$

$$\xi = \phi - \gamma, \quad \gamma = \arcsin(r / R_0), \quad (34)$$

$$p(\phi, r) = \hat{p}(\xi, \gamma), \quad (35)$$

where R_0 is the distances from x-ray source to the rotation axis. Meanwhile, between the equiangular and equidistant fan-beam geometries, there exist

$$u = D \tan \gamma, \quad \bar{p}(\xi, u) = \hat{p}(\xi, \gamma), \quad (36)$$

and

$$\begin{aligned} \partial/\partial u &= (\cos^2 \gamma/D) \partial/\partial \gamma, \\ \partial^2/\partial u^2 &= (\cos^4 \gamma/D^2) (\partial^2/\partial \gamma^2 - 2 \tan \gamma \partial/\partial \gamma). \end{aligned} \quad (37)$$

In a similar way, the DBP algorithm to reconstruct the derivative object function along the radial direction in the equiangular fan-beam geometry can be obtained,

$$\begin{aligned} H_\theta^1 \tilde{f}_{x_0}(s) &= -\frac{1}{4\pi} \int_0^{2\pi} \frac{R_0 \cos^4 \gamma^*}{T^3} \operatorname{sgn}(\cos(\phi - \theta)) \\ &\quad \times \left(\frac{\partial^2}{\partial \gamma^2} - 2 \tan \gamma \frac{\partial}{\partial \gamma} \right) (\hat{p}(\xi, \gamma) \\ &\quad \times \cos(\phi - \theta))|_{\gamma=\gamma^*} d\xi \\ &\quad - \frac{3}{2\pi} \sum_{i=1}^2 \frac{\hat{p}(\xi_i, \gamma_i^*)}{\|x - v_i\|^2}, \end{aligned} \quad (38)$$

where $\gamma_i^* = \arctan(\mathbf{x}_i \cdot \boldsymbol{\xi}_i/T_i)$, $T_i = R_0 - \mathbf{x} \cdot \boldsymbol{\xi}_i^\perp$, $i = 1, 2$, and $\xi_1 = \theta - \pi/2 + \arcsin(\mathbf{x}_0 \cdot \boldsymbol{\theta}^\perp/R_0)$, $\xi_2 = 2\theta - \xi_1$. The above DBP formula will be used to demonstrate the feasibility of the proposed imaging method of radial differential interior tomography.

2.B. Projection of differentiated backprojection onto convex sets (DBP-POCS)

It should be noted that the right side of both Eqs. (32) and (38) represent the radial Hilbert transform of the derivative object function $\partial_1 \tilde{f}_{x_0}(s, \theta)$. Moreover, it is important to note that the Hilbert transform is not mathematically local.^{31,32} Hence, the reconstruction of the derivative object function $\partial_1 \tilde{f}_{x_0}(s, \theta)$ inside an ROI using either Eq. (32) or Eq. (38) becomes an interior tomography problem that can be dealt with using the DBP-POCS based methods.¹⁸⁻²³ Hereafter, the dependence on x_0 and θ will be omitted for brevity. The implementation of a DBP-POCS based method is carried out along each Hilbert line associated with a local coordinate system,¹⁸⁻²³ and thus the derivative object function

$\partial_1 \tilde{f}(s)$ can be viewed as a 1D function of variable s with a definition domain of normalized interval $(-1, 1)$. On each Hilbert line, Λ_K , Λ_H , Λ , and X represent the intervals with the *a priori* knowledge $\partial_1 \tilde{f}^{(p)}(s) = 0$, the DBP values that can be calculated from Eq. (38), the compact support of the object function $\partial_1 \tilde{f}(s)$, and the entire interval wherein the DBP-POCS based method is implemented.¹⁸⁻²³ For the case considered in this paper, there is a relationship among these intervals: $\Lambda_H \subseteq X$, $\Lambda_K \subseteq \Lambda \subseteq X = (-1, 1)$. $L_W^2(X)$ represents a weighted L^2 space with $W(s) = (1 - s^2)^{0.5}$, and the associated inner product and norm are defined by

$$\begin{aligned} (\partial_1 \tilde{f}_1, \partial_1 \tilde{f}_2)_W &= \int_{-1}^1 ds \partial_1 \tilde{f}_1(s) \partial_1 \tilde{f}_2(s) W(s), \\ \|\partial_1 \tilde{f}\|_W^2 &= (\partial_1 \tilde{f}, \partial_1 \tilde{f})_W. \end{aligned} \quad (39)$$

To implement the DBP-POCS based method, four convex sets are defined¹⁸⁻²³

$$\begin{aligned} C_1 &= \{\partial_1 \tilde{f} \in L_W^2(X) | (H_X \partial_1 \tilde{f})(s) = g(s) \text{ for } s \in \Lambda_H\}, \\ (H_X \partial_1 \tilde{f})(s) &= \frac{1}{\pi} p.v. \int_{-1}^1 ds \frac{1}{s - s'} \partial_1 \tilde{f}(s'); \\ C_2 &= \{\partial_1 \tilde{f} \in L_W^2(X) | \partial_1 \tilde{f}(s) = 0 \text{ for } s \notin \Lambda\}; \\ C_3 &= \{\partial_1 \tilde{f} \in L_W^2(X) | \partial_1 \tilde{f}(s) = \partial_1 \tilde{f}^{(p)}(s) = 0 \text{ for } s \in \Lambda_K\}; \\ C_4 &= \left\{ \partial_1 \tilde{f} \in L_W^2(X) \left| \int_{\Lambda \setminus \Lambda_K} ds \partial_1 \tilde{f}(s) = C_\Lambda^{(p)} \right. \right\}, \\ C_\Lambda^{(p)} &= \pi C_\Lambda - \int_{\Lambda_K} ds \partial_1 \tilde{f}^{(p)}(s) = \pi C_\Lambda; \end{aligned} \quad (40)$$

where πC_Λ is equal to the ideal projection data of the derivative object function acquired along the Hilbert line. In the equiangular fan-beam geometry, we have

$$\begin{aligned} C_\Lambda &= \frac{1}{\pi} \int_{\Lambda} \partial_1 \tilde{f}_{x_0}(s, \theta) ds = \frac{1}{\pi} \int_{\Lambda} \frac{\partial}{\partial s} f(s\boldsymbol{\theta} + \mathbf{x}_0) ds \\ &= \frac{1}{\pi} f(s\boldsymbol{\theta} + \mathbf{x}_0)|_{-\infty}^{+\infty} \equiv 0, \end{aligned} \quad (41)$$

and then $C_\Lambda^{(p)} = 0$.

Projection operator P_i corresponding to each convex set C_i is required to implement the DBP-POCS based algorithm.^{18,19} Projectors P_2 and P_3 are trivial, and P_1 and P_4 are specified as^{18,19}

$$(P_1 \partial_1 \tilde{f})(s) = \left(\frac{1}{\pi} \frac{1}{W(s)} \int_{-1}^1 ds' \partial_1 \tilde{f}(s') \right) + (H_X^+ M H_X \partial_1 \tilde{f})(s),$$

$$(H_X^+ h)(s) = \frac{1}{\pi} \frac{1}{W(s)} p.v. \int_{-1}^1 ds' \frac{1}{s' - s} h(s') W(s'),$$

$$(Mh)(s) = \begin{cases} g(s) & (s \in \Lambda_H), \\ h(s) & (s \notin \Lambda_H); \end{cases}$$

$$(P_4 \partial_1 \tilde{f})(s) = \begin{cases} \partial_1 \tilde{f}(s) + \frac{\left(C_{\Lambda}^{(p)} - \int_{\Lambda \setminus \Lambda_K} ds' \partial_1 \tilde{f}(s') \right) / W(s)}{\int_{\Lambda \setminus \Lambda_K} ds' / W(s')} & (s \in \Lambda \setminus \Lambda_K) \\ \partial_1 \tilde{f}(s) & (s \notin \Lambda \setminus \Lambda_K). \end{cases}$$

$$= \begin{cases} \partial_1 \tilde{f}(s) - \frac{\int_{\Lambda \setminus \Lambda_K} ds' \partial_1 \tilde{f}(s') / W(s)}{\int_{\Lambda \setminus \Lambda_K} ds' / W(s')} & (s \in \Lambda \setminus \Lambda_K), \\ \partial_1 \tilde{f}(s) & (s \notin \Lambda \setminus \Lambda_K). \end{cases} \quad (42)$$

To determine the derivative object function $\partial_1 \tilde{f}(s)$ that falls into the intersection of the four convex sets defined in Eq. (40), the following iterative algorithm is utilized,

$$\partial_1 \tilde{f}^{(k+1)} = P_4 P_3 P_2 P_1 \partial_1 \tilde{f}^{(k)}, \quad k = 0, 1, \dots, K-1, K, \quad (43)$$

where $\partial_1 \tilde{f}^{(0)}$ is the initial image with each pixel set to zero. In this work, the maximal iteration number K is empirically set as 100, since no improvement is noticeable after the 100th iteration.

3. PERFORMANCE EVALUATION

The proposed imaging method of radial differential interior tomography and its reconstruction algorithm are evaluated using the projection data simulated by computer and acquired by CT scanner.

3.A. Evaluation with projection data simulated by computer

The modified Shepp-Logan mathematical phantom³³ is used to simulate the projection data in the equiangular fan-beam geometry,³⁴ in which the distance from the x-ray source to the rotation axis (R_0) is 541 mm. The projection data are uniformly acquired in a full scan (360°) at 1160 angular positions, with a detector array consisting of 888 cells that span a 52.1° full fan-angle. The interior tomography is simulated by setting the radius of the ROI to be scanned as 40.5 mm and truncating the projection data appropriately with lateral collimation. The origin x_0 of the local polar coordinate system is fixed at (0, 0) mm. In such a way, the *a priori* knowledge of the Shepp-Logan phantom can be determined as 0.3. Transaxial tomographic images are initially reconstructed in the polar coordinate system at dimension 2,048 × 2,048, i.e., 2048 sampling points along the azimuthal direction (360°) and radial direction (a distance of 128 mm from the origin x_0), and then converted into a 512 × 512 matrix with pixel size 0.5664 × 0.5664 mm² in the Cartesian coordinate system. An air-filled cavity in the sheep's body (the bronchus with its attenuation approximately equal to zero, centered at origin x_0 , and with a radius of ten sampling points along the radial direction) is chosen as the small round area wherein the *a priori* knowledge is required.

3.B. Evaluation with projection data acquired by CT scanner

The performance of the proposed imaging method and its reconstruction algorithm is further evaluated and verified using the projection data of a large animal (sheep) acquired by a CT scanner. In data acquisition, the distance from x-ray source to the rotation axis is 570 mm. The projection data are also uniformly acquired at 1160 angular positions over a full scan (360°). The detector array consists of 672 cells spanning a 52.1° full fan-angle. Truncated projection data are acquired by setting the radius of the ROI to be scanned as 50 mm. Again, transaxial tomographic images are initially reconstructed in the polar coordinate system at dimension 2,048 × 2,048, i.e., 2048 sampling points along the azimuthal direction (360°) and radial direction (a distance of 128 mm from the origin x_0), and then converted into a 512 × 512 matrix with pixel size 0.5664 × 0.5664 mm² in the Cartesian coordinate system. An air-filled cavity in the sheep's body (the bronchus with its attenuation approximately equal to zero, centered at origin x_0 , and with a radius of ten sampling points along the radial direction) is chosen as the small round area wherein the *a priori* knowledge is required.

4. RESULTS

The simulation study focuses on the evaluation of reconstruction accuracy, while the animal study verifies the performance in the presence of noise in a practical situation.

4.A. Performance evaluation–phantom study

The modified Shepp-Logan phantom³³ is utilized as the basis for performance evaluation. Shown in Fig. 1(a) is the sinogram of the modified Shepp-Logan phantom simulated in the equiangular fan-beam geometry, in which no lateral truncation occurs. The transaxial image reconstructed from the sinogram by the FBP algorithm is presented in Fig. 1(b).

The transaxial images displayed in the upper row of Fig. 2 are obtained from the projection data with lateral truncation, while those from the data without truncation are presented in the lower row as a reference. The images shown in Figs. 2(a) and 2(a') are reconstructed using the DBP-POCS algorithm²³ and those in Figs. 2(c) and 2(c') are reconstructed using the radial differential DBP-POCS

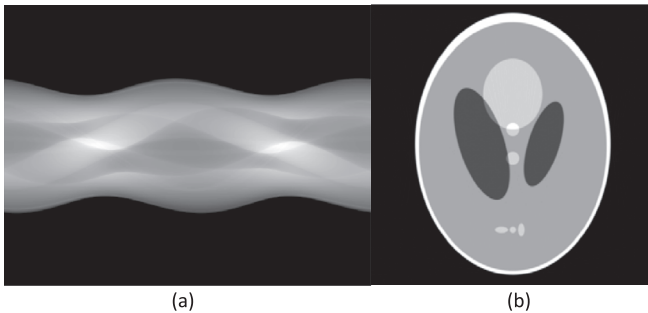


FIG. 1. (a) The sinogram of the modified Shepp-Logan phantom; and (b) a transaxial image reconstructed from the sinogram [display window ($0\text{--}0.5$) mm^{-1}].

algorithm proposed in this work. For comparison, the images obtained by applying a postreconstruction radial differentiation on the image reconstructed by the DBP-POCS algorithm, i.e., the two-step radial differential tomography, are presented in Figs. 2(b) and 2(b'). Meanwhile, the numerical radial derivative of the Shepp-Logan phantom obtained via one-dimensional radial differential filtering with adequate windowing in the frequency domain is included in Figs. 2(d) and 2(d') as the ground truth for comparison. As demonstrated in the areas indicated by the dotted and solid arrows in Figs. 2(a) and 2(c), the proposed radial differential DBP-POCS algorithm outperforms the DBP-POCS algorithm in reconstruction accuracy. We speculate that such an advantage may be attributed to the fact that the *a priori* knowledge required by the proposed radial differential DBP-POCS reconstruction is always zero, rather than a constant as required in

the DBP-POCS reconstruction. Moreover, it is observed that the artifact existing in the image reconstructed by the DBP-POCS algorithm is picked up by the postreconstruction radial differentiation [see Fig. 2(b)].

For quantitative evaluation, the profiles along the central horizontal and vertical lines of the images obtained by the postreconstruction radial differentiation [Figs. 2(b) and 2(b')] and the proposed radial differential DBP-POCS algorithm [Figs. 2(c) and 2(c')] are plotted in Fig. 3. The RMSE (root mean square error) between Figs. 2(b) and 2(d) and Figs. 2(c) and 2(d) are 0.0242 and 0.0173, respectively, showing that the proposed radial differential interior tomography method indeed outperforms the two-step method significantly (almost 40%) in artifact avoidance.

4.B. Performance evaluation–animal study

The transaxial images presented in the left column of Fig. 4 are obtained from the projection data without lateral truncation, while those from the data with truncation are presented in the right column. The images shown in the top row [display window ($0\text{--}0.5$) mm^{-1}] of Fig. 4 are reconstructed using the DBP-POCS algorithm²³ and those in the bottom row [display window ($-0.02\text{--}0.02$) mm^{-2}] are reconstructed using the radial differential DBP-POCS algorithm proposed in this work. For comparison, the images generated by the two-path method are presented in the middle row. A close inspection of Fig. 4(b') shows that edges of the sheep's tissues/organs in the ROI are enhanced significantly, verifying that the proposed radial differential interior tomography

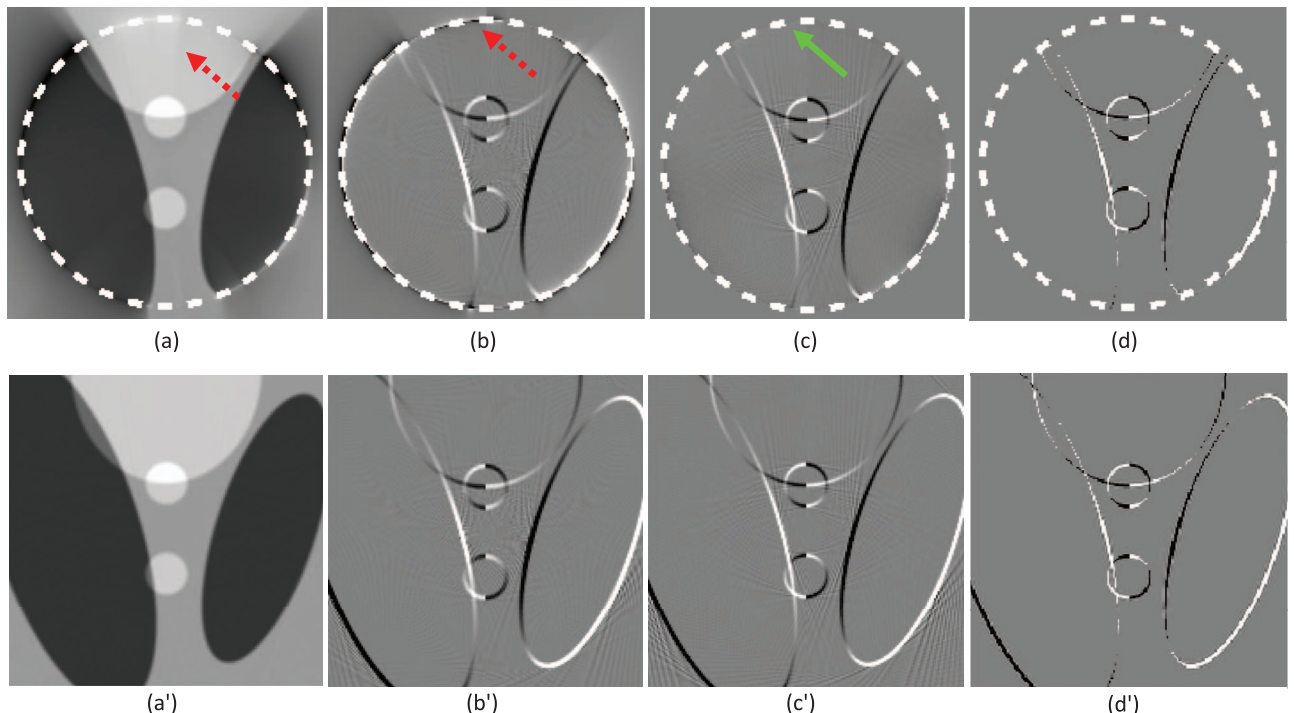


FIG. 2. Transaxial images of the Shepp-Logan phantom reconstructed from the projection data with (top) and without (bottom) lateral truncation using: (a-a') the DBP-POCS algorithm, (b-b') a postreconstruction radial differentiation algorithm, (c-c') the radial differential DBP-POCS algorithm, and (d-d') numerical derivative of the Shepp-Logan phantom [display window: ($-0.1\text{--}0.1$) mm^{-1} in (a-a'), and ($-0.1\text{--}0.1$) mm^{-2} in (b-b'), (c-c'), and (d-d')].

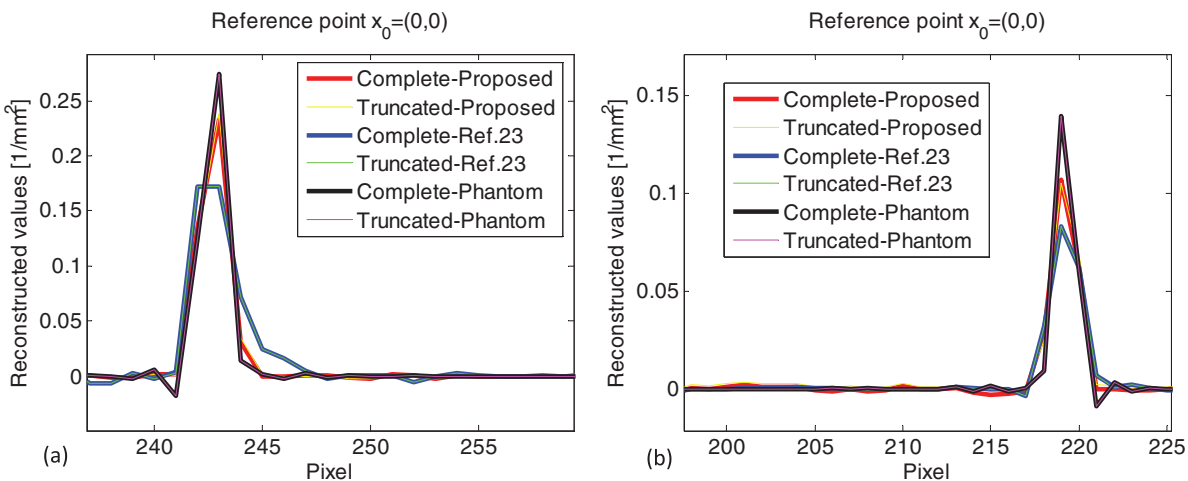


FIG. 3. Profiles along the horizontal (left) and vertical (right) lines of the central areas in the images displayed in Figs. 2(b)–2(b'), 2(c)–2(c'), and 2(d)–2(d').

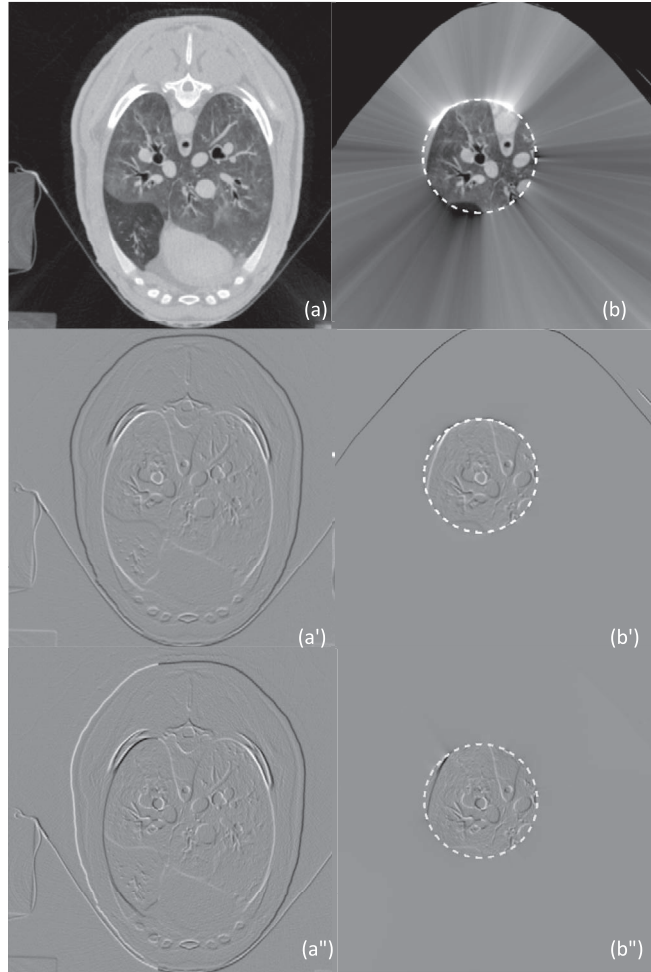


FIG. 4. Transaxial images of the sheep reconstructed from the projection data without (left) and with (right) lateral truncation: (a-a'') using the DBP-POCS algorithm, (a'-b') the postreconstruction radial differentiation algorithm, and (a''-b'') the proposed radial differential DBP-POCS algorithm [display window: (0 0.5) mm^{-1} in (a-a'') and (-0.02 0.02) mm^{-2} in (a'-b') and (a''-b'')].

and its associated reconstruction algorithm indeed can provide information complementary to the original reconstruction. Meanwhile, it also shows that the proposed radial differential interior tomography and its image reconstruction perform well in the presence of noise. For quantitative evaluation, the profiles along the central horizontal and vertical lines of the images obtained by the proposed radial differential DBP-POCS algorithm [Figs. 4(a')–4(b')] are plotted in Fig. 5.

5. DISCUSSIONS AND CONCLUSIONS

In this work, we propose the imaging method of radial differential interior tomography and derive the associated image reconstruction algorithm. Using the projection data of the phantom simulated by computer and a large animal (sheep) acquired by a CT scanner, we evaluate and verify its imaging performance. The results of the preliminary phantom study demonstrate the reconstruction accuracy of the proposed radial differential interior tomography, while the animal study data show its robustness in the presence of noise. What follows is a summary of the points we would like to make based on the preliminary results.

It is important for us to point out that the radial differential interior tomography proposed in this work is essentially different from the so-called Lambda tomography.^{35–40} In general, the Lambda tomography is under the framework of local tomography, in which the algorithm for image reconstruction is in the fashion of FBP. Specifically, in the Lambda tomography, the projection data undergo a 2nd-order differentiation that is mathematically local and then are backprojected to form a tomographic image. As such, the two-dimensional Fourier transform of the Lambda tomographic image is equal to that of the conventional tomographic image with a radial ramp filtering.^{35–38} It should be noted that a ramp filtered conventional tomographic image is actually equivalent

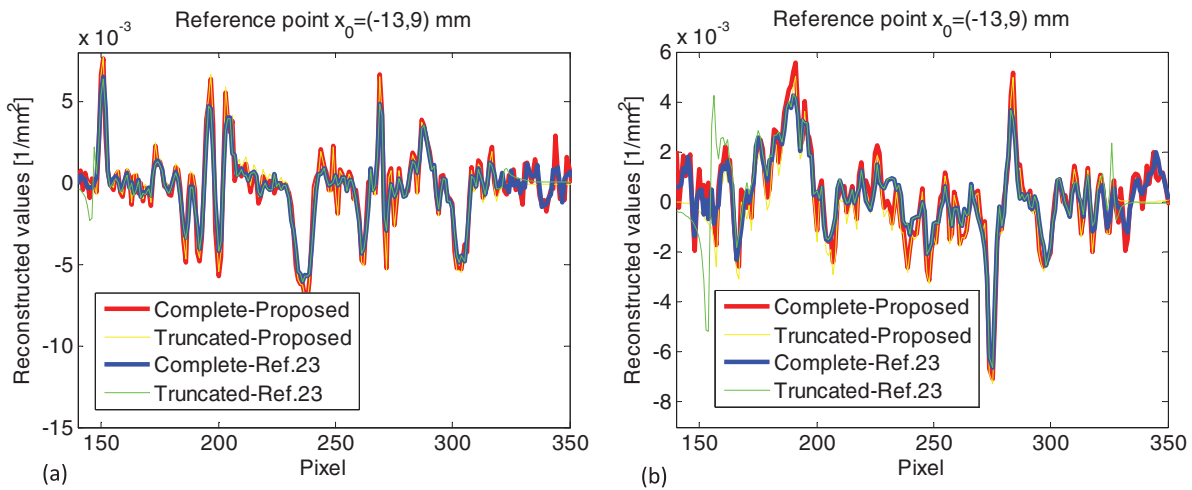


FIG. 5. Profiles along the central horizontal (left) and vertical (right) lines of Figs. 4(a')–4(b') and 4(a'')–4(b'').

to an Hilbert transform of the differentiated conventional tomographic image.³² It should also be noted that another local tomography image reconstruction algorithm called local BPF algorithm³⁹ has been proposed in the literature, in which the projection data go through a 1st-order differentiation, back-projection onto chords and then another 1st-order differentiation along the chords. It should be pointed out that such a tomographic image is actually equivalent to a Hilbert transform of the differentiated conventional tomographic image^{31,32} too.

On the other hand, the image generated by the radial differential interior tomography proposed in this work is a version of the conventional tomographic image with a radial differential filtering carried out in the image domain, rather than a version with a Hilbert transform applied. Hence, the proposed imaging method is under the framework of interior tomography. This is the underlying reason why either the POCS method,^{18–23} which is adopted in this work, or the TV-minimization based compressed sensing method,^{16,17} has to be employed. It is our opinion that, from the practical point of view of image processing, visualization, fusion, and understanding, a differentiated conventional tomographic image should be more meaningful than its counterpart with a Hilbert transform applied.

In the DBP-POCS based image reconstruction solution for the interior tomography, *a priori* knowledge in a small area inside the ROI to be reconstructed is required. The *a priori* knowledge can be available in a small area that is relatively uniform in attenuation, such as air-filled cavities (sinus) or fluid-filled compartments (ventricles). In the proposed radial differential interior tomography, the reconstructed image is a version of the object function with a radial differential operation. Consequently, the required *a priori* knowledge becomes zero if the air-filled cavity or fluid-filled compartment, regardless of its attenuation, is still chosen as the small area to provide the *a priori* knowledge. We would like to indicate that, even though the *a priori* knowledge of zero does not differ from that of a nonzero value in principle, a zero *a*

priori knowledge may be more readily available in practical situations.

It is observed in our preliminary investigation that the proposed radial differential DBP-POCS algorithm is indeed more efficient than the DBP-POCS reconstruction with postreconstruction radial filtering. This is because the radial differential filtering in the former is actually carried out in the projection domain, whereas that in the latter is carried out postreconstruction, which results in additional computational overhead. It is also observed [see Figs. 2(a)–2(c)] that the radial differential DPB-POCS algorithm outperforms the DBP-POCS two-step reconstruction algorithm in terms of artifact avoidance. We think this may be attributed to the fact that the required *a priori* knowledge in the former is zero, whereas that in the latter is nonzero and thus is harder to obtain in practical situations.

Interior tomography has recently been recognized as one of the promising methods to reduce CT's radiation dose in diagnostic imaging without compromising image quality.^{16,40} It is straightforward to understand that, as demonstrated in Figs. 4(a') and 4(b'), a radial differential interior tomographic image may stand alone to reveal more details about the ROI in which pathophysiological lesions are suspected. Meanwhile, the radial differential interior tomographic image may provide extra information complementary to the interior tomographic image (see Fig. 4). It should be noted that such extra information may be of relevance in image analysis, e.g., contour outlining for area/volume measurement, edge detection for image segmentation and morphologic feature extraction for image registration. All these operations are of significance in the clinical applications wherein the CAD based on image processing, visualization, fusion, and understanding is desirable. Hence, it is hoped that the imaging method of radial differential interior tomography and its associated image reconstruction algorithm (i.e., the radial differential DPB-POCS algorithm) may find their applications in the future.

ACKNOWLEDGMENTS

This work is partially supported by the Telemedicine and Advanced Technology Research Center (TATRC) at the U.S. Army Medical Research and Material Command (USAMRMC), Fort Detrick, MD via the award under Contract No. W81XWH-12-1-0138 (PI: Xiangyang Tang), as well as by the US National Institutes of Health (NIH) through Grant No. 5P50CA128301. The animal CT dataset is originally acquired by Dr. Eric Hoffman, University of Iowa. The authors would like to extend their appreciation to Ms. Jessica Paulishen for her proof reading of this paper.

APPENDIX: PROPERTIES OF THE DIRAC FUNCTION USED IN ALGORITHM DERIVATION

Regarding the Dirac function,²⁴ one has

$$\delta^{(n)}(\lambda s) = \delta^{(n)}(s) / \lambda^{n+1}, \quad \lambda > 0, \quad n = 0, 1, 2, \dots, \quad (\text{A1})$$

where the n th order derivative of Dirac function, $\delta^{(n)}$, is homogeneous of degree $-(n+1)$.

In order to derive the DBP formula in the equidistant fan-beam geometry, we need to convert $\delta''(\mathbf{x} \cdot \boldsymbol{\phi} - r')$ into $\delta''(u^* - u)$ as shown below

$$\begin{aligned} \mathbf{x} \cdot \boldsymbol{\phi} - r' \\ &= x_1 \cos(\xi + \arctan(u/D)) + x_2 \sin(\xi + \arctan(u/D)) - r' \\ &= x_1 \cos \xi \cos(\arctan(u/D)) - x_1 \sin \xi \sin(\arctan(u/D)) \\ &\quad + x_2 \sin \xi \cos(\arctan(u/D)) + x_2 \cos \xi \sin(\arctan(u/D)) - r' \\ &= x_1 \cos \xi \frac{D}{\sqrt{D^2 + u^2}} - x_1 \sin \xi \frac{u}{\sqrt{D^2 + u^2}} + x_2 \sin \xi \frac{D}{\sqrt{D^2 + u^2}} + x_2 \cos \xi \frac{u}{\sqrt{D^2 + u^2}} - \frac{R_0 u}{\sqrt{D^2 + u^2}} \\ &= (x_1 \cos \xi + x_2 \sin \xi) \frac{D}{\sqrt{D^2 + u^2}} - (x_1 \sin \xi - x_2 \cos \xi + R_0) \frac{u}{\sqrt{D^2 + u^2}} \\ &= (u^* - u) \frac{T}{\sqrt{D^2 + u^2}}, \end{aligned}$$

where $T = R_0 - \mathbf{x} \cdot \boldsymbol{\xi}^\perp$, $u^* = D \mathbf{x} \cdot \boldsymbol{\xi} / T$. According to Eq. (A1), we have

$$\delta''(\mathbf{x} \cdot \boldsymbol{\phi} - r') = \delta''(u^* - u) (\sqrt{D^2 + u^2})^3 / T^3. \quad (\text{A2})$$

In the integral calculations, we have made use of the following properties of the Dirac function,

$$\int \delta(k(t)) g(t) dt = \int \delta(k(t)) \frac{g(t)}{|k'(t)|} dk(t) = \sum_{\substack{k(t)=0 \\ k'(t)\neq 0}} \frac{g(t)}{|k'(t)|}, \quad (\text{A3})$$

$$\begin{aligned} \int \delta'(k(t)) g(t) dt &= \int \delta'(k(t)) \frac{g(t)}{|k'(t)|} dk(t) = \int \delta'(\zeta) \frac{g(t(\zeta))}{|k'(t(\zeta))|} d\zeta \\ &= \sum_{\substack{k(t)=0 \\ k'(t)\neq 0}} \frac{d}{d\zeta} \left(\frac{g(t(\zeta))}{|k'(t(\zeta))|} \right) = \sum_{\substack{k(t)=0 \\ k'(t)\neq 0}} \frac{d}{dt} \left(\frac{g(t)}{|k'(t)|} \right) \frac{dt}{d\zeta} = \sum_{\substack{k(t)=0 \\ k'(t)\neq 0}} \frac{d}{dt} \left(\frac{g(t)}{|k'(t)|} \right) \frac{1}{k'(t)}. \end{aligned} \quad (\text{A4})$$

Especially, there exist

$$\begin{aligned} &\int_0^{2\pi} \Psi(\xi) \delta \left(\cos \left(\xi + \arctan \frac{u^*}{D} - \theta \right) \right) \sin \left(\xi + \arctan \frac{u^*}{D} - \theta \right) d\xi \\ &= \sum_{i=1}^2 \frac{\Psi(\xi_i) \sin \left(\xi_i + \arctan \frac{u_i^*}{D} - \theta \right)}{\left| \frac{d}{d\xi} \cos \left(\xi + \arctan \frac{u^*}{D} - \theta \right) \right|_{\xi=\xi_i}} = \sum_{i=1}^2 \frac{\Psi(\xi_i) \sin \left(\xi_i + \arctan \frac{u_i^*}{D} - \theta \right)}{\left| \sin \left(\xi_i + \arctan \frac{u_i^*}{D} - \theta \right) \right| \left| 1 + \frac{D}{D^2 + u^{*2}} \left(\frac{du^*}{d\xi} \right) \right|_{\xi=\xi_i}} \end{aligned}$$

$$\begin{aligned}
&= \sum_{i=1}^2 \frac{\Psi(\xi_i) \operatorname{sgn} \left(\sin \left(\xi_i + \arctan \frac{u_i^*}{D} - \theta \right) \right)}{\left| 1 + \frac{D}{D^2 + u^{*2}} \left(\frac{du^*}{d\xi} \right) \right|_{\xi=\xi_i}} = \sum_{i=1}^2 \frac{(-1)^i \Psi(\xi_i)}{\left| 1 + \frac{D}{D^2 + u^{*2}} \left(\frac{DR_0}{T} - \frac{D^2 + u^{*2}}{D} \right) \right|_{\xi=\xi_i}} \\
&= \sum_{i=1}^2 \frac{(-1)^i T_i (D^2 + u_i^{*2}) \Psi(\xi_i)}{D^2 R_0}, \tag{A5}
\end{aligned}$$

$$\begin{aligned}
&\int_0^{2\pi} \Psi(\xi) \delta' \left(\cos \left(\xi + \arctan \frac{u^*}{D} - \theta \right) \right) \sin \left(\xi + \arctan \frac{u^*}{D} - \theta \right) d\xi \\
&= \sum_{i=1}^2 \frac{d}{d\xi} \left(\frac{\Psi(\xi) \sin \left(\xi + \arctan \frac{u^*}{D} - \theta \right)}{\left| \frac{d}{d\xi} \cos \left(\xi + \arctan \frac{u^*}{D} - \theta \right) \right|} \right) \Bigg|_{\xi=\xi_i} \frac{1}{\frac{d}{d\xi} \cos \left(\xi + \arctan \frac{u^*}{D} - \theta \right)} \Bigg|_{\xi=\xi_i} \\
&= \sum_{i=1}^2 \frac{d}{d\xi} \left(\frac{\Psi(\xi) \sin \left(\xi + \arctan \frac{u^*}{D} - \theta \right)}{\left| \sin \left(\xi + \arctan \frac{u^*}{D} - \theta \right) \right| \left| 1 + \frac{D}{D^2 + u^{*2}} \left(\frac{du^*}{d\xi} \right) \right|} \right) \Bigg|_{\xi=\xi_i} \frac{1}{-\sin \left(\xi + \arctan \frac{u^*}{D} - \theta \right) \left(1 + \frac{D}{D^2 + u^{*2}} \left(\frac{du^*}{d\xi} \right) \right)} \Bigg|_{\xi=\xi_i} \\
&= \sum_{i=1}^2 \frac{d}{d\xi} \left(\frac{\Psi(\xi) \operatorname{sgn} \left(\sin \left(\xi + \arctan \frac{u^*}{D} - \theta \right) \right)}{\left| 1 + \frac{D}{D^2 + u^{*2}} \left(\frac{du^*}{d\xi} \right) \right|} \right) \Bigg|_{\xi=\xi_i} \frac{1}{-\sin \left(\xi + \arctan \frac{u^*}{D} - \theta \right) \left(1 + \frac{D}{D^2 + u^{*2}} \left(\frac{du^*}{d\xi} \right) \right)} \Bigg|_{\xi=\xi_i} \\
&= \sum_{i=1}^2 (-1)^i \frac{d}{d\xi} \left(\frac{\Psi(\xi)}{\left| 1 + \frac{D}{D^2 + u^{*2}} \left(\frac{DR_0}{T} - \frac{D^2 + u^{*2}}{D} \right) \right|} \right) \Bigg|_{\xi=\xi_i} \frac{1}{-\sin \left(\xi + \arctan \frac{u^*}{D} - \theta \right) \left(1 + \frac{D}{D^2 + u^{*2}} \left(\frac{DR_0}{T} - \frac{D^2 + u^{*2}}{D} \right) \right)} \Bigg|_{\xi=\xi_i} \\
&= \sum_{i=1}^2 \frac{(-1)^i}{D^4 R_0^2} \frac{d}{d\xi} (T(D^2 + u^{*2}) \Psi(\xi)) \Bigg|_{\xi=\xi_i} \frac{T_i (D^2 + u_i^{*2})}{-\sin \left(\xi_i + \tan^{-1} \frac{u_i^*}{D} - \theta \right)} \\
&= - \sum_{i=1}^2 \frac{T_i (D^2 + u_i^{*2})}{D^4 R_0^2} \frac{d}{d\xi} (T(D^2 + u^{*2}) \Psi(\xi)) \Bigg|_{\xi=\xi_i}, \tag{A6}
\end{aligned}$$

where

$$\begin{aligned}
\xi_1 &= \theta - \frac{\pi}{2} - \arctan(u_1^*/D) = \theta - \frac{\pi}{2} + \arcsin(\mathbf{x}_0 \cdot \boldsymbol{\theta}^\perp / R_0), \\
\xi_2 &= \theta + \frac{\pi}{2} - \arctan(u_2^*/D) = \theta + \frac{\pi}{2} - \arcsin(\mathbf{x}_0 \cdot \boldsymbol{\theta}^\perp / R_0), \\
u_i^* &= D\mathbf{x} \cdot \boldsymbol{\xi}_i / T_i, \quad T_i = R_0 - \mathbf{x} \cdot \boldsymbol{\xi}_i^\perp, \\
\sin(\xi_i + \arctan(u_i^*/D) - \theta) &= (-1)^i, \\
\cos(\xi_i + \arctan(u_i^*/D) - \theta) &= 0, \quad i = 1, 2. \tag{A7}
\end{aligned}$$

^aAuthor to whom correspondence should be addressed. Electronic mail: xiangyang.tang@emory.edu; Telephone: (404) 778-1732; Fax: (404) 712-5813.

¹F. R. Verdun, F. Bochud, F. Gudinchet, A. Aroua, P. Schnyder, and R. Meuli, "Radiation risk: What you should know to tell your patient," *Radiographics* **28**, 1807–1816 (2008).

²D. J. Brenner and E. J. Hall, "Computed tomography—An increasing source of radiation exposure," *N. Engl. J. Med.* **357**, 2277–2284 (2007).

³L. Yu, X. Liu, S. Leng, J. M. Kofler, J. C. Ramirez-Giraldo, M. Qu, J. Christner, J. G. Fletcher, and C. H. McCollough, "Radiation dose reduc-

tion in computed tomography: Techniques and future perspective," *Imaging Med.* **1**, 65–84 (2009).

⁴National Academics, Biological Effect of Ionizing Radiation (BEIR), "Health risks from exposure to low levels of ionizing radiation," Report VII (The National Academies Press, Washington, DC., 2006).

⁵International Commission on Radiological Protection, "Managing patient dose from multi detector computed tomography (MDCT) (ICRP Report No. 102)," Ann. ICRP **37**, 1–79 (2007).

⁶J. M. Boone, E. M. Geraghty, J. A. Seibert, and S. L. Wootton-Gorges, "Dose reduction in pediatric CT: A rational approach," *Radiology* **228**, 352–360 (2003).

⁷D. P. Frush, L. F. Donnelly, and N. S. Rosen, "Computed tomography and radiation risks: What pediatric health care providers should know," *Pediatrics* **112**, 951–957 (2003).

⁸M. K. Kalra, M. M. Maher, T. L. Toth, B. Schmidt, B. L. Westerman, H. T. Morgan, and S. Saini, "Techniques and applications of automatic tube current modulation for CT," *Radiology* **233**, 649–657 (2004).

⁹M. K. Kalra, M. M. Maher, T. L. Toth, R. S. Kamath, E. F. Halpern, and S. Saini, "Comparison of z-axis automatic tube current modulation technique with fixed tube current CT scanning of abdomen and pelvis," *Radiology* **232**, 347–353 (2004).

¹⁰X. Tang, J. Hsieh, F. Dong, J. Fan, and T. Toth, "Minimization of over-ranging in helical volumetric CT via hybrid cone beam image reconstruction—benefits in dose efficiency," *Med. Phys.* **35**, 3232–3238 (2008).

¹¹P. J. La Riviere, "Penalized-likelihood sinogram smoothing for low-dose CT," *Med. Phys.* **32**, 1676–1683 (2005).

¹²J. Wang, H. Lu, J. Wen, and Z. Liang, "Multiscale penalized weighted least-squares sinogram restoration for low-dose x-ray computed tomography," *IEEE Trans. Biomed. Imaging* **55**, 1022–1031 (2008).

¹³H. Yu, S. Zhao, E. A. Hoffman, and G. Wang, "Ultra-low dose lung CT perfusion regularized by a previous scan," *Acad. Radiol.* **16**, 363–373 (2009).

¹⁴S. Tang and X. Tang, "Statistical CT noise reduction with multiscale decomposition and penalized weighted least squares in the projection domain," *Med. Phys.* **39**, 5498–5512 (2012).

¹⁵E. Y. Sidky and X. Pan, "Image reconstruction in circular cone-beam computed tomography by constrained, total-variation minimization," *Phys. Med. Biol.* **53**, 4777–4807 (2008).

¹⁶H. Yu and G. Wang, "Compressed sensing based interior tomography," *Phys. Med. Biol.* **54**, 2791–2805 (2009).

¹⁷J. Yang, H. Yu, M. Jiang, and G. Wang, "High-order total variation minimization for interior tomography," *Inverse Probl.* **26**, 035013 (2010).

¹⁸Y. Ye, H. Yu, Y. Wei, and G. Wang, "A general local reconstruction approach based on a truncated Hilbert transform," *Int. J. Biomed. Imaging* **2007**, 63634–63641 (2007).

¹⁹H. Kudo, M. Courdurier, F. Noo, and M. Defrise, "Tiny *a priori* knowledge solves the interior problem in computed tomography," *Phys. Med. Biol.* **53**, 2207–2231 (2008).

²⁰M. Courdurier, F. Noo, M. Defrise, and H. Kudo, "Solving the interior problem of computed tomography using *a priori* knowledge," *Inverse Probl.* **24**, 065001 (2008).

²¹K. Taguchi, J. Xu, S. Srivastava, B. M. W. Tsui, J. Cammin, and Q. Tang, "Interior region-of-interest reconstruction using a small, nearly piecewise constant subregion," *Med. Phys.* **38**, 1307–1312 (2011).

²²Q. Xu, X. Mou, G. Wang, J. Sieren, E. A. Hoffman, and H. Yu, "Statistical interior tomography," *IEEE Trans. Med. Imaging* **30**, 1116–1128 (2011).

²³S. Tang, Y. Yang, and X. Tang, "Practical interior tomography with radial Hilbert filtering and *a priori* knowledge in a small round area," *J. X-Ray Sci. Technol.* **20**, 405–422 (2012).

²⁴S. Tang, X. Mou, J. Wu, H. Yan, and H. Yu, "CT gradient image reconstruction directly from projections," *J. X-Ray Sci. Technol.* **19**, 173–198 (2011).

²⁵K. L. Alfred, "Combining image reconstruction and image analysis with an application to 2D-tomography," *SIAM J. Imaging Sci.* **1**, 188–208 (2008).

²⁶J. P. Thirion, "Direct extraction of boundaries from computed tomography scans," *IEEE Trans. Med. Imaging* **13**, 322–328 (1994).

²⁷N. Srinivasa, K. Ramakrishnan, and K. Rajgopal, "Detection of edges from projections," *IEEE Trans. Med. Imaging* **11**, 76–80 (1992).

²⁸N. Sharma and L. M. Aggarwal, "Automated medical image segmentation techniques," *Med. Phys.* **35**, 3–14 (2010).

²⁹M. King, Z. Rodgers, and M. L. Giger, "Computerized method for evaluating diagnostic image quality of calcified plaque images in cardiac CT: Validation on a physical dynamic cardiac phantom," *Med. Phys.* **37**, 5777–5786 (2010).

³⁰F. Natterer, *The Mathematics of Computerized Tomography* (Wiley, New York, 1986).

³¹Y. Zou and X. Pan, "Exact image reconstruction on PI-lines from minimum data in helical cone-beam CT," *Phys. Med. Biol.* **49**, 941–959 (2004).

³²F. Noo, R. Clackdoyle, and J. D. Pack, "A two-step Hilbert transform method for 2D image reconstruction," *Phys. Med. Biol.* **49**, 3903–3923 (2004).

³³Q. Huang, J. You, G. L. Zeng, and G. T. Gullberg, "Reconstruction from uniformly attenuated SPECT projection data using the DBH method," *IEEE Trans. Med. Imaging* **28**, 17–29 (2009).

³⁴S. Tang, X. Mou, Y. Yang, Q. Xu, and H. Yu, "Application of projection simulation based on physical imaging model to the evaluation of beam hardening corrections in X-ray transmission tomography," *J. X-Ray Sci. Technol.* **16**, 95–117 (2008).

³⁵A. Faridani, E. L. Ritman, and K. T. Smith, "Local tomography," *SIAM J. Appl. Math.* **52**, 459–484 (1992).

³⁶E. T. Quinto, "Local algorithms in exterior tomography," *J. Comput. Appl. Math.* **199**, 141–148 (2007).

³⁷E. T. Quinto, U. Skoglund, and O. Öktem, "Electron lambda-tomography," *Proc. Natl. Acad. Sci. U.S.A.* **106**, 21842–21847 (2009).

³⁸M. A. Anastasio, D. Shi, X. Pan, C. Pelizzari, and P. Munro, "A preliminary investigation of local tomography for megavoltage CT imaging," *Med. Phys.* **30**, 2969–2980 (2003).

³⁹M. A. Anastasio, Y. Zou, E. Y. Sidky, and X. Pan, "Local cone-beam tomography image reconstruction on chords," *J. Opt. Soc. Am. A Opt. Image Sci. Vis.* **24**, 1569–1579 (2007).

⁴⁰G. Wang and H. Yu, "Can interior tomography outperform lambda tomography," *Proc. Natl. Acad. Sci. U.S.A.* **107**, E92–E93 (2010).

Complex dark-field contrast and its retrieval in x-ray phase contrast imaging implemented with Talbot interferometry

Yi Yang and Xiangyang Tang^{a)}

Imaging and Medical Physics, Department of Radiology and Imaging Sciences, Emory University School of Medicine, 1701 Uppergate Drive, C-5018, Atlanta, Georgia 30322

(Received 27 February 2014; revised 9 August 2014; accepted for publication 5 September 2014; published 30 September 2014)

Purpose: Under the existing theoretical framework of x-ray phase contrast imaging methods implemented with Talbot interferometry, the dark-field contrast refers to the reduction in interference fringe visibility due to small-angle x-ray scattering of the subpixel microstructures of an object to be imaged. This study investigates how an object's subpixel microstructures can also affect the phase of the intensity oscillations.

Methods: Instead of assuming that the object's subpixel microstructures distribute in space randomly, the authors' theoretical derivation starts by assuming that an object's attenuation projection and phase shift vary at a characteristic size that is not smaller than the period of analyzer grating G_2 and a characteristic length d_c . Based on the paraxial Fresnel–Kirchhoff theory, the analytic formulae to characterize the zeroth- and first-order Fourier coefficients of the x-ray irradiance recorded at each detector cell are derived. Then the concept of complex dark-field contrast is introduced to quantify the influence of the object's microstructures on both the interference fringe visibility and the phase of intensity oscillations. A method based on the phase-attenuation duality that holds for soft tissues and high x-ray energies is proposed to retrieve the imaginary part of the complex dark-field contrast for imaging. Through computer simulation study with a specially designed numerical phantom, they evaluate and validate the derived analytic formulae and the proposed retrieval method.

Results: Both theoretical analysis and computer simulation study show that the effect of an object's subpixel microstructures on x-ray phase contrast imaging method implemented with Talbot interferometry can be fully characterized by a complex dark-field contrast. The imaginary part of complex dark-field contrast quantifies the influence of the object's subpixel microstructures on the phase of intensity oscillations. Furthermore, at relatively high energies, for soft tissues it can be retrieved for imaging with a method based on the phase-attenuation duality.

Conclusions: The analytic formulae derived in this work to characterize the complex dark-field contrast in x-ray phase contrast imaging method implemented with Talbot interferometry are of significance, which may initiate more activities in the research and development of x-ray differential phase contrast imaging for extensive biomedical applications. © 2014 American Association of Physicists in Medicine. [<http://dx.doi.org/10.1118/1.4896098>]

Key words: x-ray differential phase contrast imaging, x-ray Talbot interferometry, x-ray dark-field imaging, x-ray phase contrast CT, complex dark-field contrast, phase-attenuation duality

1. INTRODUCTION

Among a variety of phase contrast imaging techniques^{1,2} based on x-ray refraction, the differential phase contrast imaging method implemented with Talbot interferometry^{3–5} is feasible with polychromatic laboratory x-ray sources, and thus has a high potential for translation into clinical applications. From a single set of projection data, the grating-based x-ray differential phase contrast imaging method is capable of providing images corresponding to the attenuation contrast, differential phase contrast, and dark-field contrast simultaneously.^{6–8} Figure 1 shows the schematic of a differential phase contrast imaging system implemented with an x-ray tube and three gratings.^{4,9} The source grating G_0 is employed to enable the system using a conventional x-ray source with a finite focal spot such that the spatial coherence condition can be satisfied.^{3,4,9} Based on the Talbot interferometry,⁹ phase grating G_1 and absorp-

tion grating G_2 work together as a shearing interferometer to detect the wavefront alteration caused by the object in the x-ray beam.^{4,8} Keeping grating G_1 fixed and shifting grating G_2 along the transverse direction x_g , the x-ray irradiance recorded at each detector pixel (m,n) oscillates as a periodic function and thus can be expanded into a Fourier series^{6,7}

$$I_{m,n}(x_g) = a_0(m,n) + \sum_{l=1}^{\infty} a_l(m,n) \cos\left(2\pi l \frac{x_g}{g_2} + \phi_l(m,n)\right), \quad (1)$$

where g_2 is the period of grating G_2 . The images corresponding to attenuation contrast, differential phase contrast, and dark-field contrast can be acquired from the zeroth- and first-order Fourier components a_0 , ϕ_1 , and a_1 , respectively, via the following equations:^{6,7,10}

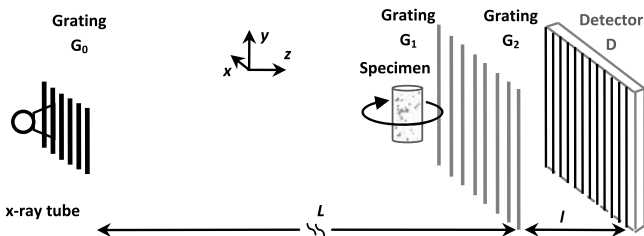


Fig. 1. Schematic of a grating based x-ray differential phase contrast CT system.

$$T(m,n) = \frac{a_0^s(m,n)}{a_0^r(m,n)}, \quad (2)$$

$$\partial_x \Phi(m,n) = \frac{g_2}{\lambda z} (\phi_1^s(m,n) - \phi_1^r(m,n)), \quad (3)$$

$$B(m,n) = -\ln V(m,n), \quad (4)$$

where

$$V(m,n) = \frac{a_1^s(m,n)/a_0^s(m,n)}{a_1^r(m,n)/a_0^r(m,n)}, \quad (5)$$

represents the reduction in interference fringe visibility (namely, visibility contrast), $B(m,n)$ is the dark-field contrast. $\partial_x \Phi(m,n)$ and $T(m,n)$ denote the gradient of projected wavefront phase profile $\Phi(m,n)$ and the normalized average transmission of the object to be imaged, respectively. λ is the wavelength of x-ray, z is the distance between gratings G_1 and G_2 , and superscripts “*s*” and “*r*” refer to the projection data obtained with and without the object in x-ray beam, respectively. It has been well established that the dark-field contrast is formed through the mechanism of small-angle x-ray scattering by subpixel microstructures of the object to be imaged.^{7,11,12} As a result, the dark-field imaging method can be used to extract the information about the object’s microstructures at a scale that is beyond the spatial resolution of the detection system.¹³ A number of theoretical and experimental investigations into the grating-based x-ray dark-field imaging method have been reported.^{6,7,10–17} For example, in Refs. 13–15, the structure of an object is assumed to fall into two categories: smooth and fine. A smooth structure is the feature at a scale that is comparable to or larger than the dimension of detector cell used for signal detection and thus is resolvable by the detector, whereas a fine structure is that at a scale that is significantly smaller than the dimension and thus is not resolvable by detector cells. An essential assumption shared in the investigations is that the object’s subpixel microstructures distribute in space randomly and a Gaussian function can describe the angular probability distribution of the scattered intensity.^{7,11–15}

In principle, one may decompose an object’s refractive index decrement δ , attenuation index β , phase shift Φ , and attenuation projection Λ into their smooth (resolvable) and

fine (unresolvable) components^{13–15}

$$\delta = \delta_s + \delta_f, \quad (6)$$

$$\beta = \beta_s + \beta_f \approx \beta_s, \quad (7)$$

$$\begin{aligned} \Phi(x,y) &= \frac{2\pi}{\lambda} \int_Z \delta(x,y,z) dz \\ &= \frac{2\pi}{\lambda} \int_Z \delta_s(x,y,z) dz + \frac{2\pi}{\lambda} \int_Z \delta_f(x,y,z) dz \\ &\equiv \Phi_s(x,y) + \Phi_f(x,y), \end{aligned} \quad (8)$$

$$\begin{aligned} \Lambda(x,y) &= \frac{4\pi}{\lambda} \int_Z \beta(x,y,z) dz \\ &\approx \frac{4\pi}{\lambda} \int_Z \beta_s(x,y,z) dz \equiv \Lambda_s(x,y), \end{aligned} \quad (9)$$

where subscripts “*s*” and “*f*” refer to the object’s smooth (resolvable) and fine (unresolvable) structures, respectively. Equations (7) and (9) indicate that the effect induced by an object’s fine structures on the attenuation index in x-ray’s propagation is negligible.¹³ Usually, $\Phi_f(x,y)$ in Eq. (8) has been modeled as a Gaussian random process and is determined by the object’s small-angle scattering,^{13,15} while $\Phi_s(x,y)$ in Eq. (8) and $\Lambda_s(x,y)$ in Eq. (9) are functions that vary in space with the characteristic sizes that are not smaller than the size of a detector cell.

It has been claimed that the dark-field contrast defined by Eqs. (4) and (5) is attributed to δ_f , the fine component of refractive index decrement δ that is dependent on the small-angle scattering caused by the microstructures of an object.^{7,11} Under the assumption that the small-angle scattering is characterized by a Gaussian angle distribution,^{11,13,15} the grating-based x-ray dark-field contrast can be determined by the width of the Gaussian angle distribution^{7,11} and its tomographic images can be obtained accordingly.⁷ On the other hand, since Eq. (3) is usually used to retrieve an object’s phase profile $\Phi(m,n)$ by 1D integration at a spatial interval that is comparable to detector cell size,^{3,18} it has been implicitly assumed that $\Phi(m,n)$ is just the smooth (resolvable) component of the object’s phase shift, i.e., $\Phi_s(x,y)$. In other words, the fine (unresolvable) component of the object’s phase shift $\Phi_f(x,y)$ is not related to the phase of intensity oscillations $\phi_1(m,n)$. Recently, Modregger *et al.*¹⁹ established a scattering-based perspective on the contrast form process of Talbot interferometry. Then, with use of the scattering-based approach, Modregger *et al.*²⁰ demonstrated that asymmetric scattering distributions lead to systematic deviation between the phase signal ($\phi_1^s - \phi_1^r$) and the expect value of the scattering angle distribution that should be proportional to the differential phase contrast. This indicates that the small-angle x-ray scattering caused by the microstructures of an object contributes to the phase signal, hence one may speculate that the ignorance of the influence of an object’s fine structure on the phase of intensity oscillations $\phi_1(m,n)$ may be arbitrary. Furthermore, having been aware of the results shown by Modregger *et al.*²¹ that the deviation of scattered intensity distribution from an isotropic Gaussian distribution can result in artifacts in tomographic images corresponding to the dark-field contrast defined by Eqs. (4) and (5), we think that the assumption—the scattered intensity distribution observes an isotropic Gaussian distribution—may

be too strong. Hence, instead of assuming that the subpixel microstructures of an object distribute randomly and $\Phi_f(x, y)$ be modeled as a Gaussian random process, we only assume that the object's attenuation projection $\Lambda(x, y)$ and phase shift $\Phi(x, y)$ vary at characteristic sizes that are not smaller than the period of grating G_2 and a characteristic length d_c that is determined by the data acquisition geometry

$$d_c = \frac{\lambda z_T}{g_2}, \quad (10)$$

where

$$z_T = m_T \frac{g_1^2}{8\lambda}, \quad m_T = 1, 3, 5, \dots, \quad (11)$$

is the m_T -th fractional Talbot distance,⁸ and g_1 is the pitch of phase grating G_1 .

Starting from the relaxed assumption, we rederive in this work Eqs. (2)–(5) for the grating-based differential phase contrast imaging system with detector cell dimension l_d large enough to satisfy

$$l_d \gg g_2 \quad \text{and} \quad l_d \gg d_c, \quad (12)$$

a condition that can be readily fulfilled in an x-ray phase contrast imaging system implemented with Talbot interferometry.^{6,7} By taking the effect of the object's subpixel microstructures into account, the analytic formulae of the zeroth- and first-order Fourier components a_0 , ϕ_1 , and a_1 in Eq. (1) are rederived through a mathematical treatment based on the paraxial Fresnel–Kirchhoff theory, which shows that the subpixel microstructures of an object indeed not only reduce the interference fringe visibility $V(m, n)$ but also contribute significantly to the phase of intensity oscillations $\phi_1(m, n)$. Then, we introduce the concept of complex dark-field contrast to fully characterize the effect of an object's subpixel microstructures on the reduction in the interference fringe visibility $V(m, n)$ and the phase of intensity oscillations $\phi_1(m, n)$. Moreover, we propose an approximate method to retrieve the imaginary part of the complex dark-field contrast for imaging. Through computer simulation studies, we evaluate and verify the derived analytic formulae with a specially designed numerical phantom. Particularly, we demonstrate that the imaginary part of the complex dark-field contrast is strongly dependent not only on the shape but also the orientation of object's microstructures. In addition, we discuss the potential of the imaginary part of the complex dark-field contrast for imaging, which may provide extra information complementary to the attenuation contrast, differential phase contrast, and the dark-field contrast defined by Eqs. (4) and (5). What follows is a detailed presentation of our investigation.

2. MATERIALS AND METHODS

The ground on which our study is based is that the interaction between the x-ray beam and an object to be imaged can be adequately described by the spatial distribution of the object's complex refractive index $n = 1 - \delta + i\beta$.^{22–24} Since the paraxial condition is met in Talbot interferometry,⁸

the analytic formulae to characterize the grating-based x-ray differential phase contrast imaging method implemented with Talbot interferometry are derived in the parallel beam geometry. As illustrated in Fig. 1, the x-ray beam propagates along the z -axis, and the object to be imaged and the detector are placed immediately in front of the phase grating G_1 and behind the analyzer grating G_2 , respectively.⁴

2.A. The complex dark-field contrast in x-ray phase imaging implemented with the Talbot interferometry

We constrain our focus on the cases where the object's features are at scales that are not smaller than g_2 and d_c . Supposing grating G_2 is linearly shifted along the transverse direction x_g , the mean of the interference fringe intensity over a cell indexed by (m, n) in a detector as a function of x_g , which is referred to as the phase-stepping curve (PSC), can be expressed as

$$I_{m,n}(x_g) = \frac{1}{l_d^2} \int_{-l_d/2}^{l_d/2} dy \int_{-l_d/2}^{l_d/2} dx |E_{x_g}(x_m + x, y_n + y, z_2)|^2, \quad (13)$$

where

$$x_m = \left(m + \frac{1}{2}\right)l_d, \quad m = 0, \pm 1, \pm 2, \dots, \quad (14)$$

$$y_n = \left(n + \frac{1}{2}\right)l_d, \quad n = 0, \pm 1, \pm 2, \dots. \quad (15)$$

$E_{x_g}(x, y, z_2)$ is the electric field at location (x, y, z_2) and z_2 the distance between the detector and x-ray source along the direction of x-ray propagation. The incident x-ray beam is assumed as a monochromatic plane wave with wavelength λ and amplitude E_0 . G_1 is a phase grating and G_2 an absorption grating with 50% duty cycle, and the distance from G_1 to G_2 is selected as the m_T -th fractional Talbot distance z_T given by Eq. (11). Furthermore, in order to maximize the interference fringe visibility in the detector plane, we set⁸

$$g_1 = 2g_2. \quad (16)$$

According to the derivation detailed in the Appendix, the intensity $I_{m,n}(x_g)$ is a periodic function of x_g with period g_2 and thus can be expanded into a Fourier series

$$I_{m,n}(x_g) = C_0(m, n) + \sum_{l=-\infty}^{\infty} C_{2l+1}(m, n) \exp\left(2\pi i l \frac{x_g}{g_2}\right), \quad (17)$$

and the zeroth- and first-order Fourier coefficients are given by

$$\begin{aligned} C_0(m, n) &= a_0(m, n) = \frac{|E_0|^2}{2l_d^2} \int_{x_m-l_d/2}^{x_m+l_d/2} dx \\ &\times \int_{y_n-l_d/2}^{y_n+l_d/2} dy \exp(-\Lambda(x, y)), \end{aligned} \quad (18)$$

and

$$\begin{aligned} C_1(m,n) &= \frac{a_1(m,n)}{2} \exp(i\phi_1(m,n)), \\ &= -i \frac{2|E_0|^2}{\pi^2 l_d^2} \int_{x_m-l_d/2}^{x_m+l_d/2} dx \int_{y_n-l_d/2}^{y_n+l_d/2} dy \\ &\quad \times \exp\left(-\Lambda(x,y) + i \frac{\Phi(x+d_c,y) - \Phi(x-d_c,y)}{2}\right) \\ &\quad \times \cos\left(\frac{\Phi(x+d_c,y) + \Phi(x-d_c,y) - 2\Phi(x,y)}{2}\right), \end{aligned} \quad (19)$$

in which Eq. (1) is utilized. It should be noted that in the derivation of Eqs. (18) and (19), we do not require that the fine (unresolvable) features of the object distribute randomly, or the phase shift related to the object's fine features be modeled as a Gaussian random process. Instead, we assume that $\Phi(x,y)$ and $\Lambda(x,y)$ vary with characteristic sizes that are not smaller than g_2 and d_c . Let

$$\bar{\Lambda}(x,y) = \frac{1}{l_d^2} \int_{x-l_d/2}^{x+l_d/2} dx_1 \int_{y-l_d/2}^{y+l_d/2} dy_1 \Lambda(x_1,y_1), \quad (20)$$

and

$$\bar{\Phi}(x,y) = \frac{1}{l_d^2} \int_{x-l_d/2}^{x+l_d/2} dx_1 \int_{y-l_d/2}^{y+l_d/2} dy_1 \Phi(x_1,y_1) \quad (21)$$

denote the mean of attenuation projection and phase shift over a region of dimension $l_d \times l_d$, respectively. One may then rewrite Eqs. (18) and (19) as

$$\begin{aligned} a_0(m,n) &= \frac{|E_0|^2}{2l_d^2} \exp(-\bar{\Lambda}(x_m,y_n)) \\ &\quad \times \int_{x_m-l_d/2}^{x_m+l_d/2} dx \int_{y_n-l_d/2}^{y_n+l_d/2} dy \exp(-\Delta\Lambda(x,y)), \end{aligned} \quad (22)$$

$$\begin{aligned} a_1(m,n) \exp(i\phi_1(m,n)) &= -i \frac{4|E_0|^2}{\pi^2 l_d^2} \exp(-\bar{\Lambda}(x_m,y_n) + id_c \partial_x \bar{\Phi}(x_m,y_n)) \\ &\quad \times \int_{x_m-l_d/2}^{x_m+l_d/2} dx \int_{y_n-l_d/2}^{y_n+l_d/2} dy \exp(-\Delta\Lambda(x,y)) \\ &\quad + id_c \Delta\Phi_x(x,y;d_c)) \\ &\quad \times \cos\left(\frac{\Phi(x+d_c,y) + \Phi(x-d_c,y) - 2\Phi(x,y)}{2}\right), \end{aligned} \quad (23)$$

where

$$\partial_x \bar{\Phi}(x_m,y_n) = \frac{\bar{\Phi}\left(x_m + \frac{l_d}{2}, y_n\right) - \bar{\Phi}\left(x_m - \frac{l_d}{2}, y_n\right)}{l_d}, \quad (24)$$

represents the averaged differential phase shift over the detector cell at (m,n) , while

$$\Delta\Lambda(x,y) = \Lambda(x,y) - \bar{\Lambda}(x_m,y_n), \quad (25)$$

and

$$\begin{aligned} \Delta\Phi_x(x,y;d_c) &= \frac{\Phi(x+d_c,y) - \Phi(x-d_c,y)}{2d_c} \\ &\quad - \partial_x \bar{\Phi}(x_m,y_n) \end{aligned} \quad (26)$$

denote the deviation of attenuation projection and differential phase shift from their mean, respectively. According to Eq. (20),

$$\begin{aligned} &\frac{1}{l_d^2} \int_{x_m-l_d/2}^{x_m+l_d/2} dx \int_{y_n-l_d/2}^{y_n+l_d/2} dy \Delta\Lambda(x,y) \\ &= \frac{1}{l_d^2} \int_{x_m-l_d/2}^{x_m+l_d/2} dx \int_{y_n-l_d/2}^{y_n+l_d/2} dy \Lambda(x,y) - \bar{\Lambda}(x_m,y_n) = 0, \end{aligned} \quad (27)$$

and thus the zeroth- Fourier coefficient can be approximated as

$$\begin{aligned} a_0(m,n) &= \frac{|E_0|^2}{2} \exp(-\bar{\Lambda}(x_m,y_n)) \\ &\quad \times \left(1 + \frac{1}{2!} \frac{1}{l_d^2} \int_{x_m-l_d/2}^{x_m+l_d/2} dx \int_{y_n-l_d/2}^{y_n+l_d/2} dy (\Delta\Lambda(x,y))^2 \right. \\ &\quad \left. - \frac{1}{3!} \frac{1}{l_d^2} \int_{x_m-l_d/2}^{x_m+l_d/2} dx \int_{y_n-l_d/2}^{y_n+l_d/2} dy (\Delta\Lambda(x,y))^3 + \dots \right) \\ &\approx \frac{|E_0|^2}{2} \exp(-\bar{\Lambda}(x_m,y_n)). \end{aligned} \quad (28)$$

On the other hand, since the linear attenuation coefficient β is much smaller than the refractive index decrement δ , it is reasonable to assume that $\Delta\Lambda(x,y)$ is negligible in comparison with $d_c \Delta\Phi_x(x,y)$. Hence the first-order Fourier coefficient can be estimated as

$$\begin{aligned} a_1(m,n) \exp(i\phi_1(m,n)) &= -i \frac{4|E_0|^2}{\pi^2 l_d^2} \exp(-\bar{\Lambda}(x_m,y_n) + id_c \partial_x \bar{\Phi}(x_m,y_n)) \\ &\quad \times \int_{x_m-l_d/2}^{x_m+l_d/2} dx \int_{y_n-l_d/2}^{y_n+l_d/2} dy \exp(id_c \Delta\Phi_x(x,y;d_c)) \\ &\quad \times \cos\left(\frac{\Phi(x+d_c,y) + \Phi(x-d_c,y) - 2\Phi(x,y)}{2}\right). \end{aligned} \quad (29)$$

Combining Eqs. (28) and (29) yields

$$\begin{aligned} &\frac{a_1^s(m,n)/a_0^s(m,n)}{a_1^r(m,n)/a_0^r(m,n)} \exp(i(\phi_1^s(m,n) - \phi_1^r(m,n))) \\ &= V_1(m,n) \exp(id_c \partial_x \bar{\Phi}(x_m,y_n)), \end{aligned} \quad (30)$$

where

$$\begin{aligned} V_1(m,n) &= \frac{1}{l_d^2} \int_{x_m-l_d/2}^{x_m+l_d/2} dx \int_{y_n-l_d/2}^{y_n+l_d/2} dy \\ &\quad \times \exp(id_c \Delta\Phi_x(x,y;d_c)) \\ &\quad \times \cos\left(\frac{\Phi(x+d_c,y) + \Phi(x-d_c,y) - 2\Phi(x,y)}{2}\right). \end{aligned} \quad (31)$$

It should be noted that in this work, we derive the analytic formulae to characterize the zeroth- and first-order Fourier

coefficients of the x-ray irradiance recorded at each detector cell without assuming that the phase shift Φ can be decomposed into smooth (resolvable) and fine (unresolvable) components. Hence, our derivation is more rigorous in terms of mathematical treatment and more systematic from the standpoint of physics. In addition, from Eq. (31) it is not hard to show that $V_1(m,n)$ is completely determined by the subpixel microstructures of an object. Actually, Eq. (31) shows that $V_1(m,n)$ is dependent on $\Delta\Phi_x(x,y;d_c)$ and $(\Phi(x+d_c,y)+\Phi(x-d_c,y)-2\Phi(x,y))$. If the object's phase shift $\Phi(x,y)$ varies with the characteristic sizes that are not less than l_d , $\overline{\Phi}(x_m+l_d/2,y_n)$ and $\overline{\Phi}(x_m-l_d/2,y_n)$ in Eq. (24) can be estimated by expanding $\Phi(x_1,y_1)$ in Eq. (21) into Taylor series around (x_m,y_n) , i.e.,

$$\begin{aligned}\Phi(x_1,y_1) \approx & \Phi(x_m,y_n) + \partial_x\Phi(x_m,y_n)(x_1-x_m) \\ & + \partial_y\Phi(x_m,y_n)(y_1-y_n),\end{aligned}\quad (32)$$

in which, according to the smooth phase condition,²⁵ the derivatives of $\Phi(x_m,y_n)$ higher than the first have been assumed negligible.¹³ Substituting Eq. (32) into Eq. (21), the averaged differential phase shift defined by Eq. (24) can be calculated as

$$\begin{aligned}\partial_x\overline{\Phi}(x_m,y_n) \approx & \frac{1}{l_d^3} \int_{x_m}^{x_m+l_d} dx_1 \int_{y_n-l_d/2}^{y_n+l_d/2} dy_1 (\Phi(x_m,y_n) \\ & + \partial_x\Phi(x_m,y_n)(x_1-x_m) + \partial_y\Phi(x_m,y_n)(y_1-y_n)) \\ & - \frac{1}{l_d^3} \int_{x_m-l_d}^{x_m} dx_1 \int_{y_n-l_d/2}^{y_n+l_d/2} dy_1 (\Phi(x_m,y_n) \\ & + \partial_x\Phi(x_m,y_n)(x_1-x_m) + \partial_y\Phi(x_m,y_n)(y_1-y_n)) \\ = & \partial_x\Phi(x_m,y_n).\end{aligned}\quad (33)$$

Then the deviation of the differential phase shift defined by Eq. (26) can be approximated as

$$\begin{aligned}\Delta\Phi_x(x,y;d_c) \approx & \partial_x\Phi(x,y) - \partial_x\Phi(x_m,y_n) \approx 0, \\ \text{for } x_m - \frac{l_d}{2} \leq x \leq x_m + \frac{l_d}{2}, y_n - \frac{l_d}{2} \leq y \leq y_n + \frac{l_d}{2},\end{aligned}\quad (34)$$

in which, Eqs. (33) and (32) are used. Furthermore, according to Eq. (12), d_c is much smaller than l_d , hence $\Phi(x+d_c,y)$ and $\Phi(x-d_c,y)$ can be expanded into Taylor series around (x,y) . Since the second and higher order derivatives of phase shift $\Phi(x,y)$ are assumed negligible, we have

$$\frac{\Phi(x+d_c,y)+\Phi(x-d_c,y)-2\Phi(x,y)}{2} \approx 0.\quad (35)$$

Inserting Eqs. (34) and (35) into Eq. (31) results in

$$V_1(m,n) = 1,\quad (36)$$

if $\Phi(x,y)$ varies at a scale that is comparable to or larger than l_d . Thus, like the visibility contrast defined by Eq. (5), the contrast related to $V_1(m,n)$ only comes from the effect induced by the subpixel features of an object. On the other hand, by combining Eqs. (30) and (5), one obtains

$$|V_1(m,n)| = V(m,n),\quad (37)$$

i.e., the absolute of $V_1(m,n)$ is just the visibility contrast $V(m,n)$ defined by Eq. (5).

From now on, we show that $V_1(m,n)$ is in general complex. We rewrite Eq. (31) by expanding the exponential function into a power series of $\Delta\Phi_x(x,y;d_c)$,

$$\begin{aligned}V_1(m,n) = & 1 + \sum_{k=1}^{\infty} i^k \frac{(d_c)^k}{k!} M_k(m,n) \\ = & 1 + \sum_{k=1}^{\infty} (-1)^k \frac{(d_c)^{2k}}{(2k)!} M_{2k}(m,n) \\ & + i \sum_{k=0}^{\infty} (-1)^k \frac{(d_c)^{2k+1}}{(2k+1)!} M_{2k+1}(m,n),\end{aligned}\quad (38)$$

where

$$\begin{aligned}M_k(m,n) = & \frac{1}{l_d^2} \int_{x_m-l_d/2}^{x_m+l_d/2} dx \int_{y_n-l_d/2}^{y_n+l_d/2} dy (\Delta\Phi_x(x,y;d_c))^k \\ & \times \cos\left(\frac{\Phi(x+d_c,y)+\Phi(x-d_c,y)-2\Phi(x,y)}{2}\right).\end{aligned}\quad (39)$$

According to Eqs. (34) and (35), both $\Delta\Phi_x(x,y;d_c)$ and $(\Phi(x+d_c,y)+\Phi(x-d_c,y)-2\Phi(x,y))$ are solely dependent on the small-angle x-ray scattering caused by object's subpixel microstructures. If the subpixel microstructures of an object distribute randomly, the chance that $\Delta\Phi_x(x,y;d_c)$ defined by Eq. (26) falls into an interval around a value F would be the same as that around the value $-F$. As a result, it is not difficult to show that

$$\begin{aligned}M_{2k+1}(m,n) = & \frac{1}{l_d^2} \int_{x_m-l_d/2}^{x_m+l_d/2} dx \int_{y_n-l_d/2}^{y_n+l_d/2} dy (\Delta\Phi_x(x,y;d_c))^{2k+1} \\ & \times \cos\left(\frac{\Phi(x+d_c,y)+\Phi(x-d_c,y)-2\Phi(x,y)}{2}\right) \approx 0.\end{aligned}\quad (40)$$

Substituting Eq. (40) into Eq. (38), one finds that the imaginary part of $V_1(m,n)$ is negligible under the assumption that an object's subpixel microstructures distribute randomly. However, in this study we do not make such an assumption and thus in general $V_1(m,n)$ is complex.

Based on the above discussions, it is reasonable to consider $V_1(m,n)$ defined in Eq. (30), which is referred as the complex visibility contrast, as a generalization of the visibility contrast defined by Eq. (5). Similar to defining the dark-field contrast $B(m,n)$ by Eqs. (4) and (5), the complex dark-field contrast $B_1(m,n)$ can be defined as

$$B_1(m,n) = B_{1r}(m,n) + i B_{1i}(m,n) = -\ln V_1(m,n),\quad (41)$$

where $B_{1r}(m,n)$ and $B_{1i}(m,n)$ are the real and imaginary parts of the complex dark-field contrast, respectively, and can be determined by

$$\begin{aligned} & B_{1r}(m,n) + iB_{1i}(m,n) \\ &= -\ln \left(\frac{1}{l_d^2} \int_{x_m-l_d/2}^{x_m+l_d/2} dx \int_{y_n-l_d/2}^{y_n+l_d/2} dy \right. \\ &\quad \times \exp(i d_c \Delta \Phi_x(x, y; d_c)) \\ &\quad \left. \times \cos \left(\frac{\Phi(x+d_c, y) + \Phi(x-d_c, y) - 2\Phi(x, y)}{2} \right) \right), \end{aligned} \quad (42)$$

in which Eq. (31) is used. Using Eqs. (41), (30), and (4) and (5) it is straightforward to show that

$$B(m,n) = -\ln \left(\frac{a_1^s(m,n)/a_0^s(m,n)}{a_1^r(m,n)/a_0^r(m,n)} \right) = B_{1r}(m,n), \quad (43)$$

$$\phi_1^s(m,n) - \phi_1^r(m,n) = d_c \partial_x \bar{\Phi}(x_m, y_n) - B_{1i}(m,n). \quad (44)$$

Equation (43) shows that the real part of the complex dark-field contrast $B_{1r}(m,n)$ is just the dark-field contrast $B(m,n)$ that quantifies the relative decrease of the visibility due to the subpixel microstructures of an object to be imaged. Noting that the visibility is defined as normalized oscillation amplitude^{6,17} $a_1(m,n)/a_0(m,n)$, we may refer to the real part of the complex dark-field contrast $B_{1r}(m,n)$ as amplitude-based dark-field contrast. Similarly, we may refer to the imaginary part of the complex dark-field contrast $B_{1i}(m,n)$ as phase-based dark-field contrast, since Eq. (44) shows that the imaginary part of the complex dark-field contrast $B_{1i}(m,n)$ represents the influences of the object's subpixel microstructures on the phase of intensity oscillations $\phi_1(m,n)$. It should be pointed out that a nonzero $B_{1i}(m,n)$ means a violation of Eq. (3), the formula that is widely employed to calculate the differential phase contrast in x-ray differential phase contrast imaging implemented with Talbot interferometry.

2.B. The retrieval of complex dark-field contrast in grating-based x-ray phase contrast imaging at high photon energy

From the experimentally measured phase-stepping curve, immediately one can calculate the Fourier coefficients $C_0(m,n)$ and $C_1(m,n)$, or equivalently, $a_0(m,n)$, $a_1(m,n)$, and $\phi_1(m,n)$. Then Eq. (43) can be utilized to estimate the real part of the dark-field contrast $B_{1r}(m,n)$. To retrieve the imaginary part of complex dark-field contrast $B_{1i}(m,n)$ using Eq. (44), however, the average differential phase shift defined by Eq. (24) must be determined at first. In this section, for soft tissues to be imaged with x-ray Talbot interferometry at high energies, we propose an approximate method to calculate the average differential phase shift using the x-ray phase-attenuation duality,^{26,27} which was first observed by Wu *et al.* in their investigation of propagation-based in-line x-ray phase contrast imaging. According to Wu *et al.*, among the three types of interactions between x-ray and soft tissues, i.e., photoelectric absorption, incoherent scattering (Compton scattering), and coherent scattering, Compton scattering is the dominating attenuation process at high x-ray energies. As a result, the soft-tissue attenuation cross sections are well approximated by those of x-ray incoherent scattering for x-rays of approximately 60–500 keV.^{26,27} Thus the average of attenuation projection and phase shift can

be expressed as^{26,27}

$$\begin{aligned} \bar{\Lambda}(x_m, y_n) &= \sigma_{\text{KN}} \frac{1}{l_d^2} \int_{x_m-l_d/2}^{x_m+l_d/2} dx \int_{y_n-l_d/2}^{y_n+l_d/2} dy \\ &\quad \times \int_Z \rho_e(x, y, z) dz, \end{aligned} \quad (45)$$

$$\begin{aligned} \bar{\Phi}(x_m, y_n) &= \lambda r_e \frac{1}{l_d^2} \int_{x_m-l_d/2}^{x_m+l_d/2} dx \int_{y_n-l_d/2}^{y_n+l_d/2} dy \\ &\quad \times \int_Z \rho_e(x, y, z) dz, \end{aligned} \quad (46)$$

respectively. $\rho_e(x, y, z)$ is the electron density, r_e is the classic electron radius, and σ_{KN} is the total cross section of Compton scattering from a free electron derived from the Klein–Nishina equation,^{26,27}

$$\begin{aligned} \sigma_{\text{KN}} &= 2\pi r_e^2 \left(\frac{1+\eta}{\eta^2} \left(\frac{2(1+\eta)}{1+2\eta} - \frac{1}{\eta} \ln(1+2\eta) \right) \right. \\ &\quad \left. + \frac{1}{2\eta} \ln(1+2\eta) - \frac{1+3\eta}{(1+2\eta)^2} \right), \end{aligned} \quad (47)$$

where

$$\eta = \frac{h}{\lambda m_e c}. \quad (48)$$

h is the plank constant, c is the speed of light, and m_e is the rest mass of an electron. Eqs. (45) and (46) indicate that both the attenuation projection and the phase shift of the object to be imaged are proportional to the projected electron density, i.e., the x-ray phase-attenuation duality holds for soft tissues at high photon energies. Eliminating the integration over the electron density $\rho_e(x, y, z)$ from Eqs. (45) and (46) leads to

$$\bar{\Phi}(x_m, y_n) = \frac{\lambda r_e}{\sigma_{\text{KN}}} \bar{\Lambda}(x_m, y_n). \quad (49)$$

Using Eqs. (49) and (28), the average differential phase shift of an object can be approximated as

$$\begin{aligned} & \partial_x \bar{\Phi}(x_m, y_n) \\ & \approx \frac{\bar{\Phi}(x_{m+1}, y_n) - \bar{\Phi}(x_{m-1}, y_n)}{2l_d} \\ &= \frac{\lambda r_e}{\sigma_{\text{KN}}} \frac{\bar{\Lambda}(x_{m+1}, y_n) - \bar{\Lambda}(x_{m-1}, y_n)}{2l_d} \\ &= \frac{\lambda r_e}{2l_d \sigma_{\text{KN}}} \left(\ln \left(\frac{a_0^s(m-1, n)}{a_0^r(m-1, n)} \right) - \ln \left(\frac{a_0^s(m+1, n)}{a_0^r(m+1, n)} \right) \right). \end{aligned} \quad (50)$$

Equation (50) indicates that for the x-ray phase contrast imaging implemented with the Talbot interferometry at energy that is higher than 60 keV, for soft tissues the average differential phase shift can be approximately estimated using the zeroth-order Fourier coefficient $a_0(m,n)$. Hence, the imaginary part of complex dark-field contrast $B_{1i}(m,n)$ can be retrieved with resort to Eq. (44).

3. NUMERICAL EVALUATION

In this section, we evaluate and validate the analytic formulae given in Sec. 2.A to describe the zeroth- and first-order

Fourier coefficients and the resultant complex dark-field contrast. In addition, we evaluate and verify the approximate method proposed in section Sec. 2.B to retrieve the imaginary part of the complex dark-field signal for imaging implemented with x-ray Talbot interferometry at high energy. Below is a brief description of the tasks to be accomplished.

3.A. Modeling of x-ray differential phase contrast imaging with Talbot interferometry

The modeling of x-ray differential phase contrast imaging implemented with Talbot interferometry is based on Fresnel analysis, which has been evaluated and verified previously.^{28–30} In the simulation study, the detector cell dimension is set at 256 μm , and the period of gratings G_1 and G_2 are 4 and 2 μm , respectively. The x-ray source is assumed monochromatic at 30 or 80 keV, and the distance between the gratings G_1 and G_2 is 4.84 or 12.91 cm, respectively, corresponding to the first fractional Talbot distance. The x-ray flux is set at 10^8 photon/cm² per projection and observes the Poisson distribution. A 360° full scan at 1° step is carried out in data acquisition. To assure the simulation study at high fidelity, the dimension of finite x-ray along x -direction is 10 nm, corresponding to 200 samplings within one period of grating G_2 , while the number of steps in shifting grating G_2 is 20.

3.B. Validation of the formulae to characterize the zeroth- and first- order Fourier coefficients

It is straightforward to show that Eqs. (28) and (42)–(44) are equivalent to Eqs. (28) and (29) and thus they can be used to characterize the zeroth- and first-order Fourier coefficients. Our effort in this work is dedicated to investigating the grating-based x-ray dark-field contrast imaging in the parallel beam geometry. A 2D numerical phantom that is a disc made of water and 7056 embedded microstructures is designed to evaluate and verify the accuracy of Eqs. (28) and (42)–(44). As illustrated in Fig. 2(a), the diameter of the water disc is 3.6864 cm, and the microstructures are deliberately grouped into three tilted 3×3 matrices labeled with A, B, and C. The refractive index of water is assumed to be $1 - 2.559 \times 10^{-7} + i6.042 \times 10^{-11}$ for x-ray source at 30 keV and $1 - 3.598 \times 10^{-8} + i2.266 \times 10^{-11}$ for x-ray source at 80 keV, respectively. In each matrix, the dimension of each cluster is $256 \times 256 \mu\text{m}^2$. Matrix A is designed to simulate air spheres,³¹ and accordingly the microstructures are discs with identical complex refractive index $n = 1$. The air discs in each column are of identical size. The diameters of air discs in the left, middle, and right columns are 4, 8, and 12 μm , respectively, while the total number of air discs in the corresponding columns are 1728, 432, and 192. It should be noted that the ratio of the total area occupied by the air discs in a cluster to the cluster's dimension ($256 \times 256 \mu\text{m}^2$) is kept constant (0.11). As demonstrated in Fig. 2(b), among all 192 air discs of diameter 12 μm in the right column of matrix A, one third of them (64 air discs) are distributed in the left half of the cluster at the top row and form a 16×4 pattern, another third of them (64 air discs) are distributed in the cluster at the middle row and form

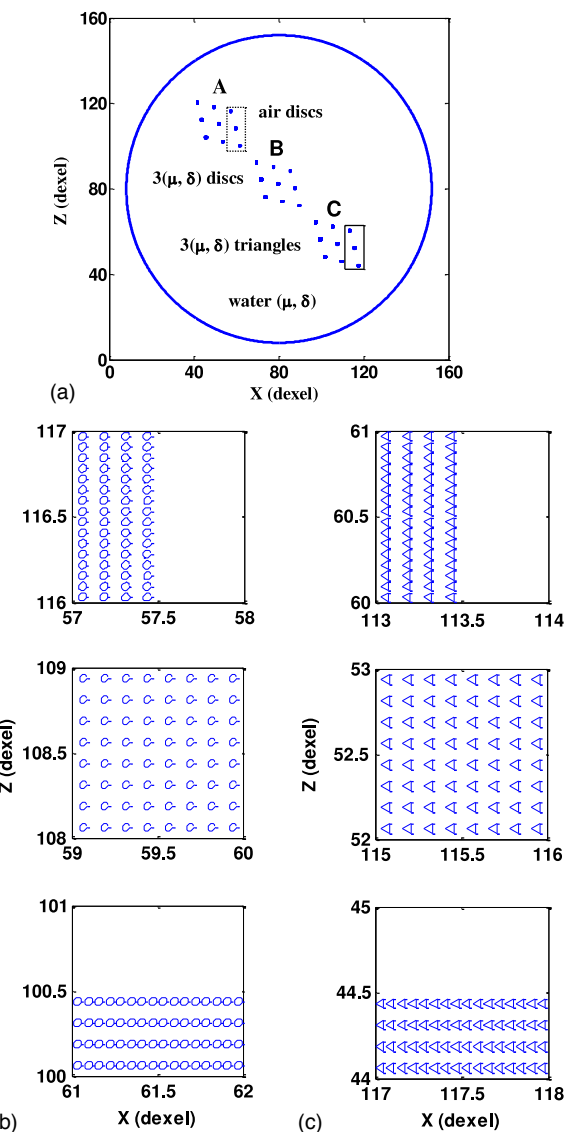


FIG. 2. Transaxial view of the numerical phantom (a) and zoomed views of the air discs and triangle plates in the areas marked by dashed lines (b) and solid lines (c), respectively.

a 8×8 pattern, and the rest one third of them (64 air discs) are distributed in the bottom half of the cluster at the bottom row and form a 4×16 pattern. Similarly, among all 432 air discs of diameter 8 μm in the middle column of matrix A, one third of them (144 air discs) are distributed in the left half of the cluster in the top row and form a 24×6 pattern, another third of them are distributed in the cluster in the middle row and form a 12×12 pattern, and the rest of them are distributed in the bottom half of the cluster in the bottom row and form a 6×24 pattern. In a same way, all 1728 air discs of diameter 4 μm are distributed in the left column of matrix A. That is, one third of them (576 air discs) form a 48×12 pattern in the left half of the cluster in the top row, another third of them form a 24×24 pattern in the cluster in the middle row, and the rest of them form a 12×48 pattern in the bottom half of the cluster in the bottom row. In addition, the configuration of the microstructures in matrix B is same as that in matrix A except that the

refractive index of each microstructure in matrix B is $n = 1 - 3\delta_{\text{water}} + 3i\beta_{\text{water}}$. Finally, matrix C in Fig. 2(a) is produced by replacing the discs of diameters 4, 8, and 12 μm in matrix B with equilateral triangle plates of sides 4.6188, 9.2376, and 13.8564 μm , respectively. As illustrated in Fig. 2(c), for each equilateral triangle plate in matrix C, one of its edges is along the z -direction and a vertex of the triangle is on the left side of the edge. It should be noted that in the top rows and the bottom rows of matrices A, B, and C, the microstructures are intentionally distributed in the left and bottom half of the clusters, respectively. Thus, the distribution of the subpixel microstructures in these clusters deviates significantly from a random distribution. Note that the phantom is deliberately designed to assess the accuracy of Eqs. (42)–(44) and (28) over the variation in refractive index, dimension, shape, and distribution of the subpixel microstructures, and can be used to show that the complex dark-field contrast is jointly determined by the number, distribution, dimension, shape, and refractive index of subpixel microstructures, as predicted by Eq. (42).

Using the parameters specified above, it is quite straightforward to calculate the phase shift Φ and attenuation projection Λ using Eqs. (8) and (9). Subsequently, the average phase shift and average differential phase shift at detector cell (m, n) are given by Eqs. (21) and (24), respectively, and the average attenuation is given by Eq. (20). The complex dark-field contrast can be attained using Eq. (42), and the zeroth-order Fourier coefficient can be estimated using Eq. (28). To evaluate the accuracy of Eqs. (42)–(44) and (28) in predicting the dark-field contrast defined by Eqs. (4) and (5), the relative phase shift of intensity oscillations $\phi_1(m, n)$, and the zeroth-order Fourier coefficient, we carry out a noiseless computer simulation and take the simulation result as reference. To assure the simulation study at high fidelity, the dimension of finite x-ray along x -direction is 10 nm, corresponding to 200 samplings within one period of grating G_2 . The number of steps in shifting grating G_2 is increased from 20 to 100, because the number of incident x-ray photons available at each step is not a concern in a noiseless simulation.

3.C. Exploring the potential of complex dark-field contrast imaging

The numerical phantom described above is also employed to explore the potential of the complex dark-field contrast for imaging. Specifically, the real part of complex dark-field, or the amplitude-based dark-field contrast, can be directly retrieved from the zeroth- and first-order Fourier coefficients using Eq. (43). In addition, based on the phase-attenuation duality approach, for soft tissues the average differential phase shift can be approximately retrieved from the zeroth-order Fourier coefficient using Eq. (50) at high energies. Then, the imaginary part of the complex dark-field contrast $B_{1i}(m, n)$, or the phase-based dark-field contrast, can be calculated using Eq. (44). By comparing the $B_{1i}(m, n)$ retrieved by Eq. (44) with that calculated by Eq. (42), the accuracy of the approximate retrieval method based on the phase-attenuation duality can be evaluated.

4. RESULTS

Below is a presentation of the preliminary results.

4.A. Validation of the approach to the zeroth- and first-order Fourier coefficients

For x-ray sources at 30 and 80 keV, the profiles of the zeroth-order Fourier coefficient over x_m at 0° and 45° view angles are analytically calculated using Eqs. (28), (20), and (9) and plotted in Figs. 3(a)–3(d). The profiles corresponding to the real part of the complex dark-field contrast, i.e., the quantity calculated using the right side of Eq. (43) at 0° and 45° view angles are plotted in Figs. 4(a)–4(d) in which Eqs. (42), (26), (24), (21), and (8) are utilized. The profile corresponding to

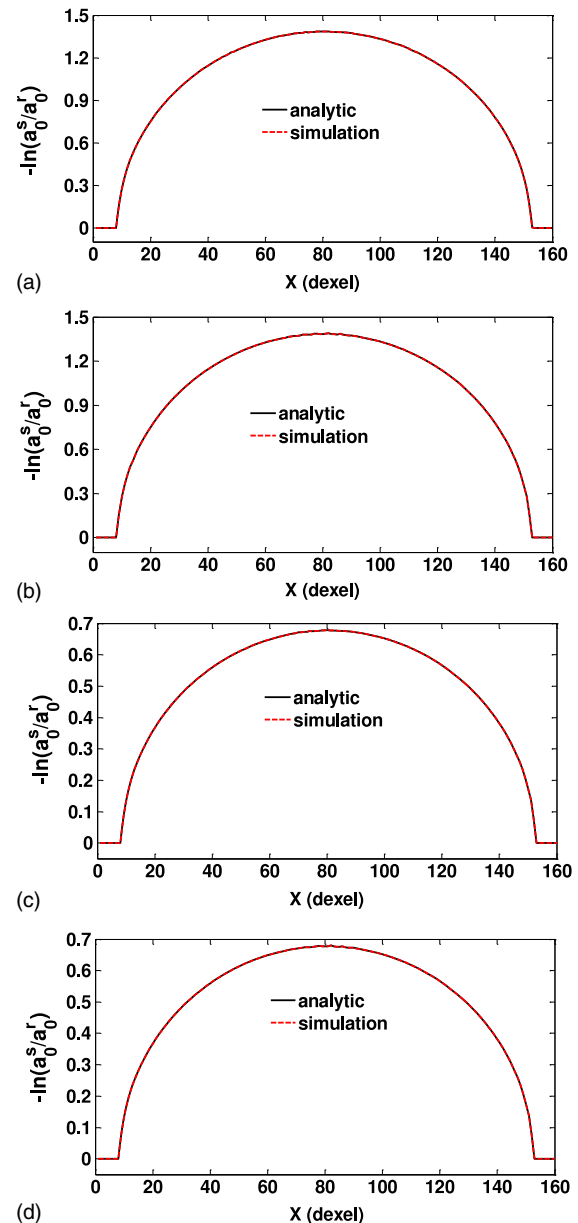


FIG. 3. Profiles of the zeroth-order Fourier coefficient obtained using Eqs. (28), (20), and (9) compared with the noiseless simulation result (baseline reference, G_2 shifting steps: 100) for x-ray source at 30 keV and view angle 0° (a), 30 keV and 45° (b), 80 keV and 0° (c), and 80 keV and 45° (d).

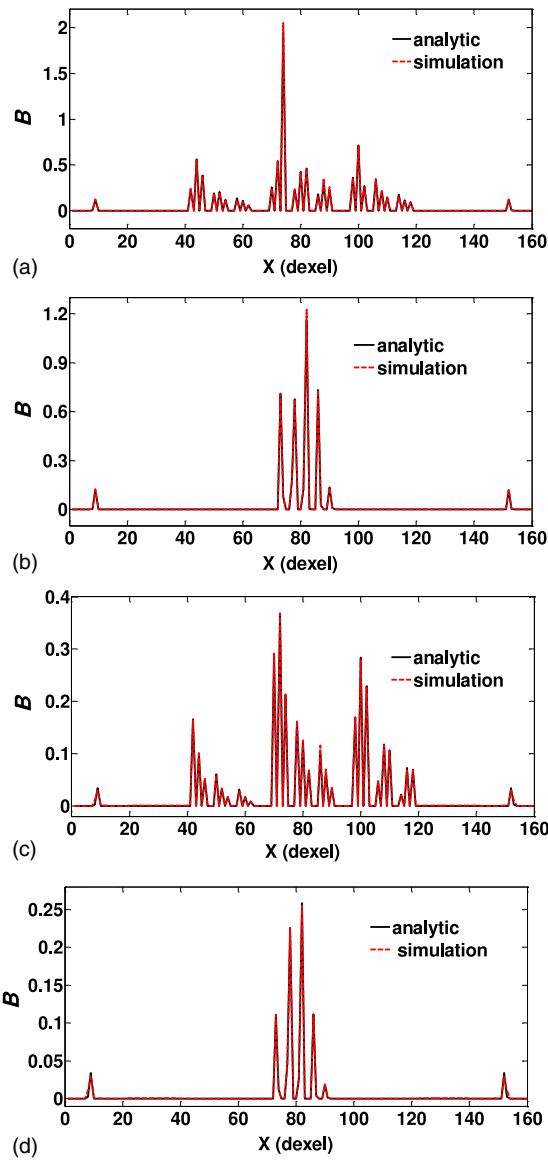


Fig. 4. Profiles of dark-field contrast defined by Eqs. (4) and (5) obtained using Eqs. (43), (42), (26), (24), (21), and (8) compared with the noiseless simulation result (baseline reference, G_2 shifting steps: 100) for x-ray source at 30 keV and view angle at 0° (a), 30 keV and 45° (b), 80 keV and 0° (c), and 80 keV and 45° (d).

the quantity calculated using the right side of Eq. (44) at the same angularizations are plotted in Figs. 5(a)–5(d), in which Eqs. (42), (26), (24), (21), and (8) are used. Meanwhile, the profiles of the zeroth-order Fourier coefficient, the dark-field contrast defined by Eqs. (4) and (5) [the left side of Eq. (43)], and the relative phase shift of the intensity oscillations [the left side of Eq. (44)] which are obtained from the modeling and noiseless simulation of the differential phase contrast imaging system, are plotted in Fig. 3(a)–3(d), 4(a)–4(d), and 5(a)–5(d) as reference (dashed lines). From Figs. 3–5, it is observed that for x-ray sources at 30 and 80 keV, the zeroth-order Fourier coefficient, the dark-field contrast defined by Eq. (4) and (5), and the relative phase shift of the intensity oscillations obtained with Eqs. (28), (43), and (44) agree very well with the simulation results (the references). It should be pointed out that

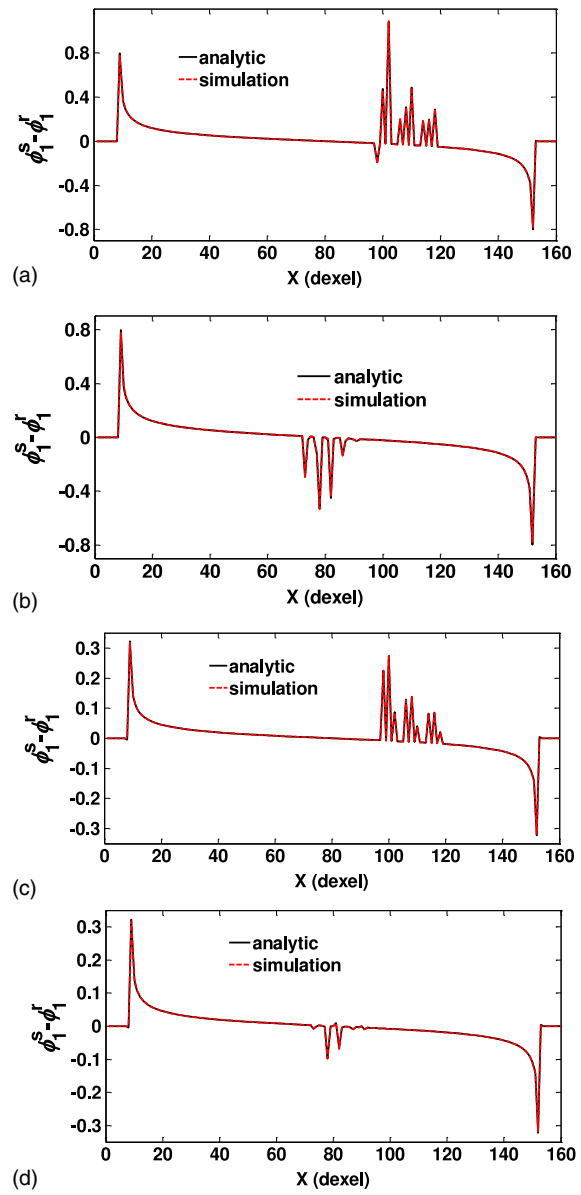


Fig. 5. Profiles of the relative phase shift of the intensity oscillations obtained using Eqs. (44), (42), (26), (24), (21), and (8) compared with the noiseless simulation result (baseline reference, G_2 shifting steps: 100) for x-ray source at 30 keV and view angle at 0° (a), 30 keV and 45° (b), 80 keV and 0° (c), and 80 keV and 45° (d).

although the phase-attenuation duality approach holds only for x-ray sources at high photon energies, the analytic formulae we derive in this work to characterize the zeroth- and first-order Fourier coefficients, i.e., Eqs. (28) and (29), or equivalently Eqs. (28) and (42)–(44), are valid for an x-ray source at any energy, as illustrated in Figs. 3–5. Hence, Eqs. (28) and (42)–(44) may form a theoretical foundation for extensive investigation of x-ray imaging implemented with Talbot interferometry.

4.B. Retrieval of complex dark-field contrast

From the zeroth- and first-order Fourier coefficients obtained from the modeling and simulation of the differential phase contrast imaging system with x-ray source at 80 keV,

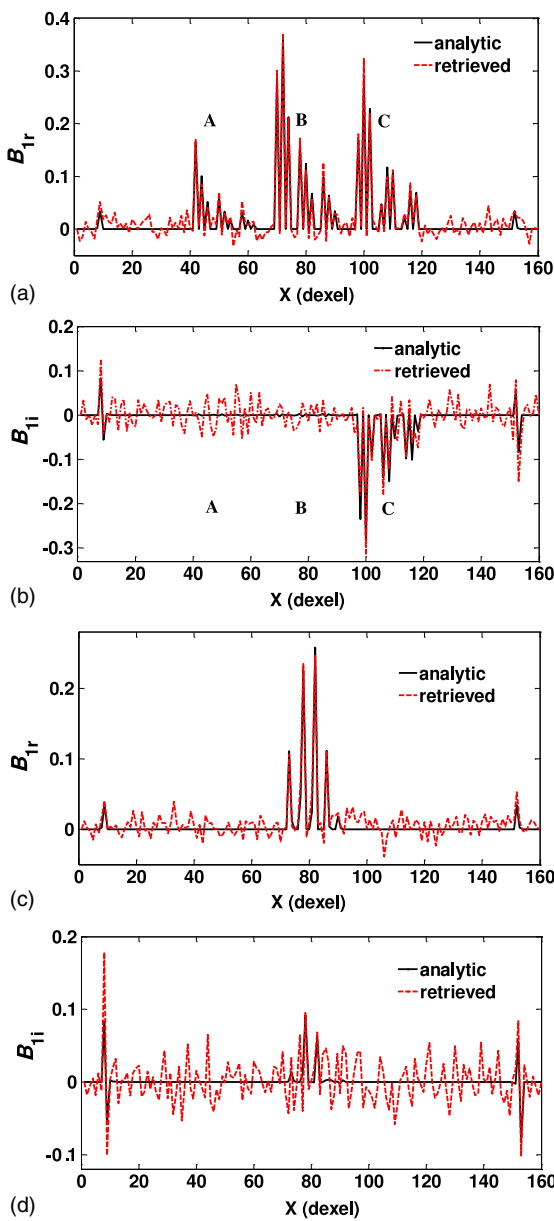


FIG. 6. Profiles of the real and imaginary parts of complex dark-field contrast retrieved using Eq. (43) and by the proposed method [Eqs. (44) and (50)] compared with that is analytically calculated using Eqs. (42), (26), (24), (21), and (8) for x-ray source at 80 keV and view angles at 0° (a, b) and 45° (c, d) (G_2 shifting steps: 20; exposure: 1.0×10^8 photon/cm 2 per image).

the real part of complex dark-field contrast is retrieved using Eq. (43), while the imaginary part of complex dark-field contrast is retrieved for imaging by using the proposed method based on the phase-attenuation duality [Eqs. (44) and (50)]. The profiles of the retrieved real and imaginary parts of the complex dark-field contrast over x_m at 0° and 45° view angles are plotted in Figs. 6(a)–6(d), respectively. Meanwhile, the profiles corresponding to the real and imaginary parts of complex dark-field contrast that are analytically calculated using Eq. (42) are also plotted in Figs. 6(a)–6(d) as references. It is observed that the complex dark-field contrast retrieved using Eq. (43) and the phase-attenuation duality based method proposed in this work agree well with the analytical result.

In addition, as illustrated in Figs. 6(a) and 2(a), all three regions A, B, and C where subpixel microstructures exist can generate significant signals corresponding to the dark-field contrast defined by Eqs. (4) and (5), or the amplitude-based dark-field contrast, but only region C where the microstructures are equilateral triangle plates generates significant signal corresponding to the imaginary part of complex dark-field contrast, or the phase-based dark-field contrast. The absence of signal corresponding to the imaginary part of the complex dark-field contrast in regions A and B can be attributed to the fact that the shape of the microstructures in regions A and B is spatially symmetric. Though the discs in regions A and B are not distributed randomly, the symmetry in their shape may cause the probability that $\Delta\Phi_x(x,y;d_c)$ defined by Eq. (26) falls into an interval around a value F is the same as that around the value $-F$. Then, Eq. (40) can apply and finally leads to a negligible imaginary part of the complex dark-field contrast. Furthermore, a close inspection of Figs. 2(a)–2(c), 6(a) and 6(b) shows that both the real and imaginary parts of complex dark-field contrast decrease with the dimension of microstructures, and are dependent on the distribution pattern and orientation of the subpixel microstructures.

4.C. Tomographic imaging of phase contrast

Under the existing theoretical framework of x-ray differential phase contrast imaging implemented with Talbot interferometry, the differential phase contrast can be directly retrieved from the relative phase shift of intensity oscillations using Eq. (3). Subsequently, the retrieved differential phase contrast can be employed to reconstruct tomographic images corresponding to the phase contrast. The tomographic images corresponding to the phase contrast and reconstructed from data acquired at 30 and 80 keV using Eq. (3) are presented in Figs. 7(a), 7(b), 8(a) and 8(b), respectively. It is observed that the subpixel microstructures in region C generate streak artifacts. This is due to the fact that, according to Eq. (41), (38), and (39), the imaginary part of the complex dark-field contrast or the phase component of the complex visibility contrast is a nonlinear function of phase shift $\Phi(x,y)$ and the deviation of the differential phase shift from its mean $\Delta\Phi_x(x,y;d_c)$. The nonlinear relationship results in inconsistency in the projection and generates streak artifacts in the reconstructed image. It is also important to note that, since the refractive index decrement δ decreases with x-ray energy, the streak artifacts in the images acquired at 30 keV are stronger than those at 80 keV.

5. DISCUSSIONS

We investigate the contrast generated by the subpixel microstructures of an object in the x-ray dark-field imaging method implemented with Talbot interferometer. Instead of assuming that the object's subpixel microstructures distribute randomly, we only assume that an object's attenuation projection $\Lambda(x,y)$ and phase shift $\Phi(x,y)$ vary at a characteristic size that is not smaller than the grating period g_2 and the

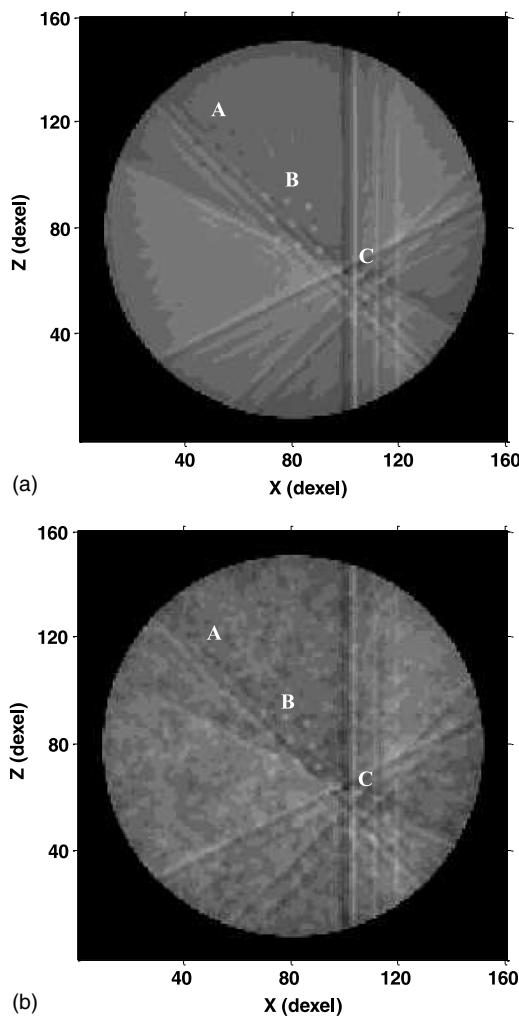


Fig. 7. Using Eq. (3), the phase contrast tomographic images reconstructed from the noiseless projection data simulated at 30 keV (G_2 shifting steps: 100) (a) and the projection data simulated at exposure 1.0×10^8 photon/cm 2 per angular position (G_2 shifting steps: 20) (b).

characteristic length d_c . Based on the Fresnel–Kirchhoff diffraction theory under the paraxial condition, we derive the analytic formulae to characterize the zeroth- and first-order Fourier coefficients $C_0(m,n)$ and $C_1(m,n)$ of the x-ray irradiance recorded at the detector cell index by (m,n) . The concept of complex dark-field contrast is introduced and the equations governing the complex dark-field contrast are derived. Special emphasis is placed on the imaginary part of complex dark-field contrast. In addition, for soft tissues to be imaged with x-ray Talbot interferometry at high x-ray energies, we propose a method based on the phase-attenuation duality to retrieve the imaginary part for potential imaging applications. A computer simulation study with a specially designed numerical phantom is carried out to validate the derived analytic formulae and the proposed retrieval method. Below is a summary of the major points we want to make based on our findings in this work.

A number of studies have been conducted to investigate how the dark-field contrast defined by Eqs. (4) and (5) is determined by the fine features of an object to be imaged, or, in

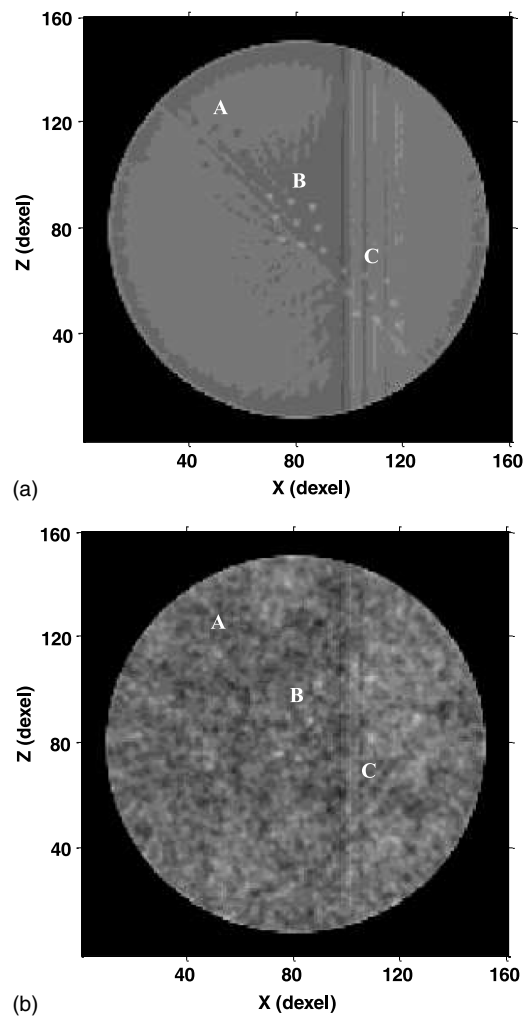


Fig. 8. Using Eq. (3), the phase contrast tomographic images reconstructed from the noiseless projection data simulated at 80 keV (G_2 shifting steps: 100) (a) and the projection data simulated at exposure 1.0×10^8 photon/cm 2 per angular position (G_2 shifting steps: 20) (b).

other words, how $a_1(m,n)/a_0(m,n)$ —the normalized oscillation amplitude^{6,17}—is affected by the object's unresolvable features. Recently, Modregger *et al.*^{19,20} demonstrated that small-angle x-ray scattering with an asymmetric distribution of scattering angles contributes to the phase signal $(\phi_1^s - \phi_1^r)$. In addition, they derived an analytic formula to characterize the influence of asymmetric scattering distribution on the phase signal.²⁰ In this work, our effort also focuses on investigation of the influence of an object's subpixel microstructures on $\phi_1(m,n)$, the phase of the first-order Fourier coefficient $C_1(m,n)$ [see Eq. (19)]. However, unlike Modregger *et al.*²⁰ who carried out the derivation with the use of a scattering-based approach,¹⁹ we derive the analytic formula from first-principle wave calculations to characterize the dark-field contrast that is formed through the mechanism of small-angle x-ray scattering by the object's subpixel microstructures. As a result, in the analytic formula derived by us, the dark-field contrast is explicitly quantified in the terms of the object's phase shift [see Eq. (42)], which, according to Eq. (46), is closely related to the electron density distribution in the object to be imaged.

In addition, we generalize the dark-field contrast that is a real quantity as defined in Eqs. (4) and (5) into a complex quantity in a way such that the dark-field contrast defined in Eqs. (4) and (5) is just the real part of the complex dark-field contrast derived in this work, while the effect of the object's subpixel microstructures on $\phi_1(m,n)$ is the imaginary part. We also propose an approximate method to retrieve the imaginary part of the complex dark-field contrast for imaging based on the phase-attenuation duality. The simulation study shows that the subpixel microstructures that form a highly ordered distribution inside an object may generate a complex dark-field contrast with an imaginary part that is comparable to the dark-field contrast defined by Eqs. (4) and (5) in intensity (see Fig. 6). Furthermore, our simulation shows that for a grating-based x-ray phase contrast imaging system implemented at 80 keV, the imaginary part of the complex dark-field contrast retrieved using the phase-attenuation duality based method agrees well with the analytic results. It should be noted that, owing to its ability to penetrate dense or thick objects and its potential for radiation dose reduction, a higher energy x-ray may benefit the grating-based phase contrast imaging methods or systems in preclinical and eventually clinical applications^{17,32,33}. However, a large area analyzer grating G_2 with a high aspect ratio is necessary for the x-ray Talbot interferometry to function at high energy.³³ For example,³⁴ for an analyzer grating made of gold and with 2.4 μm period, to achieve a reasonable imaging contrast, the transmission of absorbing lamella should be at least below 20%. Thus a gold thickness of 170 μm or more and a depth-to-period ratio of 71 or more are needed for energy of 100 keV. Though the fabrication of large and high aspect-ratio grating is still a challenge, significant progress in the manufacturing process has been made and routine application of differential phase contrast imaging implemented with Talbot interferometry at high energies might become available soon.^{33–35}

It is observed in Figs. 6(a) and 6(b) that, in comparison to the dark-field contrast defined by Eqs. (4) and (5), i.e., the real part of the complex dark-field contrast, the imaginary part of the complex dark-field contrast exhibits significantly stronger selectivity on the shape of the object's subpixel microstructures. Such a difference in the shape selectivity should be readily understandable if we inspect Eqs. (38), (39), and (41) in detail. Equation (41) indicates that the imaginary part of the complex dark-field is the negative phase of the complex visibility contrast $V_1(m,n)$, and thus should be closely relevant to the imaginary part of $V_1(m,n)$. On the other hand, according to Eqs. (38) and (39), the imaginary part of the complex visibility contrast is determined by M_{2k+1} , $k = 0, 1, 2, \dots$, a weighted average of the terms with the deviation $\Delta\Phi_x(x,y;d_c)$ in odd power [see Eq. (26)], and thus is strongly dependent on the asymmetry of the microstructures' shape, or the asymmetry of scattering angle distribution.^{19,20} Hence, it should not be hard to understand that the imaginary part of the complex dark-field is more sensitive to the microstructures' asymmetry in shape than the real part, which, according to Eq. (41), is the negative logarithm of the magnitude of the complex visibility contrast $V_1(m,n)$. Because of the significant difference in shape selectivity between the real and imaginary parts of

the complex dark-field contrast, an imaging of the imaginary part of the complex dark-field contrast may provide additional information complementary to that corresponding to the attenuation contrast, phase contrast, and dark-field contrast defined by Eqs. (4) and (5). Moreover, we would like to point out that the strong shape selectivity of the imaginary part of complex dark-field contrast may be used for advanced biomedical applications with nanoparticulated microstructures as the contrast agent.

It is also observed in Figs. 6(a)–6(d) that both the projections corresponding to the real and imaginary parts of complex dark-field contrast are strongly dependent on the view angle at which the projection is acquired, or equivalently, on the orientation of the object's subpixel microstructures. A close inspection of the simulation results shows us that the signal generated by the imaginary part of the complex dark-field contrast is strong enough to be visible in the projection acquired at certain angulations. Hence, similar to the so-called directional dark-field imaging that was studied by Jensen *et al.*,^{36,37} the projection corresponding to the real and imaginary parts of dark-field contrast can be used to extract orientational information of microstructures at a dimension that is beyond the spatial resolution of a detection system. In addition, such an orientational selectivity may enhance the biomedical imaging with nanoparticulated microstructures as the contrast agent.

It has been demonstrated^{19,20} that asymmetric scattering distribution leads to systematic errors in the retrieval of differential phase contrast by using Eq. (3). Similar to Modregger *et al.*,²⁰ in this study we generalize Eq. (3) into Eq. (44) by explicitly taking the effect of an object's subpixel microstructures into account. The deviation of Eq. (3) into Eq. (44) is quantified by the imaginary part of the complex dark-field contrast, which, according to Eq. (42), is solely determined by the subpixel microstructures of an object and is nonlinear with respect to the phase shift and the differential phase shift. Hence, it is straightforward to understand that Eq. (3) no longer holds when the imaginary part of the complex dark-field contrast is not negligible, and Eq. (44) is a more general theoretical treatment than Eq. (3) for phase contrast characterization. In addition, the non-negligible imaginary part of complex dark-field contrast may result in an inconsistency in the x-ray transform. As a result, if Eq. (3) is still used to reconstruct the tomographic images corresponding to x-ray phase contrast for highly ordered microstructures, streak artifacts can appear in the reconstructed images, as observed in Figs. 7 and 8. Our investigation on the invalidity of Eq. (3) in the highly ordered microstructures of an object is of theoretical significance, because, from the very beginning, Eq. (3) has been serving as a theoretical foundation for x-ray phase contrast CT implemented with Talbot interferometry.

6. CONCLUSIONS

Both theoretical analysis and computer simulation study based on the paraxial Fresnel–Kirchhoff theory show that the effect of an object's subpixel microstructures on x-ray phase

contrast imaging implemented with Talbot interferometry can be characterized by a complex dark-field contrast. The imaginary part of complex dark-field contrast quantifies the influence of the object's subpixel microstructures on the phase of the first-order Fourier coefficient, which can be retrieved for imaging using the proposed method based on the phase-attenuation duality for soft tissues to be imaged with Talbot interferometry at high x-ray energy. The x-ray imaging corresponding to the imaginary part of complex dark-field contrast can provide additional and complementary information to that corresponding to the attenuation contrast, phase contrast, and the existing dark-field contrast. Therefore, it is believed that the theoretical derivation and simulation findings presented in this paper may provide a foundation for the exploration of extensive biomedical applications by making use of this new imaging mechanism.

ACKNOWLEDGMENTS

This work is partially supported by the Telemedicine and Advanced Technology Research Center (TATRC) at the U.S. Army Medical Research and Material Command (US-AMRMC) Fort Detrick, MD via the award under Contract No. W81XWH-12-1-0138. In addition, one of the authors (Y. Y.) wishes to thank Dr. Yu Zou for helpful discussion and the authors would like to extend their appreciation to Ms. Jessica Paulishen for her proof reading of this paper.

APPENDIX: DERIVATION OF THE FOURIER COEFFICIENTS FOR THE INTERFERENCE FRINGE INTENSITY IN THE GRATING-BASED DIFFERENTIAL PHASE CONTRAST IMAGING

Supposing grating G_2 is linearly shifted along the transverse direction x_g , the mean intensity of interference fringe intensity recorded at the detector cell indexed by (m,n) is^{13,38}

$$I_{m,n}(x_g) = \frac{1}{l_d^2} \int_{-l_d/2}^{l_d/2} dy \int_{-l_d/2}^{l_d/2} dx |E_{x_g}(x_m + x, y_n + y, z_2)|^2, \quad (\text{A1})$$

where

$$x_m = \left(m + \frac{1}{2}\right) l_d, \quad m = 0, \pm 1, \pm 2, \dots, \quad (\text{A2})$$

$$y_n = \left(n + \frac{1}{2}\right) l_d, \quad n = 0, \pm 1, \pm 2, \dots, \quad (\text{A3})$$

l_d is the detector cell dimension, $E_{x_g}(x, y, z_2)$ is the electric field at location (x, y, z_2) , and z_2 is the distance between the detector and x-ray source along the direction of x-ray propagation. The incident x-ray beam is assumed as a monochromatic plane wave with wavelength λ and amplitude E_0 . G_1 is a phase grating and G_2 is an absorption grating with 50% duty cycle. The distance from G_1 to G_2 is selected as the m_T -th fractional Talbot distance

$$z_T = m_T \frac{g_1^2}{8\lambda}, \quad m_T = 1, 3, 5, \dots, \quad (\text{A4})$$

where g_1 is the pitch of the phase grating G_1 . In order to maximize the interference fringe visibility, one usually sets

$$g_1 = 2g_2, \quad (\text{A5})$$

where g_2 is the pitch of grating G_2 . Furthermore, we focus on the grating-based differential phase contrast imaging system with its detector cell dimension l_d being large enough to satisfy

$$l_d \gg g_2 \quad \text{and} \quad l_d \gg d_c, \quad (\text{A6})$$

where d_c is a length given by

$$d_c = \frac{\lambda z_T}{g_2} = \frac{m_T}{2} g_2, \quad (\text{A7})$$

in which Eqs. (A4) and (A5) are used. Let G_1 and G_2 be analytically represented as

$$P_1(x) = (-1)^n, \quad \text{for } n \frac{g_1}{2} \leq x < (n+1) \frac{g_1}{2}, \\ n = 0, \pm 1, \pm 2, \dots, \quad (\text{A8})$$

$$P_2(x, x_g) = \frac{1 + (-1)^n}{2}, \quad \text{for } n \frac{g_2}{2} \leq x - x_g < (n+1) \frac{g_2}{2}, \\ n = 0, \pm 1, \pm 2, \dots \quad (\text{A9})$$

Since the projection approximation^{13,15,28} can be used to estimate the electrical field immediately behind the object to be imaged and the paraxial approximation holds valid in the x-ray's propagation from G_1 to G_2 ^{8,13,15,28}, the electric field at (x, y, z_2) in the detector can be written as³⁸

$$E_{x_g}(x, y, z_{2b}) = \frac{E_0}{i\lambda z_T} \exp\left(2\pi i \frac{z_2}{\lambda}\right) P_2(x, x_g) \\ \times \int_{-L_y/2}^{L_y/2} dy_1 \int_{-L_x/2}^{L_x/2} dx_1 P_1(x_1) \\ \times \exp\left(-\frac{1}{2} \Lambda(x_1, y_1) - i\Phi(x_1, y_1)\right) \\ \times \exp\left(i\pi \frac{(x - x_1)^2 + (y - y_1)^2}{\lambda z_T}\right), \quad (\text{A10})$$

where

$$\Lambda(x, y) = \frac{4\pi}{\lambda} \int_Z \beta(x, y, z) dz, \quad (\text{A11})$$

$$\Phi(x, y) = \frac{2\pi}{\lambda} \int_Z \delta(x, y, z) dz \quad (\text{A12})$$

are the projection of linear attenuation index β and refractive index decrement δ , respectively, along x-ray propagation path z . L_x and L_y are the dimensions of gratings along the x and y directions, respectively.

Substituting Eq. (A10) into Eq. (A1), and noting the fact that

$$P_2(x, x_g) P_2^*(x, x_g) = P_2(x, x_g), \quad (\text{A13})$$

we get

$$\begin{aligned}
I_{m,n}(x_g) &= \frac{|E_0|^2}{\lambda^2 l_d^2 z_T^2} \int_{x_m-l_d/2}^{x_m+l_d/2} dx \int_{y_n-l_d/2}^{y_n+l_d/2} dy P_2(x, x_g) \\
&\times \int_{-L_x/2}^{L_x/2} dx_1 \int_{-L_y/2}^{L_y/2} dy_1 P_1(x_1) \exp\left(-\frac{1}{2}\Lambda(x_1, y_1) - i\Phi(x_1, y_1)\right) \exp\left(i\pi \frac{(x-x_1)^2 + (y-y_1)^2}{\lambda z_T}\right) \\
&\times \int_{-L_x/2}^{L_x/2} dx_2 \int_{-L_y/2}^{L_y/2} dy_2 P_1^*(x_2) \exp\left(-\frac{1}{2}\Lambda(x_2, y_2) + i\Phi(x_2, y_2)\right) \exp\left(-i\pi \frac{(x-x_2)^2 + (y-y_2)^2}{\lambda z_T}\right). \tag{A14}
\end{aligned}$$

Since $P_1(x)$ and $P_2(x, x_g)$ are periodic functions with periods g_1 and g_2 , respectively, they can be expressed in Fourier series

$$P_1(x) = - \sum_{j=-\infty}^{\infty} \frac{2i}{\pi(2j+1)} \exp\left(i \frac{2\pi(2j+1)}{g_1} x\right), \tag{A15}$$

$$P_2(x, x_g) = \frac{1}{2} \sum_{l=-\infty}^{\infty} \exp\left(-i \frac{\pi}{2} l\right) \text{sinc}\left(\frac{l}{2}\right) \exp\left[i \frac{2\pi l}{g_2} (x - x_g)\right], \tag{A16}$$

where the sinc function is defined as $\text{sinc}(x) = \sin(\pi x)/(\pi x)$. Substituting Eqs. (A15) and (A16) into (A14) leads to

$$\begin{aligned}
I_{m,n}(x_g) &= \frac{2|E_0|^2}{\pi^3 \lambda^2 z_T^2} \sum_{l=-\infty}^{\infty} \exp\left(-2\pi i l \left(\frac{x_g}{g_2} + \frac{1}{4}\right)\right) \text{sinc}\left(\frac{l}{2}\right) \sum_{j_1=-\infty}^{\infty} \sum_{j_2=-\infty}^{\infty} \frac{\exp\left(\pi i l \frac{j_1+j_2+1}{2} m_T\right)}{(2j_1+1)(2j_2+1)} \\
&\times \int_{-L_x/2}^{L_x/2} dx_1 \int_{-L_y/2}^{L_y/2} dy_1 \int_{-L_x/2}^{L_x/2} dx_2 \int_{-L_y/2}^{L_y/2} dy_2 \exp\left(2\pi i (j_1 - j_2 + l) \frac{x_1 + x_2}{2g_2}\right) \\
&\times \exp\left(-\frac{\Lambda(x_1, y_1) + \Lambda(x_2, y_2)}{2} - i\Phi(x_1, y_1) + i\Phi(x_2, y_2)\right) \text{sinc}\left(\frac{x_2 - x_1 + ld_c}{d_f}\right) \text{sinc}\left(\frac{y_2 - y_1}{d_f}\right) \\
&\times \exp\left(2\pi i \frac{x_m - \frac{j_1+j_2+1}{2} d_c - \frac{x_1+x_2}{2}}{l_d} \frac{x_2 - x_1 + ld_c}{d_f}\right) \times \exp\left(2\pi i \frac{y_n - \frac{y_1+y_2}{2}}{l_d} \frac{y_2 - y_1}{d_f}\right), \tag{A17}
\end{aligned}$$

in which Eq. (A4)–(A5) are used, and

$$d_f = \frac{\lambda z_T}{l_d} = \frac{d_c}{l_d/g_2}. \tag{A18}$$

Equation (A17) means that the intensity $I_{m,n}(x_g)$ is a periodic function of x_g with period g_2 and thus can be expanded into a

Fourier series

$$I_{m,n}(x_g) = \sum_{l=-\infty}^{\infty} C_l(m, n) \exp\left(2\pi i l \frac{x_g}{g_2}\right), \tag{A19}$$

with the Fourier coefficient given by

$$\begin{aligned}
C_l(m, n) &= \frac{4|E_0|^2}{\pi^3 \lambda^2 z_T^2} \exp\left(i \frac{l}{2} \pi\right) \frac{\sin(\frac{l}{2} \pi)}{l} \sum_{j_1=-\infty}^{\infty} \sum_{j_2=-\infty}^{\infty} \frac{\exp\left(-\pi i l \frac{j_1+j_2+1}{2} m_T\right)}{(2j_1+1)(2j_2+1)} \\
&\times \int_{-L_x/2}^{L_x/2} dx_1 \int_{-L_y/2}^{L_y/2} dy_1 \int_{-L_x/2}^{L_x/2} dx_2 \int_{-L_y/2}^{L_y/2} dy_2 \exp\left(2\pi i (j_1 - j_2 - l) \frac{x_1 + x_2}{2g_2}\right) \\
&\times \exp\left(-\frac{\Lambda(x_1, y_1) + \Lambda(x_2, y_2)}{2} - i\Phi(x_1, y_1) + i\Phi(x_2, y_2)\right) \text{sinc}\left(\frac{x_2 - x_1 - ld_c}{d_f}\right) \text{sinc}\left(\frac{y_2 - y_1}{d_f}\right) \\
&\times \exp\left(2\pi i \frac{x_m - \frac{j_1+j_2+1}{2} d_c - \frac{x_1+x_2}{2}}{l_d} \frac{x_2 - x_1 - ld_c}{d_f}\right) \exp\left(2\pi i \frac{y_n - \frac{y_1+y_2}{2}}{l_d} \frac{y_2 - y_1}{d_f}\right). \tag{A20}
\end{aligned}$$

On the other hand, we can rewrite Eq. (A19) in a well-known form

$$I_{m,n}(x_g) = a_0(m,n) + \sum_{l=1}^{\infty} a_l(m,n) \cos\left(2\pi l \frac{x_g}{g_2} + \phi_l(m,n)\right). \quad (\text{A21})$$

Comparing Eq. (A21) with Eq. (A19), we obtain

$$a_0(m,n) = C_0(m,n), \quad (\text{A22})$$

$$\frac{a_1(m,n)}{2} \exp(i\phi_1(m,n)) = C_1(m,n). \quad (\text{A23})$$

Equations (A22) and (A23) mean that all information needed for the formation of attenuation contrast, differential phase contrast, and dark-field contrast is available in the zeroth- and first-order Fourier coefficients $C_0(m,n)$ and $C_1(m,n)$. Because of the two sinc functions on the right side of Eq. (A20), the dominant contribution to the Fourier coefficients $C_l(m,n)$ ($l = 0, 1$) comes from the electric field at locations (x_1, y_1) and (x_2, y_2) that satisfies

$$|x_2 - x_1 - ld_c| \ll d_f \ll d_c \quad \text{and} \quad |y_2 - y_1| \ll d_f \ll d_c, \quad (\text{A24})$$

in which Eqs. (A18) and (A6) are used. In this study we assume that $\Lambda(x,y)$ and $\Phi(x,y)$ vary with characteristic sizes that are not smaller than g_2 and d_c (namely, characteristic size condition). Noting that

$$x_1 = \frac{x_1 + x_2 - ld_c}{2} - \frac{x_2 - x_1 - ld_c}{2}, \\ y_1 = \frac{y_1 + y_2}{2} - \frac{y_2 - y_1}{2}, \quad (\text{A25})$$

$$x_2 = \frac{x_1 + x_2 + ld_c}{2} + \frac{x_2 - x_1 - ld_c}{2}, \\ y_2 = \frac{y_1 + y_2}{2} + \frac{y_2 - y_1}{2}, \quad (\text{A26})$$

it should be straightforward for us to understand that, given (x_1, y_1) and (x_2, y_2) that satisfy the condition specified by Eq. (A24), $\Lambda(x_1, y_1)$, and $\Phi(x_1, y_1)$ can be expanded into Taylor series around $((x_1 + x_2 - ld_c)/2, (y_1 + y_2)/2)$, and $\Lambda(x_2, y_2)$ and $\Phi(x_2, y_2)$ can be expanded into Taylor series around $((x_1 + x_2 + ld_c)/2, (y_1 + y_2)/2)$. As $\Lambda(x,y)$ and $\Phi(x,y)$ meet the characteristic size condition, we may approximate the projections $\Lambda(x,y)$ and $\Phi(x,y)$ with a zeroth-order Taylor expansion, i.e.,

$$\Lambda(x_1, y_1) \approx \Lambda\left(\frac{x_1 + x_2 - ld_c}{2}, \frac{y_1 + y_2}{2}\right), \quad (\text{A27})$$

$$\Lambda(x_2, y_2) \approx \Lambda\left(\frac{x_1 + x_2 + ld_c}{2}, \frac{y_1 + y_2}{2}\right), \quad (\text{A28})$$

$$\Phi(x_1, y_1) \approx \Phi\left(\frac{x_1 + x_2 - ld_c}{2}, \frac{y_1 + y_2}{2}\right), \quad (\text{A29})$$

$$\Phi(x_2, y_2) \approx \Phi\left(\frac{x_1 + x_2 + ld_c}{2}, \frac{y_1 + y_2}{2}\right). \quad (\text{A30})$$

On the other hand, since $L_x \gg l_d$ is always satisfied in x-ray phase contrast imaging implemented with the Talbot interferometry, changing the domain of integration in Eq. (A20) from $[-L_x/2, L_x/2]$ and $[-L_y/2, L_y/2]$ to $(-\infty, \infty)$ can only lead to a negligible error. Hence, inserting Eqs. (A27)–(A30) into Eq. (A20), changing the variables of integration with

$$u = \frac{x_1 + x_2}{2}, \quad v = \frac{x_2 - x_1}{2}, \quad (\text{A31})$$

$$\sigma = \frac{y_1 + y_2}{2}, \quad \eta = \frac{y_2 - y_1}{2}, \quad (\text{A32})$$

and replacing L_x and L_y with ∞ (Ref. 13), we can approximate the Fourier coefficients as

$$C_l(m,n) = \frac{|E_0|^2}{\pi^3 l_d^2} \exp\left(i \frac{l}{2} \pi\right) \frac{\sin(\frac{l}{2} \pi)}{l} \sum_{j_1=-\infty}^{\infty} \sum_{j_2=-\infty}^{\infty} \frac{\exp(-\pi i l \frac{j_1+j_2+1}{2} m_T)}{(2j_1+1)(2j_2+1)} \\ \times \int_{-\infty}^{\infty} du \int_{-\infty}^{\infty} d\sigma \exp\left(2\pi i(j_1 - j_2 - l) \frac{u}{g_2}\right) \\ \times \exp\left(-\frac{\Lambda(u - l \frac{d_c}{2}, \sigma) + \Lambda(u + l \frac{d_c}{2}, \sigma)}{2} + i\Phi\left(u + l \frac{d_c}{2}, \sigma\right) - i\Phi\left(u - l \frac{d_c}{2}, \sigma\right)\right) \\ \times \left(\operatorname{sgn}\left(1 + \frac{x_m - \frac{j_1+j_2+1}{2} d_c - u}{l_d/2}\right) + \operatorname{sgn}\left(1 - \frac{x_m - \frac{j_1+j_2+1}{2} d_c - u}{l_d/2}\right) \right) \\ \times \left(\operatorname{sgn}\left(1 + \frac{y_n - \sigma}{l_d/2}\right) + \operatorname{sgn}\left(1 - \frac{y_n - \sigma}{l_d/2}\right) \right), \quad (\text{A33})$$

in which Eq. (A18) is used and $\text{sgn}(x)$ is the sign function. From Eq. (A33), we immediately get

$$\begin{aligned} C_l(m,n) = & \frac{4|E_0|^2}{\pi^3 l_d^2} \exp\left(i \frac{l}{2} \pi\right) \frac{\sin(\frac{l}{2} \pi)}{l} \\ & \times \int_{x_m-l_d/2}^{x_m+l_d/2} dx \int_{y_n-l_d/2}^{y_n+l_d/2} dy \sum_{j_1, j_2=-\infty}^{\infty} \frac{\exp(i \frac{m_T \pi}{2} (j_2 - j_1)(j_1 + j_2 + 1))}{(2j_1 + 1)(2j_2 + 1)} \exp\left(i \frac{2\pi}{g_2} (j_1 - j_2 - l)x\right) \\ & \times \exp\left(-\frac{\Lambda(x - (j_1 + j_2 + 1 + l)\frac{d_c}{2}, y) + \Lambda(x - (j_1 + j_2 + 1 - l)\frac{d_c}{2}, y)}{2}\right) \\ & \times \exp\left(i\left(\Phi\left(x - (j_1 + j_2 + 1 - l)\frac{d_c}{2}, y\right) - \Phi\left(x - (j_1 + j_2 + 1 + l)\frac{d_c}{2}, y\right)\right)\right). \end{aligned} \quad (\text{A34})$$

Again, since $\Lambda(x, y)$ and $\Phi(x, y)$ meet the characteristic size condition, it is not hard to show that the dominant contribution to the Fourier coefficients comes from the terms corresponding to the j_1 and j_2 that satisfy

$$j_1 - j_2 - l = 0. \quad (\text{A35})$$

Substituting Eq. (A35) into Eq. (A34) yields

$$C_0(m,n) = \frac{2|E_0|^2}{\pi^2 l_d^2} \int_{x_m-l_d/2}^{x_m+l_d/2} dx \int_{y_n-l_d/2}^{y_n+l_d/2} dy \sum_{j_1=-\infty}^{\infty} \frac{\exp(-\Lambda(x - (2j_1 + 1)\frac{d_c}{2}, y))}{(2j_1 + 1)^2}, \quad (\text{A36})$$

$$\begin{aligned} C_1(m,n) = & i \frac{4|E_0|^2}{\pi^3 l_d^2} \int_{x_m-l_d/2}^{x_m+l_d/2} dx \int_{y_n-l_d/2}^{y_n+l_d/2} dy \sum_{j_1=-\infty}^{\infty} \frac{\exp(-im_T j_1 \pi)}{(2j_1 + 1)(2(j_1 - 1) + 1)} \\ & \times \exp\left(-\frac{\Lambda(x - (2(j_1 - 1) + 1)\frac{d_c}{2}, y) + \Lambda(x - (2j_1 + 1)\frac{d_c}{2}, y)}{2}\right) \\ & \times \exp\left(i\left(\Phi\left(x - (2(j_1 - 1) + 1)\frac{d_c}{2}, y\right) - \Phi\left(x - (2j_1 + 1)\frac{d_c}{2}, y\right)\right)\right). \end{aligned} \quad (\text{A37})$$

Because of the factors $1/(2j_1 + 1)^2$ on the right side of Eq. (A36), the dominant contribution to the Fourier coefficient $C_0(m,n)$ comes from the terms corresponding to the j_1 that satisfy

$$|2j_1 + 1| \sim 10^0. \quad (\text{A38})$$

Due to the fact that the attenuation projection $\Lambda(x, y)$ meets the characteristic size condition and β is usually much smaller than δ , we can approximate $\Lambda(x, y)$ with a zeroth-order Taylor expansion

$$\Lambda\left(x - (2j_1 + 1)\frac{d_c}{2}, y\right) \approx \Lambda(x, y). \quad (\text{A39})$$

Using Eq. (A39) and formula³⁹

$$\sum_{j=0}^{\infty} \frac{1}{(2j + 1)^2} = \frac{\pi^2}{8}, \quad (\text{A40})$$

one may estimate the Fourier coefficient $C_0(m,n)$ as

$$C_0(m,n) = \frac{|E_0|^2}{2l_d^2} \int_{x_m-l_d/2}^{x_m+l_d/2} dx \int_{y_n-l_d/2}^{y_n+l_d/2} dy \exp(-\Lambda(x, y)). \quad (\text{A41})$$

On the other hand, noting that m_T is odd number and

$$\begin{aligned} & \sum_{j_1=-\infty}^{\infty} \frac{\exp(-im_T j_1 \pi)}{(2j_1 + 1)(2(j_1 - 1) + 1)} \exp\left(-\frac{\Lambda(x - (2(j_1 - 1) + 1)\frac{d_c}{2}, y) + \Lambda(x - (2j_1 + 1)\frac{d_c}{2}, y)}{2}\right) \\ & \times \exp\left(i\left(\Phi\left(x - (2(j_1 - 1) + 1)\frac{d_c}{2}, y\right) - \Phi\left(x - (2j_1 + 1)\frac{d_c}{2}, y\right)\right)\right), \\ & = -\frac{1}{2} \sum_{j_1=-\infty}^{\infty} \left(\frac{(-1)^{j_1}}{2j_1 + 1} + \frac{(-1)^{j_1-1}}{2(j_1 - 1) + 1} \right) \exp\left(-\frac{\Lambda(x - (2(j_1 - 1) + 1)\frac{d_c}{2}, y) + \Lambda(x - (2j_1 + 1)\frac{d_c}{2}, y)}{2}\right) \end{aligned}$$

$$\begin{aligned}
& \times \exp \left(i \left(\Phi \left(x - (2(j_1 - 1) + 1) \frac{d_c}{2}, y \right) - \Phi \left(x - (2j_1 + 1) \frac{d_c}{2}, y \right) \right) \right) \\
& = -\frac{1}{2} \sum_{j_1=-\infty}^{\infty} \frac{(-1)^{j_1}}{2j_1 + 1} \left(\exp \left(-\frac{\Lambda \left(x - (2(j_1 - 1) + 1) \frac{d_c}{2}, y \right) + \Lambda \left(x - (2j_1 + 1) \frac{d_c}{2}, y \right)}{2} \right) \right. \\
& \quad \times \exp \left(i \left(\Phi \left(x - (2(j_1 - 1) + 1) \frac{d_c}{2}, y \right) - \Phi \left(x - (2j_1 + 1) \frac{d_c}{2}, y \right) \right) \right) \\
& \quad + \exp \left(-\frac{\Lambda \left(x - (2j_1 + 1) \frac{d_c}{2}, y \right) + \Lambda \left(x - (2(j_1 + 1) + 1) \frac{d_c}{2}, y \right)}{2} \right) \\
& \quad \times \exp \left(i \left(\Phi \left(x - (2j_1 + 1) \frac{d_c}{2}, y \right) - \Phi \left(x - (2(j_1 + 1) + 1) \frac{d_c}{2}, y \right) \right) \right) \Bigg). \tag{A42}
\end{aligned}$$

Equation (A37) can be rewritten as

$$\begin{aligned}
C_1(m,n) &= -i \frac{2|E_0|^2}{\pi^3 l_d^2} \int_{x_m-l_d/2}^{x_m+l_d/2} dx \int_{y_n-l_d/2}^{y_n+l_d/2} dy \sum_{j_1=-\infty}^{\infty} \frac{(-1)^{j_1}}{2j_1 + 1} \\
&\quad \times \left(\exp \left(-\frac{\Lambda \left(x - (2j_1 + 1) \frac{d_c}{2} + d_c, y \right) + \Lambda \left(x - (2j_1 + 1) \frac{d_c}{2}, y \right)}{2} \right) \right. \\
&\quad \times \exp \left(i \left(\Phi \left(x - (2j_1 + 1) \frac{d_c}{2} + d_c, y \right) - \Phi \left(x - (2j_1 + 1) \frac{d_c}{2}, y \right) \right) \right) \\
&\quad + \exp \left(-\frac{\Lambda \left(x - (2j_1 + 1) \frac{d_c}{2}, y \right) + \Lambda \left(x - (2j_1 + 1) \frac{d_c}{2} - d_c, y \right)}{2} \right) \\
&\quad \times \exp \left(i \left(\Phi \left(x - (2j_1 + 1) \frac{d_c}{2}, y \right) - \Phi \left(x - (2j_1 + 1) \frac{d_c}{2} - d_c, y \right) \right) \right) \Bigg). \tag{A43}
\end{aligned}$$

Because $\Lambda(x, y)$ and $\Phi(x, y)$ meet the characteristic size condition, a function $f(x, y)$ that is determined by $\Lambda(x, y)$ and $\Phi(x, y)$ can be well approximated by a truncated Fourier transform

$$f(x, y) = \frac{1}{2\pi} \int_{-k_M}^{k_M} dk F_k(y) \exp(ikx), \tag{A44}$$

where

$$k_M = \frac{\pi}{d_c}. \tag{A45}$$

Using Eqs. (A44) and (A45), it is easy to show that

$$\begin{aligned}
\sum_{j=-\infty}^{\infty} \frac{(-1)^j}{2j+1} f \left(x - (2j+1) \frac{d_c}{2}, y \right) &= \frac{1}{2\pi} \int_{-k_M}^{k_M} dk F_k(y) \exp(ikx) \sum_{j=-\infty}^{\infty} \frac{(-1)^j}{2j+1} \exp \left(-i(2j+1) \frac{kd_c}{2} \right) \\
&= \frac{1}{2\pi} \int_{-k_M}^{k_M} dk F_k(y) \exp(ikx) \sum_{j=-\infty}^{\infty} \frac{(-1)^j}{2j+1} \cos \left((2j+1) \frac{kd_c}{2} \right) \\
&= \frac{\pi}{2} \frac{1}{2\pi} \int_{-k_M}^{k_M} dk F_k(y) \exp(ikx) = \frac{\pi}{2} f(x, y), \tag{A46}
\end{aligned}$$

in which the formula³⁹

$$\sum_{j=0}^{\infty} (-1)^j \frac{\cos((2j+1)\alpha)}{2j+1} = \frac{\pi}{4}, \quad |\alpha| < \frac{\pi}{2} \quad (\text{A47})$$

is used to sum the corresponding series. Applying Eq. (A46) to Eq. (A43), the Fourier coefficient $C_1(m,n)$ can be calculated as

$$\begin{aligned} C_1(m,n) &= -i \frac{|E_0|^2}{\pi^2 l_d^2} \int_{x_m-l_d/2}^{x_m+l_d/2} dx \int_{y_n-l_d/2}^{y_n+l_d/2} dy \left(\exp\left(-\frac{\Lambda(x+d_c,y)+\Lambda(x,y)}{2}\right) \right. \\ &\quad \times \exp(i(\Phi(x+d_c,y)-\Phi(x,y))) + \exp\left(-\frac{\Lambda(x,y)+\Lambda(x-d_c,y)}{2}\right) \exp(i(\Phi(x,y)-\Phi(x-d_c,y))) \Big) \\ &\approx -i \frac{2|E_0|^2}{\pi^2 l_d^2} \int_{x_m-l_d/2}^{x_m+l_d/2} dx \int_{y_n-l_d/2}^{y_n+l_d/2} dy \exp(-\Lambda(x,y)) \exp\left(i\frac{\Phi(x+d_c,y)-\Phi(x-d_c,y)}{2}\right) \\ &\quad \times \cos\left(\frac{\Phi(x+d_c,y)+\Phi(x-d_c,y)-2\Phi(x,y)}{2}\right), \end{aligned} \quad (\text{A48})$$

in which, based on a discussion the same as that for Eq. (A39), the equation

$$\Lambda(x-d_c,y) \approx \Lambda(x+d_c,y) \approx \Lambda(x,y), \quad (\text{A49})$$

is used.

It should be noted that in the derivation of the expressions of the zeroth- and first-order Fourier coefficients $C_0(m,n)$ and $C_1(m,n)$, i.e., Eqs. (A41) and (A48), we do not make assumptions that the subpixel microstructures of an object are distributed randomly.

^aAuthor to whom correspondence should be addressed. Electronic mail: xiangyang.tang@emory.edu; Telephone: (404) 778-1732; Fax: (404) 712-5813.

¹A. Momose, "Recent advances in x-ray phase imaging," *Jpn. J. Appl. Phys., Part 1* **44**, 6355–6367 (2005).

²S. A. Zhou and A. Brahme, "Development of phase-contrast X-ray imaging techniques and potential medical applications," *Phys. Med.* **24**, 129–148 (2008).

³T. Weitkamp, A. Diaz, C. David, F. Pfeiffer, M. Stampanoni, P. Cloetens, and E. Ziegler, "X-ray phase imaging with a grating interferometer," *Opt. Express* **13**, 6296–6304 (2005).

⁴F. Pfeiffer, T. Weitkamp, O. Bunk, and C. David, "Phase retrieval and differential phase-contrast imaging with low-brilliance x-ray sources," *Nat. Phys.* **2**, 258–261 (2006).

⁵A. Momose and J. Fukuda, "Phase-contrast radiographs of nonstained rat cerebellar specimen," *Med. Phys.* **22**, 375–379 (1995).

⁶F. Pfeiffer, M. Bech, O. Bunk, P. Kraft, E. F. Eikenberry, C. Bronnimann, C. Grunzweig, and C. David, "Hard-x-ray dark-field imaging using a grating interferometer," *Nat. Mater.* **7**, 134–137 (2008).

⁷M. Bech, O. Bunk, T. Donath, R. Feidenhans'l, C. David, and F. Pfeiffer, "Quantitative x-ray dark-field computed tomography," *Phys. Med. Biol.* **55**, 5529–5539 (2010).

⁸M. Bech, "X-ray imaging with a grating interferometer," Ph.D. thesis, University of Copenhagen, Denmark, 2009.

⁹A. Momose, S. Kawamoto, I. Koyama, Y. Hamaishi, K. Takai, and Y. Suzuki, "Demonstration of x-ray Talbot interferometry," *Jpn. J. Appl. Phys., Part 2* **42**, L866–L868 (2003).

¹⁰T. Michel *et al.*, "On a dark-field signal generated by micrometer-sized calcifications in phase-contrast mammography," *Phys. Med. Biol.* **58**, 2713–2732 (2013).

¹¹Z. T. Wang, K. J. Kang, Z. F. Huang, and Z. Q. Chen, "Quantitative grating-based x-ray dark-field computed tomography," *Appl. Phys. Lett.* **95**, 094105–094108 (2009).

¹²G. H. Chen, N. Bevins, J. Zambelli, and Z. Qi, "Small-angle scattering computed tomography (SAS-CT) using a Talbot-Lau interferometer and a rotating anode x-ray tube: theory and experiments," *Opt. Express* **18**, 12960–12970 (2010).

¹³W. Yashiro, Y. Terui, K. Kawabata, and A. Momose, "On the origin of visibility contrast in x-ray Talbot interferometry," *Opt. Express* **18**, 16890–16901 (2010).

¹⁴Y. I. Nesterets, "On the origins of decoherence and extinction contrast in phase-contrast imaging," *Opt. Commun.* **281**, 533–542 (2008).

¹⁵S. K. Lynch, V. Pai, J. Auxier, A. F. Stein, E. E. Bennett, C. K. Kemble, X. Xiao, W. Lee, N. Y. Morgan, and H. H. Wen, "Interpretation of dark-field contrast and particle-size selectivity in grating interferometers," *Appl. Opt.* **50**, 4310–4319 (2011).

¹⁶A. Malecki, G. Potdevin, and F. Pfeiffer, "Quantitative wave-optical numerical analysis of the dark-field signal in grating-based x-ray interferometry," *EPL* **99**, 48001 (2012).

¹⁷F. Pfeiffer, J. Herzen, M. Willner, M. Chabior, S. Auweter, M. Reiser, and F. Bamberg, "Grating-based x-ray phase contrast for biomedical imaging applications," *Z. Med. Phys.* **23**, 176–185 (2013).

¹⁸R. Raupach and T. G. Flohr, "Analytic evaluation of the signal and noise propagation in x-ray differential phase-contrast computed tomography," *Phys. Med. Biol.* **56**, 2219–2244 (2011).

¹⁹P. Modregger, F. Scattarella, B. R. Pinzer, C. David, R. Bellotti, and M. Stampanoni, "Imaging the ultrasmall-angle x-ray scattering distribution with grating interferometry," *Phys. Rev. Lett.* **108**, 048101 (2012).

²⁰P. Modregger, B. R. Pinzer, and M. Stampanoni, "A systematic error in X-ray grating interferometry due to asymmetric scattering distributions," *AIP Conf. Proc.* **1466**, 288–292 (2012).

²¹P. Modregger, Z. Wang, T. Thuering, B. Pinzer, and M. Stampanoni, "Artifacts in x-ray darkfield tomography," *AIP Conf. Proc.* **1365**, 269–272 (2011).

²²R. Fitzgerald, "Phase-sensitive x-ray imaging," *Phys. Today* **53**(7), 23–26 (2000).

²³M. Born and E. Wolf, *Principles of Optics: Electromagnetic Theory of Propagation, Interference and Diffraction of Light*, 7th ed. (Cambridge University Press, Cambridge, England, 1999).

²⁴R. A. Lewis, "Medical phase contrast x-ray imaging: Current status and future prospects," *Phys. Med. Biol.* **49**, 3573–3583 (2004).

²⁵D. Shi and M. A. Anastasio, "Relationships between smooth- and small-phase conditions in x-ray phase-contrast imaging," *IEEE Trans. Med. Imaging* **28**, 1969–1973 (2009).

²⁶X. Wu, H. Liu, and A. Yan, "X-ray phase-attenuation duality and phase retrieval," *Opt. Lett.* **30**, 379–381 (2005).

²⁷X. Wu and A. Yan, "Phase retrieval from one single phase contrast x-ray image," *Opt. Express* **17**, 11187–11196 (2009).

²⁸T. Köhler and E. Roessl, "Noise properties of grating-based x-ray phase contrast computed tomography," *Med. Phys.* **38**, S106–S116 (2011).

²⁹X. Tang, Y. Yang, and S. Tang, "Characterization of imaging performance in differential phase contrast CT compared with the conventional CT – Noise power spectrum NPS(k)," *Med. Phys.* **38**, 4386–4395 (2011).

³⁰X. Tang, Y. Yang, and S. Tang, "Characterization of imaging performance in differential phase contrast CT compared with the conventional CT: Spectrum of noise equivalent quanta NEQ(k)," *Med. Phys.* **39**, 4367–4382 (2012).

³¹A. Velroyen, M. Bech, A. Malecki, A. Tapfer, A. Yaroshenko, M. Ingrisch, C. C. Cyran, S. D. Auweter, K. Nikolaou, M. Reiser, and F. Pfeiffer, "Microbubbles as a scattering contrast agent for grating-based x-ray dark-field imaging," *Phys. Med. Biol.* **58**, N37–N46 (2013).

³²H. Hetterich *et al.*, "Grating-based X-ray phase-contrast tomography of atherosclerotic plaque at high photon energies," *Z. Med. Phys.* **23**, 194–203 (2013).

³³M. Willner, M. Bech, J. Herzen, I. Zanette, D. Hahn, J. Kenntner, J. Mohr, A. Rack, T. Weitkamp, and F. Pfeiffer, "Quantitative X-ray phase-contrast computed tomography at 82 keV," *Opt. Express* **21**, 4155–4166 (2013).

³⁴J. Mohr, T. Grund, D. Kunka, J. Kenntner, J. Leuthold, J. Meiser, J. Schulz, and M. Walter, "High aspect ratio gratings for X-ray phase contrast imaging," *AIP Conf. Proc.* **1466**, 41–50 (2012).

³⁵J. Kenntner, V. Altapova, T. Grund, F. J. Pantenburg, J. Meiser, T. Baumbach, and J. Mohr, "Fabrication and characterization of analyzer gratings with high aspect ratios for phase contrast imaging using a Talbot interferometer," *AIP Conf. Proc.* **1437**, 89–93 (2012).

³⁶T. H. Jensen, M. Bech, O. Bunk, T. Donath, C. David, R. Feidenhans'l, and F. Pfeiffer, "Directional x-ray dark-field imaging," *Phys. Med. Biol.* **55**, 3317–3323 (2010).

³⁷T. H. Jensen, M. Bech, I. Zanette, T. Weitkamp, C. David, H. Deyhle, S. Rutishauser, E. Reznikova, J. Mohr, R. Feidenhans'l, and F. Pfeiffer, "Directional x-ray dark-field imaging of strongly ordered systems," *Phys. Rev. B* **82**, 214103 (2010).

³⁸Y. Yang and X. Tang, "The second-order differential phase contrast and its retrieval for imaging with x-ray Talbot interferometry," *Med. Phys.* **39**, 7237–7253 (2012).

³⁹V. Mangulis, *Handbook of Series for Scientists and Engineers* (Academic, New York, NY, 1965).

Grating-based x-ray differential phase contrast imaging with twin peaks in phase-stepping curves—phase retrieval and dewrapping

Yi Yang and Huiqiao Xie

Imaging and Medical Physics, Department of Radiology and Imaging Sciences, Emory University School of Medicine, 1701 Uppergate Dr., C-5018, Atlanta, Georgia 30322

Weixing Cai

Department of Radiation Oncology, Brigham and Women's Hospital Harvard Medical School, 75 Francis Street, Boston, Massachusetts 02115

Hui Mao

Laboratory of Functional and Molecular Imaging and Nanomedicine, Department of Radiology and Imaging Sciences, Emory University School of Medicine, 1841 Clifton Road NE, Atlanta, Georgia 30329

Xiangyang Tang^{a)}

Imaging and Medical Physics, Department of Radiology and Imaging Sciences, Emory University School of Medicine, 1701 Uppergate Dr., C-5018, Atlanta, Georgia 30322

(Received 27 June 2015; revised 22 March 2016; accepted for publication 25 April 2016; published 13 May 2016)

Purpose: X-ray differential phase contrast CT implemented with Talbot interferometry employs phase-stepping to extract information of x-ray attenuation, phase shift, and small-angle scattering. Since inaccuracy may exist in the absorption grating G_2 due to an imperfect fabrication, the effective period of G_2 can be as large as twice the nominal period, leading to a phenomenon of twin peaks that differ remarkably in their heights. In this work, the authors investigate how to retrieve and dewrap the phase signal from the phase-stepping curve (PSC) with the feature of twin peaks for x-ray phase contrast imaging.

Methods: Based on the paraxial Fresnel–Kirchhoff theory, the analytical formulae to characterize the phenomenon of twin peaks in the PSC are derived. Then an approach to dewrap the retrieved phase signal by jointly using the phases of the first- and second-order Fourier components is proposed. Through an experimental investigation using a prototype x-ray phase contrast imaging system implemented with Talbot interferometry, the authors evaluate and verify the derived analytic formulae and the proposed approach for phase retrieval and dewrapping.

Results: According to theoretical analysis, the twin-peak phenomenon in PSC is a consequence of combined effects, including the inaccuracy in absorption grating G_2 , mismatch between phase grating and x-ray source spectrum, and finite size of x-ray tube's focal spot. The proposed approach is experimentally evaluated by scanning a phantom consisting of organic materials and a lab mouse. The preliminary data show that compared to scanning G_2 over only one single nominal period and correcting the measured phase signal with an intuitive phase dewrapping method that is being used in the field, stepping G_2 over twice its nominal period and dewrapping the measured phase signal with the proposed approach can significantly improve the quality of x-ray differential phase contrast imaging in both radiograph and CT.

Conclusions: Using the phase retrieval and dewrapping methods proposed to deal with the phenomenon of twin peaks in PSCs and phase wrapping, the performance of grating-based x-ray differential phase contrast radiography and CT can be significantly improved. © 2016 American Association of Physicists in Medicine. [<http://dx.doi.org/10.1118/1.4948690>]

Key words: x-ray differential phase contrast imaging, x-ray Talbot interferometry, microfocus x-ray source, x-ray phase contrast CT, phase-stepping curve, phase retrieval, phase de-wrapping

1. INTRODUCTION

As an emerging imaging modality with great potential in a variety of applications, including medical diagnosis, biological study, and material sciences, the x-ray differential phase contrast imaging implemented with Talbot interferometry is compatible to a polychromatic x-ray source and can produce radiographic and tomographic images with higher contrast in soft tissues compared to the conventional attenuation-

based x-ray imaging.^{1–3} From a single set of projection data, this imaging method is capable of generating images corresponding to the attenuation contrast, differential phase contrast, and dark-field contrast simultaneously.^{4–6} Figure 1 shows the schematic of a Talbot interferometry with a microfocus x-ray tube and two gratings—phase grating G_1 and absorption grating G_2 ^{6,7}—that work together as a shearing interferometer to detect the wavefront alteration caused by an object in the x-ray beam.^{2,6} Keeping G_1 fixed and shifting G_2

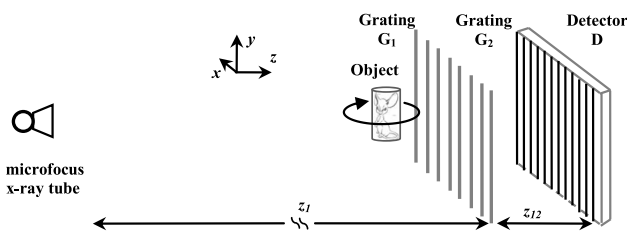


Fig. 1. Schematic of a grating based x-ray differential phase contrast CT system with a microfocus x-ray source.

along transverse direction x_g , the x-ray irradiance recorded at each detector pixel (m,n) oscillates as a periodic function of x_g , which is referred to as the phase-stepping curve (PSC), and can be expanded into a Fourier series,^{4,5}

$$I_{m,n}(x_g) = b_0(m,n) + \sum_{l=1}^{\infty} b_l(m,n) \cos\left(2\pi l \frac{x_g}{g_2} + \theta_l(m,n)\right), \quad (1)$$

where g_2 is the period of grating G_2 . Figure 2 shows two typical PSCs in a grating-based x-ray differential phase contrast imaging system. It has been well established that the images corresponding to the attenuation contrast, differential phase contrast, and dark-field contrast (or visibility contrast) can be acquired from the PSCs' zeroth- and first-order Fourier components b_0 , θ_1 , and b_1 , respectively, via the following equations:^{4,5}

$$\Lambda(m,n) = \ln\left(\frac{b_0^s(m,n)}{b_0^r(m,n)}\right), \quad (2)$$

$$\partial_x \Phi(m,n) = \frac{g_2}{\lambda z_{12}} (\theta_1^s(m,n) - \theta_1^r(m,n)), \quad (3)$$

$$V(m,n) = \frac{b_1^s(m,n)/b_0^s(m,n)}{b_1^r(m,n)/b_0^r(m,n)}, \quad (4)$$

where $\Lambda(m,n)$ and $\Phi(m,n)$ denote the projection data corresponding to attenuation and phase, respectively. λ is the x-ray's wavelength, z_{12} the distance between gratings G_1 and G_2 , and superscripts "s" and "r" refer to the data obtained with and without the object to be imaged in x-ray beam. As illustrated in Fig. 2, in the PSCs generated by perfect gratings G_1 and G_2 , only one peak should be observed in g_2 —the nominal period of grating G_2 . Recently, however, it has been reported^{8,9} that the effective period of PSC may be as large as twice G_2 's nominal period g_2 , and two peaks at significantly

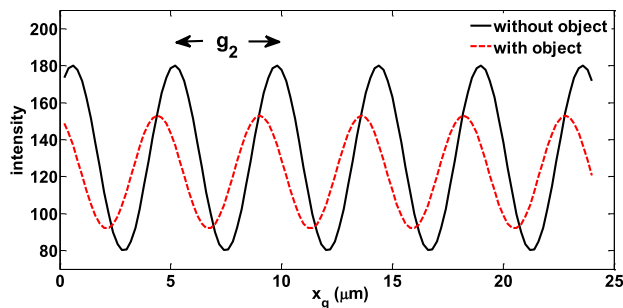


Fig. 2. The PSCs, or intensity modulation, recorded at a detector cell in an x-ray differential phase contrast imaging system, as a function of transverse grating shift x_g .

different heights can exist in the PSC over the distance $2g_2$ [see Fig. 2 in Ref. 8, Fig. 3(a) in Ref. 9, and Fig. 5 in this paper]. As a result, Eq. (1) should be rewritten as

$$I_{m,n}(x_g) = a_0(m,n) + \sum_{l=1}^{\infty} a_l(m,n) \cos\left(\pi l \frac{x_g}{g_2} + \phi_l(m,n)\right). \quad (5)$$

In order to ensure periodicity in the phase retrieval from PSC, it has been suggested^{8,9} that the absorption grating (or equivalently, the phase grating) should be shifted over double of its nominal period. Hence, instead of getting the zeroth- and first-order Fourier coefficients b_0 , θ_1 , and b_1 in Eq. (1), the zeroth-, first-, and second-order Fourier coefficients a_0 , ϕ_1 , and a_1 , and ϕ_2 and a_2 in Eq. (5) should be calculated from the PSC with an effective period of $2g_2$. To correctly acquire the information corresponding to the contrasts generated x-ray attenuation, refraction (phase), and small-angle scattering (dark-field) from the PSC with the feature of twin peaks, one should develop a theoretical framework similar to that in Eqs. (2)–(4). This is the initial motivation of our work to be presented in this paper.

Based on the paraxial Fresnel–Kirchhoff theory,⁶ we derive the analytical formulae to characterize the Fourier coefficients of the PSC with the feature of twin peaks, in which its effective period is as large as twice the nominal period of absorption grating G_2 . A set of equations similar to Eqs. (2)–(4) that can be utilized to extract information corresponding to the attenuation contrast, differential phase contrast, and dark-field contrast is derived. Furthermore, using the derived analytical formulae, we propose an approach to dewrap the retrieved phase signal by jointly using the first- and second-order Fourier components ϕ_1 and ϕ_2 . To evaluate and verify the derived analytic formulae and the proposed approaches for phase retrieval and dewrapping, an experimental investigation is conducted using a prototype x-ray phase contrast imaging system implemented with Talbot interferometry.

2. METHODS

The ground on which our study is based is that the interaction between the x-ray beam and an object to be imaged can be adequately described by the spatial distribution of the object's complex refractive index $n = 1 - \delta + i\beta$.^{10–12} Given an x-ray Talbot interferometry with twin peaks in its PSCs, we derive the analytic formulae to characterize the grating-based x-ray differential phase contrast imaging method in cone beam geometry. As illustrated in Fig. 1, the microfocus x-ray tube, phase grating G_1 , and absorption grating G_2 are placed at the planes $z = 0$, $z = z_1$, and $z = z_2 = z_1 + z_{12}$, respectively. The object to be imaged is placed in front of grating G_1 and the detector immediately behind grating G_2 .

2.A. Phenomenon of twin peaks in phase-stepping curve

We constrain our focus on the Talbot interferometry with a microfocus x-ray tube that is assumed to act as an extended incoherent source and emanate monochromatic spherical

wave at wavelength λ . Since a microfocus x-ray tube is in fact a polychromatic source, this wavelength λ should be conceived as the effective wavelength of a polychromatic x-ray source. To achieve an optimum visibility, it is quite often to design the phase grating G_1 in such a way that the resultant phase shift is π . An ideal phase grating G_1 can be represented as a projection operator¹³

$$P_1(x) = \begin{cases} 1, & ng_1 \leq x < \left(n + \frac{1}{2}\right)g_1, \\ -1, & \left(n + \frac{1}{2}\right)g_1 \leq x < (n+1)g_1, \end{cases} \quad n = 0, \pm 1, \pm 2, \dots, \quad (6)$$

where g_1 is the pitch of phase grating G_1 . Similarly, a perfect absorption grating G_2 can be expressed as another projection operator¹³

$$P_2(x) = \begin{cases} 1, & ng_2 \leq x < \left(n + \frac{1}{2}\right)g_2, \\ 0, & \left(n + \frac{1}{2}\right)g_2 \leq x < (n+1)g_2, \end{cases} \quad n = 0, \pm 1, \pm 2, \dots. \quad (7)$$

It should be noted that Eqs. (6) and (7) imply that both gratings G_1 and G_2 are designed to have a duty circle of 0.5. For an actual x-ray Talbot interferometry, the effective period of the PSC may be twice the nominal period of grating

G_2 , which may be mainly due to the imperfection in grating fabrication, according to Refs. 8 and 9. Figure 3 provides an illustration of grating G_2 's structure that is formed via a conventional fabrication process.¹⁴ It is possible, in practice, that the thickness of the gold layers at top is different from that of the layer at the bottom, leading to the fact that the effective period of absorption grating G_2 is as large as twice its nominal period g_2 . Consequently, one needs to modify the projection operator in Eq. (7) into

$$P_2(x) = \begin{cases} 1, & 2ng_2 \leq x < \left(2n + \frac{1}{2}\right)g_2, \\ 0, & \left(2n + \frac{1}{2}\right)g_2 \leq x < (2n+1)g_2, \\ W_{si}, & (2n+1)g_2 \leq x < \left(2n + \frac{3}{2}\right)g_2, \\ 0, & \left(2n + \frac{3}{2}\right)g_2 \leq x < 2(n+1)g_2, \end{cases} \quad n = 0, \pm 1, \pm 2, \dots, \quad (8)$$

where W_{si} is the relative transmission of grating G_2 's ridge compared to that of its groove. Given a wavelength λ , the phase shift by grating G_1 is designed to be π . However, a polychromatic x-ray source is usually utilized in an actual grating-based differential phase contrast imaging system. Hence, instead of using the operator in Eq. (6), a more general one

$$P_1(x) = \begin{cases} 1, & ng_1 \leq x < \left(n + \frac{1}{2}\right)g_1, \\ \exp(iQ_1), & \left(n + \frac{1}{2}\right)g_1 \leq x < (n+1)g_1, \end{cases} \quad n = 0, \pm 1, \pm 2, \dots \quad (9)$$

should be used to represent the phase grating G_1 , where Q_1 is the actual phase shift due to grating G_1 . In general, a linear shifting of grating G_2 along the direction of x_g generates an oscillation in intensity at the detector cell indexed by (m,n) , i.e., a function over x_g , which is referred to as the PSC and can be expressed as

$$I_{m,n}(x_g) = \frac{1}{l_d^2} \int_{x_m - \frac{l_d}{2}}^{x_m + \frac{l_d}{2}} dx \int_{y_n - \frac{l_d}{2}}^{y_n + \frac{l_d}{2}} dy P_2(x - x_g) I(x, y, z_2), \quad (10)$$

where

$$x_m = \left(m + \frac{1}{2}\right)l_d, \quad y_n = \left(n + \frac{1}{2}\right)l_d, \quad m, n = 0, \pm 1, \pm 2, \dots \quad (11)$$

$I(x, y, z_2)$ denotes the intensity immediately in front of grating G_2 , which can be expressed as the convolution between the

intensity generated by a point source, i.e., with infinitesimal focal spot, and the geometrical projection of the source distribution $I_{\text{source}}(x, y)$ with finite focal spot through the object on the detector,^{15,16}

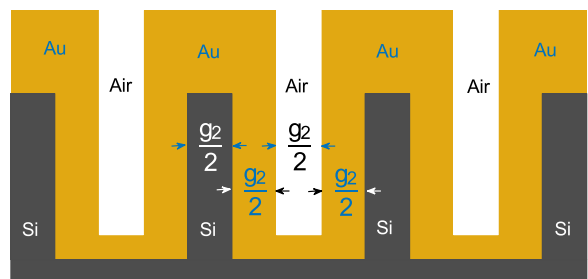


FIG. 3. Schematic of an imperfect absorption grating produced with a conventional fabrication process (Ref. 14), in which the thickness of gold above the silicon is different from that under the air.

$$I(x, y, z_2) = \frac{z_1^2}{z_{12}^2} \iint dx_0 dy_0 I_{\text{source}} \left(-\frac{z_1}{z_{12}} x_0, -\frac{z_1}{z_{12}} y_0 \right) \\ \times |E_{\text{point}}(x-x_0, y-y_0, z_2)|^2, \quad (12)$$

where $E_{\text{point}}(x, y, z_2)$ denotes the electric field produced by a point source at the origin. The distance z_{12} is selected as the m_T -th fractional Talbot distance

$$z_{12} = z_2 - z_1 = m_T \frac{g_1^2}{8\gamma\lambda}, \quad m_T = 1, 3, 5, \dots, \quad (13)$$

where

$$\gamma = \frac{z_1}{z_2}. \quad (14)$$

In order to maximize the interference fringe visibility, one usually sets

$$g_1 = 2\gamma g_2. \quad (15)$$

According to the derivation detailed in the Appendix, intensity $I_{m,n}(x_g)$ is a periodic function of x_g with period $2g_2$ and thus can be expanded into a Fourier series,

$$I_{m,n}(x_g) = \sum_{l=-\infty}^{\infty} C_l(m,n) \exp\left(\pi i l \frac{x_g}{g_2}\right), \quad (16)$$

and the zeroth-, first-, and second-order Fourier coefficients are given by

$$C_0(m,n) \\ = a_0(m,n) \\ = |A|^2 \frac{1+W_{si}}{4z_{12}^2 l_d^2} \iint dx_0 dy_0 I_{\text{source}} \left(-\frac{z_1}{z_{12}} x_0, -\frac{z_1}{z_{12}} y_0 \right) \\ \times \int_{\gamma(x_m-x_0)-\frac{\gamma l_d}{2}}^{\gamma(x_m-x_0)+\frac{\gamma l_d}{2}} du \int_{\gamma(y_n-y_0)-\frac{\gamma l_d}{2}}^{\gamma(y_n-y_0)+\frac{\gamma l_d}{2}} d\sigma \exp(-\Lambda(u,\sigma)), \quad (17)$$

$$C_1(m,n) \\ = \frac{a_1(m,n)}{2} \exp(i\phi_1(m,n)) \\ = |A|^2 \frac{\sin(\pi \frac{m_T}{8})(i-1)}{\pi^2 z_{12}^2 l_d^2} (1-W_{si}) \sin(Q_1) \\ \times \iint dx_0 dy_0 I_{\text{source}} \left(-\frac{z_1}{z_{12}} x_0, -\frac{z_1}{z_{12}} y_0 \right) \exp\left(-i\pi \frac{x_0}{g_2}\right) \\ \times \int_{\gamma(x_m-x_0)-\frac{\gamma l_d}{2}}^{\gamma(x_m-x_0)+\frac{\gamma l_d}{2}} du \int_{\gamma(y_n-y_0)-\frac{\gamma l_d}{2}}^{\gamma(y_n-y_0)+\frac{\gamma l_d}{2}} d\sigma \\ \times \exp\left(-\Lambda(u,\sigma) + i\left(\Phi\left(u+\frac{d_c}{2}, \sigma\right) - \Phi\left(u-\frac{d_c}{2}, \sigma\right)\right)\right), \quad (18)$$

$$C_2(m,n) \\ = \frac{a_2(m,n)}{2} \exp(i\phi_2(m,n)) \\ = -i|A|^2 \frac{1+W_{si}}{2\pi^2 z_{12}^2 l_d^2} (1-\cos(Q_1)) \\ \times \iint dx_0 dy_0 I_{\text{source}} \left(-\frac{z_1}{z_{12}} x_0, -\frac{z_1}{z_{12}} y_0 \right) \exp\left(-i2\pi \frac{x_0}{g_2}\right)$$

$$\times \int_{\gamma(x_m-x_0)-\frac{\gamma l_d}{2}}^{\gamma(x_m-x_0)+\frac{\gamma l_d}{2}} du \int_{\gamma(y_n-y_0)-\frac{\gamma l_d}{2}}^{\gamma(y_n-y_0)+\frac{\gamma l_d}{2}} d\sigma \\ \times \exp\left(-\Lambda(u,\sigma) + i\left(\Phi\left(u+\frac{d_c}{2}, \sigma\right) - \Phi\left(u-\frac{d_c}{2}, \sigma\right)\right)\right), \quad (19)$$

in which Eq. (5) is utilized, (u,σ) denotes a point at the plane of G_1 ($z=z_1$), and d_c is given by

$$d_c = \frac{\lambda z_{12}}{g_2} = \frac{m_T}{4} g_1. \quad (20)$$

$$\Lambda(x,y) = \frac{4\pi}{\lambda} \int_Z \beta\left(\frac{z}{z_1} x, \frac{z}{z_1} y, z\right) \sqrt{1 + \frac{x^2 + y^2}{z_1^2}} dz \quad (21)$$

is the projection data corresponding to attenuation, and

$$\Phi(x,y) = \frac{2\pi}{\lambda} \int_Z \delta\left(\frac{z}{z_1} x, \frac{z}{z_1} y, z\right) \sqrt{1 + \frac{x^2 + y^2}{z_1^2}} dz \quad (22)$$

is that corresponding to phase. It should be noted that in the derivation of Eqs. (17)-(19), we assume that the fine (unresolvable) features of the object to be imaged, if they exist, distribute randomly. As a result, the fine components of attenuation projection $\Lambda(x,y)$ and phase shift $\Phi(x,y)$ can be modeled as a Gaussian random process.^{5,17} For sake of simplicity, we further suppose in this study that the intensity profile of the microfocus x-ray source obeys Gaussian distribution with a root mean square width σ_s ,

$$I_{\text{source}}(x,y) = \frac{1}{2\pi\sigma_s^2} \exp\left(-\frac{x^2 + y^2}{2\sigma_s^2}\right). \quad (23)$$

Then one may rewrite Eq. (17) into

$$a_0(m,n) = \frac{|A|^2(1+W_{si})}{8\pi z_{12}^2 l_d^2 w_s^2} \iint dx_0 dy_0 \exp\left(-\frac{x_0^2 + y_0^2}{2w_s^2}\right) \\ \times \int_{\gamma(x_m-x_0)-\frac{\gamma l_d}{2}}^{\gamma(x_m-x_0)+\frac{\gamma l_d}{2}} du \int_{\gamma(y_n-y_0)-\frac{\gamma l_d}{2}}^{\gamma(y_n-y_0)+\frac{\gamma l_d}{2}} d\sigma \\ \times \exp(-\Lambda(u,\sigma)), \quad (24)$$

where

$$w_s = \frac{z_{12}}{z_1} \sigma_s \quad (25)$$

is the demagnified source size.⁶ In a typical Talbot interferometry with a microfocus x-ray tube, one usually has $\sigma_s \sim 10^1 \mu\text{m}$, $z_{12}/z_1 \sim 10^{-1}$. According to Eq. (25), the demagnified source size w_s ($\sim 10^0 \mu\text{m}$) is much smaller than the detector cell size l_d ($\sim 10^2 \mu\text{m}$). Hence, using Eq. (11), it is not hard to show that the Fourier coefficient $a_0(m,n)$ can be approximated as

$$a_0(m,n) \approx |A|^2 \frac{1+W_{si}}{8\pi z_{12}^2 l_d^2 w_s^2} \iint dx_0 dy_0 \exp\left(-\frac{x_0^2 + y_0^2}{2w_s^2}\right) \\ \times \int_{\gamma x_m - \frac{\gamma l_d}{2}}^{\gamma x_m + \frac{\gamma l_d}{2}} du \int_{\gamma y_n - \frac{\gamma l_d}{2}}^{\gamma y_n + \frac{\gamma l_d}{2}} d\sigma \exp(-\Lambda(u,\sigma)) \\ \approx |A|^2 \frac{1+W_{si}}{4z_2^2} \exp(-\bar{\Lambda}(\gamma x_m, \gamma y_n)), \quad (26)$$

where

$$\bar{\Lambda}(x, y) = \frac{1}{\gamma^2 l_d^2} \int_{x-\frac{\gamma l_d}{2}}^{x+\frac{\gamma l_d}{2}} dx_1 \int_{y-\frac{\gamma l_d}{2}}^{y+\frac{\gamma l_d}{2}} dy_1 \Lambda(x_1, y_1) \quad (27)$$

denotes the mean of attenuation projection over an area $\gamma l_d \times \gamma l_d$. Similarly, the first- and second-order Fourier coefficients in Eq. (5) can be estimated as

$$\begin{aligned} \frac{a_1(m,n)}{2} \exp(i\phi_1(m,n)) \\ \approx \sqrt{2}|A|^2 \frac{1-W_{si}}{\pi^2 z_2^2} \sin(Q_1) \exp\left(-\frac{\pi^2}{2} \left(\frac{z_{12}\sigma_s}{z_1 g_2}\right)^2\right) \\ \times \sin\left(\frac{m_T}{8}\pi\right) V_1(m,n) \exp(-\bar{\Lambda}(\gamma x_m, \gamma y_n)) \\ \times \exp\left(i\left(d_c \partial_x \bar{\Phi}(\gamma x_m, \gamma y_n) + \frac{3}{2}\pi\right)\right), \end{aligned} \quad (28)$$

$$\begin{aligned} \frac{a_2(m,n)}{2} \exp(i\phi_2(m,n)) \\ \approx |A|^2 \frac{1+W_{si}}{2\pi^2 z_2^2} (1 - \cos(Q_1)) \\ \times \exp\left(-2\pi^2 \left(\frac{z_{12}\sigma_s}{z_1 g_2}\right)^2\right) V_2(m,n) \exp(-\bar{\Lambda}(\gamma x_m, \gamma y_n)) \\ \times \exp\left(i\left(d_c \partial_x \bar{\Phi}(\gamma x_m, \gamma y_n) + \frac{3}{2}\pi\right)\right), \end{aligned} \quad (29)$$

where

$$\bar{\Phi}(x, y) = \frac{1}{\gamma^2 l_d^2} \int_{x-\frac{\gamma l_d}{2}}^{x+\frac{\gamma l_d}{2}} dx_1 \int_{y-\frac{\gamma l_d}{2}}^{y+\frac{\gamma l_d}{2}} dy_1 \Phi(x_1, y_1) \quad (30)$$

denotes the mean of phase shift over an area $\gamma l_d \times \gamma l_d$. By definition, one has

$$\partial_x \bar{\Phi}(\gamma x_m, \gamma y_n) = \frac{\bar{\Phi}(\gamma x_m + \frac{\gamma l_d}{2}, \gamma y_n) - \bar{\Phi}(\gamma x_m - \frac{\gamma l_d}{2}, \gamma y_n)}{\gamma l_d}, \quad (31)$$

the averaged differential phase shift over the detector cell at (m, n) ,

$$\begin{aligned} V_1(m,n) &= \frac{1}{\gamma^2 l_d^2} \int_{\gamma x_m - \frac{\gamma l_d}{2}}^{\gamma x_m + \frac{\gamma l_d}{2}} du \int_{\gamma y_n - \frac{\gamma l_d}{2}}^{\gamma y_n + \frac{\gamma l_d}{2}} d\sigma \\ &\times \exp\left(i\left(\Phi\left(u + \frac{d_c}{4}, \sigma\right) - \Phi\left(u - \frac{d_c}{4}, \sigma\right) - \frac{d_c}{2} \partial_x \bar{\Phi}(\gamma x_m, \gamma y_n)\right)\right), \end{aligned} \quad (32)$$

$$\begin{aligned} V_2(m,n) &= \frac{1}{\gamma^2 l_d^2} \int_{\gamma x_m - \frac{\gamma l_d}{2}}^{\gamma x_m + \frac{\gamma l_d}{2}} du \int_{\gamma y_n - \frac{\gamma l_d}{2}}^{\gamma y_n + \frac{\gamma l_d}{2}} d\sigma \\ &\times \exp\left(i\left(\Phi\left(u + \frac{d_c}{2}, \sigma\right) - \Phi\left(u - \frac{d_c}{2}, \sigma\right) - d_c \partial_x \bar{\Phi}(\gamma x_m, \gamma y_n)\right)\right). \end{aligned} \quad (33)$$

It should not be hard to show¹³ that, if phase shift $\Phi(x, y)$ varies at a scale comparable to or larger than l_d , both

$$\Phi\left(u + \frac{d_c}{4}, \sigma\right) - \Phi\left(u - \frac{d_c}{4}, \sigma\right) - \frac{d_c}{2} \partial_x \bar{\Phi}(\gamma x_m, \gamma y_n)$$

on the right side of Eq. (32) and

$$\Phi\left(u + \frac{d_c}{2}, \sigma\right) - \Phi\left(u - \frac{d_c}{2}, \sigma\right) - d_c \partial_x \bar{\Phi}(\gamma x_m, \gamma y_n)$$

on the right side of Eq. (33) can be approximated as zero, which immediately results in $V_1(m,n) = V_2(m,n) = 1$, indicating that $V_1(m,n)$ and $V_2(m,n)$ are mainly induced by the object's subpixel features, i.e., they correspond to the dark-field contrast.¹³ On the other hand, since the object's subpixel microstructures, if they exist, are assumed to distribute randomly, the chance that

$$\Phi\left(u + \frac{d_c}{4}, \sigma\right) - \Phi\left(u - \frac{d_c}{4}, \sigma\right) - \frac{d_c}{2} \partial_x \bar{\Phi}(\gamma x_m, \gamma y_n)$$

falls into an interval around a value F would be the same as that around the value— F .¹³ As a result, it is not difficult to show that

$$\begin{aligned} \frac{1}{\gamma^2 l_d^2} \int_{\gamma x_m - \frac{\gamma l_d}{2}}^{\gamma x_m + \frac{\gamma l_d}{2}} du \int_{\gamma y_n - \frac{\gamma l_d}{2}}^{\gamma y_n + \frac{\gamma l_d}{2}} d\sigma \\ \times \sin\left(\Phi\left(u + \frac{d_c}{4}, \sigma\right) - \Phi\left(u - \frac{d_c}{4}, \sigma\right) - \frac{d_c}{2} \partial_x \bar{\Phi}(\gamma x_m, \gamma y_n)\right) = 0. \end{aligned} \quad (34)$$

Similarly, one may write

$$\begin{aligned} \frac{1}{\gamma^2 l_d^2} \int_{\gamma x_m - \frac{\gamma l_d}{2}}^{\gamma x_m + \frac{\gamma l_d}{2}} du \int_{\gamma y_n - \frac{\gamma l_d}{2}}^{\gamma y_n + \frac{\gamma l_d}{2}} d\sigma \\ \times \sin\left(\Phi\left(u + \frac{d_c}{2}, \sigma\right) - \Phi\left(u - \frac{d_c}{2}, \sigma\right) - d_c \partial_x \bar{\Phi}(\gamma x_m, \gamma y_n)\right) = 0. \end{aligned} \quad (35)$$

Substituting Eqs. (34) and (35) into Eqs. (32) and (33) yields

$$\begin{aligned} V_1(m,n) &= \frac{1}{\gamma^2 l_d^2} \int_{\gamma x_m - \frac{\gamma l_d}{2}}^{\gamma x_m + \frac{\gamma l_d}{2}} du \int_{\gamma y_n - \frac{\gamma l_d}{2}}^{\gamma y_n + \frac{\gamma l_d}{2}} d\sigma \\ &\times \cos\left(\Phi\left(u + \frac{d_c}{4}, \sigma\right) - \Phi\left(u - \frac{d_c}{4}, \sigma\right) - \frac{d_c}{2} \partial_x \bar{\Phi}(\gamma x_m, \gamma y_n)\right), \end{aligned} \quad (36)$$

$$\begin{aligned} V_2(m,n) &= \frac{1}{\gamma^2 l_d^2} \int_{\gamma x_m - \frac{\gamma l_d}{2}}^{\gamma x_m + \frac{\gamma l_d}{2}} du \int_{\gamma y_n - \frac{\gamma l_d}{2}}^{\gamma y_n + \frac{\gamma l_d}{2}} d\sigma \\ &\times \cos\left(\Phi\left(u + \frac{d_c}{2}, \sigma\right) - \Phi\left(u - \frac{d_c}{2}, \sigma\right) - d_c \partial_x \bar{\Phi}(\gamma x_m, \gamma y_n)\right), \end{aligned} \quad (37)$$

which indicates that the dark-field contrasts $V_1(m,n)$ and $V_2(m,n)$ are real. In a typical x-ray Talbot interferometry with an extended incoherent source, the contribution of the third-

or higher order Fourier components can be negligible,⁶ and thus, one may approximate the PSC as

$$\begin{aligned} I_{m,n}(x_g) &= a_0(m,n) + a_1(m,n)\cos\left(\pi\frac{x_g}{g_2} + \phi_1(m,n)\right) \\ &\quad + a_2(m,n)\cos\left(2\pi\frac{x_g}{g_2} + \phi_2(m,n)\right) \\ &= |A|^2 \frac{1+W_{si}}{4z_2^2} \exp(-\bar{\Lambda}(\gamma x_m, \gamma y_n)) \\ &\quad \times \left(1 + \frac{8\sqrt{2}(1-W_{si})}{\pi^2(1+W_{si})} \sin(Q_1) \exp\left(-\frac{\pi^2}{2}\left(\frac{z_{12}\sigma_s}{z_1g_2}\right)^2\right)\right) \\ &\quad \times \sin\left(\frac{m_T}{8}\pi\right) V_1(m,n) \\ &\quad \times \cos\left(\pi\frac{x_g}{g_2} + \frac{d_c}{2}\partial_x\bar{\Phi}(\gamma x_m, \gamma y_n) + \frac{3}{4}\pi\right) \\ &\quad + \frac{4(1-\cos(Q_1))}{\pi^2} \exp\left(-2\pi^2\left(\frac{z_{12}\sigma_s}{z_1g_2}\right)^2\right) \\ &\quad \times V_2(m,n) \cos\left(2\pi\frac{x_g}{g_2} + d_c\partial_x\bar{\Phi}(\gamma x_m, \gamma y_n) + \frac{3}{2}\pi\right), \end{aligned} \quad (38)$$

in which Eqs. (26), (28), and (29) are used. An inspection of Eq. (38) should enable one to recognize the existence of twin peaks in the PSC, which are determined by

$$I_{\max 1}(m,n) = a_0(m,n) + a_1(m,n) + a_2(m,n), \quad (39)$$

$$I_{\max 2}(m,n) = a_0(m,n) - a_1(m,n) + a_2(m,n). \quad (40)$$

This means that the twin peaks exist in the PSC of x-ray Talbot interferometry if and only if $a_1(m,n) \neq 0$, i.e., the PSC's twin-peak feature is determined by its first-order Fourier component that corresponds to the spatial frequency $1/(2g_2)$, as shown in Eq. (38).

It should be noted that, according to Eq. (28), if there is no imperfection in analyzer grating G_2 ($W_{si} = 1$), or phase grating G_1 performs perfectly ($Q_1 = \pi$), one has $a_1(m,n) = 0$, and then Eqs. (39) and (40) become

$$\begin{aligned} I_{\max 1}(m,n) &= I_{\max 2}(m,n) \\ &= |A|^2 \frac{1+W_{si}}{4z_2^2} \exp(-\bar{\Lambda}(\gamma x_m, \gamma y_n)) \\ &\quad \times \left(1 + \frac{4(1-\cos(Q_1))}{\pi^2} \exp\left(-2\pi^2\left(\frac{z_{12}\sigma_s}{z_1g_2}\right)^2\right)\right) V_2(m,n), \end{aligned} \quad (41)$$

and the PSC of x-ray Talbot interferometry becomes

$$\begin{aligned} I_{m,n}(x_g) &= a_0(m,n) + a_2(m,n)\cos\left(2\pi\frac{x_g}{g_2} + \phi_2(m,n)\right) \\ &= |A|^2 \frac{1+W_{si}}{4z_2^2} \exp(-\bar{\Lambda}(\gamma x_m, \gamma y_n)) \\ &\quad \times \left(1 - i\frac{4(1-\cos(Q_1))}{\pi^2} \exp\left(-2\pi^2\left(\frac{z_{12}\sigma_s}{z_1g_2}\right)^2\right)\right) V_2(m,n) \\ &\quad \times \cos\left(2\pi\frac{x_g}{g_2} + d_c\partial_x\bar{\Phi}(\gamma x_m, \gamma y_n)\right). \end{aligned} \quad (42)$$

Equation (42) tells us that there exists no twin peaks in the PSC and the period of PSC is the same as the analyzer grating's nominal period g_2 . Thus, ideally, by shifting the analyzer grating G_2 just over its nominal period g_2 , one may produce a PSC and extract the signal corresponding to the contrasts of attenuation, differential phase, and dark-field, respectively. However, in an actual x-ray Talbot interferometry with an imperfect grating G_2 and phase grating G_1 that mismatches x-ray's spectrum, one has $W_{si} \neq 1$ and $Q_1 \neq \pi$. Consequently, according to Eq. (28), $a_1(m,n) \neq 0$ and the phenomenon of twin peaks occurs, with its period being as large as twice grating G_2 's nominal period g_2 . Hence, to cope with the feature of twin peaks in PSCs, one should shift the analyzer grating G_2 over its effective period $2g_2$ to produce the PSC and to extract the information on attenuation contrast, differential phase contrast, and dark-field contrast. We would like to indicate that Eq. (38) is the key result obtained by us in this work, which is the foundation for grating-based x-ray differential phase contrast imaging with the feature of twin peaks in PSCs, and can be conceived as the counterpart of Eq. (1).

Prior to ending this subsection, it is worthwhile inspecting the relative significance of the first-order Fourier component compared to the second-order one, which can be quantified by the ratio

$$\begin{aligned} \chi(m,n) &= \frac{a_1(m,n)}{a_2(m,n)} \\ &= 2\sqrt{2} \left| \sin\left(\frac{m_T}{8}\pi\right) \frac{1-W_{si}}{1+W_{si}} \tan\left(\frac{Q_1-\pi}{2}\right) \right. \\ &\quad \left. \times \exp\left(\frac{3\pi^2}{2}\left(\frac{z_{12}\sigma_s}{z_1g_2}\right)^2\right) \frac{V_1(m,n)}{V_2(m,n)} \right|, \end{aligned} \quad (43)$$

where Eqs. (28) and (29) are used. Equation (43) shows that, in addition to the imperfection in the analyzer grating and the mismatch between phase grating and x-ray spectrum, the focal size of x-ray source (σ_s) may also significantly influence the twin peak phenomenon. Specifically, the larger the x-ray source's focal spot size σ_s , the stronger the first-order Fourier component compared to the second-order one, and accordingly, the more apparent may be the feature of twin peaks in PSCs.

2.B. Phase dewrapping in grating-based x-ray differential phase contrast imaging with the feature of twin peaks in PSC

Due to the fact that phase is of periodicity and thus nonambiguous only in a bounded interval, phase wrapping may occur and has been recognized as a limitation to the applicability of phase contrast imaging.¹⁸ In addition to the phase dewrapping methods reported in the literature,^{19–21} we propose a novel approach herein by jointly making use of the phase information in PSCs' first- and second-order Fourier components.

Using Eqs. (28) and (29), it should not be difficult to show that

$$\frac{d_c}{2}\partial_x\bar{\Phi}(\gamma x_m, \gamma y_n) = \varphi_1(m,n), \quad (44)$$

$$d_c \partial_x \bar{\Phi}(\gamma x_m, \gamma y_n) = \varphi_2(m, n), \quad (45)$$

where

$$\varphi_1(m, n) = \phi_1^s(m, n) - \phi_1^r(m, n), \quad (46)$$

$$\varphi_2(m, n) = \phi_2^s(m, n) - \phi_2^r(m, n) \quad (47)$$

denote the phase difference corresponding to the first- and second-order Fourier components, respectively. Equations (44) and (45) indicate that the relationship holds as follows:

$$\varphi_1(m, n) = \frac{1}{2} \varphi_2(m, n). \quad (48)$$

From the measured PSC, immediately one can calculate the Fourier coefficients $a_0(m, n)$, $a_1(m, n)$, and $\phi_1(m, n)$ and $\phi_2(m, n)$. Thus, in principle, both Eqs. (44) and (45) can be utilized to estimate the average differential phase shift defined in Eq. (31). However, in the case wherein the phenomenon of twin peaks occurs (see Fig. 5 in Sec. 4), the first-order Fourier coefficient [corresponding to spatial frequency $1/(2g_2)$] is remarkably smaller in magnitude than the second-order coefficient (corresponding to spatial frequency $1/g_2$). As a result, the measurement of the first-order Fourier coefficient may suffer more than the second-order coefficient from noise. Thus one should utilize Eq. (45) and the phase difference of the second-order Fourier component $\phi_2(m, n)$ to estimate the differential phase shift of the object to be imaged.

Let $\varphi_{2w}(m, n)$ denote the measured phase difference of the second-order Fourier coefficients that may have been corrupted by phase wrapping, i.e., deviated from the genuine phase difference $\varphi_2(m, n)$ by multiple of 2π ,

$$\varphi_{2w}(m, n) = \varphi_2(m, n) - 2l_2\pi, \quad l_2 = 0, \pm 1, \pm 2, \dots, \quad (49)$$

where subscript “w” indicates that the phase may have been wrapped. It should not be hard to understand that, if the phase difference $\varphi_{2w}(m, n)$ has indeed been wrapped and is substituted into Eq. (45), the retrieved differential phase shift is erroneous, which may cause artifacts in x-ray differential phase contrast imaging.¹⁸ To get the genuine phase difference $\varphi_2(m, n)$ from $\varphi_{2w}(m, n)$, a dewrapping method is proposed by assuming $\varphi_2(m, n)$ is small enough to meet²⁰

$$|\varphi_2(m, n)| < \pi. \quad (50)$$

Note that according to Eq. (45), Eq. (50) imposes a constraint on the gradient of phase shift, which is referred to as the moderate phase-variation condition henceforth. Combining Eqs. (49) and (50) yields

$$\varphi_2(m, n) = W(\varphi_{2w}(m, n)), \quad (51)$$

where $W(\cdot)$ denotes the dewrapping function that is defined as

$$W(\Psi) = \Psi - 2\pi \times \text{round}\left(\frac{\Psi}{2\pi}\right), \quad (52)$$

and the function $\text{round}(x)$ returns an integer that is the nearest to x . For sake of convenience, the method described by Eqs. (51) and (52) is called the conventional phase dewrapping method.¹⁹

Unfortunately, however, the conventional phase dewrapping method cannot be applied in the cases where the genuine

differential phase signal $\varphi_2(m, n)$ is large enough to violate Eq. (50).¹⁹ Hence, based on Eq. (48) and making use of the measured phase difference of first-order Fourier component, i.e., $\varphi_{1w}(m, n)$, we propose an approach for phase dewrapping to get $\varphi_2(m, n)$ from $\varphi_{2w}(m, n)$. To do so, we first estimate the integer l_2 in Eq. (49) and then add back $2l_2\pi$ to $\varphi_{2w}(m, n)$. Similar to what has been done in Ref. 21, we at first calculate the gradient of the genuine phase difference $\varphi_2(m, n)$. The two components of the gradient are expressed as $D_x \varphi_2(m, n)$ and $D_y \varphi_2(m, n)$, where D_x and D_y denote finite difference operators and are defined, respectively, by

$$D_x \Psi(m, n) = \Psi(m+1, n) - \Psi(m, n), \quad (53)$$

$$D_y \Psi(m, n) = \Psi(m, n+1) - \Psi(m, n). \quad (54)$$

Combining Eq. (45) with Eq. (53), one obtains

$$D_x \varphi_2(m, n) = \gamma l_d d_c \partial_{xx} \bar{\Phi}\left(\gamma x_m + \frac{\gamma l_d}{2}, \gamma y_n\right), \quad (55)$$

i.e., the gradient component $D_x \varphi_2(m, n)$ is proportional to the second-order derivatives of the object’s average differential phase shift, which, according to the smooth-phase condition²²

$$\left| \frac{\lambda z_{12}}{2\pi} \partial_{xx} \bar{\Phi}(\gamma x_m, \gamma y_n) \right| \ll 1, \quad (56)$$

is actually small in the vast majority of the objects to be imaged. Then it is reasonable to estimate $D_x \varphi_2(m, n)$ as

$$D_x \varphi_2(m, n) = D_x \varphi_{2w}(m, n), \quad (57)$$

if

$$|D_x \varphi_{2w}(m, n)| < \pi, \quad (58)$$

where $D_x \varphi_{2w}(m, n)$ is the gradient component of measured phase difference corresponding to the second-order Fourier coefficient along the x -direction.

There exist two situations where the condition specified by Eq. (58) is not met by an object’s measured phase difference $\varphi_{2w}(m, n)$. In the first scenario, phase wrapping occurs in $D_x \varphi_{2w}(m, n)$, i.e., $D_x \varphi_{2w}(m, n)$ jumps to a false value while the genuine gradient component $D_x \varphi_2(m, n)$ is actually small and the smooth-phase condition specified in Eq. (56) is still satisfied. In this case the genuine gradient component should be calculated as

$$D_x \varphi_2(m, n) = W(D_x \varphi_{2w}(m, n)), \quad (59)$$

i.e., applying the conventional phase dewrapping method on $D_x \varphi_2(m, n)$. In the second scenario, an object’s refractive index decrement δ is so large that $D_x \varphi_{2w}(m, n)$ becomes large enough to violate the condition specified in Eq. (58). In this case, however, Eq. (57) holds and similar equation is applicable to $D_x \varphi_{1w}(m, n)$, the gradient component of measured phase difference corresponding to the first-order Fourier coefficient along the x -direction. Hence, one may write

$$D_x \varphi_1(m, n) = D_x \varphi_{1w}(m, n). \quad (60)$$

Combining Eqs. (48), (57), and (60) yields

$$D_x \varphi_{1w}(m, n) = \frac{1}{2} D_x \varphi_{2w}(m, n). \quad (61)$$

Note that if phase wrapping occurs, $D_x\varphi_{2w}(m,n)$ jumps by 2π , but $D_x\varphi_{1w}(m,n)$ does not jump by π , which means that Eq. (61) does not hold whenever a phase wrapping occurs. Thus one can use Eq. (61) as a criterion to identify the case, in which a large magnitude of measured gradient

component $D_x\varphi_{2w}(m,n)$ is caused by the fact that the object's δ is really large, rather than a phase wrapping. Based on the arguments above, the gradient of the genuine phase difference along the x -direction can be determined by

$$D_x\varphi_2(m,n) = \begin{cases} W(D_x\varphi_{2w}(m,n)), & \text{if } |D_x\varphi_{2w}(m,n)| \geq \pi \text{ and } \left| \frac{D_x\varphi_{1w}(m,n)}{D_x\varphi_{2w}(m,n)} - \frac{1}{2} \right| > \varepsilon, \\ D_x\varphi_{2w}(m,n), & \text{else} \end{cases}, \quad (62)$$

where parameter ε is a small positive number. Similarly, the genuine gradient along the y -direction can be estimated as

$$D_y\varphi_2(m,n) = \begin{cases} W(D_y\varphi_{2w}(m,n)), & \text{if } |D_y\varphi_{2w}(m,n)| \geq \pi \text{ and } \left| \frac{D_y\varphi_{1w}(m,n)}{D_y\varphi_{2w}(m,n)} - \frac{1}{2} \right| > \varepsilon, \\ D_y\varphi_{2w}(m,n), & \text{else} \end{cases}. \quad (63)$$

In practice, a detector cell is of finite dimension, and its index (m,n) satisfies

$$-M_a \leq m \leq M_b, \text{ and } -N_a \leq n \leq N_b, \quad (64)$$

where M_a , M_b , N_a , and N_b are positive integers. Usually the top-left corner $(-M_a, -N_a)$ is assumed to be outside an object to be imaged, and the differential phase shift there should be close to zero. Hence, using Eq. (58) we may write

$$\varphi_2(-M_a, -N_a) = W(\varphi_{2w}(-M_a, -N_a)). \quad (65)$$

At any other locations $(-M_a, n+1)$ with $n \geq -N_a$, the integer l_2 in Eq. (49) can be calculated by

$$l_2 = \text{round}\left(\frac{\varphi_2(-M_a, n+1) - \varphi_{2w}(-M_a, n+1)}{2\pi}\right) = \text{round}\left(\frac{D_y\varphi_2(-M_a, n) + \varphi_2(-M_a, n) - \varphi_{2w}(-M_a, n+1)}{2\pi}\right), \quad (66)$$

in which Eq. (54) has been utilized. Using Eq. (49), the dewrapped phase difference at $(-M_a, n+1)$ with $n \geq -N_a$ can be recursively determined by

$$\varphi_2(-M_a, n+1) = \varphi_{2w}(-M_a, n+1) + 2\pi \times \text{round}\left(\frac{D_y\varphi_2(-M_a, n) + \varphi_2(-M_a, n) - \varphi_{2w}(-M_a, n+1)}{2\pi}\right), \quad n \geq -N_a. \quad (67)$$

It is noted that Eq. (67) is recursive. With the genuine gradient component $D_y\varphi_2(-M_a, n)$ in Eq. (63) and the phase difference at the top-left corner $\varphi_2(-M_a, -N_a)$ given by Eq. (65), one can use Eq. (67) recursively to dewrap the measured phase difference at location $(-M_a, n+1)$ with $n \geq -N_a$. In the same manner, the following recursive formula

$$\varphi_2(m+1, -N_a) = \varphi_{2w}(m+1, -N_a) + 2\pi \times \text{round}\left(\frac{D_x\varphi_2(m, -N_a) + \varphi_2(m, -N_a) - \varphi_{2w}(m+1, -N_a)}{2\pi}\right), \quad m \geq -M_a \quad (68)$$

can be used to dewrap at location $(m+1, -N_a)$ with $m \geq -M_a$.

At location $(m+1, n+1)$ with $m \geq -M_a$ and $n \geq -N_a$, it is easy to show that there are two ways to estimate the genuine phase difference $\varphi_2(m+1, n+1)$. One is based on integration along the y -direction

$$\varphi_{2a}(m+1, n+1) = \varphi_{2w}(m+1, n+1) + 2\pi \times \text{round}\left(\frac{D_y\varphi_2(m+1, n) + \varphi_2(m+1, n) - \varphi_{2w}(m+1, n+1)}{2\pi}\right), \quad m \geq -M_a, \quad n \geq -N_a, \quad (69)$$

and the other is based on integration along the x -direction

$$\varphi_{2b}(m+1, n+1) = \varphi_{2w}(m+1, n+1) + 2\pi \times \text{round}\left(\frac{D_x\varphi_2(m, n+1) + \varphi_2(m, n+1) - \varphi_{2w}(m+1, n+1)}{2\pi}\right), \quad m \geq -M_a, \quad n \geq -N_a. \quad (70)$$

Because there exists noise in the measured phase difference $\varphi_{2w}(m,n)$, the dewrapped phase difference using Eq. (69), $\varphi_{2a}(m,n)$, might be different from that dewrapped using Eq. (70), $\varphi_{2b}(m,n)$.²¹ According to Eqs. (69) and (70), the difference between them should be a multiple of 2π . It should

be noted that the smooth-phase condition specified by Eq. (56) is satisfied in vast majority of detector cells. Hence, between $\varphi_{2a}(m,n)$ and $\varphi_{2b}(m,n)$, it is reasonable to choose the one having smaller magnitude as an estimation of the genuine phase difference $\varphi_2(m,n)$, i.e.,

$$\varphi_2(m+1,n+1) = \begin{cases} \varphi_{2a}(m+1,n+1), & \text{if } |\varphi_{2a}(m+1,n+1)| \leq |\varphi_{2b}(m+1,n+1)| \\ \varphi_{2b}(m+1,n+1), & \text{else} \end{cases}, \quad m \geq -M_a, \quad n \geq -N_a. \quad (71)$$

Hence, the dewrapped phase difference $\varphi_2(m,n)$ can be calculated using the recursive formulae Eqs. (67)–(71), and the differential phase contrast of the object to be imaged is retrieved with resort to Eq. (45). In summary, Eqs. (62), (63), (65), (67)–(71) constitute the phase dewrapping approach, which is based on a joint utilization of the first- and second-order Fourier coefficients in the PSC with twin peaks, and are another important result of the presented work.

3. EXPERIMENTAL EVALUATION

A prototype grating-based differential x-ray phase contrast imaging system, as illustrated in Fig. 4, is utilized to evaluate and validate the analytic formulae derived above and the approaches proposed for phase retrieval and phase dewrapping with the feature of twin peaks in PSCs. The experimental setup consists of a microfocus x-ray tube (Trufocus Corporation, Watsonville, CA), a flat panel x-ray detector (Remote RadEye4, Teledyne Dalsa, Waterloo, ON), a rotating motion stage (Velmex, Bloomfield, NY), and gratings G_1 and G_2 that are fabricated via the process described in Ref. 14. The nominal periods of gratings G_1 and G_2 are 8 and 4.6 μm , respectively. The microfocus x-ray tube used in the system is of a 10 μm nominal focal spot size and operates continuously at 40 kVp and 0.22 mA tube current. An optimum visibility is reached when the distance between the two gratings and that between x-ray source and grating G_1 are adjusted to be 18.4 and 120.0 cm, respectively. The detector consists of a 1024×2048 array, with each cell at dimension $48 \times 48 \mu\text{m}^2$.

A cylindrical water phantom consisting of four tubes filled with glycerol, alcohol, isopropanol, and air (namely organic phantom) and a lab mouse are utilized to experimentally evaluate and verify the proposed approaches for phase retrieval and phase dewrapping. The projection data acquisition is carried out as a 360° full scan at 2° angular interval, and

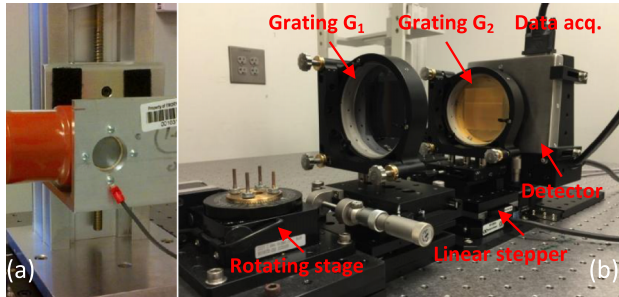


Fig. 4. Photograph of the prototype x-ray differential phase contrast imaging system implemented with Talbot interferometry: (a) microfocus x-ray source; (b) the rest of the system.

thus, a total of 180 projection views are acquired for CT image generation. At each angular position in data acquisition, grating G_2 shifts 12 steps over a 9.6 μm distance, and the x-ray exposure time at each step is 6.5 s. At each detector cell, a PSC consisting of 23 data points over a 9.2 μm span is obtained from the raw PSC (12 data points) via linear interpolation. Note that 9.2 μm is exactly twice the nominal period of grating G_2 . The Fourier coefficients $a_0(m,n)$, $a_1(m,n)$ and $\phi_1(m,n)$, and $a_2(m,n)$ and $\phi_2(m,n)$ corresponding to the PSCs with and without the object in x-ray beam are calculated. With the phase differences $\varphi_{1w}(m,n)$ and $\varphi_{2w}(m,n)$ obtained using Eqs. (46) and (47), one can obtain the gradient of the genuine phase difference according to Eqs. (62) and (63) with parameter ε being selected as 0.05. Then Eqs. (65) and (67)–(71) can be utilized to dewrap the measured phase difference $\varphi_{2w}(m,n)$ into the genuine phase difference $\varphi_2(m,n)$.

Having gone through the phase dewrapping process using the proposed approach, one can calculate the differential phase contrast according to Eq. (45). The FDK-like reconstruction algorithm,⁶ which is actually the FDK algorithm with its ramp filtering kernel replaced by the Hilbert filtering kernel, can be utilized to reconstruct the phase contrast CT images.

4. RESULTS

4.A. The phenomenon of twin peaks in phase-shifting curves

A flat-field PSC, i.e., an air scan without an object in x-ray beam, is recorded by shifting grating G_2 120 times at step 0.2 μm . The total travel distance is 24 μm , roughly 5.2 times G_2 's nominal period g_2 . The detector cells are 2×2 binned into an effective dimension $96 \times 96 \mu\text{m}^2$, and the x-ray exposure time at each step is 39 s, which is relatively long, to mitigate the influence of Poisson noise. As an example, a flat-field PSC exhibiting the twin-peak feature as well as its first- and second-order harmonics is presented in Fig. 5.

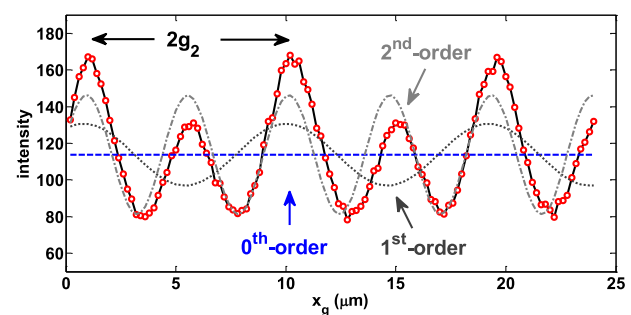


Fig. 5. A flat-field (air scan) phase shifting curve plotted with data acquired by shifting the absorption grating G_2 120 steps over 24 μm .

4.B. Quality improvement in x-ray differential phase contrast CT by dealing with the twin-peak phenomenon

To show the performance improvement in x-ray differential phase contrast CT by dealing with the phenomenon of twin peaks in phase retrieval, the transverse image of the organic phantom generated using the proposed approach is presented in Fig. 6(b). The PSC is measured by stepping grating G_2 12 times over twice its nominal period and the retrieved signal goes through phase dewrapping with the proposed approach. The counterpart image generated without dealing with twin peaks is displayed in Fig. 6(a), in which the PSC is acquired by stepping grating G_2 6 times over only one nominal period. The retrieved signal is dewrapped using the conventional approach. To mitigate noise influence, detector cells are 2×2 binned into an effective dimension $96 \times 96 \mu\text{m}^2$. It is observed that the severe glaring and shading artifacts existing in Fig. 6(a) disappear in Fig. 6(b), showing that the performance of grating-based differential phase contrast CT is significantly improved by stepping grating G_2 over twice its nominal period in data acquisition and dewrapping the data with the proposed approach. In addition, the profiles corresponding to the horizontal lines labeled in Figs. 6(a) and 6(b) are plotted in Fig. 6(c), and those to the vertical lines in Fig. 6(d). The improvement in image quality can be quantified as large as 450 [Fig. 6(c)] and 350 [Fig. 6(d)] Hounsfield units (HUs), where the Hounsfield unit is defined using water's refractive index decrement (δ) at 25 keV.

To demonstrate robustness of the proposed approach for phase retrieval, a transverse phase contrast CT image of the mouse produced in a way identical to that used in obtaining the image shown in Fig. 6(b) is presented in

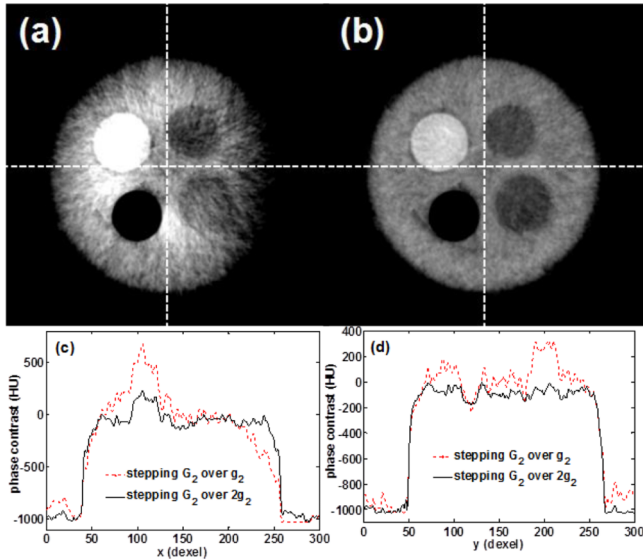


FIG. 6. Transverse images of the organic phantom reconstructed from the data acquired by (a) stepping grating G_2 over its nominal period and dewrapping with conventional method, and (b) stepping G_2 over twice its nominal period and dewrapping with the proposed approach. The profiles in (c) are along the horizontal lines in (a) and (b), while those in (d) along the vertical lines in (a) and (b) [display: $[-400 300]$ HU in (a) and (b)].

Fig. 7(b). Meanwhile, the image reconstructed from the data obtained with phase retrieved from the PSC over one nominal period of grating G_2 and corrected with the conventional phase dewrapping method is presented in Fig. 7(a). It is observed in Fig. 7(a) that the phenomenon of twin peaks causes severe shading artifacts. However, with the phase retrieval and dewrapping methods proposed in this work, those artifacts can be substantially reduced, if not eliminated. The visual improvement in image quality can be quantitatively reinforced by the profiles presented in Figs. 7(c) and 7(d), which corresponds to the horizontal and vertical lines labeled in Figs. 7(a) and 7(b), respectively.

4.C. Quality improvement in x-ray differential phase contrast projection imaging by phase dewrapping

Phase wrapping may induce disruptive variations in the differential phase contrast projection image acquired by the proposed phase retrieval approach, as illustrated by the dark and bright dots in the image presented in Fig. 8(a). Those disruptive artifacts can be removed by either the conventional or the proposed dewrapping method, as shown in Figs. 8(b) and 8(c). To have a zoomed inspection, small portions labeled in Figs. 8(b) and 8(c) and their difference are presented in Figs. 8(d), 8(e), and 8(f). Each bright dot in Fig. 8(f) indicates a difference of either 2π or -2π between the images in Figs. 8(d) and 8(e), showing that the proposed dewrapping approach performs differently from the conventional method.

To compare the proposed dewrapping approach with the conventional approach, an experiment is carried out using the organic phantom. Presented in Fig. 9(a) is the differential phase contrast projection image of the organic

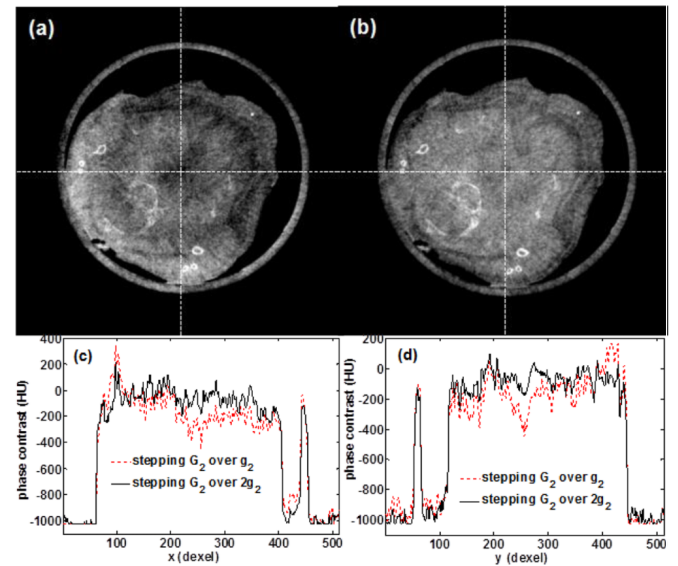


FIG. 7. Transverse images of the mouse reconstructed from the data acquired by (a) stepping grating G_2 over its nominal period and dewrapping with conventional method, and (b) stepping G_2 over twice its nominal period and dewrapping with the proposed approach. The profiles in (c) are along the horizontal lines in (a) and (b), while those in (d) along the vertical lines in (a) and (b) [display: $[-400 300]$ HU in (a) and (b)].

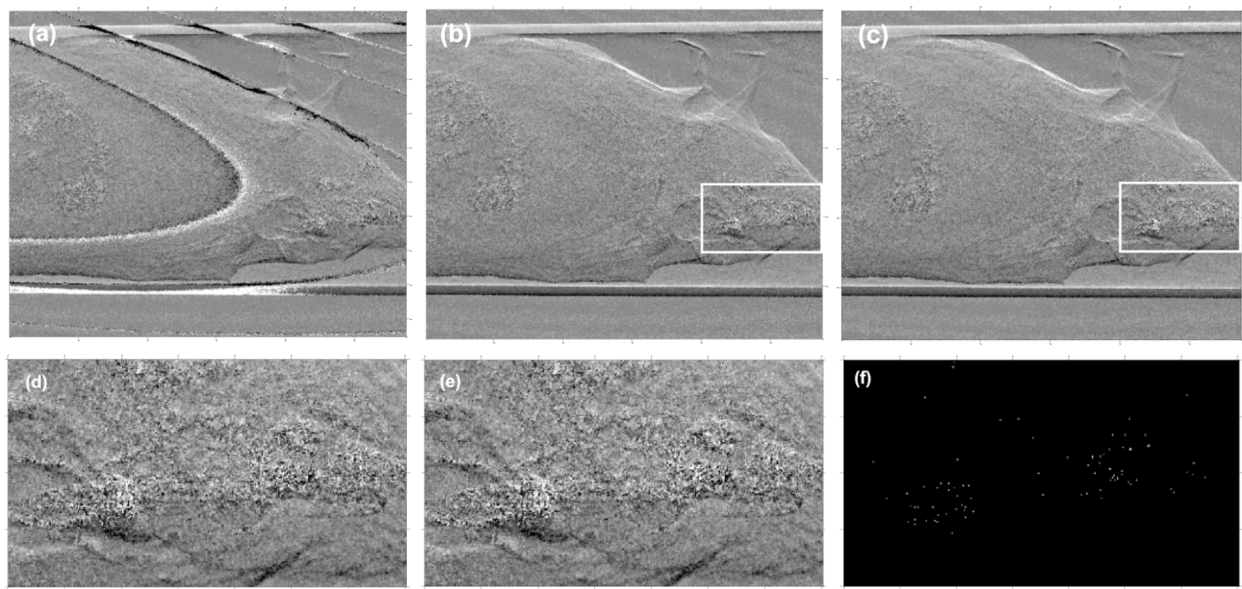


FIG. 8. Projection images of the mouse obtained from the original measured phase difference $\varphi_{2w}(m, n)$ (a), that corrected with the conventional phase dewrapping method (b), and that corrected with the proposed approach (c). (d) and (e) are zoomed viewing of the areas marked in (b) and (c), respectively. (f) is the absolute value of the difference between (d) and (e) [display window: $[-\pi/2 \pi/2]$ in (a)–(e), $[0 2\pi]$ in (f)].

phantom acquired by the proposed phase retrieval approach. Visually, the disruptive artifacts in Fig. 9(a) can be removed by both the conventional [Fig. 9(b)] and the proposed dewrapping methods [Fig. 9(c)]. However, the plotting of profiles [Fig. 9(d)] shows that the conventional approach may cause new phase wrapping at other locations, whereas the proposed phase dewrapping approach does not lead to any new phase wrapping at other locations. The maximum gradient along each profile in Fig. 9(d) is used to quantitatively assess the phase dewrapping performance, and the results corresponding to the original, conventional, and proposed approaches are 2.0π , 1.96π , and 0.29π , which enforces our visual inspection of the profiles presented in Fig. 9(d).

5. DISCUSSIONS AND CONCLUSIONS

In this work, we derive the analytic formulae to characterize the phenomenon of twin peaks in the PSC acquired by Talbot interferometry with a microfocus x-ray tube. Through a mathematical treatment based on the paraxial Fresnel–Kirchhoff theory, a theoretical framework, as described by Eqs. (26), (28), and (29), is developed for the retrieval of attenuation contrast, differential phase contrast, and dark-field contrast from the PSC with the feature of twin peaks. As demonstrated by our theoretical study [Eq. (43)], the twin-peak phenomenon in PSC is a consequence of combined effects, including the defects in absorption grating G_2 's fabrication, mismatch between phase grating G_1 and x-ray source spectrum, and finite size of x-ray tube's focal spot. The preliminary data provided by the prototype x-ray phase contrast imaging system validate the derived analytic formulae and verify the performance of the proposed approaches for phase retrieval and dewrapping.

An absorption grating with a large area and high aspect ratio is the key component in x-ray differential phase contrast imaging implemented with Talbot interferometry.¹⁴ Although significant progress has been made,^{23,24} the fabrication of a large and high aspect-ratio absorption grating G_2 is still a major challenge. It is possible that imperfection may exist in an absorption grating if those challenges cannot be readily overcome by current nanofabrication technologies, especially in the cases wherein a reasonable yield rate is desired. As analyzed in this and other papers,^{8,9} it is not uncommon that the effective period of the absorption grating G_2 can be as large as twice its nominal one. Modregger *et al.*⁸ and McDonald *et al.*⁹ reported the phenomenon of twin peaks in PSC and suggested that the absorption grating G_2 should be shifted over a distance that is equal to twice its nominal period to acquire the intensity modulation data for x-ray phase contrast imaging. However, to the best of our knowledge, no systematic

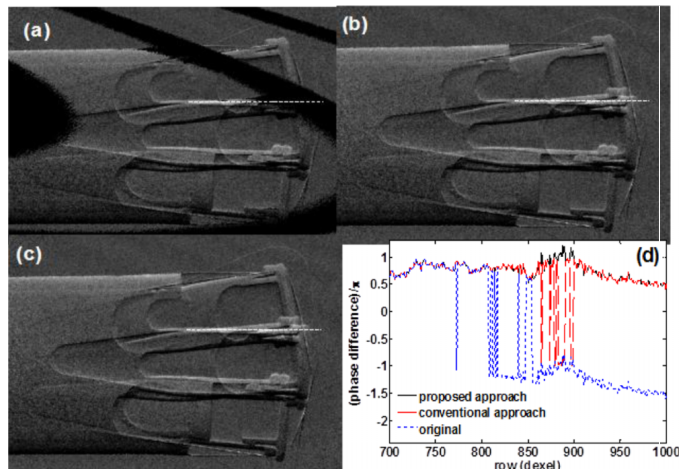


FIG. 9. Projection images of the organic phantom obtained from the original measured phase difference $\varphi_{2w}(m, n)$ (a), after phase dewrapping by conventional method (b), and by the proposed approach (c). Profiles along the dashed horizontal lines labeled in (a), (b), and (c) are presented in (d) [display window: $[\pi/3 \pi]$ in (a)–(c)].

investigation into the grating-based x-ray differential phase contrast imaging with the phenomenon of twin peaks in PSC has thus far been derived and presented.

Different from the conventional phase dewrapping method, which is quite intuitive from the perspective of data processing, the approach proposed in this study does not require that the phase signal be small enough to satisfy the moderate phase-variation condition specified by Eq. (50). It should be noted that the case presented in Fig. 9 is an exemplification of the cases in which the moderate phase-variation condition is violated. Accordingly, the conventional dewrapping method may not work well, but the proposed dewrapping approach still works well, as we visually observed and quantitatively verified in Sec. 4.C. Thus, the approach proposed by us is applicable in more general cases, which may be of higher practical potential in a variety of x-ray phase contrast imaging applications, ranging from medical diagnosis and biological study to material sciences.

Generally speaking, imperfections in the absorption grating G_2 diminish the visibility in PSC. Moreover, shifting the absorption grating G_2 over a distance that is as large as twice its nominal period can slow down the data acquisition in the x-ray differential phase contrast imaging implemented with the Talbot interferometry. However, the phenomenon of twin peaks existing in the PSCs in practice can actually provide an opportunity for one to obtain more Fourier coefficients in comparison to the case with ideal gratings. As a result, more information about the phase contrast and dark-field contrast of the object to be imaged can be acquired. This means that, if imperfection in the absorption grating G_2 cannot be readily eliminated using currently available nanofabrication technologies, this limitation can actually be turned into a benefit in the phase retrieval process. Specifically, based on a joint utilization of the first- and second-order Fourier coefficients in the PSC with twin peaks, we proposed an approach for phase dewrapping in phase retrieval. It should be noted that phase dewrapping is a challenging task in x-ray phase contrast imaging implemented with the Talbot interferometry or other measures. Hence, the approach proposed in this work to address this challenge is of practical importance.

It is a straightforward thought that shifting the absorption grating G_2 over twice its nominal period may double the x-ray dose and time for data acquisition proportionally, if the step of shifting remains unchanged. However, it is our current speculation that the step (Δ_2) of shifting G_2 over twice its nominal period can be larger than the step (Δ_1) of shifting G_2 over its nominal period, i.e., $\Delta_2 = \eta \cdot \Delta_1$ and $\eta \geq 1.0$. As such, the needed dose and time for data acquisition using the proposed approach can be reduced proportionally. A thorough investigation is under the way and we will report the results in the near future.

The analytical derivation presented in this work was initially motivated to deal with the phenomenon of twin peaks in a PSC that hinders accurate or precise phase retrieval in practice. Later on, we realized that the derived formulae can be effectively utilized for phase dewrapping that is another challenging task in the differential x-ray phase contrast imaging system implemented with Talbot interferometer. We

would like to indicate that the analytic formulae derived in this work may be of the relevance beyond what has been presented thus far, and their extended applications in differential x-ray phase contrast imaging system are anticipated.

ACKNOWLEDGMENTS

This work is partially supported by the Telemedicine and Advanced Technology Research Center (TATRC) at the U.S. Army Medical Research and Material Command (USAMRMC) Fort Detrick, MD via the award under Contract No.: W81XWH-12-1-0138. In addition, one of the authors (Y.Y.) wishes to thank Dr. Shaojie Tang for informative discussion and the authors would like to extend their appreciation to Jessica Paulishen for proof reading of the paper.

CONFLICT OF INTEREST DISCLOSURE

The authors have no COI to report.

APPENDIX: CONCISE DERIVATION OF FOURIER COEFFICIENTS FOR INTERFERENCE FRINGE IN GRATING-BASED DIFFERENTIAL PHASE CONTRAST IMAGING

Let x-ray propagate along the z direction, and place the microfocus x-ray source, phase grating G_1 , and absorption grating G_2 at the planes $z=0$, $z=z_1$, and $z=z_2$, respectively (Ref. 27). Supposing the detector is immediately behind absorption grating G_2 , which is linearly shifted along the transverse direction x_g , then the mean intensity of interference fringe recorded at the detector cell indexed by (m,n) is given by^{13,25}

$$I_{m,n}(x_g) = \frac{1}{l_d^2} \int_{x_m - \frac{l_d}{2}}^{x_m + \frac{l_d}{2}} dx \int_{y_n - \frac{l_d}{2}}^{y_n + \frac{l_d}{2}} dy P_2(x - x_g) I(x, y, z_2), \quad (\text{A1})$$

where

$$x_m = \left(m + \frac{1}{2}\right) l_d, \quad y_n = \left(n + \frac{1}{2}\right) l_d, \quad m, n = 0, \pm 1, \pm 2, \dots \quad (\text{A2})$$

$P_2(x)$ is a projection function representing the analyzer grating G_2 , l_d the detector cell dimension, and $I(x, y, z_2)$ the intensity immediately in front of G_2 , which can be expressed as^{15,16}

$$I(x, y, z_2) = \frac{z_1^2}{z_{12}^2} \iint dx_0 dy_0 I_{\text{source}} \left(-\frac{z_1}{z_{12}} x_0, -\frac{z_1}{z_{12}} y_0 \right) \times |E_{\text{point}}(x - x_0, y - y_0, z_2)|^2, \quad (\text{A3})$$

where $E_{\text{point}}(x, y, z_2)$ denotes the electric field produced by the point source. As assumed in Sec. 2.A, the incident x-ray beam is assumed as a spherical wave that is monochromatic with wavelength λ . The distance from G_1 to G_2 is selected as the

m_T th fractional Talbot distance⁶

$$z_{12} = z_2 - z_1 = m_T \frac{g_1^2}{8\gamma\lambda}, \quad m_T = 1, 3, 5, \dots, \quad (\text{A4})$$

where g_1 is the pitch of the phase grating G_1 , and $\gamma = z_1/z_2$. In order to maximize the interference fringe visibility, one usually sets⁶

$$g_1 = 2\gamma g_2, \quad (\text{A5})$$

where g_2 is the nominal period of grating G_2 . Furthermore, we

focus on the grating-based differential phase contrast imaging system with detector cell dimension l_d large enough to meet

$$l_d \gg g_2 \text{ and } l_d \gg d_c, \quad (\text{A6})$$

where d_c is a length given by

$$d_c = \frac{\lambda z_{12}}{g_2} = \frac{m_T}{4} g_1. \quad (\text{A7})$$

As discussed in Sec. 2, one may analytically represent the gratings G_1 and G_2 as

$$P_1(x) = \begin{cases} 1, & ng_1 \leq x < \left(n + \frac{1}{2}\right)g_1, \\ \exp(iQ_1), & \left(n + \frac{1}{2}\right)g_1 \leq x < (n+1)g_1, \end{cases} \quad n = 0, \pm 1, \pm 2, \dots, \quad (\text{A8})$$

$$P_2(x) = \begin{cases} 1, & 2ng_2 \leq x < \left(2n + \frac{1}{2}\right)g_2, \\ 0, & \left(2n + \frac{1}{2}\right)g_2 \leq x < (2n+1)g_2, \\ W_{si}, & (2n+1)g_2 \leq x < \left(2n + \frac{3}{2}\right)g_2, \\ 0, & \left(2n + \frac{3}{2}\right)g_2 \leq x < 2(n+1)g_2, \end{cases} \quad n = 0, \pm 1, \pm 2, \dots, \quad (\text{A9})$$

where Q_1 is the actual phase shift due to grating G_1 , and W_{si} denotes the relative transmission of the ridge in grating G_2 compared to that of the groove (see Fig. 3). Based on the projection approximation^{13,16,25} and the paraxial Fresnel-Kirchhoff theory,^{6,13,16,25} the electric field immediately in front of the analyzer grating G_2 can be written as¹⁵

$$E_{\text{point}}(x, y, z_2) = A \frac{\exp\left(i\frac{2\pi}{\lambda} \sqrt{x^2 + y^2 + z_2^2}\right)}{i\lambda z_1 z_{12}} \int dx_1 \int dy_1 \exp\left(-\frac{\Lambda(x_1, y_1)}{2} - i\Phi(x_1, y_1)\right) P_1(x_1) \exp\left(i\pi \frac{(x_1 - \gamma x)^2 + (y_1 - \gamma y)^2}{\lambda \gamma z_{12}}\right), \quad (\text{A10})$$

where A is a constant, and

$$\Lambda(x, y) = \frac{4\pi}{\lambda} \int_Z \beta\left(\frac{z}{z_1} x, \frac{z}{z_1} y, z\right) \sqrt{1 + \frac{x^2 + y^2}{z_1^2}} dz, \quad (\text{A11})$$

$$\Phi(x, y) = \frac{2\pi}{\lambda} \int_Z \delta\left(\frac{z}{z_1} x, \frac{z}{z_1} y, z\right) \sqrt{1 + \frac{x^2 + y^2}{z_1^2}} dz \quad (\text{A12})$$

are the projections of linear attenuation index β and refractive index decrement δ , respectively, along x-ray path from the point source at coordinate origin to a point (x, y, z_1) at the plane of G_1 .

Substituting Eqs. (A10) and (A3) into Eq. (A1), one can show that the intensity $I_{m,n}(x_g)$ is a periodic function of x_g with period $2g_2$,

$$I_{m,n}(x_g) = \sum_{l=-\infty}^{\infty} C_l(m,n) \exp\left(\pi i l \frac{x_g}{g_2}\right), \quad (\text{A13})$$

and the Fourier coefficients are given by

$$\begin{aligned} C_l(m,n) = |A|^2 \sum_{l=-\infty}^{\infty} \frac{1 + (-1)^l W_{si}}{4\lambda^2 z_{12}^4} \operatorname{sinc}\left(\frac{l}{4}\right) \exp\left(i\frac{l\pi}{4} - il\pi \frac{x_m}{g_2}\right) \iint dx_0 dy_0 I_{\text{source}}\left(-\frac{z_1}{z_{12}} x_0, -\frac{z_1}{z_{12}} y_0\right) \\ \times \int dx_1 \int dy_1 \int dx_2 \int dy_2 \exp\left(-\frac{\Lambda(x_1, y_1) + \Lambda(x_2, y_2)}{2} + i(\Phi(x_2, y_2) - \Phi(x_1, y_1))\right) \end{aligned}$$

$$\begin{aligned} & \times \exp\left(i \frac{2\pi}{\lambda\gamma z_{12}} \left(\frac{x_1+x_2}{2} - \gamma(x_m-x_0)\right)(x_1-x_2)\right) \exp\left(i \frac{2\pi}{\lambda\gamma z_{12}} \left(\frac{y_1+y_2}{2} - \gamma(y_n-y_0)\right)(y_1-y_2)\right) \\ & \times \text{sinc}\left(\frac{x_2-x_1-\frac{l}{2}d_c}{d_f}\right) \text{sinc}\left(\frac{y_2-y_1}{d_f}\right) \sum_{j_1=-\infty}^{\infty} \frac{1+(-1)^{j_1}\exp(iQ_1)}{2} \text{sinc}\left(\frac{j_1}{2}\right) \exp\left(i2\pi j_1\left(\frac{x_1}{g_1}-\frac{1}{4}\right)\right) \\ & \times \sum_{j_2=-\infty}^{\infty} \frac{1+(-1)^{j_2}\exp(-iQ_1)}{2} \text{sinc}\left(\frac{j_2}{2}\right) \exp\left(-i2\pi j_2\left(\frac{x_2}{g_1}-\frac{1}{4}\right)\right), \end{aligned} \quad (\text{A14})$$

where the sinc function is defined as $\text{sinc}(x) = \sin(\pi x)/(\pi x)$, and

$$d_f = \frac{\lambda z_{12}}{l_d} = \frac{d_c}{l_d/g_2}. \quad (\text{A15})$$

Because of the two sinc functions on the right side of Eq. (A14), the dominant contribution to Fourier coefficients $C_l(m,n)$ comes from the electric field at (x_1, y_1) and (x_2, y_2) that satisfies

$$\left|x_2-x_1-\frac{l}{2}d_c\right| \ll d_f \ll d_c \text{ and } |y_2-y_1| \ll d_f \ll d_c. \quad (\text{A16})$$

As a consequence, the projections $\Lambda(x,y)$ and $\Phi(x,y)$ can be approximated as

$$\Lambda(x_1, y_1) \approx \Lambda\left(\frac{x_1+x_2-\frac{l}{2}d_c}{2}, \frac{y_1+y_2}{2}\right),$$

$$\Phi(x_1, y_1) \approx \Phi\left(\frac{x_1+x_2-\frac{l}{2}d_c}{2}, \frac{y_1+y_2}{2}\right), \quad (\text{A17})$$

$$\Lambda(x_2, y_2) \approx \Lambda\left(\frac{x_1+x_2+\frac{l}{2}d_c}{2}, \frac{y_1+y_2}{2}\right),$$

$$\Phi(x_2, y_2) \approx \Phi\left(\frac{x_1+x_2+\frac{l}{2}d_c}{2}, \frac{y_1+y_2}{2}\right). \quad (\text{A18})$$

Inserting Eqs. (A17) and (A18) into Eq. (A14) and changing the variables of integration with

$$u = \frac{x_1+x_2}{2}, \quad v = \frac{x_2-x_1}{2}, \quad (\text{A19})$$

$$\sigma = \frac{y_1+y_2}{2}, \quad \eta = \frac{y_2-y_1}{2}, \quad (\text{A20})$$

we can approximate the Fourier coefficients as

$$\begin{aligned} C_l(m,n) = & |A|^2 \frac{1+(-1)^l W_{si}}{4z_{12}^2 l_d^2} \text{sinc}\left(\frac{l}{4}\right) \exp\left(-il\frac{l\pi}{4}\right) \iint dx_0 dy_0 \\ & \times I_{\text{source}}\left(-\frac{z_1}{z_{12}}x_0, -\frac{z_1}{z_{12}}y_0\right) \exp\left(-il\pi\frac{x_0}{g_2}\right) \\ & \times \Gamma_l(Q_1, m_T) \int_{\gamma(x_m-x_0)-\frac{\gamma l_d}{2}}^{\gamma(x_m-x_0)+\frac{\gamma l_d}{2}} du \int_{\gamma(y_n-y_0)-\frac{\gamma l_d}{2}}^{\gamma(y_n-y_0)+\frac{\gamma l_d}{2}} d\sigma \\ & \times \exp\left(-\frac{\Lambda(u-\frac{l}{4}d_c, \sigma) + \Lambda(u+\frac{l}{4}d_c, \sigma)}{2}\right) \\ & \times \exp\left(i\left(\Phi\left(u+\frac{l}{4}d_c, \sigma\right) - \Phi\left(u-\frac{l}{4}d_c, \sigma\right)\right)\right), \end{aligned} \quad (\text{A21})$$

where

$$\begin{aligned} \Gamma_l(Q_1, m_T) = & \sum_{j=-\infty}^{\infty} \frac{1+(-1)^j \exp(iQ_1)}{2} \frac{1+(-1)^{j-l} \exp(-iQ_1)}{2} \text{sinc}\left(\frac{j}{2}\right) \\ & \times \text{sinc}\left(\frac{j-l}{2}\right) \exp\left(il\pi m_T \frac{l-2j}{8}\right). \end{aligned} \quad (\text{A22})$$

It should be noted that in the derivation of Eq. (A21), we assume that the fine (unresolvable) features of the object to be imaged, if they exist, distribute randomly.^{5,17} And it is straightforward to show that

$$\Gamma_0(Q_1, m_T) = 1, \quad \Gamma_1(Q_1, m_T) = -\frac{2\sin(Q_1)}{\pi} \sin\left(\pi \frac{m_T}{8}\right), \quad \Gamma_2(Q_1, m_T) = \frac{1-\cos(Q_1)}{\pi}, \quad (\text{A23})$$

in which the formulae²⁶

$$\sum_{j=0}^{\infty} \frac{1}{(2j+1)^2} = \frac{\pi^2}{8}, \quad \sum_{j=0}^{\infty} \frac{(-1)^j}{2j+1} = \frac{\pi}{4} \quad (\text{A24})$$

are used to sum the corresponding series. Applying Eq. (A23) to Eq. (A21), the Fourier coefficients can be calculated as

$$C_0(m,n) = |A|^2 \frac{1+W_{si}}{4z_{12}^2 l_d^2} \iint dx_0 dy_0 I_{\text{source}}\left(-\frac{z_1}{z_{12}}x_0, -\frac{z_1}{z_{12}}y_0\right) \int_{\gamma(x_m-x_0)-\frac{\gamma l_d}{2}}^{\gamma(x_m-x_0)+\frac{\gamma l_d}{2}} du \int_{\gamma(y_n-y_0)-\frac{\gamma l_d}{2}}^{\gamma(y_n-y_0)+\frac{\gamma l_d}{2}} d\sigma \exp(-\Lambda(u, \sigma)), \quad (\text{A25})$$

$$C_1(m,n) = |A|^2 \frac{\sin(\pi \frac{m_T}{8})(i-1)}{\pi^2 z_{12}^2 l_d^2} (1 - W_{si}) \sin(Q_1) \iint dx_0 dy_0 I_{\text{source}} \left(-\frac{z_1}{z_{12}} x_0, -\frac{z_1}{z_{12}} y_0 \right) \exp \left(-i\pi \frac{x_0}{g_2} \right) \\ \times \int_{\gamma(x_m-x_0)-\frac{\gamma l_d}{2}}^{\gamma(x_m-x_0)+\frac{\gamma l_d}{2}} du \int_{\gamma(y_n-y_0)-\frac{\gamma l_d}{2}}^{\gamma(y_n-y_0)+\frac{\gamma l_d}{2}} d\sigma \exp \left(-\Lambda(u, \sigma) + i \left(\Phi \left(u + \frac{d_c}{4}, \sigma \right) - \Phi \left(u - \frac{d_c}{4}, \sigma \right) \right) \right), \quad (\text{A26})$$

$$C_2(m,n) = -i|A|^2 \frac{1+W_{si}}{2\pi^2 z_{12}^2 l_d^2} (1 - \cos(Q_1)) \iint dx_0 dy_0 I_{\text{source}} \left(-\frac{z_1}{z_{12}} x_0, -\frac{z_1}{z_{12}} y_0 \right) \exp \left(-i2\pi \frac{x_0}{g_2} \right) \\ \times \int_{\gamma(x_m-x_0)-\frac{\gamma l_d}{2}}^{\gamma(x_m-x_0)+\frac{\gamma l_d}{2}} du \int_{\gamma(y_n-y_0)-\frac{\gamma l_d}{2}}^{\gamma(y_n-y_0)+\frac{\gamma l_d}{2}} d\sigma \exp \left(-\Lambda(u, \sigma) + i \left(\Phi \left(u + \frac{d_c}{2}, \sigma \right) - \Phi \left(u - \frac{d_c}{2}, \sigma \right) \right) \right). \quad (\text{A27})$$

^aAuthor to whom correspondence should be addressed. Electronic mail: xiangyang.tang@emory.edu; Telephone: (404) 778-1732; Fax: (404) 712-5813.

¹T. Weitkamp, A. Diaz, C. David, F. Pfeiffer, M. Stampanoni, P. Cloetens, and E. Ziegler, "X-ray phase imaging with a grating interferometer," *Opt. Express* **13**, 6296–6304 (2005).

²F. Pfeiffer, T. Weitkamp, O. Bunk, and C. David, "Phase retrieval and differential phase-contrast imaging with low-brilliance x-ray sources," *Nat. Phys.* **2**, 258–261 (2006).

³A. Momose and J. Fukuda, "Phase-contrast radiographs of nonstained rat cerebellar specimen," *Med. Phys.* **22**, 375–379 (1997).

⁴F. Pfeiffer, M. Bech, O. Bunk, P. Kraft, E. F. Eikenberry, C. Bronnimann, C. Grunzweig, and C. David, "Hard-x-ray dark-field imaging using a grating interferometer," *Nat. Mater.* **7**, 134–137 (2008).

⁵M. Bech, O. Bunk, T. Donath, R. Feidenhans'l, C. David, and F. Pfeiffer, "Quantitative x-ray dark-field computed tomography," *Phys. Med. Biol.* **55**, 5529–5539 (2010).

⁶M. Bech, "X-ray imaging with a grating interferometer," Ph.D. thesis, University of Copenhagen, Denmark, 2009.

⁷A. Momose, S. Kawamoto, I. Koyama, Y. Hamaishi, K. Takai, and Y. Suzuki, "Demonstration of x-ray Talbot interferometry," *Jpn. J. Appl. Phys., Part 2* **42**, L866–L868 (2003).

⁸P. Modregger, F. Scattarella, B. R. Pinzer, C. David, R. Bellotti, and M. Stampanoni, "Imaging the ultrasmall-angle x-ray scattering distribution with grating interferometry," *Phys. Rev. Lett.* **108**, 048101 (2012).

⁹S. A. McDonald, F. Marone, C. Hintermuller, G. Mikuljan, C. David, F. Pfeiffer, and M. Stampanoni, "Advanced phase-contrast imaging using a grating interferometer," *J. Synchrotron Radiat.* **16**, 562–572 (2009).

¹⁰R. Fitzgerald, "Phase-sensitive x-ray imaging," *Phys. Today* **53**(7), 23–26 (2000).

¹¹M. Born and E. Wolf, *Principles of Optics: Electromagnetic Theory of Propagation, Interference and Diffraction of Light*, 7th ed. (Cambridge University Press, Cambridge, England, 1999).

¹²R. A. Lewis, "Medical phase contrast x-ray imaging: Current status and future prospects," *Phys. Med. Biol.* **49**, 3573–3583 (2004).

¹³Y. Yang and X. Tang, "Complex dark-field contrast and its retrieval in x-ray phase contrast imaging implemented with Talbot interferometry," *Med. Phys.* **41**, 101914 (19pp.) (2014).

¹⁴C. David, J. Bruder, T. Rohbeck, C. Grunzweig, C. Kottler, A. Diaz, O. Bunk, and F. Pfeiffer, "Fabrication of diffraction gratings for hard x-ray phase contrast imaging," *Microelectron. Eng.* **84**, 1172–1177 (2007).

¹⁵B. Golosio, P. Delogu, I. Zanette, M. Carpinelli, G. L. Masala, P. Oliva, A. Stefanini, and S. Stumbo, "Phase contrast imaging simulation and measurements using polychromatic sources with small source-object distances," *J. Appl. Phys.* **104**, 093102 (2008).

¹⁶M. Engelhardt, C. Kottler, O. Bunk, C. David, C. Schroer, J. Baumann, M. Schuster, and F. Pfeiffer, "The fractional Talbot effect in differential x-ray phase-contrast imaging for extended and polychromatic x-ray sources," *J. Microsc.* **232**, 145–157 (2008).

¹⁷Y. I. Nesterets, "On the origins of decoherence extinction contrast in phase-contrast imaging," *Opt. Commun.* **281**, 533–542 (2008).

¹⁸R. Raupach and T. G. Flohr, "Analytical evaluation of the signal and noise propagation in x-ray differential phase-contrast computed tomography," *Phys. Med. Biol.* **56**, 2219–2244 (2011).

¹⁹I. Jerjen, V. Revol, P. Schuetz, C. Kottler, R. Kaufmann, T. Luethi, K. Jefimovs, C. Urban, and U. Sennhauser, "Reduction of phase artifacts in differential phase contrast computed tomography," *Opt. Express* **19**, 13604–13611 (2011).

²⁰D. C. Ghiglia and M. D. Pritt, *Two-Dimensional Phase Unwrapping: Theory, Algorithms, and Software* (Wiley Interscience, New York, NY, 1998).

²¹H. Y. Huang, L. Tian, Z. Zhang, Y. Liu, Z. Chen, and G. Barbastathis, "Path-independent phase unwrapping using phase gradient and total-variation (TV) denoising," *Opt. Express* **20**, 14075–14089 (2012).

²²D. Shi and M. A. Anastasio, "Relationships between smooth- and small-phase conditions in x-ray phase-contrast imaging," *IEEE Trans. Med. Imaging* **28**, 1969–1973 (2009).

²³J. Mohr, T. Grund, D. Kunka, J. Kenntner, J. Leuthold, J. Meiser, J. Schulz, and M. Walter, "High aspect ratio gratings for x-ray phase contrast imaging," *AIP Conf. Proc.* **1466**, 41–50 (2012).

²⁴J. Kenntner, V. Altapova, T. Grund, F. J. Pantenburg, J. Meiser, T. Baumbach, and J. Mohr, "Fabrication and characterization of analyzer gratings with high aspect ratios for phase contrast imaging using a Talbot interferometer," *AIP Conf. Proc.* **1437**, 89–93 (2012).

²⁵Y. Yang and X. Tang, "The second-order differential phase contrast and its retrieval for imaging with x-ray Talbot interferometry," *Med. Phys.* **39**, 7237–7253 (2012).

²⁶V. Mangulis, *Handbook of Series for Scientists and Engineers* (Academic, New York, NY, 1965).

²⁷See supplementary material at <http://dx.doi.org/10.1118/1.4948690> for a full version of derivation of Fourier coefficients for interference fringe in grating-based differential phase contrast imaging.

1. INTRODUCTION: As the elderly population increases, dementia due to Alzheimer's disease (AD) has emerged as a major threat to human's health¹⁻³. Recently, the x-ray CT based on a new imaging mechanism—refraction—is emerging as a new technology to improve CT's capability of differentiating soft tissues⁴⁻¹⁰. We propose to develop the x-ray phase contrast CT imaging method with an x-ray tube and gratings for direct detecting of amyloid plaques in Alzheimer's brain. It is hypothesized that the disparity in their refractive property can generate contrast between amyloid plaques and surrounding neuronal tissues in AD and the contrast is sufficient for imaging. Without the involvement of contrast agent or molecular probes, the so-called BBB (brain blood barrier) can thus be avoided. The project started on 05/15/2012 and ended on 05/14/2016, with a no cost one year extension from 05/15/2015 to 05/14/2016. Here is the final report of the project, covering the key research accomplishments, reportable outcomes and conclusions, based on the preliminary data acquired over the span of four years.

2. KEYWORDS: Alzheimer's disease, amyloid plaque, A-beta, x-ray phase contrast, CT, x-ray phase contrast CT, x-ray differential phase contrast CT, Talbot interferometer, grating-based differential phase contrast CT.

3. ACCOMPLISHMENTS:

What were the major goals of the project?

In order to be objective and complete, the three Specific Aims (SAs) specified in the Statement of Work (SOW) are reiterated here, and the final report is organized in line with these SAs as adequately as possible.

SA#1 Develop and optimize an x-ray phase CT to explore the methodology of direct imaging of AP;
Outcome: An x-ray tube- and grating-based phase CT as the foundation for the pursuit of SA #2 and #3.

SA#2 Evaluate the x-ray phase CT's capability of imaging $A\beta_{1-40}/A\beta_{1-42}$ peptides/fibrils at the concentrations existing in AD brain;

Outcome: A quantitative understanding of x-ray phase CT's capability in imaging the $A\beta_{1-40}$ and $A\beta_{1-42}$ fibrils.

SA#3 Verify the x-ray phase CT's capability of direct imaging of AP in AD using postmortem brain specimens.

Outcome: Quantitatively evaluated and verified performance of x-ray phase CT for imaging APs in AD.

What was accomplished under these goals?

Project Timeline: The original timeline specified in the SOW is presented in Table I. Mainly due to two reasons – (i) the fabrication/optimization of x-ray gratings were much more complicated and challenging than what we initially anticipated and (ii) the acquisition of one set of projection data in the x-ray phase contrast CT takes about 12 hours because of the limitation in output power of the micro-focus x-ray tube, a one year no-cost extension of this project has been request and approved. Presented in Table II is the revised timeline, with the new ending date at 05/14/2016/.

Table I. The original project timeline specified in the project's SOW.

Tasks	Q1	Q2	Q3	Q4	Q5	Q6	Q7	Q8	Q9	Q10	Q11	Q12
D.1.1: System construction			→									
D.1.2: System optimization				→								
D.2: Performance: Phantom study						→						
D.3: Performance: Specimen study									→			

Table II. The revised project timeline specified in the project's SOW with one year extension.

Tasks	Q ₁	Q ₂	Q ₃	Q ₄	Q ₅	Q ₆	Q ₇	Q ₈	Q ₉	Q ₁₀	Q ₁₁	Q ₁₂	Q ₁₃	Q ₁₄	Q ₁₅	Q ₁₆
D.1.1: System construction																
D.1.2: System optimization																
D.2: Phantom study																
D.3: Specimen study																

Accomplishments towards Specific Aim 1 and 2:

An x-ray phase contrast CT, which consists of a micro-focus tube, a C-MOS flat panel x-ray detector with $48\mu m$ detector cell dimension, a linear motor-driven stepper and two x-ray gratings G_1 and G_2 , has been prototyped in the PI's lab (see Fig. 1) for carrying out the tasks of this project. The two gratings G_1 and G_2 are the key components of the prototype system, which were fabricated in the NanoTechnology Research Center of GaTech (see Fig. 2). The imaging performance of this prototype system has gone through optimization, with an emphasis on coping with phase wrapping¹¹ and the imperfection¹³ in G_1 and G_2 and the possible negative influence on imaging performance. The prototype x-ray phase contrast CT system is now fully functioning, with every aspect of imaging performance, but the x-ray source power and the resultant data acquisition time, approaches what is designed (see Fig. 1). The relatively long data acquisition time can be proportionally shortened using a micro-focus tube with a larger output power. We summarize the development and optimization that have been made by us to substantially improve the prototype x-ray phase contrast CT system's imaging performance for imaging specimen of AD brain as listed below.

A. System integration and optimization–Phase de-wrapping: There inevitably exists imperfection in either grating G_1 or G_2 , or both, which may cause the so-called phase wrapping phenomenon in projection data, as illustrated in Fig. 3 (a). We developed a phase de-wrapping approach based on a theoretical framework derived by us¹¹, which can substantially reduce, if not eliminate, the artifacts caused by the phase-wrapping phenomenon, as demonstrated in Fig. 3 (b), in which a cylindrical water phantom consisting of four (4) cylindrical targets made of glycerol, alcohol, isopropanol and air (namely organic phantom henceforth) is utilized.

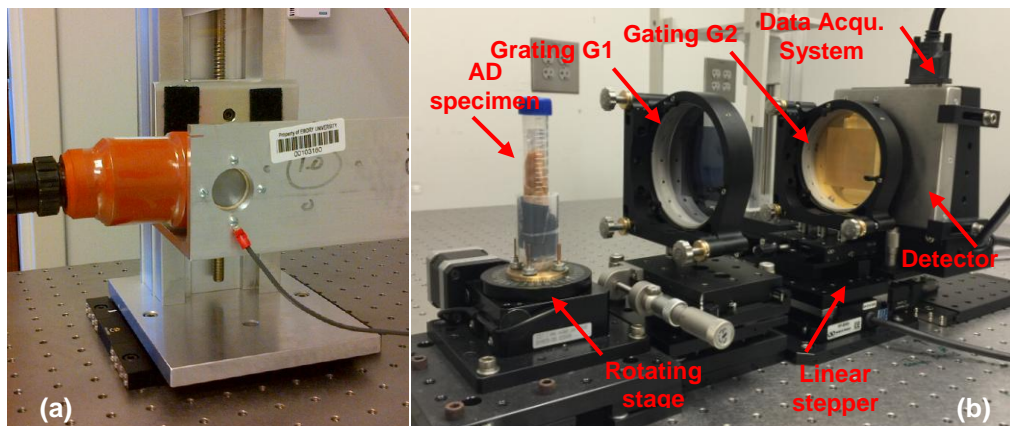


Figure 1. A picture of the prototype x-ray phase CT system that is fully functioning in the PI's lab: (a) the micro focus x-ray tube and (b) the rest of the system, including rotating stage, grating G1, grating G2, linear stepper, flat panel x-ray detector and data acquisition system.

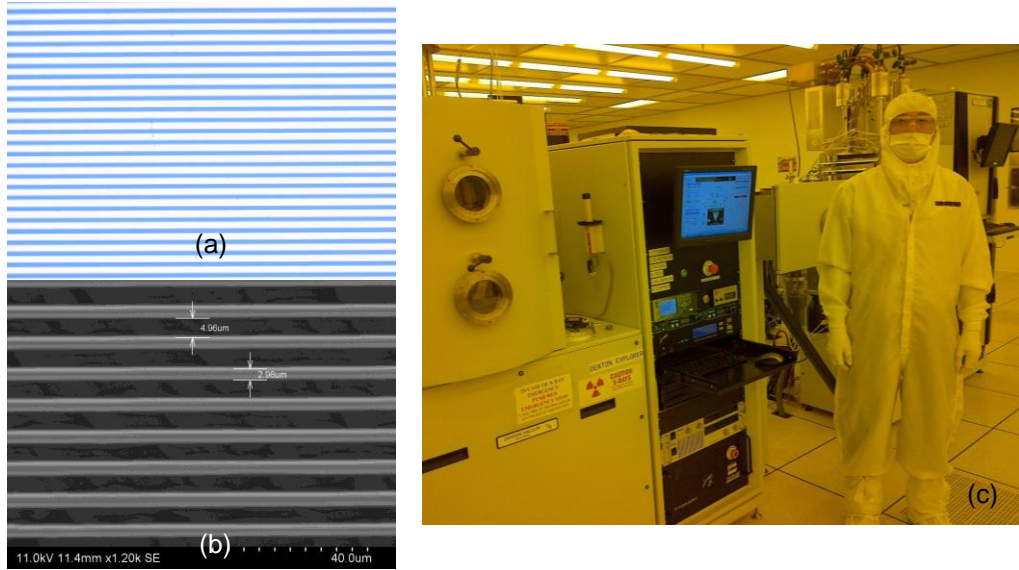


Figure 2. The lithography mask of phase grating G_1 photographed by a microscope at 50 time magnification (a), the grating G_1 photographed by an SEM (scanning electronic microscope) (b), and a picture of the PI who is working at the clean room of GaTech's NanoTechnology Research Center (c).

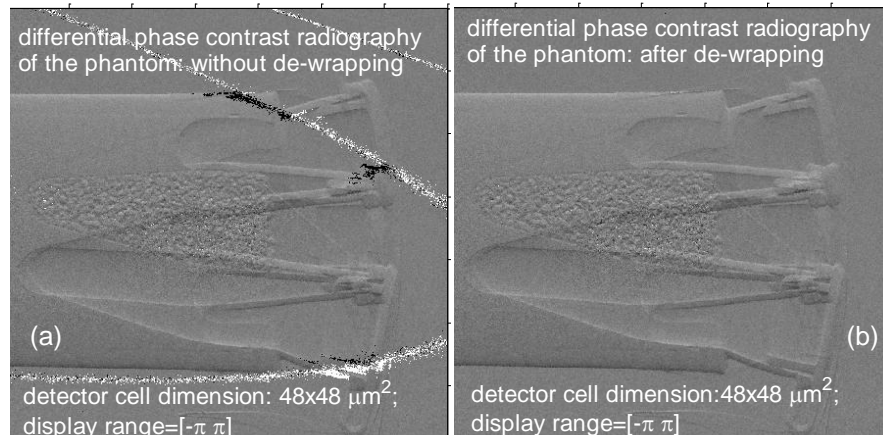


Figure 3. The x-ray phase contrast projection images of an organic material phantom without phase de-wrapping (a) and with phase de-wrapping (b).

B. System integration and optimization—Extension of FOV: As we can see in Fig. 4, with phase de-wrapping, the field of view in the projection image can be effectively extended to be equal to the active area of gratings G_1 and G_2 ($60 \times 60 \text{ mm}^2$). As such, the FOV in tomographic image can be extended accordingly, as demonstrated in Fig. 4.

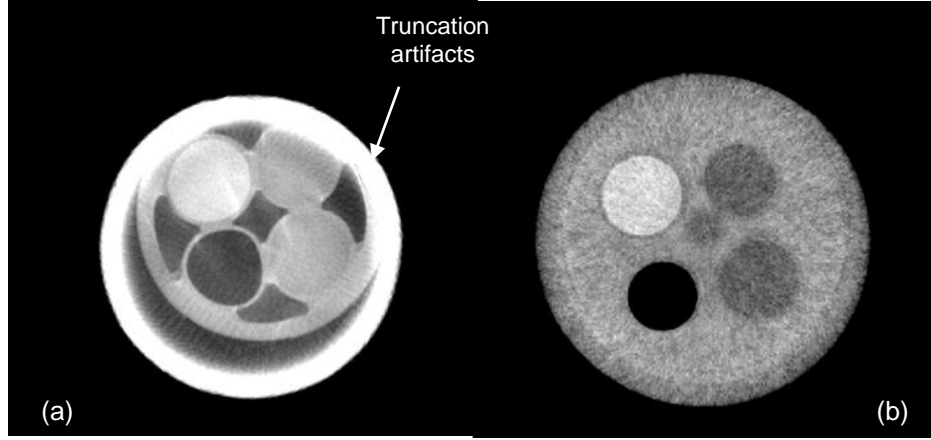


Figure 4. The x-ray phase contrast CT images of the organic material phantom with FOV truncated by artifacts due to phase-wrapping (**a**) and with FOV extended by removing the artifacts caused by phase wrapping in the projection domain (**b**).

C. System integration and optimization—Reduction of artifacts caused by twin-peaks: The imperfection in fabrication of grating G1 and G2 causes not only phase wrapping in data acquisition, but also the so-called feature of “twin-peaks” in the phase-shifting curves (PSCs), as illustrated in Fig. 5(a)^{13,14}. If not handled adequately, the twin-peaks can generate artifacts in reconstructed x-ray phase contrast images, as exemplified in Fig. 5 (b). We derived a theoretical framework to characterize the twin-peaks phenomenon and developed an algorithm to significantly reduce, if not eliminate, the artifacts caused by the phenomenon of twin peaks, as shown in Fig. 5 (c).

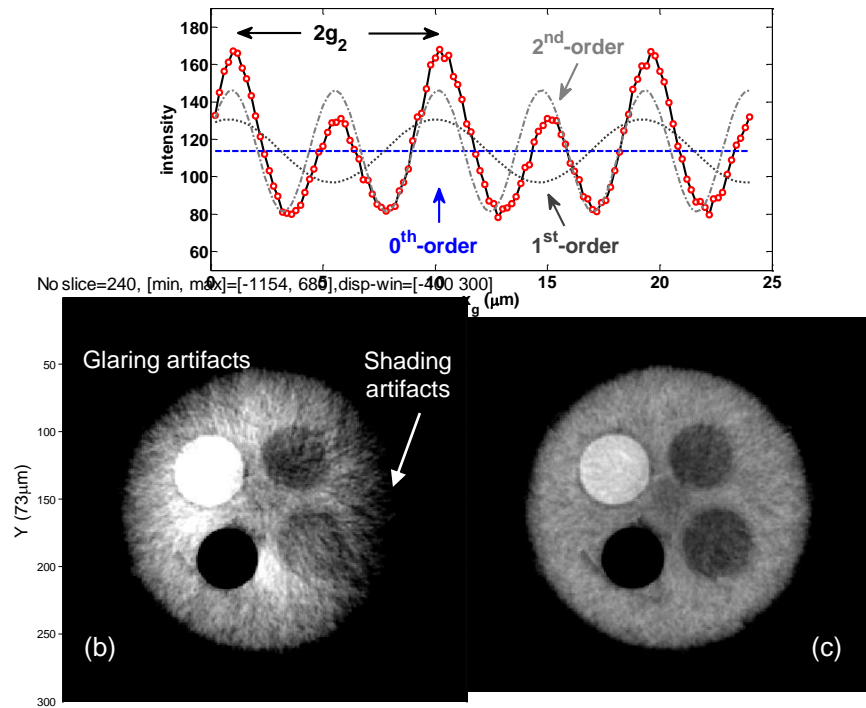


Figure 5. The twin-peaks phenomenon existing in phase stepping curve of the phase contrast CT prototyped in the PI’s lab (**a**) and image of the organic material phantom with artifacts caused by the twin-peaks phenomenon (**b**) and that with the artifacts removed.

D. System integration & optimization–Imaging performance: Transverse x-ray phase contrast CT image of the organic material phantom reconstructed from the projection data acquired at cell dimension $96 \times 96 \mu\text{m}^2$ and $144 \times 144 \mu\text{m}^2$ are presented in Fig. 6 (a') and (b'), respectively. For comparison, their counterparts in the attenuation contrast acquired at roughly identical x-ray dose are displayed in Fig. 6 (a) and (b). The contrast-to-noise ratio (CNR) is measured between the glycerol target and its surroundings. It is observed that, given identical x-ray dose, the CNR in phase contrast CT images at detector cell dimension $96 \times 96 \mu\text{m}^2$ and $144 \times 144 \mu\text{m}^2$ are 140- and 76-folds larger than their counterparts in the attenuation contrast, showing the huge potential capability of x-ray phase contrast CT in soft tissue differentiation.

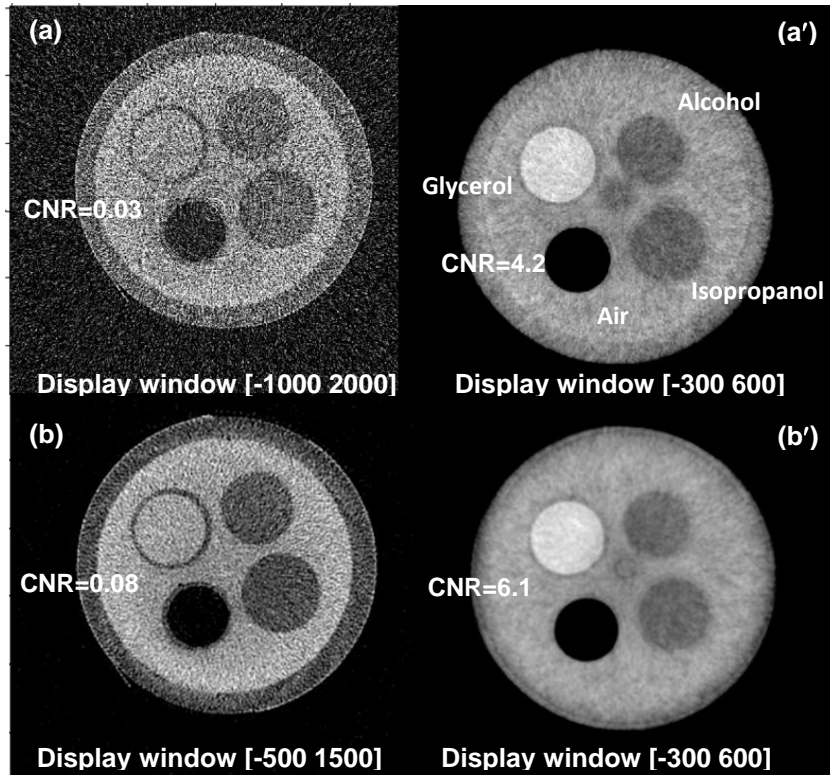


Figure 6. CT images of the organic material phantom corresponding to attenuation contrast (left column) and phase contrast (right column) at detector cell dimension $96 \mu\text{m}$ (top row) and $144 \mu\text{m}$ (bottom row).

E. Subsystem/components–A β -peptide phantoms: As specified in SA#2 of the SOW, using the specially designed A β -phantoms, we'll investigate the CNR of A β_{1-40} and A β_{1-42} fibrils in x-ray phase contrast CT imaging, as a function over the molar concentrations corresponding to normal, pathologic and Alzheimer's brains, in which the amyloid precursor protein (APP) will be included as a reference. Toward this goal, we have made three PMMA (Polymethyl methacrylate) frames for installing the A β -phantoms, and shown in Fig. 7(a) are the major parts (bodies and caps). As initially specified, the tunnels drilled in the PMMA body will be filled with A β_{1-40} /A β_{1-42} peptides/fibrils solutions at selected concentrations (see Table I). The A β -phantoms with the A β_{1-40} and A β_{1-42} fibrils filled and sealed will be installed in the rotation stage of the prototype x-ray phase contrast CT in the way illustrated in Fig. 1(b) to carry out the tasks toward SA#2. However, to avoid biological decay, these targets filled with the A β_{1-40} and A β_{1-42} and their fibrils have to be stored in refrigerator at -20°C . For convenience in storage and

repeated scan, the $\text{A}\beta_{1-40}$ and $\text{A}\beta_{1-42}$ peptides and fibrils are filled in PCR (Polymerase Chain Reaction) tubes as illustrated in Fig. 7(b). These A-beta targets are stored in refrigerator and are mounted on top of the $\text{A}\beta$ -phantom body made of PMMA (Fig. 7(a)) during scan.

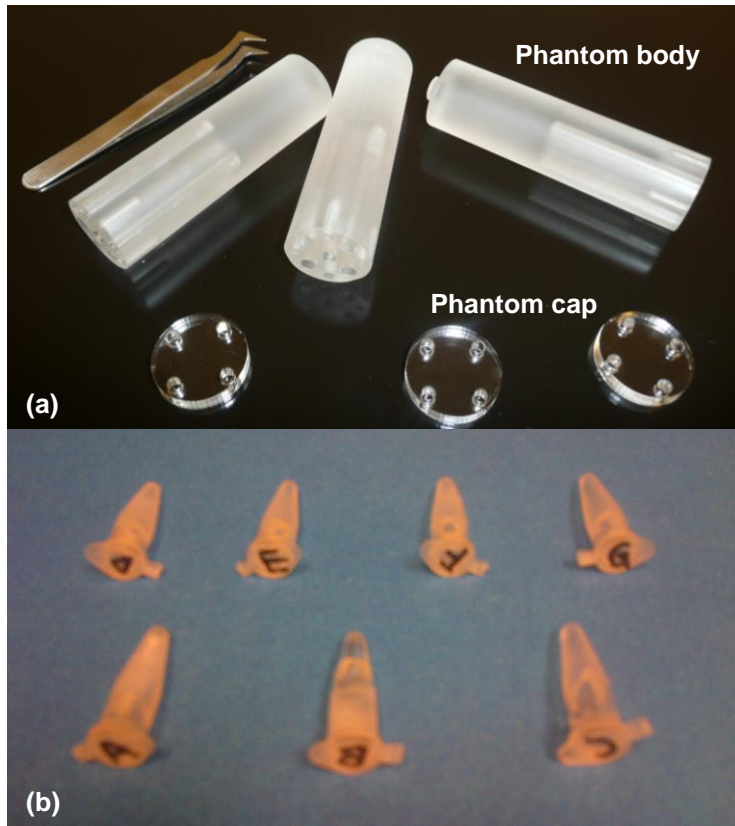


Figure 7. A picture showing: (a) the phantom body made of PMMA for making the image quality phantom and (b) the PCR tubes filled with amyloid precursor protein (A) and $\text{A}\beta$ peptides (B, C, D) and $\text{A}\beta$ peptides/fibrils (E, F, G) to be installed on top of the phantom body (see Table I).

Accomplishments towards Specific Aim 3.

To complete the tasks towards Specific Aim 3, we need to have a collection of specimen of AD brain, normally aged brain and pathologically aged brain. Then, we scan them using the prototyped x-ray phase contrast CT, sort and analyze the acquired images.

A. **Collection of AD brain specimen:** Itemized in Table III are the specimen, including AD brain, normally aged brain and pathologically aged brain, collected by us for the project at the Emory Alzheimer Disease Research Center. Displayed in Fig. 8 are the pictures of an AD brain specimen (Fig. 8(a)) and a normally aged brain. Note that amyloid plaques are visible in the AD brain specimen (Fig. 8(a)).

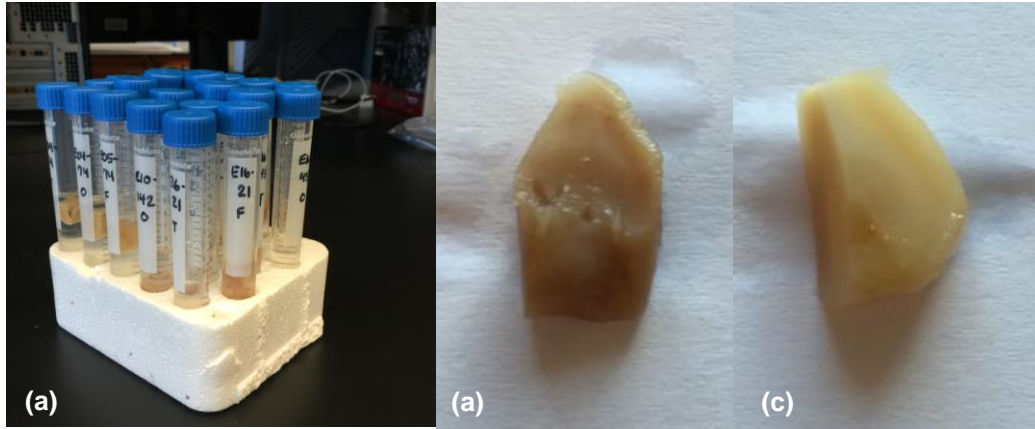


Figure 8. Photographs showing the collection of brain tissue specimen (a), a AD brain specimen with amyloid plaques (b) and normal brain specimen without amyloid plaques (c).

Table III. Collection of postmortem specimen of AD brain and normal pathologically aged brain.

Case Number	Emory Number	Wet Tissues Provided	Primary Neuro Diag.	Secondary Neuro Diag.	Tertiary Neuro Diagnosis
E07-38	A07-38	F,T,O	AD		
E16-21	A16-21	F,T,O	AD		
E11-97	A11-97	F	AD		
E11-139	A11-139	F	AD		
E05-74	A05-74	F,T,O	Control		
E10-142	A10-142	F,T,O	Control	Microinfarct-Hp	NFT-Braak stage II
E16-45	A16-45	F,T,O	Control	Braak I	
E04-74	A04-74	F,T,O	Control/MCI	AD - possible	
E15-97	A15-97	F,T,O	Control	Possible AD	Braak IV
= normal aging					
= asymptomatic AD or pathological aging					

B. Evaluation and comparison of imaging AD specimen in phase contrast and attenuation contrast: Typical transverse CT images corresponding to the attenuation contrast and phase contrast acquired by the prototype x-ray phase contrast CT system are presented in Fig. 9 (a) and (b), respectively. Given identical dose, it is observed that, in the tomographic image corresponding to phase contrast, the gray material and white material are in different CT number, though there is no clear boundary between them. However, no such difference in their CT number is observed in the image corresponding to attenuation contrast. In addition, there seem some microstructures in the AD brain specimen visible in the image corresponding to phase contrast, though they need further verification.

Key Research Accomplishments: We have accomplished the tasks specified in the Statement of Work and below is a summary of our major findings, including positive and negative, and related discussions.

Development of x-ray phase contrast CT, system integration and Performance Optimization: The prototype x-ray phase contrast CT has been built and working at its full functionality as a “three-in-one”

imaging system that generates images corresponding to the attenuation contrast, differential phase contrast and dark field contrast, respectively. The imaging performance of the prototype system has been optimized by significantly improving quality of the key components – gratings G1 and G2, as well as the mechanical accuracy and precision in optical component installation and alignment.

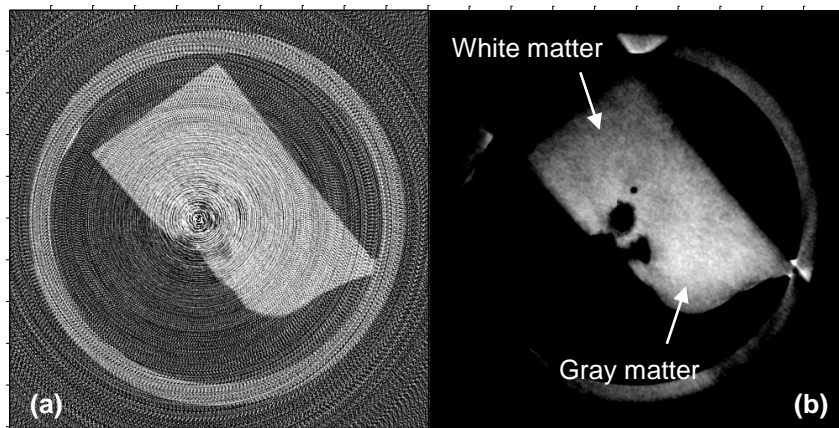


Figure 9. CT images of the AD brain specimen corresponding to attenuation contrast (a) and phase contrast (b) (image in-plane resolution: $48 \times 48 \mu\text{m}$; image slice thickness: 0.96 mm).

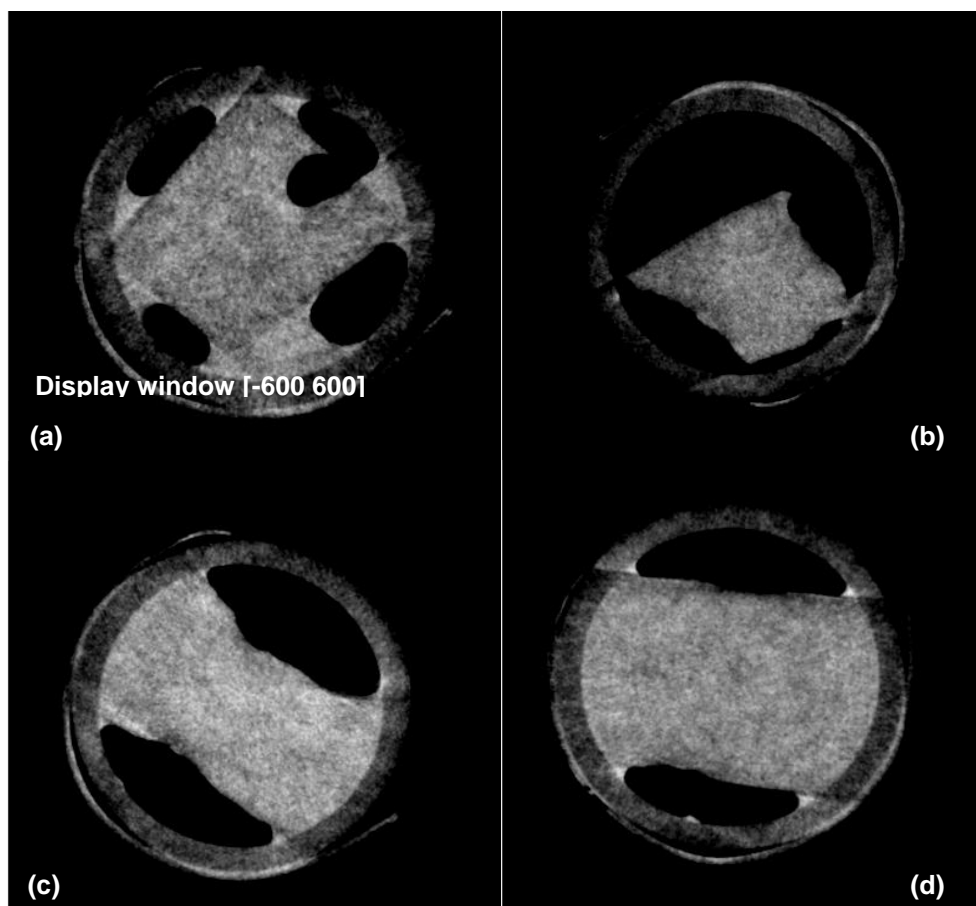


Figure 10. Transverse phase contrast CT images of postmortem AD brain specimen from the front lobe (a), temporal lobe (b), occipital lobe (c) and that of normally aged brain specimen (d) (resolution $48 \mu\text{m}^3$; display window: [-600 600]).

Imaging specimen of AD brain, normally aged brain, and pathologically aged brain, with x-ray phase contrast CT:

- To the best of our knowledge, it is the first time that the specimen of AD brain is imaged and compared to normally aged brain specimen and pathologically aged brain specimen using the grating-based x-ray differential phase contrast CT (Fig. 10).
- It has been shown that the contrast between grey matter and white matter in the grating based differential x-ray phase contrast CT image is substantially higher than that in conventional attenuation contrast CT image (Fig. 9).
- It has been demonstrated that, given identical x-ray dose, the phase contrast CT image of brain specimen is of substantially better signal-to-noise ratio (SNR) than that of conventional attenuation contrast CT image (Fig. 9).
- However, even with substantially improved SNR, the x-ray phase contrast CT still cannot convincingly differentiate the AD brain specimen with amyloid plaques from the normal aged brain specimen without amyloid plaques (Fig. 10).
- Two major factors may contribute to the insufficient SNR for differentiation of the AD brain specimen with amyloid plaques from the normal aged brain specimen without amyloid plaques: (i) the micro-focus x-ray tube is of limited power and cannot reach the tube current that may generate the desired SNR; (ii) the time to acquire the projection data for tomographic image generation is approximately 12 hours, during which the working conditions of both micro-focus x-ray tube and C-MOS x-ray detector drift significantly, which may significantly degrade the performance in SNR.
- These two factors can be effectively addressed simultaneously using a micro-focus tube with significantly larger power and this is believed to be a major opportunity for continuation of the investigation initiated and carried out in this project in the near future.

Scientific leadership establishment: With the valued support by this grant, the research group led by the PI at Emory University has established an international scientific leadership in x-ray phase contrast CT imaging, demonstrated by its publication in the prestigious scientific journals and conferences, and the invitation by journal's editorial board to review manuscripts, and by federal and non-profit funding agencies for the study sections to review research proposals related to x-ray phase contrast CT imaging. Especially, the PI was the co-chair of a session entitled "Phase-contrast CT and Few View CT" in the 3rd International Conference on CT Image Formation in X-ray Computed Tomography (Salt Lake City, Utah, June 22-25, 2014), as well as the chair of another session entitled "Optical, Ultrasound, and Emerging Imaging Techniques" in the AAPM's (American Association of Physicists in Medicine) 52nd Annual Meeting in Austin, TX (August 20-24, 2014).

What opportunities for training and professional development has the project provided?

The project provided a training opportunity for Yi Yang, PhD, a post-doc fellow at the Department of Radiology and Imaging Sciences, Emory University School of Medicine, to transit from the career path of an atomic/plasma physicist and successfully grow into an imaging scientist, with a formal position of senior research associate initially at the Department of Radiology and Imaging Sciences, Emory University School of Medicine and then switched to a formal job position in CT industry after he has gained knowledge, expertise and extensive experience in CT sciences and technologies, via his training supported under this grant.

How were the results disseminated to communities of interest?

Nothing to report.

What do you plan to do during the next reporting period to accomplish the goals?

The project completes at the end of this reporting period.

4. IMPACT

What was the impact on the development of the principal discipline(s) of the project?

- We found that, in addition to the 1st-order derivative (existing art), the 2nd-order derivative also play a significant role in the grating based x-ray phase contrast imaging. We derived the theoretical foundation for system modeling and analysis and provide a practical approach for imaging applications, which has been published in Medical Physics – the scientific journal of American Society of Physicist in Medicine (AAPM)¹¹.
- We found that the dark field signal in the grating based x-ray phase contrast imaging is actually a complex signal, rather than only a real signal as what has been assumed in the literature (existing knowledge). We derived the theoretical foundation for system modeling and analysis and provide a practical approach for signal retrieval and imaging, which has been published in Medical Physics – the scientific journal of AAPM¹².
- We found that there inevitably exists imperfection in gratings – the key components of x-ray phase contrast CT. We derived the theoretical foundation for system modeling and analysis and provide an effective approach to successfully cope with it, which has been published in Medical Physics – the scientific journal of AAPM¹³.
- We found that, in the situation with twin-peaks, the radiation dose required by grating based x-ray phase contrast CT can still be significantly reduced by algebraic method. We derived the theoretical foundation for system modeling and analysis and provide an effective approach to successfully reduce radiation dose. The method and preliminary data have been submitted to Medical Physics as a paper that is in revision¹⁴.

What was the impact on other disciplines?

Nothing to report.

What was the impact on technology transfer?

Nothing to report.

What was the impact on society beyond science and technology?

Nothing to report.

5. CHANGES/PROBLEMS

Nothing to report.

6. PRODUCTS:

Publications, conference papers, and presentations

In Peer-reviewed Journals (manuscript attached in appendix): Five papers that are partially supported by the grant or related to the subject of the project were published in Medical Physics, one of the leading scientific journals in Medical Imaging. In addition, one manuscript has been submitted to Medical Physics and in the revision process.

1. Tang X, Yang Y and Tang S, "Characterization of imaging performance in differential phase contrast CT compared with the conventional CT – Spectrum of noise equivalent quanta NEQ(k)" *Med. Phys.*, 39(7): 4467-82, 2012.
2. Yang Y and Tang X, "The second-order differential phase contrast and its retrieval for imaging with x-ray Talbot interferometry," *Med. Phys.*, v.39, pp.7237-53, 2012.
3. Tang S and Tang X, "Radial differential interior tomography and its image reconstruction with differentiated backprojection and projection onto convex sets," *Med. Phys.*, v.40, 101914 (14pp.), 2013.
4. Yang Y and Tang X, "Complex dark-field contrast and its retrieval in x-ray phase contrast imaging implemented with Talbot interferometry," *Med. Phys.*, v.41, 101914 (19pp.), 2014.
5. Yang Y, Xie H, Cai W, Mao H and Tang X, "Grating-based x-ray differential phase contrast imaging with twin peaks in phase-stepping curves—phase retrieval and dewrapping," *Med. Phys.*, v.42, pp.2855-69, 2016.
6. Xie H, Cai W, Yang L, Mao H and Tang X, "Reducing radiation dose in grating based x-ray phase contrast CT with twin-peaks in its phase stepping curves," submitted to *Med. Phys.*, *in revision*, 2016

In peer-reviewed Conferences (manuscript not attached in appendix): Seven papers were published in SPIE Medical Imaging Conference, RSNA's Scientific Assembly and Exhibition, and AAPM Annual Meetings etc..

1. X Tang, Y Yang and S Tang, "The potential imaging performance of differential phase contrast CT – NPS(k), MTF(k) and NEQ(k)," *Proc. 2nd International Conf. Image Formation in X-ray CT*, pp.271-74, 2012.
2. X. Tang, Y. Yang and S. Tang, "NEQ(k): The signal and noise transfer properties in differential phase contrast CT," 54th AAPM (American Association of Physicists in Medicine) annual Meeting, Charlotte, NC, July 29 – Aug. 2, 2012.
3. X. Tang, Y. Yang and S. Tang, "The property of signal-to-noise and its variation over spatial frequency in differential phase contrast CT," IEEE Medical Imaging Conference, Anaheim, Oct. 27 – Nov. 3, 2012.
4. X. Tang, Y. Yang and S. Tang, "Spectrum of noise equivalent quanta NEQ(k) – Differential phase contrast CT vs. conventional CT," RSNA 98th Scientific Assembly and Annual Meeting Program, Chicago, Nov. 25 – 30, 2012.
5. X Tang, Y Yang and S Tang, "Detectability index of differential phase contrast CT compared with conventional CT: a preliminary channelized Hotelling observer study," *Proc. SPIE*, v.8668, 2013.
6. X. Tang and Y. Yang, "Internal noise in channelized Hotelling observer (CHO) study of detectability index – differential phase contrast CT vs. conventional CT," *SPIE Proc.* vol. 9033, Medical Imaging 2014: Physics of Medical Imaging, 903326 (March 19, 2014): doi:10.1117/12.2043251.
7. Y. Yang and X. Tang, "Complex dark-field contrast in grating-based x-ray phase contrast imaging," *SPIE Proc.* vol. 9421, Medical Imaging 2014: Physics of Medical Imaging, 941257 (March 18, 2015): doi:10.1117/12.2082294.

Website(s) or other Internet site(s): No

Technologies or techniques: Nothing to report.

Inventions, patent applications, and/or licenses: Nothing to report.

Other Products: Collection of specimens of AD brain, normally aged brain and pathologically aged brain.

7. PARTICIPANTS & OTHER COLLABORATING ORGANIZATIONS

What individuals have worked on the project? The senior personnel who have participated in the project are listed in Table IV.

Table IV. Senior personnel of the project.

Name	Role	Effort (m/yr)	Contribution
X. Tang, PhD	PI	1.2	Project design and leadership, x-ray phase contrast CT development, optimization, data acquisition and image analysis
C Meltzer, MD	Co-inv	0.12	Project design, AD radiologic guidance
H Mao, PhD	Co-inv	0.24	Biochemistry guidance and support
M Gearing, PhD	Co-inv	1.2	AD pathology guidance and support, collection of specimen

Has there been a change in the active other support of the PD/PI(s) or senior/key personnel since the last reporting period?

Nothing to report.

What other organizations were involved as partners?

Nothing to report.

8. SPECIAL REPORTING REQUIREMENTS

COLLABORATIVE AWARDS: Nothing to report.

QUAD CHARTS: Nothing to report.

9. APPENDICES: See attachments.

References:

1. http://www.alz.org/alzheimers_disease_facts_figures.asp, accessed on Dec. 31st, 2010.
2. Roberson ED and Mucke L, "100 years and counting: Prospects for defeating Alzheimer's disease," *Science*, 314:781-84, 2006.
3. Goedert M and Spillantini MG, "A century of Alzheimer's disease," *Science*, v.314, pp 777-81, 2006. Tang X, Ning R, Yu R. and Conover D, "Cone beam volume CT image artifacts caused by defective cells in x-ray flat panel imagers and the artifact removal using a wavelet-analysis-based algorithm" *Med. Phys.*, 28(3): 812-25, 2001.
4. X Wu and H Liu, "Clinical implementation of x-ray phase-contrast imaging: Theoretical foundations and design considerations," *Med. Phys.*, v.30, pp.2169-79, 2003.
5. DM Connor, H Benveniste, FA Dilmanian, MF Kritzer, LM Miller and Z Zhong, "Computed tomography of amyloid plaques in a mouse model of Alzheimer's disease using diffraction enhanced imaging," *NeuroImage*, v.46, pp 908-14, 2009.
6. F Pfeiffer, T Weitkamp, O Bunk, C David, "Phase retrieval and differential phase-contrast imaging with low-brilliance x-ray sources," *Nature Phys.*, v.2, pp.258-61, 2006.
7. M Bech, TH Jensen, R Feidenhan'l, O Bunk, C David and F Pfeiffer, "Soft-tissue phase-contrast tomography with x-ray tube source," *Phys. Med. Biol.*, v.54, pp.2747-53, 2009.
8. Tang X, Yang Y and Tang S, "Characterization of imaging performance in differential phase contrast CT compared with the conventional CT – Noise power spectrum NPS(k)," *Med. Phys.*, vol. 38, pp. 4386-95, 2011.
9. Tang X, Yang Y and Tang S, "Characterization of imaging performance in differential phase contrast CT compared with the conventional CT – Spectrum of noise equivalent quanta NEQ(k)" *Med. Phys.*, 39(7): 4467-82, 2012.
10. C David, J Bruder, T Rohbeck, C Grunzweig, C Kottler, A Diaz, O Bunk and F Pfeiffer, "Fabrication of diffraction gratings for hard x-ray phase contrast imaging," *Microelect. Eng.*, v.84(5-8), pp1172-77, 2007.
11. Yang Y and Tang X, "The second-order differential phase contrast and its retrieval for imaging with x-ray Talbot interferometry," *Med. Phys.*, v.39, pp.7237-53, 2012.
12. Yang Y and Tang X, "Complex dark-field contrast and its retrieval in x-ray phase contrast imaging implemented with Talbot interferometry," *Med. Phys.*, v.41, 101914 (19pp.), 2014.
13. Yang Y, Xie H, Cai W, Mao H and Tang X, "Grating-based x-ray differential phase contrast imaging with twin peaks in phase-stepping curves–phase retrieval and dewrapping," *Med. Phys.*, v.42, pp.2855-69, 2016.
14. Xie H, Cai W, Yang L, Mao H and Tang X, "Reducing radiation dose in grating based x-ray phase contrast CT with twin-peaks in its phase stepping curves," submitted to *Med. Phys.*, *in revision*, 2016